STOKES FLOW IN THIN FILMS

D.E.A. van Odyck

This research project was sponsored by NWO-Technology Foundation STW. It was carried out at the University of Twente.

ISBN: 90-9014820-5

Printed by FEBO druk B.V., Enschede.

STOKES FLOW IN THIN FILMS

PROEFSCHRIFT

ter verkrijging van
de graad van doctor aan de Universiteit Twente,
op gezag van de rector magnificus,
prof.dr. F.A. van Vught,
volgens besluit van het College voor Promoties
in het openbaar te verdedigen
op vrijdag 18 mei 2001 te 13.15 uur.

door

Daniel Ernst Albert van Odyck
geboren op 19 mei 1972
te Emmerich, Duitsland

Dit proefschrift is goedgekeurd door:

Promotor:	prof.ir. A.W.J. de Gee
Promotor:	prof.dr.ir. H. Hoeijmakers
Assistent-promotor:	dr.ir. C.H. Venner

Acknowledgement

This work could not have been carried out without the help of many people and organizations. Two organizations I would like to thank for their financial support, namely: the Dutch Technology Foundation STW and the University of Twente.

I would like to thank the (ex-)members of the tribology group of the faculty of Mechanical Engineering of the University of Twente for their cooperation and support over the past four years and for creating a pleasant atmosphere to work: Ton de Gee, Johan Ligterink, Hans Moes, Wijtze ten Napel, Matthijn de Rooij, Dik Schipper, Kees Venner, Laurens de Boer, Willy Kerver, Walter Lette, Erik de Vries, Bernd Brogle, Rob Cuperus, Mark van Drogen, Edwin Gelinck, Qiang Liu, Harald Lubbinge, Marc Masen, Henk Metselaar, Elmer Mulder, Patrick Pirson, Jan Willem Sloetjes, Ronald van der Stegen, Harm Visscher, André Westeneng and Ysbrand Wijnant.

I would like to thank Ton de Gee, Harry Hoeijmakers and Kees Venner for being my promotors. From the Texas A&M University I would like to thank Luis San Andres for his remarks concerning the theory. Special thanks to my supervisor and co-promotor Kees Venner for the many discussions and suggestions regarding this research. His positive attitude helped me through moments of set-back. I would like to thank Harry Hoeijmakers for his constructive remarks on the manuscript.

From the "Centrum voor Wiskunde en Informatica" (CWI), Amsterdam, I would like to thank Barry Koren for his suggestions and for reading part of the manuscript. Also I would like to thank the members of the Modeling, Analysis and Simulation group at the CWI for their interest and suggestions. At this point I would like to mention Jaap Noordmans, a former member of the CWI, who performed the first steps in developing a Stokes solver in the field of tribology, but unfortunate he past away too young to see the results.

I would like to thank the members of the STW user committee: Piet Lugt (SKF-ERC), Jos van der Kooij (Corus), Leon Jacobs (Corus), Hans Piekaar (STW) and Wijtze ten Napel (UT) for their interest and constructive support during the project.

For the pleasant working environment I would like to thank my (ex-)room mates: Qiang Liu, Matthijn de Rooij and André Westeneng.

Samenvatting

Om de stroming van een smeervloeistof tussen twee bijna in contact zijnde oppervlakken te beschrijven, in bijvoorbeeld kogellagers, wordt er veelvuldig gebruik gemaakt van de Reynolds vergelijking. Deze vergelijking kan afgeleid worden uit de Navier-Stokes vergelijkingen, onder de aanname dat de spleet tussen de twee oppervlakken klein is en het Reynolds getal laag is. In de meeste gevallen kan deze vergelijking de stroming van de smeervloeistof in de dunne film goed beschrijven. Als de filmdikte groot is t.o.v. de ruwheid kan de invloed van de oppervlakte ruwheid verwaarloosd worden. Echter, met afnemende filmdikte zal de invloed van de oppervlakte ruwheid belangrijker worden, en kan de Reynolds vergelijking aan geldigheid verliezen. In dit werk wordt onderzocht onder welke omstandigheden de Reynolds vergelijking niet langer de stroming van de smeervloeistof correct beschrijft. Om dit te doen wordt de veronderstelling dat de ratio filmdikte tot contact lengte klein is, losgelaten. De stroming wordt dan beschreven door de Stokes vergelijkingen. Er wordt onderzocht hoe het verschil tussen de Stokes oplossing en de Reynolds oplossing afhangt van de geometrie van de oppervlakken voor typische problemen zoals de stroming tussen twee oppervlakken met op één oppervlak een sinus vormige uitstulping. Omdat er in het algemeen geen analytische oplossing is voor het probleem is er eerst een numeriek algoritme ontwikkeld om de Stokes vergelijkingen op te lossen. Voor verschillende oppervlakte geometrieën is vervolgens het verschil tussen de Stokes oplossing en de Reynolds oplossing gequantificeerd.

Niet alleen de geometrie van de loopvlakken in een hydrodynamisch gesmeerd contact heeft invloed op de nauwkeurigheid van de Reynolds oplossing t.o.v. de Stokes oplossing, maar ook de (mogelijke) druk afhankelijkheid van de dichtheid en de viscositeit kunnen een rol spelen. Dit onderwerp is ook onderzocht. Een voorbeeld van een compressibel smeermiddel is gas (lucht). Normaliter wordt voor gas smerings problemen de Reynolds vergelijking gebruikt. In dit werk wordt de gas stroming onder een stap geometrie onderzocht om de Reynolds oplossing te valideren voor dit geval. Een ander voorbeeld waarin de dichtheid druk afhankelijk is, doet zich voor bij de simulatie van cavitatie. Om tot een realistisch model te komen van de stroming in een nauwe spleet, kan het meenemen van een cavitatie model niet achterwege gelaten worden. Het weerhoudt de druk ervan om kleiner te worden dan de damp druk. In dit werk wordt een twee fasen model geïmplementeerd in het numerieke algoritme om de Stokes vergelijkingen op te lossen.

Ten slotte, is de invloed van een druk afhankelijke viscositeit op de geldigheid van de Reynolds vergelijking onderzocht voor de stroming in een kanaal met op één van de oppervlakken een sinus vormige uitstulping. Aan het eind van het proefschrift bevinden zich de conclusies en de aanbevelingen voor vervolg onderzoek.

Abstract

To describe the flow of a lubricant between two nearly contacting surfaces, in for example bearings, frequently use is made of the Reynolds equation. This equation is deduced from the Navier-Stokes equations under the assumptions that the gap between the surfaces, and the Reynolds number is small. It has been used for the past one-hundred years to analyze all kinds of hydro/aerodynamic lubrication problems. In most cases, it can accurately predict the characteristics of the flow in the lubricant film. However, with decreasing film thickness in bearings, the roughness of the contacting surfaces becomes more important and the Reynolds equation less appropiate. In this work it is studied under which conditions the Reynolds equation no longer approximates the flow acurately. To do so the assumption that the ratio film thickness to contact length is small, is dropped. The flow can then be described by the Stokes equations. It is studied how the geometry of the contacting surfaces influences the difference between the Stokes solution and the Reynolds solution for the flow between two surfaces with on one surface a sinusoidal feature. Because generally there is no analytic solution to the problem, first a numerical algorithm was developed to solve the Stokes equations. This algorithm was subsequently used to quantify the difference between the Stokes solution and the Reynolds solution for different configurations of the contacting surfaces.

Not only the geometry of the surfaces can result in a less accurate Reynolds solution, relative to the Stokes solution, but also compressibility and piezo-viscous effects have an impact on the accuracy of the Reynolds solution relative to the Stokes solution. This subject is also studied. A clear example of a compressible lubricant is gas (air). Also for gas lubrication problems the Reynolds equation is normally used. In this work the flow under a step geometry is studied to investigate the validity of the Reynolds equation for this case. Another example of a pressure dependent density can be found in the simulation of cavitation. In order to obtain a realistic model for the lubricant flow in a narrow gap, a cavitation algorithm should be incorporated. It prevents the pressure from dropping below the vapor pressure. In this work a two-phase model is implemented in the numerical algorithm to solve the Stokes equations.

Finally, the influence of a pressure dependent viscosity on the validity of the Reynolds equation is studied for the flow in a channel containing a sinusoidal surface feature. The thesis is concluded with conclusions and with some recommendations for future research.

Contents

Notation

If the dimension is not stated the variable or parameter is dimensionless.

a_v	speed of sound in vapor $[m/s]$
a_{min}	minimal speed of sound in mixture $[m/s]$
a_1, a_2, a_3, a_4, a_5	parameters used in $h(x)$
$\mathbf{a}^{(k)}$	contravariant base vector
$\mathbf{a}_{(k)}$	covariant base vector
A	amplitude wave $[m]$
A_m	amplitude wave
$\tilde{D}$	diagonal matrix of L^h
$\mathbf{e}_m^h$	error vector $\mathbf{e}_m^h = \mathbf{u}_m^h - \mathbf{u}$
f_b	function needed in backtracking algorithm $f_b = \frac{1}{2}\mathbf{L}^h \cdot \mathbf{L}^h$
$\mathbf{f}$	right hand side vector
$\mathbf{f_e}$	external force $[N]$
$\mathbf{f}^h$	right hand side vector for discretized problem
F_p	force perpendicular to lower surface
F_w	force tangent to lower surface
F_{rey}	force perpendicular to lower surface resulting from Reynolds solution
F_{rey}^{∞}	force perpendicular to lower surface resulting from high speed Reynolds solution
$\sqrt{g}$	Jacobian of coordinate transformation
g_{kl}	metric tensor
$g_b(\lambda_b)$	backtracking function
G	computational domain
$G_{\delta\xi}$	computational grid
h	grid spacing fine grid
$h(x)$	film thickness function
$h_1(x)$	film thickness function lower surface $[m]$
$h_2(x)$	film thickness function upper surface $[m]$
H	grid spacing coarse grid
H	reference film thickness $[m]$
H_{tot}	film thickness function $[m]$
H_{loc}	local film thickness $[m]$
I_h^H	restriction operator
I_H^h	prolongation operator

J	Jacobian of coordinate transformation $J = \sqrt{g}$
J_b	Jacobian of $\mathbf{L}^h(\mathbf{u}^h)$
L	reference length $[m]$
$L()$	differential operator
L^h	matrix resulting from discretizing $L()$
$\tilde{L}$	lower triangular matrix resulting from L^h
$[L^h]$	stencil representation of L^h
$\tilde{L}^h$	matrix appearing in SCGS
$\bar{L}^h$	reduced $\tilde{L}^h$ matrix
l_1, l_2, l_3	parameters used in x-coordinate transformation
M	number of unknowns
N	number of cells in ξ^i-direction $(i = 1, 2)$ on square computational grid
N_c	number of multi-grid cycles
p	pressure, only in equations (2.1), (2.3), (2.67) and (2.69) it has dimension $[Pa]$ otherwise it is dimensionless
p_0, p_1, p_2	perturbation pressures
$\tilde{p}_1(x)$	pressure resulting from perturbation analysis
$\tilde{p}_2(x)$	pressure resulting from perturbation analysis
p_v	vapor pressure $[Pa]$
$\bar{p}_v$	scaled vapor pressure $\bar{p}_v = \frac{p_v H}{\eta_0 u_0}$
p_{ij}	discrete pressure
p_w, p_e	pressure on inflow/outflow boundary
p_r	pressure resulting from Reynolds solution
p_s	pressure resulting from Stokes solution
$\mathbf{p}_n$	Newton step in backtracking algorithm
ru_{ij}^h	discrete x-momentum residue
rw_{ij}^h	discrete z-momentum residue
rp_{ij}^h	discrete continuity residue
$\mathbf{r}^h$	discrete residue $\mathbf{r}^h = \mathbf{f}^h - L^h(\mathbf{u}^h)$
$\bar{R}$	relative lift force
$R_x(\xi)$	Auto-Correlation function x-direction $[m^2]$
$R_y(\xi)$	Auto-Correlation function y-direction $[m^2]$
$R(\xi)$	Auto-Correlation function $[m^2]$
R_e	Reynolds number $R_e = \frac{H \rho_0 u_0}{\eta_0}$
R_g	Gas constant
S	iteration matrix
$[S]$	stencil form iteration matrix
u	velocity component in x-direction, only in equations (2.1), (2.2) and (2.3) it has dimension $[m/s]$ otherwise it is dimensionless
u_r	velocity component in x-direction resulting from Reynolds solution
u_s	velocity component in x-direction resulting from Stokes solution
u_0	reference velocity component in x-direction $[m/s]$
$\mathbf{u}_0$	reference velocity vector $[m/s]$
u_1	lower surface speed
u_2	upper surface speed

u_0	zeroth-order perturbation velocity component in the x-direction
u_1	first-order perturbation velocity component in the x-direction
u_{ij}	discrete x-direction velocity component
$\mathbf{u}$	vector of unknowns
$\mathbf{u}^h$	vector of unknowns on grid with spacing h
$\mathbf{u}_0^h$	initial approximation to $\mathbf{u}^h$
$\mathbf{u}_m^h$	mth approximation to $\mathbf{u}^h$
$\tilde{\mathbf{u}}^h$	old approximation to $\mathbf{u}^h$
$\bar{\mathbf{u}}^h$	new approximation to $\mathbf{u}^h$
v	velocity component in y-direction, only in equations (2.1), (2.2) and (2.3) it has dimension $[m/s]$ otherwise it is dimensionless
v_0	reference velocity component in y-direction $[m/s]$
w	velocity component in z-direction, only in equations (2.1), (2.2) and (2.3) it has dimension $[m/s]$ otherwise it is dimensionless
$\mathbf{v}$	velocity vector $\mathbf{v} = (u, v, w)^T$ $[m/s]$
w_0	reference velocity component in z-direction $[m/s]$
w_r	velocity component in z-direction resulting from Reynolds solution
w_s	velocity component in z-direction resulting from Stokes solution
w_0	zeroth order perturbation velocity component in the z-direction
w_1	first order perturbation velocity component in the z-direction
w_{ij}	discrete z-direction velocity component
x, y, z	space coordinates, only in equations (2.1), (2.2), (2.3) and in chapter (*1*) it has dimension $[m]$ otherwise they are dimensionless
α	grid aspect angle
α_p	pressure viscosity coefficient $[1/Pa]$
$\bar{\alpha}_p$	pressure viscosity coefficient $\bar{\alpha}_p = \frac{\alpha \eta_0 u_0}{H}$
α^a	mass fraction (appendix B)
α^a_{min}	minimal mass fraction (appendix B)
β	parameter in x-coordinate transformation
β_ρ	parameter in two phase cavitation model $\beta_\rho = \frac{2\eta_0 u_0}{H \rho_l a^2_{min}}$
β_η	parameter in two phase cavitation model
γ	perturbation parameter $\gamma = \epsilon^2$
Γ	boundary domain Ω
$\delta\xi$	mesh spacing in square computational domain, $\delta\xi = 1/N$
$\delta\xi^1$	mesh spacing in computational domain in ξ^1-direction
$\delta\xi^2$	mesh spacing in computational domain in ξ^2-direction
$\Delta\rho$	parameter in two phase cavitation model $[kg/m^3]$ $\Delta\rho = \frac{1}{2}(\rho_l - \rho_v)$
Δp	parameter in two phase cavitation model $[Pa]$ $\Delta p = \frac{1}{2}\pi a^2_{min}\Delta\rho$
Δx	parameter in x-coordinate transformation
$\Delta\xi^1$	parameter in x-coordinate transformation
ϵ	ratio of domain size $\epsilon = \frac{H}{L}$
η	viscosity, only in equation (2.1) it has dimension $[Pas]$ otherwise it is dimensionless
η_0	reference viscosity $[Pas]$
$\bar{\eta}_0$	$= \frac{\eta_v}{\eta_l}$

η_l	liquid viscosity $[Pas]$
η_v	vapor viscosity $[Pas]$
η_{ij}	discrete viscosity
$\boldsymbol{\theta}$	Fourier frequency vector
λ	wavelength
$\lambda(\boldsymbol{\theta})$	eigenvalues
Λ	wavelength $[m]$
Λ_l	correlation length $[m]$
Λ_ω	correlation wavelength $[m]$
Λ_c	roughness wavelength $[m]$
Λ_n	bearing number
μ	amplification factor
ν_1, ν_2	number of relaxations before/after multi-grid cycle
ξ	correlation length $[m]$
ξ^1, ξ^2	computational coordinates
ξ_i^1, ξ_j^2	discrete computational coordinates
ρ	density, only in equations (2.1), (2.2), (2.67) and (2.69) it has dimension $[kg/m^3]$ otherwise it is dimensionless
ρ_0	reference density $[kg/m^3]$
ρ_l	liquid density $[kg/m^3]$
ρ_v	vapor density $[kg/m^3]$
$\bar{\rho}_0$	$= \frac{\rho_v}{\rho_l}$
ρ_{ij}	discrete density
ρ_{spec}	spectral radius
σ^2	Root Mean Square value $[m^2]$
$\bar{\tau}_{ij}$	shear stress tensor $[kgm^2/s^2]$
$\phi(x, z)$	stream function
Ω	physical domain

Chapter 1

Introduction

Friction plays an important role in everyday life. It occurs in all situations where a force is transmitted from one surface to another, e.g. in bearings. To control and minimize the friction in order to reduce vibrations and wear it is common to introduce a lubricant between the contacting surfaces.

1.1 Lubrication

In order to decrease the friction and wear between two contacting surfaces it is common to separate both surfaces with a lubricant, a grease or a coating. The lubricant film should fulfill two requirements. Firstly, its shear strength should be low to be able to obtain a low friction. Secondly, in the direction perpendicular to the surface, it should be sufficiently strong to carry the entire load and prevent direct contact between the two surfaces. In that case all shear takes place in the lubricant and the friction is determined by the shear strength of the lubricant.

Often, not much is needed to create a lubricant film. The lubricant adheres easily to the surfaces and the relative motion of these surfaces causes the entrainment of the lubricant into the contact. In that case the thickness of the film that is formed depends on the relative surface speeds, the shape of the surfaces and the properties of the lubricant, especially the viscosity. This type of lubrication is called Hydrodynamic Lubrication (HL) and in practice it results in film thicknesses of the order of micro meters and generated pressures of the order of Mega Pascal's.

The fact that a lubricant film can form and carry a load was first recognized by Tower [81] in his experiments. In response to his work Reynolds [65] developed the theory to explain this film formation. Starting from the Navier-Stokes equations and assuming a small film thickness relative to the contact length he derived an equation for the pressure in the gap. The main ingredients of this equation are the shape of the gap and the surface velocities. This equation is generally referred to as the Reynolds equation.

This equation turned out to be a very useful tool in bearing analysis and design. The earliest examples of the application of the Reynolds equation to bearing design are the tilting pad thrust bearing, patented by Michell [45], [46] and Kingsbury [42]. Much of the early work was further invested in the analysis of the regular journal bearing, see Sommerfeld [73]. For a detailed account of the history of lubrication the reader is referred

to the History of Tribology written by Dowson [21]. An overview of the analysis of many Hydrodynamic Lubrication problems is given by Cameron [7].

One of the complications in the early years was to obtain the solutions to the Reynolds equation for a given surface geometry with the available analytical tools. This situation changed with the introduction of the digital computer and the algorithms that were developed for the numerical solution of the Reynolds equation. One of the earliest examples of numerical analysis in tribology is the work of Sassenfeld and Walther [71] on the journal bearing problem of finite width.

Following the successful application of Reynolds' theory to journal bearings at the beginning of the previous century Martin [44] and Gümbel [33] were the first to apply it to the problem of the lubrication of gear teeth. The difference between this problem and the previous bearing problems is that the surface geometries are non-conforming which leads to a so-called concentrated contact. They assumed the gear teeth to be rigid and the lubricant to be iso viscous. The predicted film thicknesses were very small compared to the known surface roughness values of gears and it was concluded that the successful operation of gears without wear observed in practice could not (yet) be accounted for by the lubricant film.

It took about 30 years before the question was eventually answered and the two additional effects responsible for the film formation in concentrated contacts were recognized: the elastic deformation of the surfaces due to the high pressures, and the increase of the viscosity with increasing pressure. Keynote works in this sense are the works of Ertel [28] and Grubin [32] followed by the first numerical solutions obtained by Petrusevich [57]. By now the lubrication of concentrated contacts has evolved into a separate field: Elasto-Hydrodynamic Lubrication.

As a result of the additional complication of surface deformation and piezo-viscous effects EHL problems turned out to be much more difficult to solve than HL problems and here the role of the digital computer has been even larger. Dowson and Higginson [23], [24] were the first to present a film thickness formula for EHL line contacts based on numerical solutions, and Hamrock and Dowson [36], [37] did so for EHL point contacts. These studies also showed that standard iterative techniques did not work very well for EHL problems. Especially, the elastic deformation integrals caused two types of problems. Firstly computing time problems as the matrices of the discrete problem were full, rather than sparse. Secondly the coupling between pressure and film shape by the elastic deformation caused stability problems in the numerical algorithms. An important step forward in this field was the introduction of multi-grid techniques. At present efficient and stable solution algorithms are available for EHL problems. For a detailed description the reader is referred to [90]. At this point it is noted that in this field not only the numerical techniques have reached a very high level but also experimental techniques have been improved to a level which allows detailed validation of the predictions of the theoretical models [8].

It thus seems that at present all the theoretical and experimental tools are available to answer most lubrication problems. This is not entirely true. When discussing the work of Martin and Gümbel surface roughness was already mentioned. Technical surfaces are never perfectly smooth and an important question is how to account for the effect of the surface roughness on the film formation. Clearly if the surfaces are so smooth that the

computed minimum film thickness for the given operating conditions is large compared to the standard deviation of the surface roughness profile in the contact the effect of the roughness will be negligible. However, if the roughness is comparable to the thickness of the film one has to take into account its effect on film formation. The question of the effect of surface roughness on film formation is not new and has been the subject of many publications already as will be explained in section (*1.3*). However, before doing so first a brief illustration of surface roughness is given in the next section.

1.2 Surface roughness

Realistic surfaces are non-smooth and contain surface roughness. Especially when the surface roughness is of the order of the film thickness the non-smoothness of the surface must be considered. In order to illustrate this, three different type of bearings have been studied. In figures (1.1a), (1.3)(a) and (1.5) photographs of the bearings are shown. The three bearings are: a ball bearing, a cylindrical roller bearing and a spherical roller bearing. They are labeled with respectively A, B and C. An extension to this code indicates the surface type: i labels for the inner raceway, o labels for the outer raceway and r labels for the roller/ball. For these three bearings a surface study has been performed. This study has been done for the inner, outer raceway and for the roller/ball. In figures (1.1), (1.2), (1.3), (1.4) and (1.6) the surface height maps of the different bearing surfaces are shown. In these figures the colored bar on the left hand side in a picture translates a color back to a surface height. The horizontal axis represents the x-axis (running direction) and the line under an angle with the horizontal line represents the y-axis (transverse to the running direction).

The surface height maps clearly show that the surfaces are not perfectly smooth. It is also observed that some of them show a clear pattern. Figures (1.1b), (1.2a), (1.4a) and (1.6a) show a pattern of ridges and furrows. This is not the case in figures (1.2b), (1.3b) and (1.6b). This kind of surface topography is the result of the manufacturing process (grinding).

Not only in bearings the non-smoothness of the surface must be considered but also in rolling. The rolling process takes place in the mixed lubrication regime. This means that parts of the roller and the rolled sheet are in direct contact and other parts are lubricated. Figures (1.7a) and (1.7b) show two surface height maps of rolled sheet after cold rolling and after a post-rolling step. It is clear that the surfaces are non-smooth on this scale.

Besides visual inspection of the surface topography, one can study the surface height map with statistical tools (for more on this subject see [96]). To characterize the surface it is assumed that it can be described by an amplitude density function and an autocorrelation function. The first function provides the probability density of the roughness heights and the second function provides the information related to the roughness spacing. The total film thickness can be written as the sum of the nominal film thickness (H_n) and the roughness height (H_r)

$$H_{tot}(x,y) = H_n(x,y) + H_r(x,y) \ , \tag{1.1}$$

with (x,y) surface coordinates along the film. The surface height maps in figures (1.1), (1.2), (1.3), (1.4), (1.6) and (1.7) can be represented by the function $H_r(x,y)$ in equation

(1.1). Now the Root Mean Square (RMS) roughness can be defined as:

$$\sigma^2 = \frac{1}{4L^2}\int_{-L}^{L}\int_{-L}^{L} H_r^2(x,y)\ dxdy\ . \tag{1.2}$$

The Auto-Correlation Function (ACF) in x-direction is defined as:

$$R_x(\xi) = \frac{1}{4L^2}\int_{-L}^{L}\int_{-L}^{L-\xi} H_r(x,y)H_r(x+\xi,y)\ dx\ dy\ , 0 \leq \xi \leq L\ . \tag{1.3}$$

and a similar expression for $R_y(\xi)$. For many surfaces the ACF can be represented by the equation

$$R(\xi) = \sigma^2 e^{-(\xi/\Lambda_l)^2}\cos(\frac{2\pi}{\Lambda_\omega}\xi)\ , \tag{1.4}$$

where Λ_l is the correlation length and Λ_ω is the correlation wavelength. The proposed $R(\xi)$ can be fitted to the experimentally found $R_x(\xi)$ and $R_y(\xi)$, resulting in a correlation length/wavelength in, respectively, the x and y direction. The cosine in equation (1.4) indicates that there is some regularity in the surface, introduced by the manufacturing process. The smallest of the two correlation lengths, Λ_l and Λ_ω, defines the characteristic roughness wavelength Λ_c. It is now possible to analyze some real surfaces. This was also considered in [27] where a table was constructed containing information about the ratio H/Λ_c. For different bearings the same analysis will be conducted here. Because the operating conditions are unknown, the film thickness is assumed to be $H = 1.0 \cdot 10^{-6}[m]$.

In table (1.1) the σ and Λ_c have been collected for the different bearings. The Λ_c's have been split up in a Λ_c^x and a Λ_c^y. They are calculated from fitting $R(\xi)$ to the experimentally found curves of $R_x(\xi)$ and $R_y(\xi)$, respectively. Furthermore, it was not necessary to include the cosine term in equation (1.4), because if a regular pattern is present, the Λ_ω is much longer than the Λ_l. The bearing code corresponds to the code given in figures (1.1), (1.2), (1.3), (1.4) and (1.6). In table (1.1) also the statistical parameters for the rolled sheets, shown in figure (1.7), are collected.

Table (1.1) shows that H/Λ_c^x and H/Λ_c^y can reach values of the order of $O(0.1)$ but for a ten times smaller film thickness, not unusual in EHL, they are of the order $O(0.01)$. The σ, a measure for the amplitude of the surface roughness, is of order $O(1 \cdot 10^{-8})[m]$. It is observed that the σ of the roll surfaces is much larger then the σ of the bearing surfaces but the Λ_c is for both type of surfaces of the same order.

1.3 Reynolds versus Stokes

For a Newtonian fluid the Navier-Stokes (NS) equations describe the conservation of momentum. If the inertia terms are very small compared to the viscous terms, they reduce to the Stokes equations. Assuming that $H/L \ll 1$,where H is the local film thickness and L some typical length scale in the contact, it follows from the Stokes equations that the pressure is independent of the cross-film coordinate. This simplifies the Stokes equations and an expression for the velocity field as a function of the unknown pressure can be found. Substitution of the velocity field in the continuity equation and integrating it over the film thickness results in the Reynolds [65] equation. This is an equation in which the

Bearing	σ $(10^{-8}[m])$	Λ_c^y $(10^{-6}[m])$	Λ_c^x $(10^{-6}[m])$	$\frac{H}{\Lambda_c^y}$	$\frac{H}{\Lambda_c^x}$
Ai	3.3	4.4	33.5	0.23	0.03
Ao	3.7	5.4	33.7	0.19	0.03
Ar	9.4	10.3	8.8	0.10	0.11
Bi	11.0	3.6	7.5	0.28	0.13
Bo	7.6	13.3	99.6	0.08	0.01
Br	6.1	8.2	35.7	0.12	0.03
Co	49.2	72.5	12.6	0.01	0.08
Cr	9.9	5.4	12.6	0.19	0.08
cold rolling	165.0	39.3	75.8	0.03	0.01
post-rolling	147.0	26.9	49.5	0.04	0.02

Table 1.1: *Statistical parameters for different bearing types and rolled sheet. Assumption* $H = 1.0 \cdot 10^{-6}[m]$

pressure is independent of the cross-film coordinate. The assumption $H/L \ll 1$ may no longer hold in the case of non-smooth surfaces.

As mentioned in the previous section the trend in bearing design is towards more extreme conditions which lead to smaller nominal film thickness values. At a certain point obviously the amplitude of the surface roughness will be of the same order of the film thickness and the question arises to what extend the Reynolds equation is still valid. Based on the anticipated validity of the Reynolds equation one now distinguishes two types of roughness: Reynolds roughness versus Stokes roughness, see Elrod [25]. They are defined as:

- Reynolds roughness $H/\Lambda_c \ll 1$.
- Stokes roughness $H/\Lambda_c \gg 1$,

where Λ_c represents the characteristic wavelength of the surface roughness. By characteristic wavelength is meant the Λ_c introduced in section (*1.2*). It was observed in table (1.1) that ratios of $H/\Lambda_c \approx 0.1$ can occur. So, in the case of Reynolds roughness, the Reynolds equation appropriately describes the fluid flow in a lubricated contact, otherwise the Stokes equations should be used.

This separation between two types of roughness is rather academic. It only indicates which type of modeling equation(s) can be used to analyze the problem. In practice assuming Reynolds roughness simply means assuming that the film geometry is such that both on a global as well as on a local scale its effect on film formation can be analyzed by means of the Reynolds equation without justification for this assumption being given. Also, it is not clear where the border between Reynolds and Stokes roughness should be drawn and how it is related to the problem parameters. As a result Reynolds roughness in practice simply means that the models and numerical algorithms that have been developed based on the Reynolds equation and assuming smooth surfaces are modified or adapted such that rough surface effects can be incorporated.

Based on the way in which roughness effects are incorporated in a model (Stokes or Reynolds) one can distinguish two approaches:

- Deterministic approach
- Statistic approach

These two approaches are related to the ways in which rough surfaces can be analyzed as shown in the previous section. The deterministic approach is related to the exact description of the surface geometry as a function of the coordinates, i.e. equation (1.1). The film thickness given by this equation is used in the model, e.g. Reynolds' equation, which is then solved. Originally this deterministic approach was not very popular. An accurate description of a surface geometry on a local scale requires many grid points and for a long time most numerical solution algorithms could not even deal efficiently with the smooth surface problem, let alone that it could be solved with so many grid points that taking into account surface roughness or local features in a deterministic way seemed feasible. This situation has changed in the past decades. Early examples of deterministic studies in the field of EHL are [30], [31]. With the present generation of stable and efficient algorithms for the models based on Reynolds equation even transient problems can be solved using many grid points on small scale computers. As a result also the effects of surface features on film formation and performance of point contacts can now be analyzed in a deterministic way. Examples of such studies are [91], [92] and [97]. Quite encouragingly the agreement between the results of experiments using optical interferometry [41] and the computed film shapes is very good. However, in the particular case of an artificial ridge moving through the EHL contact discrepancies were observed between the experimental [41] and theoretical [89] results that could not be explained.

The numerical simulation involves the solution of the time-dependent Reynolds equation. It was found that a fluctuation of the height, for example induced by a ridge, will pass through the contact with the average speed of the contacting bodies, independent of the speed of the feature that induces it. In the numerical simulations the form of the induced fluctuation of the height does not change significantly during the passage through the contact region. In the experiments we can detect a spreading of the fluctuation of the height. This could indicate the limits of the Reynolds equation. More general we are led to the question to what extent a surface feature leads to a film pressure dependent on the cross-sectional position.

As explained in the previous section, instead of looking at surface height maps, one can try to characterize a surface roughness profile by means of statistical parameters. This way of looking at rough surfaces has led to the so-called statistic approach. In this approach one does a number of assumptions regarding the statistical properties of the roughness distribution. The statistical roughness description is then substituted in the model problem and after an often lengthy analysis a generalized Reynolds or Stokes model follows in which integrals of the surface roughness appear. The integrals can be recasted in a form that contains the Auto-Correlation Function (ACF) of the surface roughness. The resulting model is only slightly more complex then the model for the smooth surfaces which obviously explains its popularity when fast numerical solution algorithms were not yet available. The most dominant statistical quantity appearing in the equations are the

Root Mean Square (RMS) value of the roughness and the auto-correlation length of the surface roughness. In general it is observed that the occurrence of roughness yields a larger load capacity then for the smooth surface case. Examples of this approach based on Reynolds equation are the works of Tzeng and Saibel [84], [85], Christensen and co-workers [13], [14], [15], [16], Elrod [25], [26] , Cheng and Dyson [10] and also [11], [12], Sun [76], Phan Thien, [58], [60], [61], [62] and Prakash [63]. A related approach referred to as 'the flow factor method' is where the details of the roughness enter in coefficients of the Reynolds equation as so-called flow factors, see [54], [56], [78], [27], [82]. This flow factor method is widely used in practice. It has been used in both Hydrodynamic Lubrication as well as Elastohydrodynamic Lubrication problems. Examples of the latter are [70], [55], [83].

Most likely because of the additional dimension and the associated additional problems related to the analysis and numerical solution only very few studies exist in which the Stokes problem or Stokes roughness is considered. Probably the earliest examples are the work of Sun and Chen [77] using the statistical approach and of a later date [59]. Also in [48] and [49] Stokes roughness was studied using a perturbation approach.

Only a few researchers [50], [72] have tried to solve numerically the Stokes equations in the case of a hydrodynamically lubricated contact. In [50] a multi-grid solver was developed to solve the Stokes equations on a highly anisotropic-rectangular domain. In [72] the EHL problem is solved but now the fluid flow is described by modified Stokes equations (some viscous terms have been omitted). Especially for sliding, the results show differences between the Reynolds and the Stokes solution.

From the above it can be concluded that the geometry of the contact determines the validity of the Reynolds equation but one has never shown the exact conditions on the geometry. What about the other quantities that enter the Reynolds equation like the density and the viscosity? Is it possible that a rapid change in these quantities limits the validity of the Reynolds equation? This was pointed out by [1] in the case of a pressure-dependent viscosity. It was shown analytically that a cross-film flow exists for a Stokes flow between parallel plates. So, besides geometrically induced differences between the Reynolds and the Stokes solution, it was found interesting to investigate the effect of a pressure-dependent viscosity and/or density on the validity of the Reynolds equation. An application of a pressure-dependent density can be found in gas bearings where one uses the ideal gas law to describe the relation between pressure and density. The cavitation of the oil in the outflow region in bearings can be simulated with a pressure-dependent density.

Besides the investigation of the limits of the Reynolds equation, it is also a challenge to develop the necessary numerical tools. Some numerical difficulties are encountered in solving the Stokes equations. For example: the strong anisotropy of the domain, the curved boundary and the rapid change of density and viscosity. These problems may seem small for CFD-oriented readers but are rather new in tribology.

In conclusion it can be said that the applicability of the Reynolds equation is questionable in two ways: extreme geometries, severe viscosity/density pressure relations.

1.4 Outline of this thesis

In chapter (*2*) the Reynolds equation is derived. The fluid momentum equations are introduced and a perturbation approach is explained. Furthermore, some relation between viscosity, density and pressure are introduced to model gas bearings and cavitation. In chapter (*3*) the numerical techniques to solve the equations, introduced in chapter (*2*), are explained. Also, in this chapter, the multi-grid performance and numerically accuracy of the developed solvers will be illustrated. Chapter (*4*) contains the results of the numerical and perturbation work for the different types of surface features. In chapter (*5*) some applications concerning a pressure-dependent viscosity and density are presented. And, finally, the conclusions and recommendations of the present work are presented.

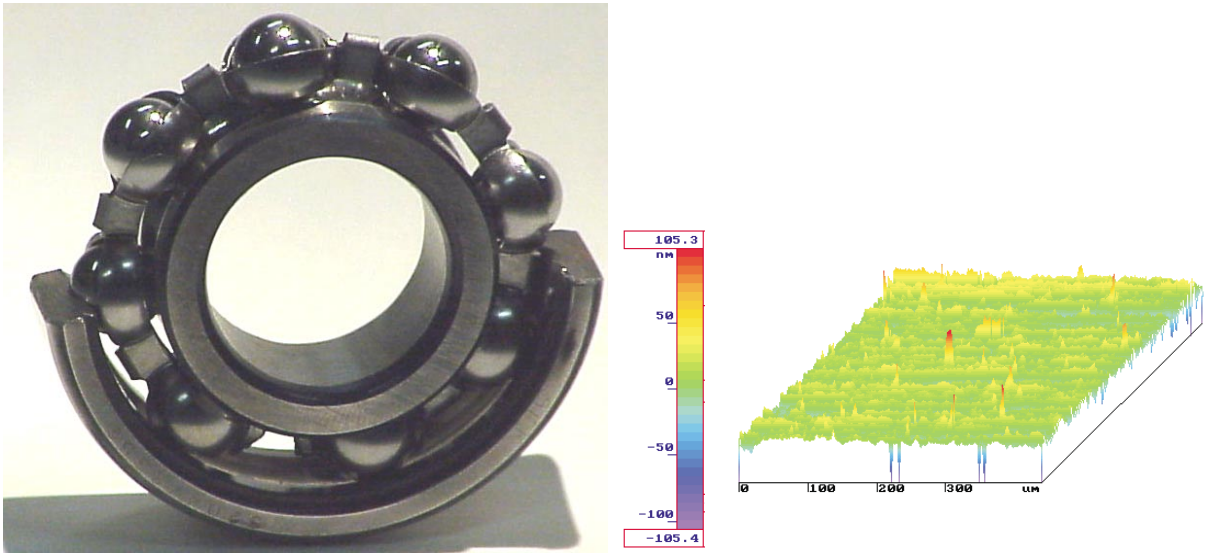

(a) *(b)*

Figure 1.1: *(a): Photo of ball bearing A. (b): Surface heights of inner raceway of bearing A.*

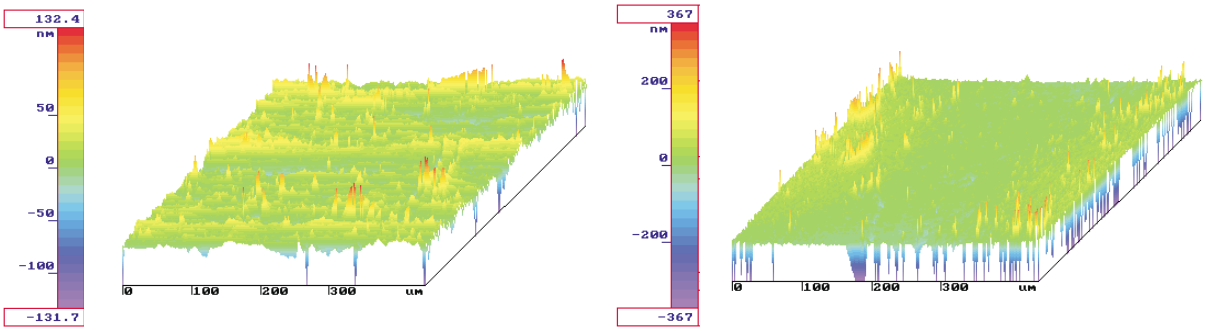

(a) *(b)*

Figure 1.2: *Surface heights of bearing A. (a): For the outer raceway. (b): For the ball.*

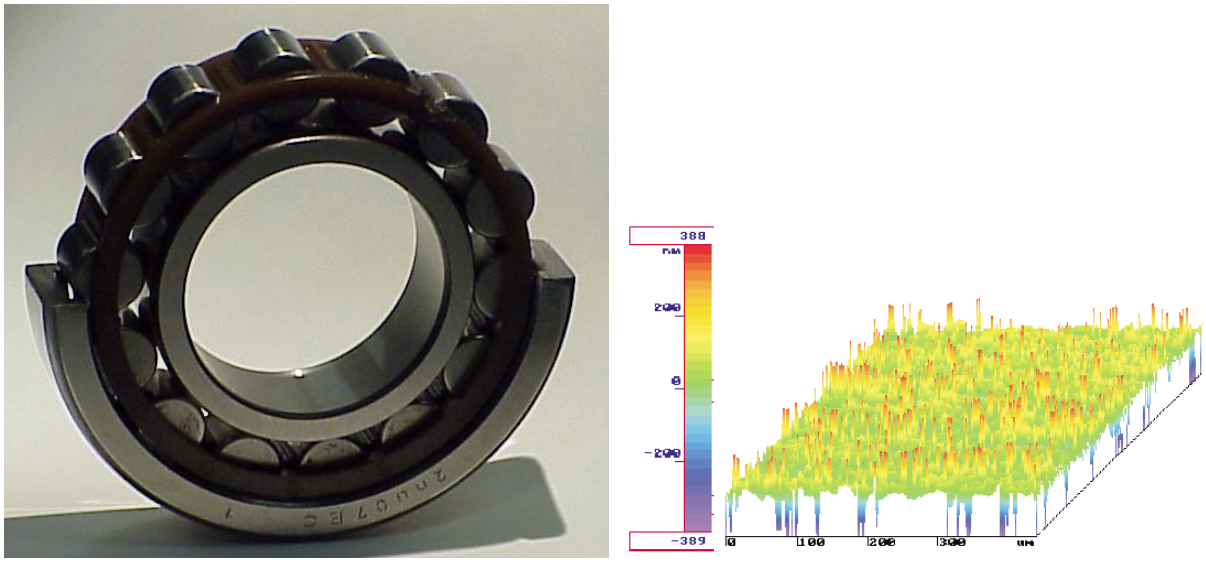

(a) *(b)*

Figure 1.3: *(a): Photo of cylindrical roller bearing B. (b): Surface heights of inner raceway of bearing B.*

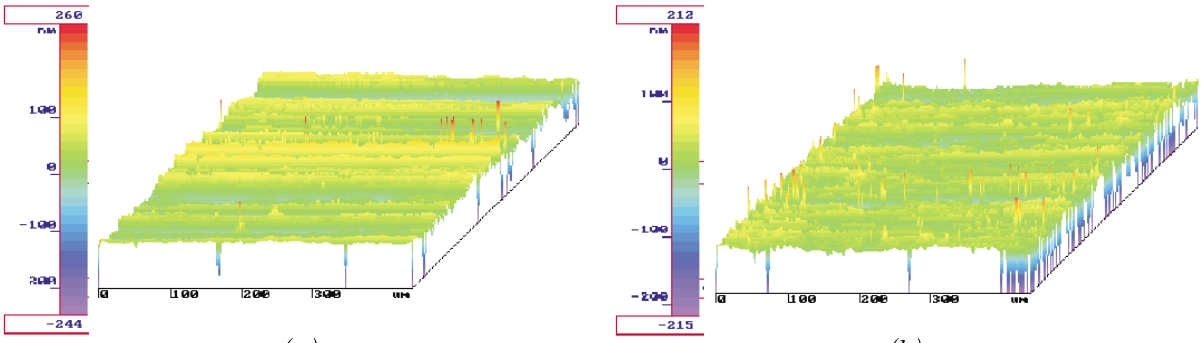

(a) *(b)*

Figure 1.4: *Surface heights of bearing B. (a): For the outer raceway. (b): For the roller.*

Figure 1.5: *Photo of spherical roller bearing C.*

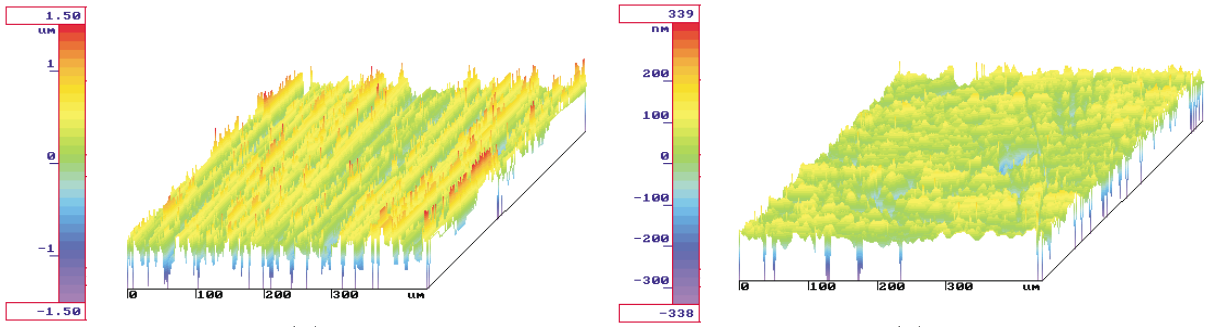

(a) *(b)*

Figure 1.6: *Surface heights of bearing C. (a): For the outer raceway. (b): For the roller.*

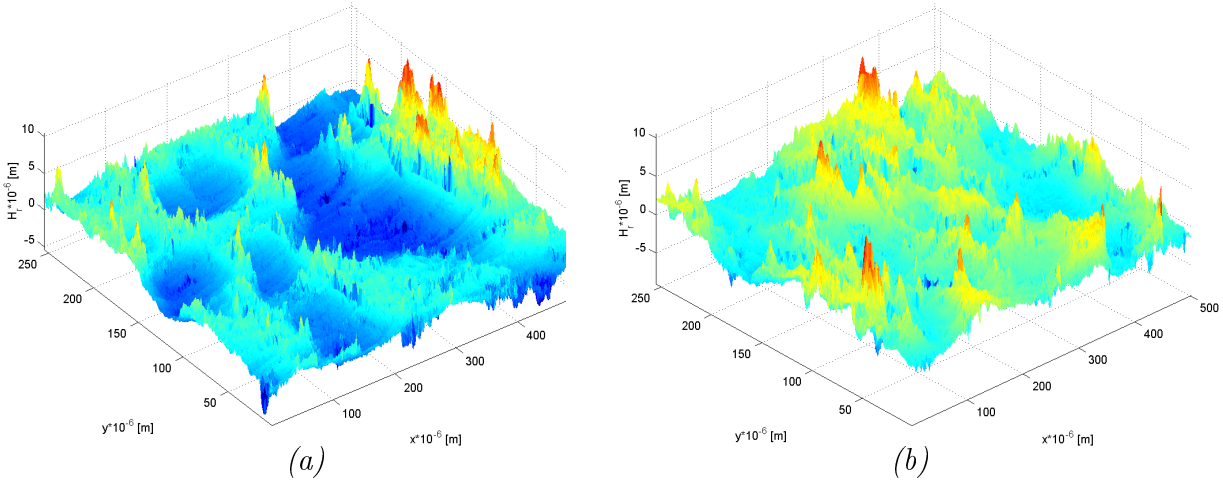

(a) *(b)*

Figure 1.7: *Surface heights of rolled sheet. (a): After cold rolling. (b): After a post-rolling step.*

Chapter 2

Theory

As explained in the previous chapter, technical surfaces are never perfectly smooth. For thinner films the influence of the roughness on the performance will increase. If the roughness is such that the gap is still locally narrow, its effects may still be predicted accurately from the Reynolds equation. However, the question is what criteria regarding amplitude, wavelength etc. should be satisfied. The investigation of the validity of the narrow gap assumption forms the topic of this thesis.

As a start, in this chapter a description of the flow between the surfaces is given, based on the Stokes equations. The Stokes equations are written in a boundary fitted coordinate system to handle non-rectangular domains. The transformed momentum and continuity equations are rather involved, but the implementation of boundary conditions is easy. It is shown how the Reynolds equation is deduced from the Stokes equations. In particular, with a perturbation analysis of the Stokes equations it is shown that the Reynolds equation is the zeroth order perturbation solution. Not only geometry limits the validity of the Reynolds equation but also a pressure dependent viscosity or density. A pressure dependent density will be used to simulate gas lubrication and cavitation. To simulate real lubrication problems, cavitation must be included, to prevent the pressure from being lower then the vapor pressure. It is mentioned that special care must be taken if one computes the lift force, in the Stokes case, because certain terms do not drop. The lift force can be used to quantify the difference between the Reynolds solution and the Stokes solution.

2.1 Stokes model

The motion of a Newtonian fluid can be described by the Navier-Stokes (N-S) equations. In Cartesian coordinates they are given by:

$$\frac{\partial(\rho \mathbf{v})}{\partial t} + \nabla \cdot (\rho \mathbf{v} \otimes \mathbf{v} + p\bar{1} - \bar{\tau}) = \rho \mathbf{f_e} \ , \tag{2.1}$$

where for $i, j = 1, 2, 3$ and $(x^1, x^2, x^3) = (x, y, z) \in \Omega$

$$(\bar{1})_{ij} \ = \ \delta_{ij} \ ,$$

$$
\begin{aligned}
(\bar{\tau})_{ij} &= \eta(\frac{\partial v^j}{\partial x^i} + \frac{\partial v^i}{\partial x^j}) - \frac{2}{3}\eta(\nabla \cdot \mathbf{v})\delta_{ij} \ , \\
\eta &= \text{viscosity} \ , \\
\rho &= \text{density} \ , \\
\mathbf{v} &= (u, v, w)^T \text{ velocity vector} \ , \\
\mathbf{f_e} &= \text{external force field} \ .
\end{aligned}
$$

In the following it will be assumed that there are no external forces. The density and the velocity have to satisfy the continuity equation:

$$\frac{\partial(\rho \mathbf{v})}{\partial t} + \nabla \cdot (\rho \mathbf{v}) = 0 \ . \tag{2.2}$$

Although, in a thin film, thermal effects can play an important role, throughout this thesis isothermal conditions are assumed. This implies that the energy equation is not required in the mathematical model of the flow. However, this does not imply that the lubricant properties are constant. Generally the viscosity and the density depend on the pressure. In this thesis only two-dimensional flow problems will be studied. Figure (2.1) shows a typical configuration of a lubricated contact between two surfaces. The boundary conditions for the flow in the gap will be given in terms of the velocity of the surfaces and the pressure at the inlet and outlet of the film. A pressure boundary condition at the inflow/outflow is needed because, generally, the velocity profiles on these boundaries are not known.

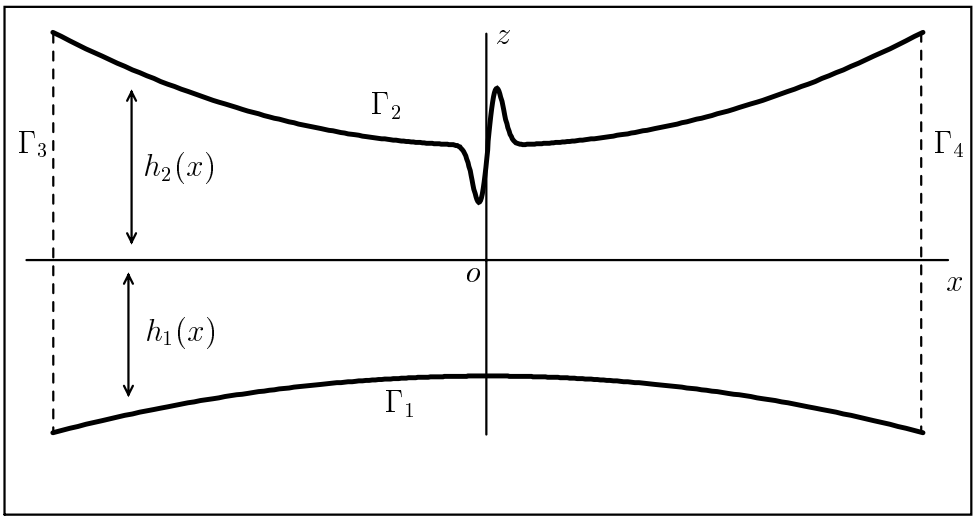

Figure 2.1: *The domain* Ω.

The boundary conditions are:

$$
\begin{aligned}
\Gamma_1 : &\quad \mathbf{v} = \mathbf{u_0} \ , \\
\Gamma_2 : &\quad u = 0, w = 0 \ , \\
\Gamma_3 : &\quad p = 0, w = 0 \ , \\
\Gamma_4 : &\quad p = 0, w = 0 \ .
\end{aligned} \tag{2.3}
$$

The pressure on the boundaries Γ_3 and Γ_4 is taken to be zero because in a hydrodynamically lubricated contact the pressure is large, compared to the ambient pressure. In this thesis only steady flow situations are considered. This implies that the surface on which a feature is present (Γ_2 in figure (2.1)) has zero velocity.

To analyze the equations, dimensionless variables have been introduced according to [49]. Assuming a characteristic speed u_0, a characteristic length L in the x-direction, a characteristic height H in the z-direction, a characteristic density ρ_0 and a characteristic viscosity η_0, the variables can be transformed according to:

$$\begin{array}{rcl} u & \rightarrow & u_0 u \ , \\ w & \rightarrow & \epsilon u_0 w \ , \quad \epsilon = \frac{H}{L} \ , \\ x & \rightarrow & L x \ , \\ z & \rightarrow & H z \ , \\ \rho & \rightarrow & \rho_0 \rho \ , \\ \eta & \rightarrow & \eta_0 \eta \ , \\ p & \rightarrow & \frac{\eta_0 u_0}{H} p \ . \end{array} \tag{2.4}$$

Substitution of (2.4) leads to the dimensionless momentum equations:

$$Re\ \epsilon \left[\frac{\partial(\rho u^2)}{\partial x} + \frac{\partial(\rho u w)}{\partial z}\right] + \epsilon^2 \frac{\partial}{\partial x}\left[\frac{2}{3}\eta\frac{\partial w}{\partial z} - \frac{4}{3}\eta\frac{\partial u}{\partial x}\right] - \frac{\partial}{\partial z}\left[\epsilon^2\eta\frac{\partial w}{\partial x} + \eta\frac{\partial u}{\partial z}\right] = -\epsilon\frac{\partial p}{\partial x} \ , \tag{2.5}$$

$$Re\ \epsilon^2 \left[\frac{\partial(\rho w u)}{\partial x} + \frac{\partial(\rho w^2)}{\partial z}\right] + \epsilon \frac{\partial}{\partial z}\left[\frac{2}{3}\eta\frac{\partial u}{\partial x} - \frac{4}{3}\eta\frac{\partial w}{\partial z}\right] - \frac{\partial}{\partial x}\left[\epsilon\eta\frac{\partial u}{\partial z} + \epsilon^3\eta\frac{\partial w}{\partial x}\right] = -\frac{\partial p}{\partial z} \ , \tag{2.6}$$

and the equation of continuity:

$$\frac{\partial(\rho u)}{\partial x} + \frac{\partial(\rho w)}{\partial z} = 0 \ , \tag{2.7}$$

where $Re = \frac{H\rho_0 u_0}{\eta_0}$ represents the Reynolds number based on film height. The above equations will henceforth be referred to as the "Navier-Stokes model". If surface roughness does not play a role (the surface heights are small compared to the film thickness) then in for example EHL contacts $\epsilon = O(0.001)$ and $Re = O(0.001)$. In that case the convective terms and certain viscous terms can be neglected in equation (2.5) and (2.6). These simplified equations then lead to the Reynolds equation as is explained in section (*2.1.2*). Otherwise, if surface roughness is considered, locally the parameter ϵ may not be small (take for H the local film thickness and for L the characteristic roughness wavelength) and certain viscous terms in equations (2.5) and (2.6) do not drop. So the viscous terms are of order one and still $Re \ll 1$. This means that the convective terms can be dropped. In [48] it has been demonstrated with a series expansion in the parameters ϵ and Re of the dependent variables in equations (2.5), (2.6) and (2.7) that for a flow between a geometry like in figure (2.1) and boundary conditions (2.4), the pressure correction

resulting from the convective terms is much smaller then the pressure correction from the viscous terms. In their study the wavelength of the harmonic surface roughness was of the order of the film thickness, the amplitude was 0.75 times the film thickness, $\epsilon = 0.003$ and $Re = 0.001$. Therefore, as a first step, in this work convective terms are neglected. In that case, equations (2.5), (2.6), (2.7) reduce to:

$$\epsilon^2 \frac{\partial}{\partial x}\left[\frac{2}{3}\eta\frac{\partial w}{\partial z} - \frac{4}{3}\eta\frac{\partial u}{\partial x}\right] - \frac{\partial}{\partial z}\left[\epsilon^2\eta\frac{\partial w}{\partial x} + \eta\frac{\partial u}{\partial z}\right] = -\epsilon\frac{\partial p}{\partial x} \ , \tag{2.8}$$

$$\epsilon \frac{\partial}{\partial z}\left[\frac{2}{3}\eta\frac{\partial u}{\partial x} - \frac{4}{3}\eta\frac{\partial w}{\partial z}\right] - \frac{\partial}{\partial x}\left[\epsilon\eta\frac{\partial u}{\partial z} + \epsilon^3\eta\frac{\partial w}{\partial x}\right] = -\frac{\partial p}{\partial z} \ , \tag{2.9}$$

$$\frac{\partial(\rho u)}{\partial x} + \frac{\partial(\rho w)}{\partial z} = 0 \ . \tag{2.10}$$

Equations (2.8), (2.9) and (2.10) will henceforth be referred to as the "Stokes model". For an incompressible flow these equations further reduce to:

$$\epsilon\frac{\partial p}{\partial x} - 2\epsilon^2\frac{\partial}{\partial x}\left[\eta\frac{\partial u}{\partial x}\right] - \frac{\partial}{\partial z}\left[\epsilon^2\eta\frac{\partial w}{\partial x} + \eta\frac{\partial u}{\partial z}\right] = 0 \ , \tag{2.11}$$

$$\frac{\partial p}{\partial z} - 2\epsilon\frac{\partial}{\partial z}\left[\eta\frac{\partial w}{\partial z}\right] - \frac{\partial}{\partial x}\left[\epsilon\eta\frac{\partial u}{\partial z} + \epsilon^3\eta\frac{\partial w}{\partial x}\right] = 0 \ , \tag{2.12}$$

$$\frac{\partial u}{\partial x} + \frac{\partial w}{\partial z} = 0 \ . \tag{2.13}$$

If η is also constant ($\eta = 1$) the momentum equations are of elliptic type and simplify to:

$$\epsilon\frac{\partial p}{\partial x} - \epsilon^2\frac{\partial^2 u}{\partial x^2} - \frac{\partial^2 u}{\partial z^2} = 0 \ , \tag{2.14}$$

$$\frac{\partial p}{\partial z} - \epsilon^3\frac{\partial^2 w}{\partial x^2} - \epsilon\frac{\partial^2 w}{\partial z^2} = 0 \ , \tag{2.15}$$

$$\frac{\partial u}{\partial x} + \frac{\partial w}{\partial z} = 0 \ . \tag{2.16}$$

If η is a function of p and the density is not, then they can be fully elliptic, partially parabolic or partially hyperbolic, depending on the value of $(\frac{d\eta}{dp})^2[(\frac{\partial u}{\partial z} + \frac{\partial w}{\partial x})^2 - 4\frac{\partial u}{\partial x}\frac{\partial w}{\partial z}] - 1$, see [1] and appendix ($A$).

An important quantity, often used to visualize the flow field, is the stream function $\phi(x, z)$ defined by:

$$\frac{\partial \phi}{\partial z} = \rho u \ , \frac{\partial \phi}{\partial x} = -\rho w \ . \tag{2.17}$$

It can be calculated according to

$$\phi(x, z) = \int_0^z \rho u \, dz' \ . \tag{2.18}$$

The streamlines are defined by the lines of constant ϕ.

2.1.1 Curvilinear coordinates

To handle non-rectangular boundaries it is convenient to introduce a transformation of the independent variables from Cartesian coordinates to curvilinear coordinates. The advantage is that the implementation of boundary conditions is much easier and also that the domain on which the problem is to be solved transforms into a rectangular domain on which it is easier to discretize. In our tribological context there will be no steep gradients in the grid lines, i.e., ϵ is small. As a result it is sufficient to transform only the x- and z- coordinate and there is no real need to transform the velocity vector too. This has the advantage that the difficult task of discretizing Christoffel symbols [93], resulting from the velocity transformation, does not arise. This idea of first transforming the momentum equations from the physical domain to the computational domain and then discretizing the equations on a rectangular grid is based on the work of Oosterlee [51].

Let the relation between the physical coordinates $\mathbf{x} = (x^1, x^2) = (x, z) \in \Omega$ and the computational coordinates $(\xi^1, \xi^2) \in G$ be given by:

$$\mathbf{x} = \mathbf{x}(\xi^1, \xi^2) \ , \tag{2.19}$$

see figure (2.2) for an illustration. It is demanded that the inverse transformation exists, so the Jacobian J of the transformation:

$$J = \begin{pmatrix} \frac{\partial x}{\partial \xi^1} & \frac{\partial z}{\partial \xi^1} \\ \frac{\partial x}{\partial \xi^2} & \frac{\partial z}{\partial \xi^2} \end{pmatrix} \ . \tag{2.20}$$

has a non-zero determinant. Subsequently, with the contravariant base vectors, the covariant base vectors and the relations between these, the Stokes equations, can be transformed from the physical domain into the computational domain. Contravariant base vectors $\mathbf{a}^{(k)},\ k = (1, 2)$ are defined as vectors normal to the $\xi^k = constant$ lines,

$$\mathbf{a}^{(k)} = \nabla \xi^k \ . \tag{2.21}$$

Covariant base vectors $\mathbf{a}_{(k)}$ are defined as vectors tangential to the coordinate lines ξ^k:

$$\mathbf{a}_{(k)} = \frac{\partial \mathbf{x}}{\partial \xi^k} \ . \tag{2.22}$$

In this coordinate system a vector is defined as:

$$\mathbf{u} = u^1 \mathbf{a}_{(1)} + u^2 \mathbf{a}_{(2)} \ . \tag{2.23}$$

As an example the covariant vectors $\mathbf{a}_{(i)}$ are shown in figure (2.2). In the following the Einstein summation convention[1] will be used. Using the metric tensor g_{kl}

$$g_{kl} = \mathbf{a}_{(k)} \cdot \mathbf{a}_{(l)} \ , \tag{2.24}$$

the following holds:

$$\det(J) = \det(g_{kl}) = \sqrt{g} = a^1_{(1)} a^2_{(2)} - a^1_{(2)} a^2_{(1)} \ . \tag{2.25}$$

[1] Summation over repeated subscript/superscript indices, for example $u^i u_i = \Sigma_i u^i u_i$

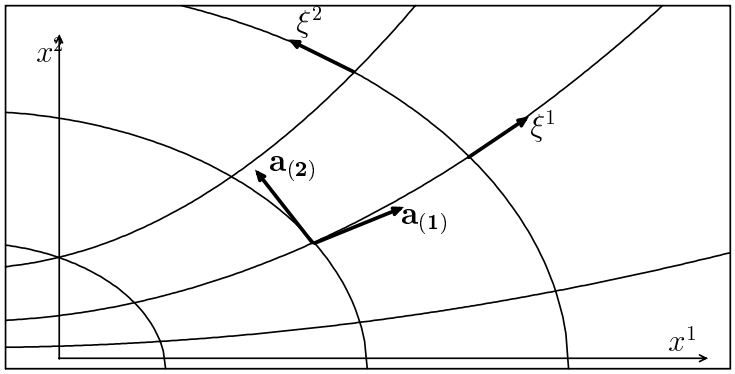

Figure 2.2: *Curvilinear coordinates ξ^1, ξ^2 with covariant base vectors.*

Introducing the definition of the gradient:

$$\nabla = \mathbf{a}^{(k)} \frac{\partial}{\partial \xi^k} \tag{2.26}$$

and using the geometrical conservation law:

$$\frac{\partial}{\partial \xi^k}(\sqrt{g}\mathbf{a}^{(k)}) = 0 \ , \tag{2.27}$$

leads to the following expressions of equations (2.8), (2.9) and (2.10), transformed to curvilinear coordinates in a conservative form:

$$\epsilon^2 \frac{\partial}{\partial \xi^k}\left[\eta\sqrt{g}a_1^{(k)}\left(\frac{4}{3}a_1^{(l)}\frac{\partial u}{\partial \xi^l} - \frac{2}{3}a_2^{(l)}\frac{\partial w}{\partial \xi^l}\right)\right] + \frac{\partial}{\partial \xi^k}\left[\eta\sqrt{g}a_2^{(k)}\left(\epsilon^2 a_1^{(l)}\frac{\partial w}{\partial \xi^l} + a_2^{(l)}\frac{\partial u}{\partial \xi^l}\right)\right] =$$

$$= \epsilon\frac{\partial}{\partial \xi^k}(\sqrt{g}a_1^{(k)}p) \ , \tag{2.28}$$

$$\frac{\partial}{\partial \xi^k}\left[\sqrt{g}a_1^{(k)}\eta\left(\epsilon a_2^{(l)}\frac{\partial u}{\partial \xi^l} + \epsilon^3 a_1^{(l)}\frac{\partial w}{\partial \xi^l}\right)\right] + \epsilon\frac{\partial}{\partial \xi^k}\left[\eta\sqrt{g}a_2^{(k)}\left(\frac{4}{3}a_2^{(l)}\frac{\partial w}{\partial \xi^l} - \frac{2}{3}a_1^{(l)}\frac{\partial u}{\partial \xi^l}\right)\right] =$$

$$= \frac{\partial}{\partial \xi^k}(\sqrt{g}a_2^{(k)}p) \ , \tag{2.29}$$

$$\frac{\partial}{\partial \xi^k}(\sqrt{g}a_l^{(k)}\rho u^l) = 0 \ . \tag{2.30}$$

The equations (2.11), (2.12) and (2.13) transform to:

$$2\epsilon^2 \frac{\partial}{\partial \xi^k}\left[\eta\sqrt{g}a_1^{(k)}a_1^{(l)}\frac{\partial u}{\partial \xi^l}\right] + \frac{\partial}{\partial \xi^k}\left[\eta\sqrt{g}a_2^{(k)}\left(\epsilon^2 a_1^{(l)}\frac{\partial w}{\partial \xi^l} + a_2^{(l)}\frac{\partial u}{\partial \xi^l}\right)\right] =$$

$$= \epsilon\frac{\partial}{\partial \xi^k}(\sqrt{g}a_1^{(k)}p) \ , \tag{2.31}$$

$$\frac{\partial}{\partial \xi^k}\left[\eta\sqrt{g}a_1^{(k)}\left(\epsilon a_2^{(l)}\frac{\partial u}{\partial \xi^l}+\epsilon^3 a_1^{(l)}\frac{\partial w}{\partial \xi^l}\right)\right]+2\epsilon\frac{\partial}{\partial \xi^k}\left[\eta\sqrt{g}a_2^{(k)}a_2^{(l)}\frac{\partial w}{\partial \xi^l}\right]=$$

$$=\frac{\partial}{\partial \xi^k}(\sqrt{g}a_2^{(k)}p)\ , \tag{2.32}$$

$$\frac{\partial}{\partial \xi^k}(\sqrt{g}a_l^{(k)}u^l)=0\ . \tag{2.33}$$

In these equations the contravariant base vectors $a_l^{(k)}$ appear. However, because $\mathbf{x}=\mathbf{x}(\xi^1,\xi^2)$, it is more convenient to use the covariant base vectors instead. The two types of base vectors form an orthonormal set,

$$\mathbf{a}^{(k)}\cdot\mathbf{a}_{(l)}=\delta_l^k\ . \tag{2.34}$$

From this it follows that:

$$\mathbf{a}^{(1)}=\frac{1}{\sqrt{g}}\begin{pmatrix} a^2_{(2)} \\ -a^1_{(2)}\end{pmatrix}\quad,\mathbf{a}^{(2)}=\frac{1}{\sqrt{g}}\begin{pmatrix} -a^2_{(1)} \\ a^1_{(1)}\end{pmatrix}\ . \tag{2.35}$$

2.1.2 Reynolds equation

From equations (2.8), (2.9) and (2.10) the Reynolds equation (see [65]) can be derived. Let the upper and lower surface be defined by $z=h_1(x)$ and $z=h_2(x)$, see figure (2.1), and it is assumed that $\rho=\rho(p),\eta=\eta(p)$. If in equation (2.8) the terms containing ϵ^2 are omitted and if in equation (2.9) the terms containing ϵ and ϵ^3 are omitted, it follows that:

$$\epsilon\frac{\partial p}{\partial x}-\frac{\partial}{\partial z}(\eta\frac{\partial u}{\partial z})=0\ , \tag{2.36}$$

$$\frac{\partial p}{\partial z}=0\ , \tag{2.37}$$

$$\frac{\partial(\rho u)}{\partial x}+\frac{\partial(\rho w)}{\partial z}=0\ . \tag{2.38}$$

From equation (2.37) it follows that $p(x,z)=p(x)$. Integrating equation (2.36) twice with respect to z using the boundary conditions $u(x,z=h_1(x))=u_1$ and $u(x,z=h_2(x))=u_2$ gives:

$$u(x,z)=\frac{\epsilon}{2\eta}\frac{dp}{dx}(z^2-z(h_1+h_2)+h_1h_2)+z\frac{(u_2-u_1)}{h_2-h_1}+\frac{h_1u_2-h_2u_1}{h_1-h_2}\ . \tag{2.39}$$

Because the pressure is now invariant under a z-coordinate transformation $z\rightarrow z-h_1$ and $h=h_2-h_1$, the above equation can be transformed into:

$$u=\frac{\epsilon}{2\eta}\frac{dp}{dx}(z^2-zh)+z\frac{(u_2-u_1)}{h}+u_1\ . \tag{2.40}$$

Integrating the continuity equation with respect to z,

$$\int_{z=0}^{h(x)} \frac{\partial(\rho u)}{\partial x} dz + \int_{z=0}^{h(x)} \frac{\partial(\rho w)}{\partial z} dz = 0 \ , \tag{2.41}$$

leads to

$$\frac{d}{dx} \int_{z=0}^{h(x)} (\rho u) dz - \rho u(x, h(x)) \frac{dh}{dx} + \rho w(x, h(x)) - \rho w(x, 0) = 0 \ . \tag{2.42}$$

where use has been made of the "Leibniz" rule[2]. Substitution of u from equation (2.40) and the boundary values for u,w together with $w(x, h(x)) = u(x, h(x))\frac{dh}{dx}$ gives the Reynolds equation for this specific problem (see figure (2.1)):

$$\frac{d}{dx} \left[\frac{-\epsilon\rho}{12\eta} \frac{dp}{dx} h^3 + \rho h \frac{(u_1 + u_2)}{2} \right] = 0 \ . \tag{2.43}$$

So, in the Reynolds case the domain can be transformed to the height function $h(x)$. Summarizing, if $\epsilon \ll 1$ the pressure will not depend on z. As a result, solving p, u, w as a function of x, z can be replaced by solving $p(x)$ from (2.43) with the gap function $h(x)$ given and appropriate boundary conditions. The velocity $u(x, z)$ can then be obtained from equation (2.40). Finally, the velocity profile $w(x, z)$ follows from the equation of continuity:

$$\rho w = -\int_0^z \frac{\partial(\rho u)}{\partial x} dz \ . \tag{2.44}$$

After substitution of (2.40) in (2.44) and using (2.43) to eliminate $\frac{d^2p}{dx^2}$ an expression for w follows:

$$\begin{aligned} w = \quad & \left[u_1(1 - \frac{z}{h}) + u_2(2 - \frac{z}{h}) \right] \frac{z^2}{h^2} \frac{dh}{dx} + (\frac{z}{h} - 1) \frac{\epsilon z^2}{2\eta} \frac{dh}{dx} \frac{dp}{dx} + \\ & \left[u_1(2 - \frac{h}{z} - \frac{z}{h}) + u_2(1 - \frac{z}{h}) \right] \frac{z^2}{\rho h} \frac{d\rho}{dp} \frac{dp}{dx} \ . \end{aligned} \tag{2.45}$$

So, if ϵ is small, rather then solving a two-dimensional flow problem, it suffices to solve a one-dimensional flow problem. However, if ϵ is not small, the assumption that $p = p(x)$ will no longer be valid and the complete system of equations must be solved on a two-dimensional domain.

2.2 Perturbation

For small ϵ, the Reynolds equation is expected to yield accurate results. For large ϵ, Stokes must be solved. However, one may expect that there is an intermediate regime in which a "corrected" Reynolds solution can be useful. In particular, is it possible to produce a better approximation than the Reynolds solution, in the tribologically interesting

[2] $\frac{d}{dx}(\int_{h_1(x)}^{h_2(x)} g(x, z) dz) = g(x, h_2(x)) \frac{dh_2}{dx} - g(x, h_1(x)) \frac{dh_1}{dx} + \int_{h_1(x)}^{h_2(x)} \frac{\partial g}{\partial x} dz$

operating range? Such a solution can indeed be obtained from a perturbation analysis. This analysis is presented below.

A regular expansion in ϵ^2 for the dependent variables in equations (2.14), (2.15) and (2.16) was used, as proposed in [49]. The parameter ϵ^2, occurring in these equations, must be small to give a convergent expansion. However, even for small ϵ^2 the expansion can break down when the gradient in the surface is too large, which may be due to a local surface feature. After introduction of the parameter $\gamma = \epsilon^2$, the Stokes equations can be written as:

$$\epsilon\frac{\partial p}{\partial x} - \frac{\partial^2 u}{\partial z^2} - \gamma\frac{\partial^2 u}{\partial x^2} = 0 \ , \tag{2.46}$$

$$\epsilon\frac{\partial p}{\partial z} - \gamma\frac{\partial^2 w}{\partial z^2} - \gamma^2\frac{\partial^2 w}{\partial x^2} = 0 \ , \tag{2.47}$$

$$\frac{\partial u}{\partial x} + \frac{\partial w}{\partial z} = 0 \ . \tag{2.48}$$

These are the same as equations (2.14), (2.15) and (2.16), only equation (2.15) is multiplied by ϵ. So effectively a new variable is introduced, namely ϵp. If another scaling had been used, like $p \rightarrow \frac{\eta_0 u_0 L}{H^2} p$, then equations (2.14), (2.15) and (2.16) would only contain γ and γ^2 and series expansion in γ would be obvious. For $\gamma = 0$ they give equations (2.36), (2.37) and (2.38) (with $\eta = 1$ and $\rho = 1$), which lead to the Reynolds equation. The following expansion of the dependent variables will be substituted in the above equations:

$$\begin{array}{rcl} u(x,z) & = & u_0(x) + \gamma u_1(x,z) + O(\gamma^2) \ , \\ w(x,z) & = & w_0(x,z) + \gamma w_1(x,z) + O(\gamma^2) \ , \\ p(x,z) & = & p_0(x) + \gamma p_1(x,z) + O(\gamma^2) \ . \end{array} \tag{2.49}$$

Equating equal orders in γ, gives to zeroth-order:

$$\epsilon\frac{\partial p_0}{\partial x} - \frac{\partial^2 u_0}{\partial z^2} = 0 \ , \tag{2.50}$$

$$\epsilon\frac{\partial p_0}{\partial z} = 0 \ , \tag{2.51}$$

$$\frac{\partial u_0}{\partial x} + \frac{\partial w_0}{\partial z} = 0 \ . \tag{2.52}$$

Upon integration of equation (2.50) twice, with respect to z and using the velocity boundary conditions $u_0(x,0) = 1$, $u_0(x,h) = 0$, it follows that

$$u_0 = \frac{\epsilon}{2}\frac{dp_0}{dx} z(z-h) - \frac{z}{h} + 1 \ . \tag{2.53}$$

After substitution of u_0 in equation (2.52) and integration with respect to z, the Reynolds equation for $p_0(x)$ results:

$$\frac{d}{dx}\left[6h(x) - \epsilon h^3(x)\frac{dp_0}{dx}\right] = 0 \ . \tag{2.54}$$

With the help of equation (2.45) an expression for w_0 can be deduced:

$$w_0 = \frac{z^2(z-h)\frac{dh}{dx}(\epsilon h^2 \frac{dp_0}{dx} - 2)}{2h^3} \ . \tag{2.55}$$

The equations for the first-order terms are the same as the equations given above, however, now the right-hand side is not zero but formed by derivatives of the zeroth-order solution.

$$\epsilon\frac{\partial p_1}{\partial x} - \frac{\partial^2 u_1}{\partial z^2} = \frac{\partial^2 u_0}{\partial x^2} \ , \tag{2.56}$$

$$\epsilon\frac{\partial p_1}{\partial z} = \frac{\partial^2 w_0}{\partial z^2} \ , \tag{2.57}$$

$$\frac{\partial u_1}{\partial x} + \frac{\partial w_1}{\partial z} = 0 \ . \tag{2.58}$$

The set of equations (2.56), (2.57) and (2.58) can be solved in a similar way as the set of equations (2.50), (2.51) and (2.52). The integration of equation (2.57) with respect to z gives an expression for the pressure correction,

$$\epsilon p_1 = \frac{\partial w_0}{\partial z} + \tilde{p}_1(x) \ . \tag{2.59}$$

The double integration of equation (2.56) with respect to z results in an expression for u_1. The unknown variable p_1 in the equation for u_1 follows from equation (2.59). After integration of equation (2.58) with respect to z and substitution of the expression for u_1 and the correct boundary values, an equation for $\tilde{p}_1$ follows:

$$\frac{d}{dx}\left[\left(\frac{dh}{dx}\right)^2(6c_1\epsilon + 28h(x)) + \frac{d^2h}{dx^2}h(x)(c_1\epsilon + 4h(x)) \ -10h(x)^3\frac{d\tilde{p}_1}{dx}\right] = 0 \ . \tag{2.60}$$

where c_1 is an integration constant[3] resulting from integration of equation (2.54). As $p_0 = p_0(x)$ it is clear that the z-dependency in the first-order correction comes from $\frac{\partial w_0}{\partial z}$ which is already known when the Reynolds solution is available. The $\tilde{p}_1(x)$ gives an overall correction. Hence, to first order in γ, the z-dependency can be easily found. So a local surface feature does not only affect the pressure locally, but also globally.

Finally, to show that even for small γ the perturbation series and hence the Reynolds equation loses its validity, the Stokes equations have been written out with $a^1_{(1)} = 1$, $a^2_{(2)} = h(\xi^1)$ and $a^2_{(1)} = \xi^2\frac{dh}{d\xi^1}$ in the transformed coordinate system. For the u-momentum equation it follows that:

$$\begin{aligned}
&\epsilon h\frac{\partial p}{\partial \xi^1} - \frac{1}{h}\frac{\partial^2 u}{\partial(\xi^2)^2} - \epsilon\xi^2\frac{dh}{d\xi^1}\frac{\partial p}{\partial \xi^2} - \\
&\gamma\left[\frac{dh}{d\xi^1}\frac{\partial u}{\partial \xi^1} + h\frac{\partial^2 u}{\partial(\xi^1)^2} - \xi^2\frac{d^2h}{d(\xi^1)^2}\frac{\partial u}{\partial \xi^2} - \xi^2\frac{dh}{d\xi^1}\frac{\partial^2 u}{\partial\xi^1\partial\xi^2}\right] - \\
&\gamma\left[-\frac{dh}{d\xi^1}\frac{\partial u}{\partial \xi^1} - \xi^2\frac{dh}{d\xi^1}\frac{\partial^2 u}{\partial\xi^1\partial\xi^2} + \frac{2\xi^2}{h}\left(\frac{dh}{d\xi^1}\right)^2\frac{\partial u}{\partial \xi^2} + \frac{(\xi^2)^2}{h}\left(\frac{dh}{d\xi^1}\right)^2\frac{\partial^2 u}{\partial(\xi^2)^2}\right] = 0 \ .
\end{aligned} \tag{2.61}$$

[3] $\frac{dp_0}{dx} = \frac{6h(x)+c_1\epsilon}{\epsilon h^3(x)}$

For the w-momentum equation it follows that:

$$\begin{aligned}
&\epsilon\frac{\partial p}{\partial \xi^2} - \gamma\left[\frac{1}{h}\frac{\partial^2 w}{\partial(\xi^2)^2}\right] - \\
&\gamma^2\left[\frac{dh}{d\xi^1}\frac{\partial w}{\partial \xi^1} + h\frac{\partial^2 w}{\partial(\xi^1)^2} - \xi^2\frac{d^2h}{d(\xi^1)^2}\frac{\partial w}{\partial \xi^2} - \xi^2\frac{dh}{d\xi^1}\frac{\partial^2 w}{\partial \xi^1 \partial \xi^2}\right] - \\
&\gamma^2\left[-\frac{dh}{d\xi^1}\frac{\partial w}{\partial \xi^1} - \xi^2\frac{dh}{d\xi^1}\frac{\partial^2 w}{\partial \xi^1 \partial \xi^2} + \frac{2\xi^2}{h}\left(\frac{dh}{d\xi^1}\right)^2\frac{\partial w}{\partial \xi^2} + \frac{(\xi^2)^2}{h}\left(\frac{dh}{d\xi^1}\right)^2\frac{\partial^2 w}{\partial(\xi^2)^2}\right] = 0 \ .
\end{aligned} \tag{2.62}$$

For the continuity equation one obtains:

$$\frac{\partial}{\partial \xi^1}\left[hu\right] + \frac{\partial}{\partial \xi^2}\left[-\xi^2\frac{dh}{d\xi^1}u + w\right] = 0 \ . \tag{2.63}$$

For the equations (2.61),(2.62) and (2.63) to reduce to the Reynolds equation it is necessary that the terms with γ and γ^2 in the above equations are small. However, these terms also contain factors like $\frac{1}{h}$, $\frac{dh}{d\xi^1}$ and $\frac{d^2h}{d(\xi^1)^2}$. Now, for a small γ a product like $\gamma\frac{dh}{d\xi^1}$ can nevertheless be large and the terms containing these factors can not be omitted as was done in the derivation of the Reynolds equation. If the contact surface is considered to be built up out of Fourier components, a function for h, consisting of a single wave, could look like:

$$h(\xi^1) = 1 - A_m \sin\left(\frac{2\pi\xi^1}{\lambda}\right) \ , \tag{2.64}$$

where λ is a typical wavelength. And the factors which can counteract for a small γ look like:

$$\frac{1}{h} = \frac{1}{1 - A_m \sin(\frac{2\pi\xi^1}{\lambda})}, \quad \frac{dh}{d\xi^1} = -\frac{A_m}{\lambda}\cos\left(\frac{2\pi\xi^1}{\lambda}\right), \quad \frac{d^2h}{d(\xi^1)^2} = \frac{A_m}{\lambda^2}\sin\left(\frac{2\pi\xi^1}{\lambda}\right) \ . \tag{2.65}$$

So, even for surface features with a small amplitude, if the wavelength is sufficiently small, the Reynolds equation is not appropriate.

2.3 Pressure-dependent viscosity and/or density

Not only the geometry of the domain determines if the Reynolds approximation is valid but also the functional dependence of the density and the viscosity on the pressure. For mineral oils which are commonly used as lubricant, the viscosity may increase exponentially with pressure. It has been pointed out in [1] that this rapid change of viscosity as function of pressure can have a bad influence on the validity of the Reynolds equation. What about a pressure dependent density?

To study the validity of the Reynolds equation in the case of a pressure dependent density the simulation of gas lubrication will be used. For this purpose the model will be extended with an equation of state.

Finally, some kind of a cavitation algorithm is needed to prevent the pressure from dropping below the vapor pressure. A more realistic lift force can then be calculated. In

this work the cavitation is modeled with a two-phase model. In this model the density, as function of the pressure, changes abruptly, in the neighborhood of the vapor pressure, from the liquid density to the vapor density.

2.3.1 Piezo viscosity

In the field of lubrication the most widely used equations for a pressure-dependent viscosity are exponential: the Barus law [2] and the Roelands law [68]. To study the effect of a pressure-dependent viscosity on the validity of the Reynolds equation, in this thesis the Barus law has been used. In scaled variables it reads:

$$\eta = e^{\bar{\alpha}_p p} \ , \tag{2.66}$$

where $\bar{\alpha}_p = \alpha_p \eta_0 u_0 / H$. So, at the inflow/outflow boundary where $p = 0$, the un-scaled viscosity equals η_0, the ambient viscosity.

2.3.2 Gas lubrication

In the field of gas lubrication the Reynolds equation is also widely used. Generally, a constant viscosity is assumed. For the density the ideal gas law is assumed to be valid ,

$$p = \rho R_g T \ , \tag{2.67}$$

where R_g is the gas constant. The Reynolds equation is then deduced from the Navier-Stokes equations in the same way as was done in section (*2.1.2*). See [17] for an extensive discussion. Here we directly give the Reynolds equation:

$$\frac{d}{dx}[\frac{-\epsilon p}{12}\frac{dp}{dx}h^3 + ph\frac{(u_1+u_2)}{2}] = 0 \ . \tag{2.68}$$

This is a nonlinear equation containing effectively only one parameter $(u_1 + u_2)/\epsilon$. An intermediate model between the N-S equations and the Reynolds equation is formed by the Stokes equations. The use of the ideal gas law in the Stokes equations does not lead to an extra parameter in the Stokes equations. If the pressure is put equal to unity on the in- and outflow boundaries ($p = 0$ is unrealistic in a physical sense) and the velocity of the upper surface u_2 is taken zero, the solutions of the Stokes equations for different velocities of the lower surface are independent of each other. The solutions to the problem are then governed by two parameters ϵ and u_1. This is in contrast to the Reynolds equation, where for the case $u_2 = 0$ only one parameter u_1/ϵ remains.

2.3.3 Cavitation model

In the following it is assumed that the pressure at the inflow/outflow boundary is equal to the ambient pressure. This ambient pressure is taken equal to zero because it is, compared to the large pressure in a hydrodynamically-lubricated contact, very small. Furthermore it is assumed that the contact is fully flooded. So, there can be no air sucked in from the inflow/outflow boundaries. To quantify the difference between the Stokes solution for

the flow in a narrow gap and the Reynolds solution, the force exerted by the fluid on the surfaces can be used. However, for the case of Stokes flow, zero pressure boundary and a symmetric height function, there will be no net force on the boundary. To obtain a realistic result cavitation must be incorporated. In that case the pressure profile is no longer anti-symmetric and there will indeed be a net force.

Next, some more details concerning the treatment of cavitation in this work are given. The pressure is allowed to drop below the saturation pressure because it is assumed there is no gas dissolved in the fluid. The only mechanism that introduces bubbles or gas cavities in the film, is the "vaporization" of the liquid when the pressure drops below the vapor pressure. For this situation it is experimentally found [22] that there is a vapor/gas bubble downstream of the narrowest gap (see figure (2.3)). On the surface which is moving, there is still a layer of fluid.

Assuming a single cavity two major descriptions exist: (a) consider the boundary of the bubble as a free surface. In the cavity the pressure equals the vapor pressure and the velocity is zero. There is no flow in or out of the cavity. In [9] a numerical scheme has been developed to calculate this free surface. Especially in the region where the cavity closes there are some difficulties; (b) to describe the bubble with a two-phase (TP) model. There is no distinction between the cavitated region and the non-cavitating region, in the sense that there is no distinct boundary. The advantage of this model is that it is easier to implement in a computational method. It may not correctly describe the physical reality, but it will effectively prevent the pressure from dropping below the vapor pressure. In a tribological context it does not seem strange to take the same pressure (zero) for the ambient pressure, the saturation pressure as well as the vapor pressure, because the pressure in the contact is usually high compared to these three pressures.

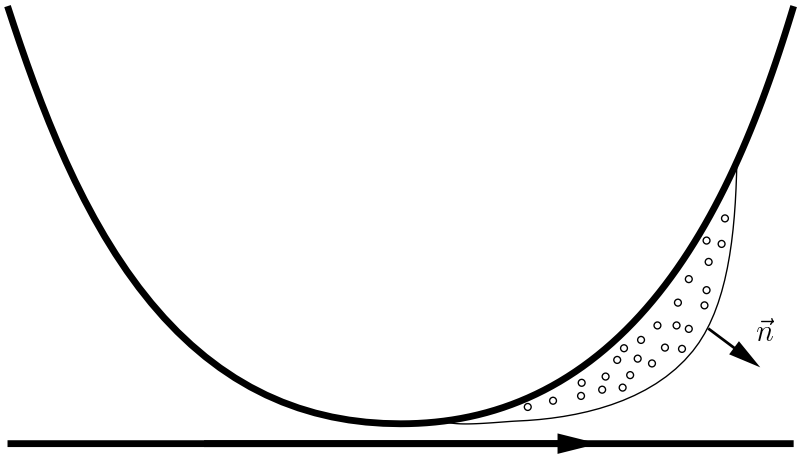

Figure 2.3: *Cavitation bubble in downstream part of the contact.*

The model that will be explained here, is based on the work described in [19] and [39]. The flow of the mixture is described by equations (2.8), (2.9) and (2.10). The vapor and the liquid move at the same speed, otherwise for each state separate equations with interaction terms would be needed. The dependent variables now refer to the mixture. An equation of state is used to complete the system of equations.

$$\rho = \begin{cases} \rho_l \text{ if } p > p_v + \Delta p \ , \\ \rho_v \text{ if } p < p_v - \Delta p \ , \\ \rho_v + \Delta\rho[1 + \sin(\frac{p-p_v}{\Delta\rho a_{min}^2})] \end{cases} , \tag{2.69}$$

where

$$\begin{array}{lcl} p_v & = & \text{vapor pressure ,} \\ \rho_l & = & \text{density liquid ,} \\ \rho_v & = & \text{density vapor ,} \\ \Delta\rho & = & \frac{1}{2}(\rho_l - \rho_v) \ , \\ \Delta p & = & \frac{1}{2}\pi a_{min}^2 \Delta\rho \ , \\ a_{min} & = & \text{minimal speed of sound in mixture .} \end{array} \tag{2.70}$$

Figure (2.4) gives a graphical representation of $\rho(p)$. The parameter a_{min} can be approximated by $a_{min} \approx 2a_v\sqrt{\frac{\rho_v}{\rho_l}}$ if $\rho_l \gg \rho_v$ with a_v the sound of speed in the vapor (for derivation see appendix (B)). For water at standard conditions it follows that $a_{min} = 25$[m/s]. There is still discussion about the correct relation between viscosity and pressure when the pressure approaches the vapor pressure. In [43] different options are mentioned, for example, a constant viscosity or a viscosity that exhibits the same behavior as the density as a function of the pressure, i.e., (2.69) with η_l replacing ρ_l and η_v replacing ρ_v. Numerical results for both models will be given in the present work.

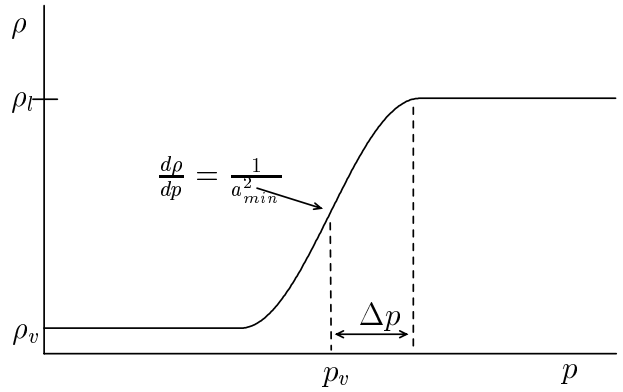

Figure 2.4: *Pressure-density diagram for the liquid/vapor mixture.*

After scaling according to (2.4) it follows that

$$\bar{\rho} = \begin{cases} 1 \text{ if } \bar{p} > \bar{p}_v + \frac{\pi}{2\beta_\rho} \ , \\ \bar{\rho}_0 \text{ if } \bar{p} < \bar{p}_v - \frac{\pi}{2\beta_\rho} \ , \\ \bar{\rho}_0 + \frac{1}{2}(1-\bar{\rho}_0)[1 + \sin(\beta_\rho(\bar{p} - \bar{p}_v))] \text{ if } \bar{p}_v - \frac{\pi}{2\beta_\rho} \le \bar{p} \le \bar{p}_v + \frac{\pi}{2\beta_\rho} \end{cases} , \tag{2.71}$$

where

$$\begin{array}{lcl} \bar{\rho}_0 & = & \frac{\rho_v}{\rho_l} \ , \\ \beta_\rho & = & \frac{2\eta_0 u_0}{H\rho_l a_{min}^2} \ , \\ \bar{p}_v & = & \frac{p_v H}{\eta_0 u_0} \ . \end{array} \tag{2.72}$$

For convenience the bars on the scaled quantities will be dropped from now on.

To show that a model of this form yields the same satisfactory behavior as a cavitation model, usually applied in tribology, we consider its implementation in the Reynolds equation for a model problem: the flow in a parabolically shaped gap.

In table (2.1) the two-phase (TP) model and the Reynolds cavitation model (RR) are summarized. In the RR model, cavitation is modeled through the condition, if $p > p_v$ the Reynolds equation is valid, otherwise $p = 0$. This means that when a zone cavitates it remains cavitated. In the present model problem, the boundary is in the cavitated region. In the two-phase model the outflow boundary condition in the cavitated region is $\frac{dp}{dx} = 0$ because the exact value for the pressure is unknown.

$h(x) = (1-\alpha)x^2 + \alpha$ $u_1 = 1, \quad u_2 = 0$	
TP	RR
$\frac{d}{dx}[\frac{-\epsilon\rho}{\eta}\frac{dp}{dx}h^3 + 6h\rho] = 0$	if $p > p_v$: $\frac{d}{dx}[-\epsilon\frac{dp}{dx}h^3 + 6h] = 0$ if $p \leq p_v$: $p = 0$
$p(x=-1) = 1, \quad \frac{dp}{dx}\Big\|_{x=1} = 0$	$p(x=-1) = 1, \quad p(x=1) = 0$

Table 2.1: *Description of the two models.*

The two models, TP and RR have been solved numerically, with an upwind discretization for the TP model, see section (*3.4*), and second-order central discretization for the RR model. For the viscosity the same relation has been used as for the density, equation (2.71), but now with ρ replaced by η. The following values have been used: $\epsilon = 0.01$, $\alpha = 0.2$ and $\rho_0 = 0.01, \eta_0 = 0.01$. In figures (2.5) and (2.6) the results are shown.

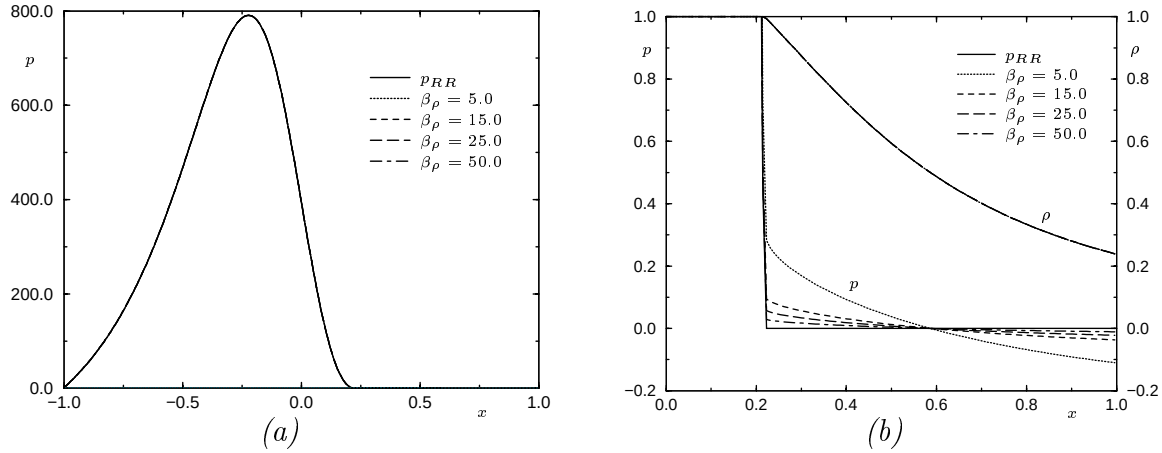

Figure 2.5: *(a): Pressure for different $\beta_\rho = \beta_\eta$. (b): Pressure and density for different $\beta_\rho = \beta_\eta$.*

First, figure (2.5) shows p as a function of x for different values of $\beta_\rho = \beta_\eta$. The figure shows that a change in the parameter β_ρ hardly influences the pressure profile; in figure (2.5a) all curves coincide. Only near the vapor pressure (= 0) a difference between the

solutions occurs see figure (2.5b). For increasing β_ρ the TP pressure approaches the RR pressure. The density is nearly the same for all β_ρ.

With the TP model it is also possible to simulate a cavitated region inside the contact. The RR model can not be used for this situation because in the cavitated zone continuity is not fulfilled and a return to the liquid phase is not possible without adding a special condition. In the following the same parameters have been used, but now with $p = 0$ at the outflow boundary and with $p_v = -50$ and $\beta_\rho = \beta_\eta = 50$. The results are shown in figure (2.6).

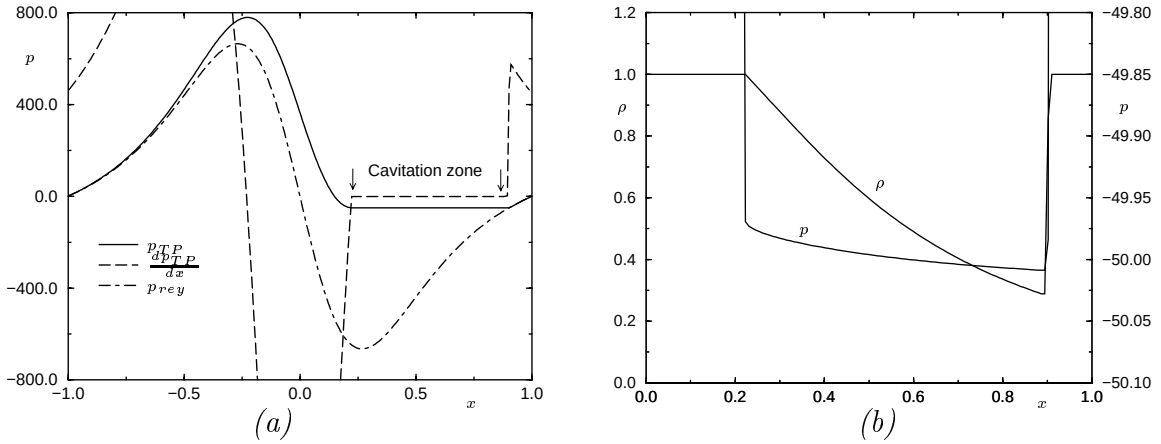

Figure 2.6: *(a): Pressure for two-phase model (p_{TP}), for Reynolds without cavitation (p_{rey}) and pressure gradient for two-phase model. (b): Pressure and density for two-phase model.*

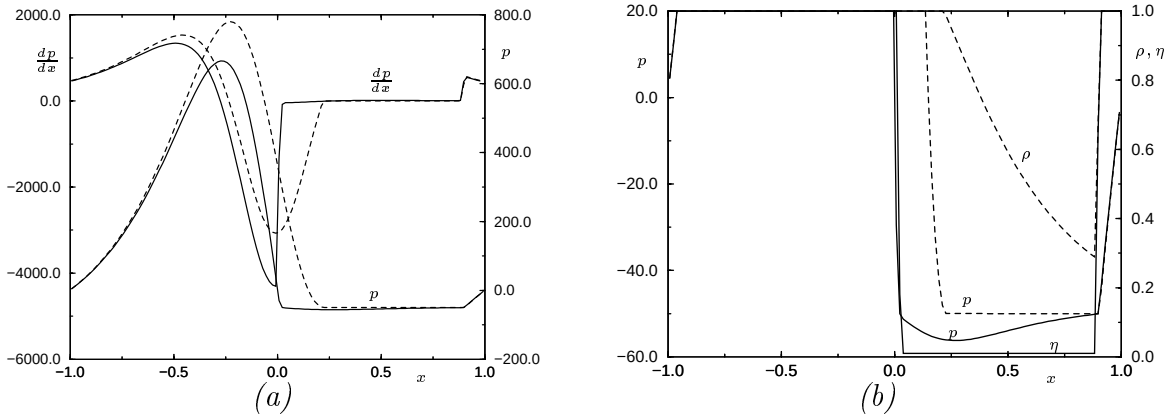

Figure 2.7: *Dotted lines represent $\eta_0 = 1.0$, $\rho_0 = 0.01$ and solid lines represent $\eta_0 = 0.01$, $\rho_0 = 1.0$. (a): Pressure and gradient of the pressure. (b): Pressure, density and viscosity.*

From figure (2.6a) it can be seen that the gradient in the pressure is discontinuous in the condensation point near $x = 0.9$. In the cavitation zone the density is not the same as the vapor density. After condensation the pressure is the same as the pressure for the Reynolds solution without cavitation (dot-dashed line in figure (2.6a)). Because p is a function of x and ρ is a function of p it is clear that $\rho < 1$ implies a vaporization of the fluid over the entire film thickness.

Further investigation shows that a constant viscosity gives the same result as in figure (2.6). Only if the density is constant and the viscosity pressure dependent, the solution changes radically. In figure (2.7) the case $\eta_0 = 1.0$, $\rho_0 = 0.01$ and the case $\eta_0 = 0.01$, $\rho_0 = 1.0$ have been plotted. In the constant-density case $\frac{dp}{dx}$ jumps at two locations, which is in contrast with the constant-viscosity case. It is also observed that the pressure can drop below p_v.

The results look promising enough to use equations (2.71) for the density and a constant viscosity together with the equations (2.8), (2.9), (2.10) for the fluid motion, to describe cavitation in the non-Reynolds case.

2.4 Lift force

The fluid moving through the channel exerts a force on the walls. This force can be calculated for the Stokes solution as well as for the Reynolds solution. It can be used to quantify the difference between both solutions. The lift force can also serve as a computational check. The force on the upper and the lower surface must be the same. However, it should be noted that the lift force should be calculated in a different way from what is normally done in tribology. This is because the assumption leading to the Reynolds equation does not hold anymore (that terms with ϵ^2 or higher order are small in the viscous part of the Stokes equations). In this section the lift force will be calculated. In general the following holds:

$$\int_\Omega \boldsymbol{\nabla} \cdot (-p\bar{\bar{1}} + \bar{\tau}) d\Omega = \sum_{i=1}^{4} \int_{\Gamma_i} (-p\bar{\bar{1}} + \bar{\tau}) \cdot \mathbf{n}_i ds = \mathbf{0} \ , \tag{2.73}$$

where the Γ_i boundaries are depicted in figure (2.1). Expressed in scaled variables, according to (2.4) for the viscous compressible case this gives:

$$\sum_{i=1}^{4} \int_{\Gamma_i} ds \begin{pmatrix} (-\epsilon p + 2\eta\epsilon^2 \frac{\partial u}{\partial x} - \frac{2}{3}\eta\epsilon^2 \boldsymbol{\nabla}\cdot\mathbf{u}) n_{xi} + \eta(\epsilon^3 \frac{\partial w}{\partial x} + \epsilon \frac{\partial u}{\partial z}) n_{zi} \\ \eta(\epsilon^2 \frac{\partial w}{\partial x} + \frac{\partial u}{\partial z}) n_{xi} + (-p + 2\eta\epsilon \frac{\partial w}{\partial z} - \frac{2}{3}\eta\epsilon \boldsymbol{\nabla}\cdot\mathbf{u}) n_{zi} \end{pmatrix} = \mathbf{0} \ . \tag{2.74}$$

Referring to figure (2.1) and taking the lower boundary horizontal, for the x-component in equation (2.74) one obtains:

$$\begin{aligned} &\int_{\Gamma_1} -\eta \left(\epsilon^3 \frac{\partial w}{\partial x} + \epsilon \frac{\partial u}{\partial z} \right) ds \ + \\ &\int_{\Gamma_2} \left((-\epsilon p + 2\eta\epsilon^2 \frac{\partial u}{\partial x} - \frac{2}{3}\eta\epsilon^2 \boldsymbol{\nabla}\cdot\mathbf{u}) n_{x2} + \eta(\epsilon^3 \frac{\partial w}{\partial x} + \epsilon \frac{\partial u}{\partial z}) n_{z2} \right) ds \ + \\ &\int_{\Gamma_3} \left(\epsilon p - 2\eta\epsilon^2 \frac{\partial u}{\partial x} + \frac{2}{3}\eta\epsilon^2 \boldsymbol{\nabla}\cdot\mathbf{u} \right) ds \ + \\ &\int_{\Gamma_4} \left(-\epsilon p + 2\eta\epsilon^2 \frac{\partial u}{\partial x} - \frac{2}{3}\eta\epsilon^2 \boldsymbol{\nabla}\cdot\mathbf{u} \right) ds = 0 \ . \end{aligned} \tag{2.75}$$

For the z-component in equation (2.74) it follows that:

$$\int_{\Gamma_1} \left(p - 2\eta\epsilon \frac{\partial w}{\partial z} + \frac{2}{3}\eta\epsilon \boldsymbol{\nabla}\cdot\mathbf{u} \right) ds \ +$$

$$\int_{\Gamma_2}\left(\eta(\epsilon^2\frac{\partial w}{\partial x}+\frac{\partial u}{\partial z})n_{x2}+(-p+2\eta\epsilon\frac{\partial w}{\partial z}-\frac{2}{3}\eta\epsilon\boldsymbol{\nabla}\cdot\mathbf{u})n_{z2}\right)ds\ +$$
$$\int_{\Gamma_3}-\eta\left(\epsilon^2\frac{\partial w}{\partial x}+\frac{\partial u}{\partial z}\right)ds\ +$$
$$\int_{\Gamma_4}\eta\left(\epsilon^2\frac{\partial w}{\partial x}+\frac{\partial u}{\partial z}\right)ds=0\ . \tag{2.76}$$

Assuming that the flow properties at inflow (Γ_3) and at outflow (Γ_4) are the same, the x-component simplifies to:

$$\int_{\Gamma_1}-\eta\left(\epsilon^3\frac{\partial w}{\partial x}+\epsilon\frac{\partial u}{\partial z}\right)ds\ +$$
$$\int_{\Gamma_2}\left((-\epsilon p+2\eta\epsilon^2\frac{\partial u}{\partial x}-\frac{2}{3}\eta\epsilon^2\boldsymbol{\nabla}\cdot\mathbf{u})n_{x2}+\eta(\epsilon^3\frac{\partial w}{\partial x}+\epsilon\frac{\partial u}{\partial z})n_{z2}\right)ds=0\ . \tag{2.77}$$

And the z-component simplifies to:

$$\int_{\Gamma_1}\left(p-2\eta\epsilon\frac{\partial w}{\partial z}+\frac{2}{3}\eta\epsilon\boldsymbol{\nabla}\cdot\mathbf{u}\right)ds\ +$$
$$\int_{\Gamma_2}\left(\eta(\epsilon^2\frac{\partial w}{\partial x}+\frac{\partial u}{\partial z})n_{x2}+(-p+2\eta\epsilon\frac{\partial w}{\partial z}-\frac{2}{3}\eta\epsilon\boldsymbol{\nabla}\cdot\mathbf{u})n_{z2}\right)ds=0\ . \tag{2.78}$$

Equations (2.77) and (2.78) show that the forces on the different surfaces (Γ_1 and Γ_2) balance each other. From equations (2.77) and (2.78) the total force vector on the lower plane can be assembled,

$$\mathbf{F}=\begin{pmatrix}\int_{\Gamma_1}(-\eta(\epsilon^3\frac{\partial w}{\partial x}+\epsilon\frac{\partial u}{\partial z})ds\\ \int_{\Gamma_1}(p-2\eta\epsilon\frac{\partial w}{\partial z}+\frac{2}{3}\eta\epsilon\boldsymbol{\nabla}\cdot\mathbf{u})ds\end{pmatrix}\ . \tag{2.79}$$

Finally, in a Reynolds approximation (ϵ small) the force on the lower surface can be described by the following vector:

$$\mathbf{F}=\begin{pmatrix}\int_{\Gamma_1}(-\epsilon\eta\frac{\partial u}{\partial z})ds\\ \int_{\Gamma_1}(p)ds\end{pmatrix}\ . \tag{2.80}$$

Comparing (2.80) with (2.79) shows that in this case only the pressure determines the lift force. In the case of an incompressible flow and a horizontal lower surface, the expression for the vertical force exerted on the lower plane is simply the integral over the pressure (in equation (2.79) $\boldsymbol{\nabla}\cdot\mathbf{u}=0$ and $\frac{\partial w}{\partial z}=-\frac{\partial u}{\partial x}=0$ on Γ_1).

As mentioned above, to quantify the difference between the Stokes and the Reynolds model the generated lift force can be used. In the tribological context the pressure rise is extreme but also the pressure drop. In principle, it is therefore necessary to have a cavitation algorithm to prevent the pressure to drop below vapor pressure. Otherwise, for the case of a symmetric feature on the upper boundary and zero pressure on the inlet and the outlet, the lift force is zero. In view of the cavitation issue a quantity to measure

the difference between the Stokes and the Reynolds solution, coupled to the lift force, can now be formulated like:

$$\bar{R} = \frac{\int_{\tilde{\Gamma}_1} p_S(x, z = 0)dx - \int_{\tilde{\Gamma}_1} p_R(x)dx}{\int_{\tilde{\Gamma}_1} p_R(x)dx} \ , \tag{2.81}$$

where the tilde in $\tilde{\Gamma}$ indicates that the pressure is only integrated for positive values.

Chapter 3

Numerical solution

Equations (2.11), (2.12) and (2.13) will be discretized in a boundary-fitted domain. The dependence of the viscosity on the spatial coordinates will be incorporated for later use. As dependent variables the Cartesian velocity components and the pressure have been chosen. The velocity components will not align with the grid lines. For not too steep grid lines there will be little loss of numerical accuracy. When contravariant velocity components are used as in [51], the discretization is more accurate, but also more complex because of the occurrence of Christoffel symbols. At this point it seems not necessary to use such an advanced discretization. A finite-volume (FV) discretization has been used to discretize equations (2.31), (2.32) and (2.33). A straightforward discretization with the variables in the cell centers would lead to an unstable discretization. The method of [66] ensures a stable discretization for cell-centered variable arrangement. An alternative, proposed in [38], where the velocity variables are placed on cell faces and the pressures on cell centers also ensures a stable discretization. This so-called staggered grid arrangement has been used in this work. Subsequently, to solve the resulting system of equations multi-grid techniques will be used. The performance of the developed solver is illustrated with some examples.

3.1 Discretization (Stokes equations)

In this section the discretization of the Stokes equations in two dimensions with constant viscosity and density is worked out. Only the continuity equation needs some revision in the case of a pressure-dependent density. The physical domain Ω is bounded by four sides. So, in the transformed space G each line with $\xi^i = 0, 1$ corresponds to one of the sides of Ω. The transformed equations are discretized on a uniform grid. This computational grid is defined by $G_{\delta\xi} = \{(\xi^1_{i-1/2}, \xi^2_{j-1/2}) = ((i-1)\delta\xi^1, (j-1)\delta\xi^2); (i,j) = 1, ..., N+1; \delta\xi^1, \delta\xi^2 = 1/N\}$ and the coordinates of the cell centers are $(\xi^1_i, \xi^2_j) = ((i-1/2)\delta\xi^1, (j-1/2)\delta\xi^2); (i,j) = 1, ..., N)$. From the definition of $G_{\delta\xi}$ it is clear that $(\delta\xi^1 = \delta\xi, \delta\xi^2 = \delta\xi)$ but for clearness the notation $(\delta\xi^1, \delta\xi^2)$ is used. For our discretization, the geometrical functions, $\mathbf{a}_{(k)}$, will be required in the grid points defined by $G_{\delta\xi/2}$.

A stable discretization is ensured by a staggered grid arrangement of the variables, as shown in figure (3.1). The pressure is defined in the cell center, the u-velocity component

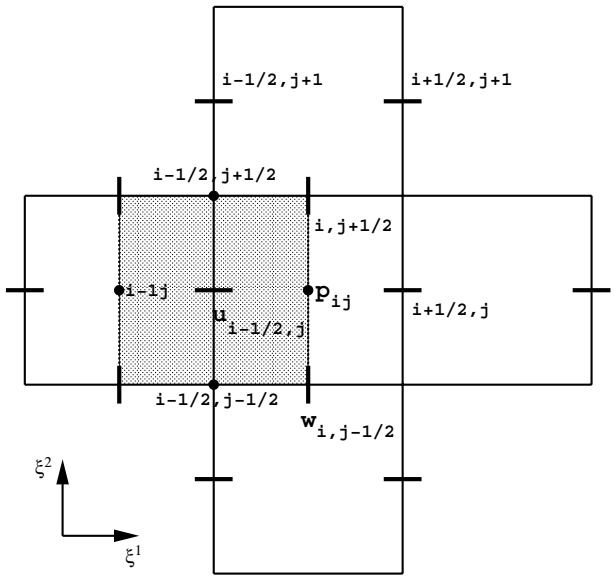

Figure 3.1: *Finite volume for the x-momentum equation on a staggered grid. Location variables: horizontal lines u-velocity, vertical lines w-velocity and dots cell centers pressure.*

on the vertical cell face and the w-velocity on the horizontal cell face. Integration of the momentum and continuity equations has been carried out over the corresponding finite volumes. In figure (3.1) the finite volume (FV), corresponding to $u_{i-\frac{1}{2}j}$ is shown. For the x-momentum equation (2.31), using the Gauss theorem, gives:

$$\int_{\Gamma_u} \left[\epsilon\sqrt{g} a_1^{(k)} p - 2\epsilon^2 \eta \sqrt{g} a_1^{(k)} a_1^{(l)} \frac{\partial u}{\partial \xi^l} - \eta\sqrt{g} a_2^{(k)} \left(\epsilon^2 a_1^{(l)} \frac{\partial w}{\partial \xi^l} + a_2^{(l)} \frac{\partial u}{\partial \xi^l} \right) \right] n_k \, ds = 0 \ , \qquad (3.1)$$

where Γ_u is the boundary of the FV for the x-momentum equation and n_k the k^{th} component of the unit normal, directed outward of this FV. Taking the dependent variables constant over the cell faces, when integrating over the cell faces, leads to:

$$\begin{aligned}
&\delta\xi^2 \left\{ \epsilon\sqrt{g} a_1^{(1)} p \right\}_{ij} - \delta\xi^2 \left\{ \epsilon\sqrt{g} a_1^{(1)} p \right\}_{i-1j} + \\
&\delta\xi^1 \left\{ \epsilon\sqrt{g} a_1^{(2)} p \right\}_{i-\frac{1}{2}j+\frac{1}{2}} - \delta\xi^1 \left\{ \epsilon\sqrt{g} a_1^{(2)} p \right\}_{i-\frac{1}{2}j-\frac{1}{2}} - \\
&\delta\xi^2 \left\{ \eta\sqrt{g} [2\epsilon^2 a_1^{(1)} a_1^{(l)} \frac{\partial u}{\partial \xi^l} + \epsilon^2 a_2^{(1)} a_1^{(l)} \frac{\partial w}{\partial \xi^l} + a_2^{(1)} a_2^{(l)} \frac{\partial u}{\partial \xi^l} \right\}_{ij} + \\
&\delta\xi^2 \left\{ \eta\sqrt{g} [2\epsilon^2 a_1^{(1)} a_1^{(l)} \frac{\partial u}{\partial \xi^l} + \epsilon^2 a_2^{(1)} a_1^{(l)} \frac{\partial w}{\partial \xi^l} + a_2^{(1)} a_2^{(l)} \frac{\partial u}{\partial \xi^l} \right\}_{i-1j} - \\
&\delta\xi^1 \left\{ \eta\sqrt{g} [2\epsilon^2 a_1^{(2)} a_1^{(l)} \frac{\partial u}{\partial \xi^l} + \epsilon^2 a_2^{(2)} a_1^{(l)} \frac{\partial w}{\partial \xi^l} + a_2^{(2)} a_2^{(l)} \frac{\partial u}{\partial \xi^l} \right\}_{i-\frac{1}{2}j+\frac{1}{2}} + \\
&\delta\xi^1 \left\{ \eta\sqrt{g} [2\epsilon^2 a_1^{(2)} a_1^{(l)} \frac{\partial u}{\partial \xi^l} + \epsilon^2 a_2^{(2)} a_1^{(l)} \frac{\partial w}{\partial \xi^l} + a_2^{(2)} a_2^{(l)} \frac{\partial u}{\partial \xi^l} \right\}_{i-\frac{1}{2}j-\frac{1}{2}} = 0 \ , \qquad (3.2)
\end{aligned}$$

where $\delta\xi^1$ and $\delta\xi^2$ are the length of the cell faces in the ξ^1- and ξ^2-direction, respectively.

A finite volume for the integration of the continuity equation is centered around p_{ij}, see figure (3.1). The integration gives:

$$\int_{\Gamma_p} [\sqrt{g} a_l^{(k)} u^l] n_k \, ds = 0 \ , \tag{3.3}$$

where Γ_p is the boundary of the FV for the continuity equation and n_k is the k^{th} component of the unit normal directed outward of the FV for the continuity equation (this FV is defined by the four points $(\xi^1_{i-\frac{1}{2}}, \xi^2_{j-\frac{1}{2}})$, $(\xi^1_{i+\frac{1}{2}}, \xi^2_{j-\frac{1}{2}})$, $(\xi^1_{i-\frac{1}{2}}, \xi^2_{j+\frac{1}{2}})$ and $(\xi^1_{i+\frac{1}{2}}, \xi^2_{j+\frac{1}{2}})$). Taking the dependent variables constant over the cell faces, when integrating over the cell faces, the discretization of equation (3.3) leads to:

$$\begin{aligned} &[\sqrt{g} a_l^{(1)} u^l]_{i+1/2j} \delta\xi^2 - [\sqrt{g} a_l^{(1)} u^l]_{i-1/2j} \delta\xi^2 + \\ &+ [\sqrt{g} a_l^{(2)} u^l]_{ij+1/2} \delta\xi^1 - [\sqrt{g} a_l^{(2)} u^l]_{ij-1/2} \delta\xi^1 = 0 \ . \end{aligned} \tag{3.4}$$

Because the transformation is from (ξ^1, ξ^2) to (x, y), the covariant base vectors will be required instead of the contravariant base vectors, see equation (2.35).

The discretization of the partial derivatives in equation (3.2) is carried out by taking the average of the partial differential over a control volume Ω. In the viscous part of (3.2) there are two types of terms. First, those where the variables are defined at the location where they are needed. For example:

$$\left\{ \frac{\partial u}{\partial \xi^1} \right\}_{ij} \equiv \frac{1}{\Omega} \int \frac{\partial u}{\partial \xi^1} \, d\Omega \approx \frac{1}{\Omega} \int \frac{(u_{i+\frac{1}{2}j} - u_{i-\frac{1}{2}j})}{\delta\xi^1} \, d\xi^1 \, d\xi^2 = \frac{u_{i+\frac{1}{2}j} - u_{i-\frac{1}{2}j}}{\delta\xi^1} \ , \tag{3.5}$$

where it is assumed that within Ω $u_{i+\frac{1}{2}j} - u_{i-\frac{1}{2}j}$ is constant along ξ^2. Second, those where the variables are not defined at the location where they are needed. For example:

$$\begin{aligned} \left\{ \frac{\partial u}{\partial \xi^2} \right\}_{ij} &\equiv \frac{1}{\Omega} \int \frac{\partial u}{\partial \xi^2} \, d\Omega \approx \frac{1}{\Omega} \int \frac{(u_{ij+\frac{1}{2}} - u_{ij-\frac{1}{2}})}{\delta\xi^2} \, d\xi^1 \, d\xi^2 = \\ &= \frac{u_{i-\frac{1}{2}j+1} + u_{i+\frac{1}{2}j+1} - u_{i-\frac{1}{2}j-1} - u_{i+\frac{1}{2}j-1}}{4\delta\xi^2} \ . \end{aligned} \tag{3.6}$$

We take $u_{ij+\frac{1}{2}} = \frac{1}{4}(u_{i-\frac{1}{2}j} + u_{i-\frac{1}{2}j+1} + u_{i+\frac{1}{2}j+1} + u_{i+\frac{1}{2}j})$ and the shifted similar expression for $u_{ij-\frac{1}{2}}$. Regarding the pressure terms in (3.2), a similar approach is used, i.e., if the value of p is needed in a point at which it is not defined, it is determined by interpolation from the surrounding values. This gives for linear interpolation:

$$p_{i-\frac{1}{2}j+\frac{1}{2}} = \frac{1}{4}(p_{ij} + p_{i-1j} + p_{ij+1} + p_{i-1j+1}) \ . \tag{3.7}$$

The viscosity in, for example, the point, $(i - \frac{1}{2}, j + \frac{1}{2})$ can be calculated with an analytic expression. If it is dependent on the pressure, a weighted average of the four neighboring points will be used. In the discretization of the other equations we do not encounter any difficulties. A more convenient notation is to write u_{ij} for $u_{i-\frac{1}{2}j}$ and w_{ij} for $w_{ij-\frac{1}{2}}$. One cell then contains five variables: u^h_{ij}, u^h_{i+1j}, w^h_{ij}, w^h_{ij+1}, p^h_{ij}.

The discretization of (3.2) can now be written in the following form:

$$\begin{aligned}
&A^1_{ij}u^h_{ij} + A^2_{ij}u^h_{i+1j} + A^3_{ij}u^h_{ij+1} + A^4_{ij}u^h_{i+1j+1} + \\
&A^5_{ij}u^h_{ij-1} + A^6_{ij}u^h_{i+1j-1} + A^7_{ij}u^h_{i-1j} + A^8_{ij}u^h_{i-1j+1} + A^9_{ij}u^h_{i-1j-1} + \\
&A^{10}_{ij}w^h_{ij+1} + A^{11}_{ij}w^h_{ij} + A^{12}_{ij}w^h_{i-1j+1} + A^{13}_{ij}w^h_{i-1j} + A^{14}_{ij}w^h_{i+1j+1} + A^{15}_{ij}w^h_{i+1j} + \\
&A^{16}_{ij}w^h_{i-2j+1} + A^{17}_{ij}w^h_{i-2j} + A^{18}_{ij}w^h_{i-1j+2} + A^{19}_{ij}w^h_{ij+2} + A^{20}_{ij}w^h_{i-1j-1} + A^{21}_{ij}w^h_{ij-1} + \\
&A^{22}_{ij}p^h_{ij} + A^{23}_{ij}p^h_{i-1j} + A^{24}_{ij}p^h_{ij+1} + A^{25}_{ij}p^h_{i-1j+1} + A^{26}_{ij}p^h_{i-1j-1} + A^{27}_{ij}p^h_{ij-1} = 0 \ . \qquad (3.8)
\end{aligned}$$

For the z-momentum equation a similar expression exists:

$$\begin{aligned}
&B^1_{ij}w^h_{ij} + B^2_{ij}w^h_{ij+1} + B^3_{ij}w^h_{i+1j} + B^4_{ij}w^h_{i+1j+1} + \\
&B^5_{ij}w^h_{i-1j} + B^6_{ij}w^h_{i-1j+1} + B^7_{ij-1}w^h_{i-1j} + B^8_{ij}w^h_{i+1j-1} + B^9_{ij}w^h_{i-1j-1} + \\
&B^{10}_{ij}u^h_{ij+1} + B^{11}_{ij}u^h_{i+1j} + B^{12}_{ij}u^h_{ij-1} + B^{13}_{ij}u^h_{i+1j-1} + B^{14}_{ij}u^h_{ij+1} + B^{15}_{ij}u^h_{i+1j+1} + \\
&B^{16}_{ij}u^h_{ij-2} + B^{17}_{ij}u^h_{i+1j-2} + B^{18}_{ij}u^h_{i+2j} + B^{19}_{ij}u^h_{i+2j-1} + B^{20}_{ij}u^h_{i-1j} + B^{21}_{ij}u^h_{i-1j-1} + \\
&B^{22}_{ij}p^h_{ij} + B^{23}_{ij}p^h_{ij-1} + B^{24}_{ij}p^h_{i+1j} + B^{25}_{ij}p^h_{i+1j-1} + B^{26}_{ij}p^h_{i-1j} + B^{27}_{ij}p^h_{i-1j-1} = 0 \ . \qquad (3.9)
\end{aligned}$$

For the continuity equation the stencil looks like:

$$\begin{aligned}
&C^1_{ij}u^h_{ij} + C^2_{ij}u^h_{i+1j} + C^3_{ij}u^h_{ij+1} + C^4_{ij}u^h_{i+1j+1} + C^5_{ij}u^h_{ij-1} + C^6_{ij}u^h_{i+1j-1} + C^7_{ij-1}w^h_{ij} + \\
&C^8_{ij}w^h_{ij+1} + C^9_{ij}w^h_{i-1j} + C^{10}_{ij}w^h_{i-1j+1} + C^{11}_{ij}w^h_{i+1j} + C^{12}_{ij}w^h_{i+1j+1} = 0 \ . \qquad (3.10)
\end{aligned}$$

The stencils have different forms at the boundaries where also the right-hand side is not zero. Next, for a pressure boundary as described in equation (2.3), a detailed description of the discretization of the Γ_3 boundary (see figure (2.1)) for the x-momentum equation will be given. After integration of equation (2.31) over the finite volume defined in figure (3.2), it follows that:

$$\begin{aligned}
&\delta\xi_2\{\epsilon\sqrt{g}a^{(1)}_1 p\}_{ij} - \delta\xi_2\{\epsilon\sqrt{g}a^{(1)}_1 p\}_{i-\frac{1}{2}j} + \\
&\frac{\delta\xi_1}{2}\{\epsilon\sqrt{g}a^{(2)}_1 p\}_{i-\frac{1}{4}j+\frac{1}{2}} - \frac{\delta\xi_1}{2}\{\epsilon\sqrt{g}a^{(2)}_1 p\}_{i-\frac{1}{4}j-\frac{1}{2}} - \\
&\delta\xi_2\{\eta\sqrt{g}[2\epsilon^2 a^{(1)}_1 a^{(l)}_1\frac{\partial u}{\partial\xi^l} + \epsilon^2 a^{(1)}_2 a^{(l)}_1\frac{\partial w}{\partial\xi^l} + a^{(1)}_2 a^{(l)}_2\frac{\partial u}{\partial\xi^l}\}_{ij} + \\
&\delta\xi_2\{\eta\sqrt{g}[2\epsilon^2 a^{(1)}_1 a^{(l)}_1\frac{\partial u}{\partial\xi^l} + \epsilon^2 a^{(1)}_2 a^{(l)}_1\frac{\partial w}{\partial\xi^l} + a^{(1)}_2 a^{(l)}_2\frac{\partial u}{\partial\xi^l}\}_{i-\frac{1}{2}j} - \\
&\frac{\delta\xi_1}{2}\{\eta\sqrt{g}[2\epsilon^2 a^{(2)}_1 a^{(l)}_1\frac{\partial u}{\partial\xi^l} + \epsilon^2 a^{(2)}_2 a^{(l)}_1\frac{\partial w}{\partial\xi^l} + a^{(2)}_2 a^{(l)}_2\frac{\partial u}{\partial\xi^l}\}_{i-\frac{1}{4}j+\frac{1}{2}} + \\
&\frac{\delta\xi_1}{2}\{\eta\sqrt{g}[2\epsilon^2 a^{(2)}_1 a^{(l)}_1\frac{\partial u}{\partial\xi^l} + \epsilon^2 a^{(2)}_2 a^{(l)}_1\frac{\partial w}{\partial\xi^l} + a^{(2)}_2 a^{(l)}_2\frac{\partial u}{\partial\xi^l}\}_{i-\frac{1}{4}j-\frac{1}{2}} = 0 \ . \qquad (3.11)
\end{aligned}$$

To calculate the partial derivatives, the surface average of the quantity will be used as in equation (3.5). For the pressure simple interpolation will give:

$$\begin{aligned}
p_{i-\frac{1}{2}j} &= p_w \ , \\
p_{i-\frac{1}{4}j-\frac{1}{2}} &= \tfrac{1}{4}(p_{ij-1} + p_{ij} + 2p_w) \ . \qquad (3.12)
\end{aligned}$$

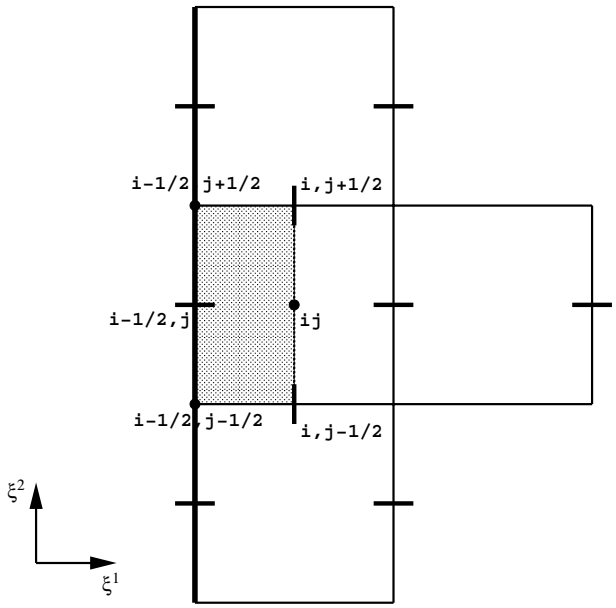

Figure 3.2: *FV volume for the x-momentum equation on a boundary where* $w = 0$ *and* $p = p_w$.

Linear interpolation will be used to approximate variables in points where they are not defined. For example:

$$\left\{\frac{\partial u}{\partial \xi^1}\right\}_{i-\frac{1}{4}j-\frac{1}{2}} \equiv \frac{1}{\Omega}\int \frac{\partial u}{\partial \xi^1}\, d\Omega \approx \frac{2}{\Omega}\int (u_{ij-\frac{1}{2}} - u_{i-\frac{1}{2}j-\frac{1}{2}})\, d\xi^2 = \\ = \frac{u_{i+\frac{1}{2}j} + u_{i+\frac{1}{2}j-1} - u_{i-\frac{1}{2}j} - u_{i-\frac{1}{2}j-1}}{2\delta\xi^1} \ . \tag{3.13}$$

All the others can be calculated in a similar way. Special care must be taken with the discretization of $\frac{\partial u}{\partial \xi^1}$ on the boundary. Normally $u_{i-\frac{1}{2}j}$ is known, but in a tribological context a pressure boundary is expected,

$$\left\{\frac{\partial u}{\partial \xi^1}\right\}_{i-\frac{1}{2}j} \equiv \frac{1}{\Omega}\int \frac{\partial u}{\partial \xi^1}\, d\Omega \approx \frac{2(u_{ij} - u_{i-\frac{1}{2}j})}{\delta\xi^1} \ , \tag{3.14}$$

where u_{ij} is approximated by $(3u_{i+\frac{1}{2}j} - u_{i+\frac{3}{2}j})/2$ and not by $(u_{i+\frac{1}{2}j} + u_{i-\frac{1}{2}j})/2$, because then the discretization of $\frac{\partial^2 u}{\partial {\xi^1}^2}$ on the boundary will be equal to zero. The other boundary elements can be discretized in a similar fashion. The discretization of the other equations at the boundaries is straightforward and is done in the same manner as explained for the x-momentum equation.

The covariant base vectors, $\mathbf{a}_{(k)}$, can be calculated directly if the analytic expressions for x, z as function of ξ^1, ξ^2 are known. But then the following identity will not hold in a transformed coordinate system:

$$\int_\Omega \nabla \cdot \mathbf{u}\ dV = \oint_{\delta\Omega} \mathbf{u} \cdot d\mathbf{s} = 0 \ , \tag{3.15}$$

where $\mathbf{u}$ is a constant vector field. The transformation is assumed to be of the form:

$$\begin{aligned} x &= x(\xi^1) \ , \\ z &= \xi^2 h(\xi^1) \ , \end{aligned} \tag{3.16}$$

thus

$$\mathbf{a}_{(1)} = \begin{pmatrix} \frac{\partial x}{\partial \xi^1} \\ \frac{\partial z}{\partial \xi^1} \end{pmatrix}, \quad \mathbf{a}_{(2)} = \begin{pmatrix} 0 \\ \frac{\partial z}{\partial \xi^2} \end{pmatrix} \ . \tag{3.17}$$

This so-called "scaling on the height" will be used in the rest of this thesis.

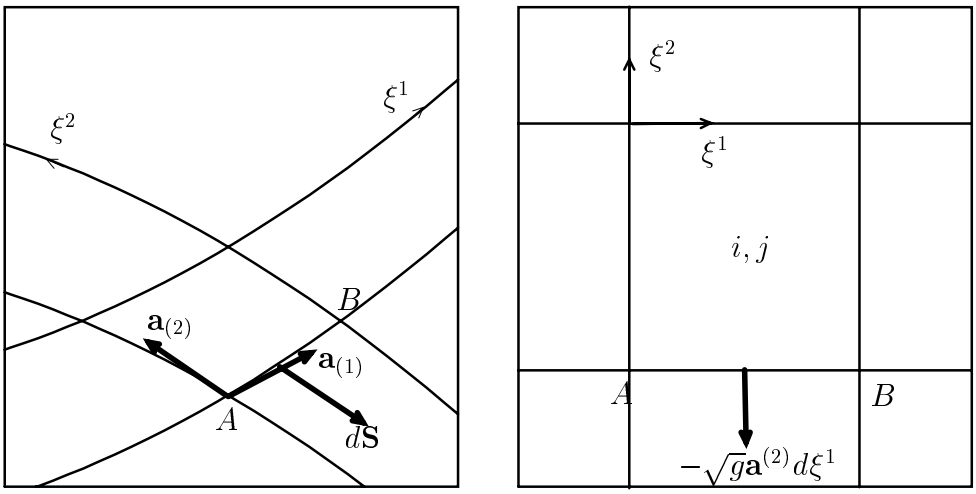

Figure 3.3: *A cell in a Cartesian and in a transformed coordinate system.*

To compute the contour integral in equation (3.15) in the transformed coordinate system, the line integral between A and B (see figure (3.3)) is evaluated, as

$$\int_A^B \mathbf{u} \cdot d\mathbf{s} = -\int_A^B \sqrt{g}\mathbf{u} \cdot \mathbf{a}^{(2)} d\xi^1 \approx \left\{ u^1 a^2_{(1)} - u^2 a^1_{(1)} \right\}_{i,j-\frac{1}{2}} \delta\xi^1 \ , \tag{3.18}$$

where the cell-face midpoint value is used for the integrand. Using this approximation, the remaining terms in equation (3.15) can be calculated, resulting in:

$$\oint \mathbf{u} \cdot d\mathbf{s} \approx u^1 \left(a^2_{(2)} \Big|^{i+\frac{1}{2},j}_{i-\frac{1}{2},j} \delta\xi^2 - a^2_{(1)} \Big|^{i,j+\frac{1}{2}}_{i,j-\frac{1}{2}} \delta\xi^1 \right) + u^2 \left(-a^1_{(2)} \Big|^{i+\frac{1}{2},j}_{i-\frac{1}{2},j} \delta\xi^2 + a^1_{(1)} \Big|^{i,j+\frac{1}{2}}_{i,j-\frac{1}{2}} \delta\xi^1 \right) \ . \tag{3.19}$$

The second term on the right side of equation (3.19) is zero because $a^1_{(2)} = 0$ and $a^1_{(1)}$ does not depend on ξ^2. The remaining term is then:

$$u^1 \left(\delta\xi^2 (h_{i+\frac{1}{2}} - h_{i-\frac{1}{2}}) - \delta\xi^1 \delta\xi^2 \left\{ \frac{dh}{d\xi^1} \right\}_i \right) \ . \tag{3.20}$$

A Taylor expansion of h gives:

$$h_{i+\frac{1}{2}} - h_{i-\frac{1}{2}} = \delta\xi^1 \left\{ \frac{dh}{d\xi^1} \right\}_i + \frac{1}{24} (\delta\xi^1)^3 \left\{ \frac{d^3 h}{d(\xi^1)^3} \right\}_i + O(\delta\xi^1)^4 \ . \tag{3.21}$$

Substituting this into the remaining term, term (3.20), gives

$$u^1 \left[\frac{1}{24} (\delta\xi^1)^3 \left\{ \frac{d^3 h}{d(\xi^1)^3} \right\}_i + \delta\xi^2 O(\delta\xi^1)^4 \right] . \tag{3.22}$$

From this, it is clear that for large $\frac{d^3h}{d(\xi^1)^3}$ the contour integral in equation (3.15) is sufficiently small if $\delta\xi^1$ is sufficiently small. On the other hand, if a numerical approximation is used for the geometrical functions, the contour integral in equation (3.15) will be exactly zero. In the following, these approximations will be presented. Because x is only a function of ξ^1 and z is scaled with the height $h(\xi^1)$, there are two types of approximations for each covariant base vector,

$$\left\{ a^1_{(1)} \right\}_i = \frac{(x_{i+\frac{1}{2}} - x_{i-\frac{1}{2}})}{\delta\xi^1}, \quad \left\{ a^1_{(1)} \right\}_{i-\frac{1}{2}} = \frac{(x_{i+\frac{1}{2}} - x_{i-\frac{3}{2}})}{2\delta\xi^1} . \tag{3.23}$$

For $a^2_{(1)}$ the approximation is found to be:

$$\left\{ a^2_{(1)} \right\}_{i,j} = \xi^2_j \frac{(h_{i+\frac{1}{2}} - h_{i-\frac{1}{2}})}{\delta\xi^1}, \quad \left\{ a^2_{(1)} \right\}_{i-\frac{1}{2},j} = \xi^2_j \frac{(h_{i+\frac{1}{2}} - h_{i-\frac{3}{2}})}{2\delta\xi^1} . \tag{3.24}$$

And for $a^2_{(2)}$ the expression is:

$$\left\{ a^2_{(2)} \right\}_i = \frac{1}{2}(h_{i-\frac{1}{2}} + h_{i+\frac{1}{2}}), \quad \left\{ a^2_{(2)} \right\}_{i-\frac{1}{2}} = h_{i-\frac{1}{2}} . \tag{3.25}$$

It can be verified easily that the contour integral in equation (3.15) is exactly zero with the above approximations for the covariant base vectors.

It can be shown, by Taylor expansion of the variables, that the described discretization of the transformed Stokes equations approximates the continuous transformed Stokes equations up to a truncation error of $O((\delta\xi)^2)$ (taking $\delta\xi^1 = \delta\xi, \delta\xi^2 = \delta\xi$, as an example, is in appendix (D) the truncation error of the discretized continuity equation derived). This means the scheme is consistent. Furthermore, a finite difference discretization of the Stokes equations on a staggered Cartesian grid is stable, see [38]. It is assumed that this also holds for the transformed Stokes equations. Consistency and stability of the scheme ensures convergence of the discrete solution of the problem to the solution of the continuous problem, see [67], i.e. the difference between these two solutions, the discretization error, decreases with decreasing mesh size. In fact, for a linear differential operator the truncation error and the discretization error are of the same order in $\delta\xi$. For more information on consistency, stability and convergence see for example [35].

3.2 Solving

The linear system, resulting from the discretization of equations (2.11), (2.12) and (2.13), consists of $3N^2$ unknowns in the case of a pressure boundary like in equation (2.3). Direct solution methods are time consuming. For example Gaussian elimination requires a number of computations of the order of b^2N^2 (where b is the bandwidth of the matrix).

So for the solution of a large system a method based on iterative techniques is required. Two of the most efficient methods are: Conjugate Gradient methods (CG) and Multi-Grid (MG) methods. For an overview of CG methods see [69]. In this work the MG method will be used. Below a short description of the method will be given. For proofs of statements in this section and for deeper explanation of MG and basic iterative methods see [5], [6], [34], [40], [95] and [75].

3.2.1 Multi-grid: general description

For simplicity, consider the linear differential operator L working on the unknown u,

$$Lu = f \ , \tag{3.26}$$

on a domain Ω with appropriate boundary conditions. Suppose that after discretization on a grid with a mesh size h a linear system of equations is obtained that can be written as:

$$L^h \mathbf{u}^h = \mathbf{f}^h \ , \tag{3.27}$$

$\mathbf{u}^h$ being the vector with unknowns and $\mathbf{f}^h$ the vector with right-hand-side values. Now, assume some initial approximation $\mathbf{u}_0^h$ to $\mathbf{u}^h$ is given. Subsequently, a sequence of successive iterates $\mathbf{u}_m^h$ is computed for $m = 1, 2, ..; \mathbf{u}_0^h \rightarrow \mathbf{u}_1^h \rightarrow \mathbf{u}_2^h \rightarrow ..\mathbf{u}_\infty^h \rightarrow ..\mathbf{u}^h$ where the arrow indicates the rule of the process. A general way to describe iterative processes is to introduce a splitting of the matrix L^h:

$$L^h = M^h - N^h \ . \tag{3.28}$$

Restricting ourselves to processes where $\mathbf{u}_{m+1}^h$ is computed using $\mathbf{u}_m^h$ only, the algorithm used to compute $\mathbf{u}_{m+1}^h$ given $\mathbf{u}_m^h$ can be written as:

$$\mathbf{u}_{m+1}^h = \mathbf{u}_m^h + (M^h)^{-1}\mathbf{r}_m^h, \quad \mathbf{r}_m^h = \mathbf{f}^h - L^h \mathbf{u}_m^h \ . \tag{3.29}$$

To analyze the behavior of the process, it is convenient to introduce the error in the iterant, defined as:

$$\mathbf{e}_m^h = \mathbf{u}_m^h - \mathbf{u}^h \ . \tag{3.30}$$

From substitution of (3.30) in (3.29) it follows that:

$$\mathbf{e}_{m+1}^h = (\overline{1} - (M^h)^{-1}L^h)\mathbf{e}_m^h = S\mathbf{e}_m^h \ . \tag{3.31}$$

From this equation it follows that the sequence $\mathbf{u}_0^h, .., \mathbf{u}_m^h$ will only converge to $\mathbf{u}^h$ for $m \rightarrow \infty$ if the spectral radius[1] ρ_{spec} of the matrix S satisfies the requirement: $\rho_{spec}(S) < 1$. This is, for example, the case if the splitting (3.28) is regular[2] and L^h is an irreducible K matrix:

[1] $\rho_{spec}(S)$=max$\{|\lambda| : \lambda$ eigenvalue of $S\}$

[2] For M^h and N^h in (3.28) holds $(M^h)^{-1} \geq 0$ and $N^h \geq 0$ elementwise

Definition 1 *A matrix L^h is called a K-matrix if*

$$(L^h)_{ii} > 0, \forall i,$$

$$(L^h)_{ij} \leq 0, \forall i,j \quad with \quad i \neq j \ ,$$

and

$$\sum_j (L^h)_{ij} \geq 0, \forall i,$$

with a strict inequality for at least one i.

Typical examples of iteration methods are Gauss-Seidel and Jacobi with $M^h = \tilde{D} + \tilde{L}$ and $M^h = \tilde{D}$, respectively, where $\tilde{D}$ is the diagonal matrix of L^h and $\tilde{L}$ is the lower-triangular matrix of L^h.

Obviously, the efficiency of the iterative method as a solution technique for the system of equations (3.27) depends on the rate of convergence. The closer the spectral radius is to unity, the larger the number of iterations, needed to obtain an approximation to $\mathbf{u}^h$ with an error smaller than some pre-set value. To analyze the efficiency of the process, the eigenvalues of S need to be determined. In general this may be a cumbersome task. However, for operators resulting from the discretization of partial differential equations often there is a high regularity in S, i.e., each row has the same entries, except for some rows representing the equation at points near the boundary. A good approximation of the behavior of the process can now be obtained by analyzing the matrix S excluding the boundary terms. Effectively this means that the system is analyzed as if it is given with periodic boundary conditions. In that case the eigenvalues of S can be computed easily. The resulting type of analysis is referred to as "local-mode analysis".

For simplicity, assume a two-dimensional infinite square grid with grid spacing h. Functions on this grid can be expressed as Fourier series. Eigenfunctions of S can be expressed in the form $e^{I\,\mathbf{k}\cdot\boldsymbol{\theta}}$ where $\mathbf{k} = \{k_1, k_2\}^T$ with $k_i \in \{0, \pm 1, \pm 2, ..., \pm\infty\}$ and $\boldsymbol{\theta}$= $\{\theta_1, \theta_2\}^T$ with $-\pi < \theta_i < \pi$. By definition, the eigenfunctions satisfy:

$$\sum_{\mathbf{l}} (S)_{\mathbf{kl}}\, e^{I\,\mathbf{l}\cdot\boldsymbol{\theta}} = \lambda(\boldsymbol{\theta}) e^{I\,\mathbf{k}\cdot\boldsymbol{\theta}} \ ,$$

$$\sum_{\mathbf{m}} (S)_{\mathbf{kk+m}}\, e^{I\,\mathbf{m}\cdot\boldsymbol{\theta}} = \lambda(\boldsymbol{\theta}) \ ,$$

$$\text{if } (S)_{\mathbf{kk+m}} = [S]_{\mathbf{m}} \text{ then } \lambda(\boldsymbol{\theta}) = \sum_{\mathbf{m}} [S]_{\mathbf{m}} e^{I\,\mathbf{m}\cdot\boldsymbol{\theta}} \ . \tag{3.32}$$

In equation (3.32) $[S]$ denotes the stencil representing S. A stencil is a geometric representation of an equation at a grid point by the weight with which the variables located at grid points appear in an equation. As an example, the stencil representation for the second-order discretized Poisson equation is:

$$[L^h]_{\mathbf{m}} = \frac{1}{h^2} \begin{bmatrix} 0 & 1 & 0 \\ 1 & -4 & 1 \\ 0 & 1 & 0 \end{bmatrix}, \quad (\mathbf{m})_i = (0, \pm 1) \tag{3.33}$$

The use of periodic boundary conditions result in a finite-dimensional matrix S. The frequencies are then reduced to the discrete points:

$$\boldsymbol{\theta} = \left\{ \frac{\pi n_1}{N}, \frac{\pi n_2}{N} \right\}^T , \quad -N < n_i < N \ , \tag{3.34}$$

where $(2N+1)^2$ is the number of grid points. Equation (3.32) can be rewritten in the form:

$$\lambda(\boldsymbol{\theta}) = \frac{\sum_{\mathbf{k}} [N]_{\mathbf{k}} e^{I\,\mathbf{k}\cdot\boldsymbol{\theta}}}{\sum_{\mathbf{k}} [M]_{\mathbf{k}} e^{I\,\mathbf{k}\cdot\boldsymbol{\theta}}}, \tag{3.35}$$

the amplification factor of an error component $e^{I\,\mathbf{k}\cdot\boldsymbol{\theta}}$ due to one iteration is defined as:

$$\mu = |\lambda(\boldsymbol{\theta})| \ . \tag{3.36}$$

The continuous spectrum of eigenvalues found by local-mode analysis can now be studied to illustrate the details of the convergence behavior of the iterative process in terms of the reduction, given to each Fourier component of the error by one step of the process. This is best shown by means of an example. For Gauss-Seidel iteration applied to the 2D Poisson problem, where L^h is given by equation (3.33), one obtains

$$\mu = \left| \frac{e^{i\theta_1} + e^{i\theta_2}}{4 - e^{-i\theta_1} - e^{-i\theta_2}} \right| \ . \tag{3.37}$$

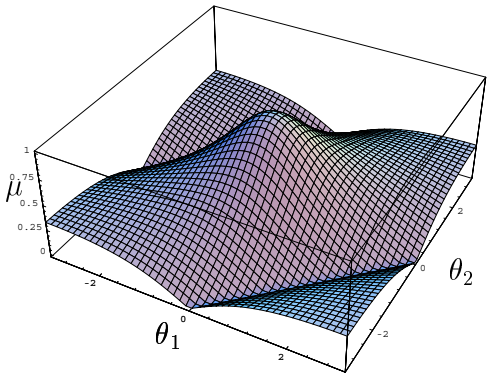

Figure 3.4: *The amplification factor for the Poisson problem with Gauss-Seidel iteration.*

Figure (3.4) shows μ as a function of (θ_1, θ_2). From this figure, it can be seen that for $(|\theta_1|, |\theta_2|) \approx (\pi, \pi), (\pi, 0), (0, \pi)$ the amplification factor $\mu \approx 0.3$ whereas for $(|\theta_1|, |\theta_2|) \approx (0, 0)$ the amplification factor $\mu \approx 1, 0$. As the set of components $(|\theta_1|, |\theta_2|)$ with $|\theta_1| \approx \pi$ or $|\theta_2| \approx \pi$ by definition represents "high-frequency" components and $(|\theta_1|, |\theta_2|) \approx (0, 0)$ "low-frequency" components, the figure shows that apparently the iterative process is very effective in reducing high-frequency components, whereas low-frequency components are hardly affected. For these components $\mu \approx 1 - O(h^2)$ if h is the mesh size of the grid. Consequently on fine grids many iterations will be needed. This explains the inefficiency of many iterative methods. It also implies that the asymptotic speed of convergence of the

process is determined by the reduction given to the low-frequency components. Moreover the situation of a poor reduction of low-frequency components aggravates going to finer and finer grids.

The idea behind multi-grid algorithms now is to utilize this specific convergence behavior to obtain a much more efficient process. As the high-frequency components converge quickly, after a few iterations the remaining error will be dominated by low-frequency components, and thus it will be smooth. Consequently one does not need a fine grid to describe it accurately. The idea is now to introduce a coarser grid and rather than continuing the iterative process solving $\mathbf{u}^h$ on the fine grid, to compute an approximation to $\mathbf{e}^h$ on the coarser grid. Generally this must also be done iteratively. However, as will be shown later, the equation from which $\mathbf{e}^h$ must be solved is the same as the original equation. Hence, the same iterative procedure can be used, but, because now it is used on a coarser grid, by definition solving an approximation $\mathbf{e}^H$ can be done more efficiently. Firstly, because the number of nodes is smaller and thus each iteration requires less work. Secondly, because the convergence rate on this grid will be higher. Once an approximation for the error on this grid is obtained, it can be used to correct the original fine grid approximation. Let H (typically $H = 2h$) denote the mesh size on the coarse grid. The entire process is depicted in the following template:

$$\begin{array}{ll} \nu_1 \text{ relaxation sweeps} & L^h\tilde{\mathbf{u}}^h = \mathbf{f}^h \\ \text{Restriction of the residual} & \mathbf{r}^H = I_h^H \mathbf{r}^h = I_h^H(\mathbf{f}^h - L^h\tilde{\mathbf{u}}^h) \\ \text{Solving coarse grid equation} & L^H\mathbf{e}^H = \hat{\mathbf{f}}^H = \mathbf{r}^H \\ \text{Prolongation} & \bar{\mathbf{u}}^h = \tilde{\mathbf{u}}^h + I_H^h\mathbf{e}^H \\ \nu_2 \text{ relaxation sweeps} & L^h\bar{\mathbf{u}}^h = \mathbf{f}^h \end{array} \tag{3.38}$$

For the case of a non-linear problem the so-called Full Approximation Scheme (FAS) can be used:

$$\begin{array}{ll} \nu_1 \text{ relaxation sweeps} & L^h(\tilde{\mathbf{u}}^h) = \mathbf{f}^h \\ \text{Restriction of the residual} & \mathbf{r}^H = I_h^H \mathbf{r}^h = I_h^H(\mathbf{f}^h - L^h(\tilde{\mathbf{u}}^h)) \\ \text{Solving coarse grid equation} & L^H(\hat{\mathbf{u}}^H) = \hat{\mathbf{f}}^H = L^H(\hat{I}_h^H\tilde{\mathbf{u}}^h) + \mathbf{r}^H \\ \text{Prolongation} & \bar{\mathbf{u}}^h = \tilde{\mathbf{u}}^h + I_H^h(\hat{\mathbf{u}}^H - I_h^H\tilde{\mathbf{u}}^h)) \\ \nu_2 \text{ relaxation sweeps} & L^h(\bar{\mathbf{u}}^h) = \mathbf{f}^h \end{array} \tag{3.39}$$

The FAS reduces to the linear MG scheme if L^h is a linear operator. In this work FAS is used. To communicate between the different grids, use is made of the restriction operator I_h^H and of the prolongation operator I_H^h.

The steps in (3.39) yield an efficient solver only if the coarse grid problem can efficiently be solved as well. However, if the fine grid has many points, also a coarse grid with $H = 2h$ will still be dense and the iterative process applied on the coarse grid will converge slowly. The natural step is then to use recurrence, i.e., to apply the algorithm recursively. Thus, to solve the coarse grid problem an even coarser grid is introduced. This can be repeated until a coarse grid is reached at which the problem can be solved with only a small amount of work. Based on the sequence in which coarser grids are used one can now distinguish different types of coarse grid correction or multi-grid cycles (see figure (3.5)).

As can be verified easily, the total work involved in a cycle going from a fine to a coarse grid and back again will be $O(M)$ if M is the number of unknowns. The gain in efficiency

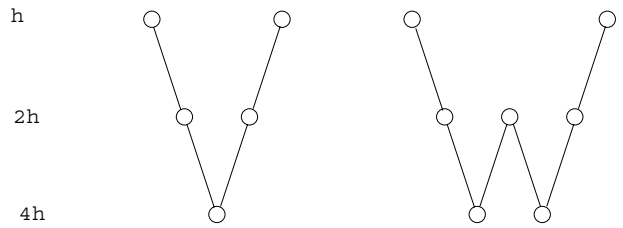

Figure 3.5: *V- and W-cycle, circle represents relaxation and lines represent inter-grid operators.*

resulting from the use of coarser grids compared with relaxation on a single grid becomes clear from the analysis of the performance of the cycle in terms of error reduction. To estimate this performance the so-called "smoothing rate" is defined as:

$$\mu = \max \{\mu(\boldsymbol{\theta}) : \quad \boldsymbol{\theta} \in [-\pi, -\pi/2) \times (\pi/2, \pi]\} \ . \tag{3.40}$$

It tells something about how effective the relaxation method is in smoothing the high frequency error components which are not visible on the coarse grid. For the 2D Poisson problem the smoothing rate has the value 0.5. The error reduction per MG cycle is estimated by: $\mu^{\nu_1+\nu_2}$ with ν_1 and ν_2 the number of relaxation sweeps before and after the coarse grid computation with a value of $\mu = 0.5$ for $\nu_1 = 2$ and $\nu_1 = 1$ an error reduction of a factor 8 is attained per cycle *independent of the mesh size*. As the total work of the cycle is only a little larger than the work of the $\nu_1 + \nu_2$ relaxations actually performed on the finest grid, the gain in efficiency is large. Assuming that the problem is solved when the numerical error is smaller than the discretization error that is made anyway, the total work needed to solve the problem using cycles is $O(M \log(M))$. The $\log(M)$ can be removed if a good first approximation is used. This is achieved through the Full Multi-Grid (FMG) process. In addition to using the coarser grids for the acceleration of convergence of the solution on the finer grid, the coarser grids are used for the generation of an accurate first approximation. If FMG is used, eventually only $O(M)$ operations are used to solve the problem to an error comparable to the discretization error. In FMG the starting point is the coarsest grid (see figure (3.6)). To go for the first time from a coarse grid to a finer grid a prolongation operator of the order of the truncation error of the differential operator is needed. This is indicated in figure (3.6) by double lines.

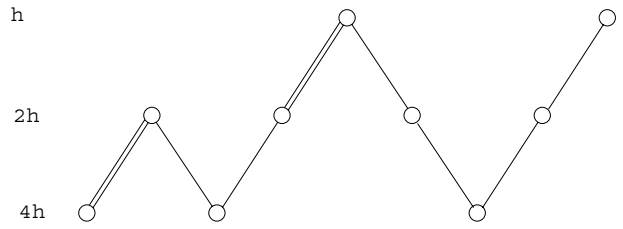

Figure 3.6: *Full Multi Grid, circle represents relaxation and lines represent inter-grid operators.*

A FMG process is often needed in non-linear problems to obtain an initial estimate on the fine grid that is close to the solution on that fine grid. Otherwise convergence problems

may occur in the relaxation step.

Finally, the convergence estimate $\mu^{\nu_1+\nu_2}$ is only accurate for small $\nu_1 + \nu_2$, because it neglects the effect of the inter-grid transfers. A more accurate estimate can be obtained from a "two-level analysis" which also takes into account the effects of the restriction, prolongation and coarse grid operator. Regarding this coarse-grid operator there are several choices. The most elegant is probably the use of Galarkin coarsening $L^H = I_h^H L^h I_H^h$. The more easy way followed in this thesis is to take the same operator as used for the fine grid but with $h \to H$. The first method has the advantage of representing fast varying coefficients on a coarse grid. In the second method it must be ensured that there are enough points on the coarsest grid to represent the original problem.

This completes a summary of MG techniques. In the following section details of the implementation for the present problem are discussed, e.g. relaxation, restriction and prolongation.

3.2.2 Relaxation

A prerequisite for a MG solver is a relaxation scheme that efficiently reduces high-frequency error components. For a discrete system of equations resulting from the discretization of a single equation (elliptic PDE) finding, such a process is not difficult, as L^h often is a K-matrix. However, if L^h is the result of the discretization of a system of partial differential equations this may not be the case. In particular, the matrix L^h resulting from (3.8),(3.9) and (3.10) is not a K-matrix, due to the zero diagonal elements of equation (3.10). A suitable relaxation can now be derived as follows. Post-multiply L^h with B^h

$$L^h B^h \mathbf{v}^h = \mathbf{f}^h, \quad \mathbf{u}^h = B^h \mathbf{v}^h \ , \tag{3.41}$$

in such a way that the splitting

$$L^h B^h = M^h - N^h \tag{3.42}$$

is convergent. The prescript to compute $\mathbf{u}_{m+1}^h$ given a $\mathbf{u}_m^h$ now becomes:

$$\mathbf{u}_{m+1}^h = \mathbf{u}_m^h + B^h (M^h)^{-1} \mathbf{r}_m^h, \quad \mathbf{r}_m^h = \mathbf{f}^h - L^h \mathbf{u}_m^h \ . \tag{3.43}$$

This is a so-called distributive method because the B^h in (3.43) distributes the result $(M^h)^{-1}\mathbf{r}_m^h$ over part of the vector $\mathbf{u}_m^h$. The choice of B^h determines if it is a coupled method or an un-coupled method. Examples of un-coupled methods are Distributed Gauss Seidel (DGS) [4], SIMPLE [53] and distributed ILU [98]. As is shown in [98] they can all be written in the form (3.43). An example of a coupled method is Symmetric Coupled Gauss Seidel (SCGS) [87]. In [99], it has been shown that also SCGS can be put in the form (3.43). In this thesis a line SCGS method will be used. It is a robust smoother with good smoothing properties. In the next section SCGS will be explained. Subsequently by means of a smoothing analysis it will be shown that for small ϵ the line version of SCGS is needed.

SCGS

For simplicity the method will not be explained in the general notation of the equations (3.41), (3.42) and (3.43) but in a way that directly shows how to implement it in a computer code. First it is explained how the method works for one grid cell (see [87]). In figure (3.7) a grid cell with a staggered-grid arrangement is shown.

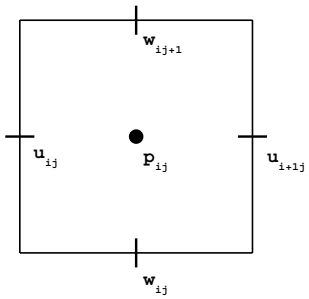

Figure 3.7: *Variable arrangement for SCGS.*

SCGS now involves scanning the grid cells in some prescribed order at each cell simultaneously solving all five unknowns of the cell from the associated five discretized equations. Thus the relaxation step for each cell involves:

$$\bar{\mathbf{u}}^h = \tilde{\mathbf{u}}^h + (\tilde{L}^h)^{-1}\mathbf{r}^h \ , \tag{3.44}$$

where $\mathbf{u}^h = \{u^h_{ij}, u^h_{i+1j}, w^h_{ij}, w^h_{ij+1}, p^h_{ij}\}^T$, $\tilde{\mathbf{u}}^h$ old approximation to $\mathbf{u}^h$, $\bar{\mathbf{u}}^h$ new approximation to $\mathbf{u}^h$ and $\tilde{L}^h$ is the 5×5 matrix resulting from equations (3.8), (3.9) and (3.10). The vector $\mathbf{r}^h$ defines the residual for $\tilde{\mathbf{u}}^h$ calculated with (3.8), (3.9) and (3.10). The matrix $\tilde{L}^h$ is given by:

$$\tilde{L}^h = \begin{pmatrix} A^1_{ij} & A^2_{ij} & A^{11}_{ij} & A^{10}_{ij} & A^{22}_{ij} \\ A^7_{i+1j} & A^1_{i+1j} & A^{13}_{i+1j} & A^{12}_{i+1j} & A^{23}_{i+1j} \\ B^{10}_{ij} & B^{11}_{ij} & B^1_{ij} & B^2_{ij} & B^{22}_{ij} \\ B^{12}_{ij+1} & B^{13}_{ij+1} & B^7_{ij+1} & B^1_{ij+1} & B^{23}_{ij+1} \\ C^1_{ij} & C^2_{ij} & C^7_{ij} & C^8_{ij} & 0 \end{pmatrix} \ . \tag{3.45}$$

Fortunate it is not needed to invert this full matrix at each step. It has been shown [99] that the reduced matrix

$$\tilde{L}^h = \begin{pmatrix} A^1_{ij} & 0 & 0 & 0 & A^{22}_{ij} \\ 0 & A^1_{i+1j} & 0 & 0 & A^{23}_{i+1j} \\ 0 & 0 & B^1_{ij} & 0 & B^{22}_{ij} \\ 0 & 0 & 0 & B^1_{ij+1} & B^{23}_{ij+1} \\ C^1_{ij} & C^2_{ij} & C^7_{ij} & C^8_{ij} & 0 \end{pmatrix} \tag{3.46}$$

already gives as good multi-grid convergence rates as the full matrix representation of $\tilde{L}^h$. This matrix can be easily inverted. For problems with $\epsilon = O(1)$ this SCGS works well. However, with decreasing ϵ its efficiency to reduce high-frequency components with respect to the z-direction diminishes. This can be overcome by using the relaxation in its line relaxation variant, see [79]. Instead of solving the system of equations for one grid

cell all equations of a column of grid cells in the z-direction are solved simultaneously. See figure (3.8) for the arrangement of the variables. As the resulting system is a band matrix, this can still be solved quickly.

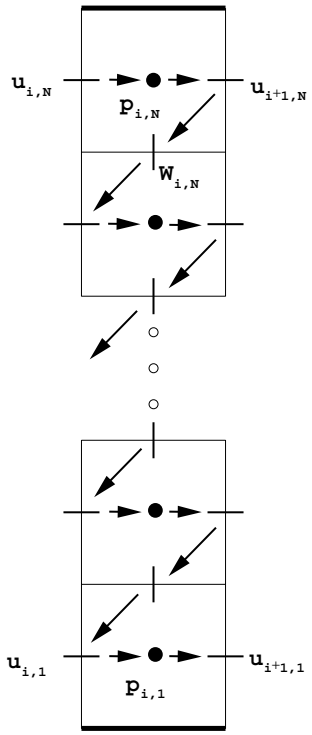

Figure 3.8: *The arrows indicate the arrangement of the variables in the equation .*

In the paragraph (*Local mode analysis*) it will be shown that this line-SCGS is a good smoother for small ϵ. The vector of unknowns is $\mathbf{u}^h = \{u^h_{iN}, p^h_{iN}, u^h_{i+1N}, w^h_{iN}, .., u^h_{ij}, p^h_{ij}, u^h_{i+1j}, w^h_{ij}, .., u^h_{i1}, p^h_{i1}, u^h_{i+11}\}^T$. The matrix $\tilde{L}^h$ is a diagonal matrix. It has been solved exactly with a band diagonal matrix solver.

Local mode analysis

As mentioned above, to obtain an efficient MG solver for small ϵ, SCGS relaxations must be used in a line manner. This is illustrated below by means of a Fourier analysis of the x-momentum equation. This analysis will also give an indication for the conditions for which smoothing problems will be encountered. The study of a single equation is justified because the problems with small ϵ are independent of the problems, related to the coupling, when solving a system of equations.

In Cartesian coordinates the x-momentum equation is:

$$\epsilon \frac{\partial p}{\partial x} - 2\epsilon^2 \frac{\partial}{\partial x}\left[\eta \frac{\partial u}{\partial x}\right] - \frac{\partial}{\partial z}\left[\eta(\epsilon^2 \frac{\partial w}{\partial x} + \frac{\partial u}{\partial z})\right] = 0 \ . \tag{3.47}$$

To simplify the procedure, the variables p, w and η are assumed to be constant. Equation (3.47) can be transformed to a curvilinear coordinate system. Taking $a^1_{(2)} = 0$ (see figure

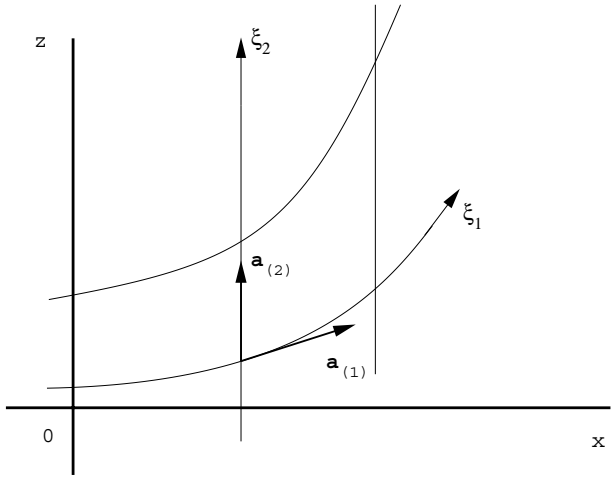

Figure 3.9: *The physical domain with covariant base vectors.*

(3.9)), as will be the case in actual computations in the next chapter, it follows that:

$$\begin{aligned}
&-2\epsilon^2\frac{\partial}{\partial\xi^1}\left[\frac{a^2_{(2)}}{a^1_{(1)}}\frac{\partial u}{\partial\xi^1}-\frac{a^2_{(1)}}{a^1_{(1)}}\frac{\partial u}{\partial\xi^2}\right]+\\
&-2\epsilon^2\frac{\partial}{\partial\xi^2}\left[-\frac{a^2_{(1)}}{a^1_{(1)}}\frac{\partial u}{\partial\xi^1}+\frac{(a^2_{(1)})^2}{a^1_{(1)}a^2_{(2)}}\frac{\partial u}{\partial\xi^2}\right]+\\
&-\frac{\partial}{\partial\xi^2}\left[\frac{a^1_{(1)}}{a^2_{(2)}}\frac{\partial u}{\partial\xi^2}\right]=0\ . \qquad (3.48)
\end{aligned}$$

Defining:

$$g_1=g_1(\xi^1)=\tfrac{a^2_{(2)}}{a^1_{(1)}},\quad g_2=g_2(\xi^1,\xi^2)=-\tfrac{a^2_{(1)}}{a^1_{(1)}},\quad g_3=g_3(\xi^1,\xi^2)=\tfrac{(a^2_{(1)})^2}{a^1_{(1)}a^2_{(2)}}\ , \qquad (3.49)$$

where $g_1\neq 0\,\forall\,\xi^1\in G$, equation (3.48) can be transformed into

$$\begin{aligned}
&-2\epsilon^2 g_1\frac{\partial^2 u}{\partial(\xi^1)^2}-\left(2\epsilon^2 g_3+\frac{1}{g_1}\right)\frac{\partial^2 u}{\partial(\xi^2)^2}-4\epsilon^2 g_2\frac{\partial u}{\partial\xi^1\partial\xi^2}+\\
&-2\epsilon^2\left(\frac{\partial g_1}{\partial\xi^1}+\frac{\partial g_2}{\partial\xi^2}\right)\frac{\partial u}{\partial\xi^1}-2\epsilon^2\left(\frac{\partial g_2}{\partial\xi^1}+\frac{\partial g_3}{\partial\xi^2}\right)\frac{\partial u}{\partial\xi^2}=0\ . \qquad (3.50)
\end{aligned}$$

Only the anisotropic diffusion part of equation (3.50) will now be analyzed. This means that it is assumed that changes of g_1, g_2 and g_3 in a cell are minimal. This leads to the following model problem: Solve u from

$$-\frac{\partial^2 u}{\partial(\xi^1)^2}-g_4\frac{\partial^2 u}{\partial(\xi^2)^2}-g_5\frac{\partial^2 u}{\partial\xi^1\partial\xi^2}=0\ , \qquad (3.51)$$

where

$$g_4=\left(\tfrac{a^2_{(1)}}{a^2_{(2)}}\right)^2+\tfrac{1}{2\epsilon^2}\left(\tfrac{a^1_{(1)}}{a^2_{(2)}}\right)^2,\quad g_5=-2\tfrac{a^2_{(1)}}{a^2_{(2)}}\ . \qquad (3.52)$$

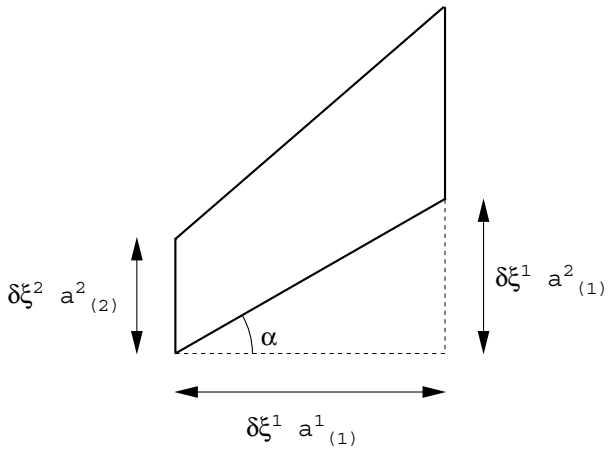

Figure 3.10: *Cell geometry.*

The coefficients g_4 and g_5 can be linked to the geometry of a cell in the physical domain, see figure (3.10). Two parameters can be identified: α_l as a measure for the angle α, and ϵ_l as a measure for the ratio of the lengths of the sides of the cell. It is assumed that the step size in the computational domain in both directions is equal ($\delta\xi^1 = \delta\xi, \delta\xi^2 = \delta\xi$) and that there is a uniform grid spacing in the x- direction, thus $a^1_{(1)} = c$. This gives:

$$\alpha_l = \tan(\alpha) = \frac{a^2_{(1)}}{c}, \quad \epsilon_l = \frac{a^2_{(2)}}{\sqrt{c^2 + (a^2_{(1)})^2}}. \tag{3.53}$$

The coefficients g_4 and g_5 are then:

$$g_4 = \frac{2\epsilon^2\alpha_l^2 + 1}{2\epsilon^2\epsilon_l^2(1+\alpha_l^2)}\ , \quad g_5 = \frac{-2\alpha_l}{\epsilon_l\sqrt{1+\alpha_l^2}}\ . \tag{3.54}$$

where $g_4 > 0$ and $g_5 \in I\!R$.

A finite-difference discretization of equation (3.51), which resembles the stencil resulting from the FV discretization of the Stokes equations, leads to the following stencil

$$[L^h] = \frac{1}{(\delta\xi)^2}[-1\ 2\ -1] + \frac{g_4}{(\delta\xi)^2}\begin{bmatrix} -1 \\ 2 \\ -1 \end{bmatrix} + \frac{g_5}{4(\delta\xi)^2}\begin{bmatrix} 1 & 0 & -1 \\ 0 & 0 & 0 \\ -1 & 0 & 1 \end{bmatrix}\ . \tag{3.55}$$

The same result can be found with an FV discretization of equation (3.48) and taking the values of the geometrical coefficients at the cell center. A Gauss-Seidel splitting results in the following stencils for M^h and N^h.

$$\begin{aligned} \left[M^h\right] &= \begin{bmatrix} \frac{g_5}{4}l_s & -g_4 l_s & 0 \\ -1 & 2+2g_4 & 0 \\ -\frac{g_5}{4} & -g_4 & (1-l_s)\frac{g_5}{4} \end{bmatrix}\ , \\ \left[N^h\right] &= \begin{bmatrix} -\frac{g_5}{4}(1-l_s) & g_4(1-l_s) & \frac{g_5}{4} \\ 0 & 0 & 1 \\ 0 & 0 & -l_s\frac{g_5}{4} \end{bmatrix},\ l_s = 0, 1\ . \end{aligned} \tag{3.56}$$

For $l_s = 0$ the above splitting corresponds to Gauss-Seidel pointwise relaxation. For $l_s = 1$ it corresponds to a vertical line Gauss-Seidel relaxation. Because of the term $g_5/4$ in equation (3.55), L^h is not a K-matrix. This means that it is not certain whether there is a splitting of L^h which leads to a convergent iterative method. Nevertheless, it can be a good smoother.

To study the quality of the smoother, the amplification factor has been calculated, according to equation (3.36): For the Gauss-Seidel pointwise case this gives

$$\mu = \left| \frac{\frac{g_5}{4}(l_s - 1)e^{I(\theta_2-\theta_1)} + g_4(1-l_s)e^{I\theta_2} + \frac{g_5}{4}e^{I(\theta_1+\theta_2)} + e^{I\theta_1} - \frac{g_5}{4}l_s e^{I(\theta_1-\theta_2)}}{2 + 2g_4 + \frac{g_5}{4}e^{I(\theta_2-\theta_1)} - g_4 l_s e^{I\theta_2} - e^{-I\theta_1} - \frac{g_5}{4}e^{-I(\theta_1+\theta_2)} - g_4 e^{-I\theta_2} + \frac{g_5}{4}(1-l_s)e^{I(\theta_1-\theta_2)}} \right| . \tag{3.57}$$

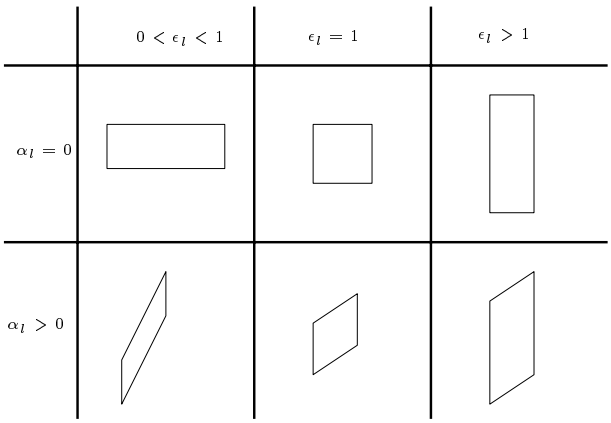

Figure 3.11: *Types of cells. If* $\alpha_l = 1$ *than* $\alpha = 45^o$.

To interpret this result, six different types of cells, which can occur on a grid, have been depicted in figure (3.11). For realistic computations the cells with $0 < \epsilon_l \leq 1$ and $\alpha_l \geq 0$ are interesting. In table (3.1) the dependence of the smoothing rate of point GS and line GS is shown for various cases.

ϵ	$\mu(l_s = 0)$	$\mu(l_s = 1)$
1	0.57	0.50
0.1	0.96	0.45
0.01	1.00	0.45
0.001	1.00	0.45

α_l	$\mu(l_s = 0)$	$\mu(l_s = 1)$
1.0	0.70	0.54
2.0	0.71	0.55
3.0	0.72	0.56
4.0	0.72	0.57

ϵ_l	$\mu(l_s = 0)$	$\mu(l_s = 1)$
0.01	1.00	0.60
0.4	0.84	0.59
0.6	0.73	0.58
0.8	0.67	0.56

Table 3.1: *Smoothing factor for point and z-line relaxation on equation (3.51). Left :* $\alpha_l = 0$, $\epsilon_l = 1$*; Center:* $\epsilon = 1.0$, $\epsilon_l = 1.0$*; Right :* $\epsilon = 1.0$, $\alpha_l = 2.0$.

The following trends can be observed. Firstly, for a given α_l and ϵ_l, with decreasing ϵ the smoothing rate of point GS deteriorates, approaching unity for very small ϵ. This value indicates that some oscillatory components are not reduced at all. These are the components that are smooth in the ξ^2-direction and oscillatory in the ξ^1-direction. However,

the ξ^2-line GS relaxation (relaxing all equations of a line at constant ξ^1 simultaneously) remains an excellent smoother, tending to $\mu = 0.45$ for small ϵ.

Secondly, for a given ϵ and ϵ_l it can be seen that the smoothing rates of both the point GS and the ξ^2-line GS relaxation are not very sensitive to the value of α_l. However, also in this case clearly the ξ^2-line GS relaxation is a more efficient smoother. Finally, for a given ϵ and α_l it can be seen that the smoothing factor of point GS deteriorates with decreasing ϵ_l, whereas, when its ξ^2-line variant is used, acceptable smoothing is obtained even for small ϵ_l.

In conclusion, from the study of the model problem (3.51), which is representive for the x-momentum equation in the full Stokes system, it is concluded that in order to obtain good smoothing for small ϵ for a wide range of practical cell configurations a ξ^2-line relaxation is needed. For the full Stokes equations this then leads to the proposed ξ^2-line SCGS process.

3.2.3 Prolongation and Restriction

After transformation of the Stokes equations to a boundary-fitted domain, the prolongation and restriction operators, given in [86] for a staggered Cartesian grid can be used. For the restriction of the dependent variables a simple operator like:

$$\begin{array}{lcl} u^H_{ij} & = & \frac{1}{2}(u^h_{2i-1,2j} + u^h_{2i-1,2j-1}) \ , \\ w^H_{ij} & = & \frac{1}{2}(w^h_{2i,2j-1} + w^h_{2i-1,2j-1}) \ , \\ p^H_{ij} & = & \frac{1}{4}(p^h_{2i-1,2j} + p^h_{2i-1,2j-1} + p^h_{2i,2j} + p^h_{2i,2j-1}) \end{array} \tag{3.58}$$

is sufficient. The restriction of residuals is done with a weighting operator:

$$\begin{array}{lcl} ru^H_{i,j} & = & 4[\frac{1}{8}(ru^h_{2i-2,2j} + ru^h_{2i-2,2j-1} + ru^h_{2i,2j} + ru^h_{2i,2j-1}) + \frac{1}{4}(ru^h_{2i-1,2j} + ru^h_{2i-1,2j-1})] \ , \\ rw^H_{i,j} & = & 4[\frac{1}{8}(rw^h_{2i,2j-2} + rw^h_{2i-1,2j-2} + rw^h_{2i,2j} + rw^h_{2i-1,2j}) + \frac{1}{4}(rw^h_{2i,2j-1} + rw^h_{2i-1,2j-1})] \ , \\ rp^H_{i,j} & = & 4[\frac{1}{4}(rp^h_{2i-1,2j} + rp^h_{2i-1,2j-1} + rp^h_{2i,2j} + rp^h_{2i,2j-1})] \ . \end{array} \tag{3.59}$$

The factor 4 in the right-hand sides in the above equations results from the requirement that the system of equations on the fine grid is consistent with the system of equations on the coarse grid. This is the so-called scaling rule ([95], pp. 71):

$$\sum_{\mathbf{j}} [I^H_h]_{\mathbf{j}} = (\frac{H}{h})^d \ , \tag{3.60}$$

where $[I^H_h]_{\mathbf{j}}$ represents the stencil for the restriction operator and $d = 2$ the dimension. Prolongation is done with a bilinear operator. For u^h the prolongation operator is:

$$\begin{array}{lcl} u^h_{2i-1,2j+1} & = & \frac{1}{4}(u^H_{i,j} + 3u^H_{i,j+1}) \ , \\ u^h_{2i,2j+1} & = & \frac{1}{8}(u^H_{i,j} + 3u^H_{i,j+1} + u^H_{i+1,j} + 3u^H_{i+1,j+1}) \ , \\ u^h_{2i-1,2j} & = & \frac{1}{4}(3u^H_{i,j} + u^H_{i,j+1}) \ , \\ u^h_{2i,2j+1} & = & \frac{1}{8}(3u^H_{i,j} + u^H_{i,j+1} + 3u^H_{i+1,j} + u^H_{i+1,j+1}) \ . \end{array} \tag{3.61}$$

For w^h the prolongation operator is:

$$\begin{array}{lcl} w^h_{2i+1,2j-1} &=& \frac{1}{4}(w^H_{i,j} + 3w^H_{i+1,j}) \ , \\ w^h_{2i+1,2j} &=& \frac{1}{8}(w^H_{i,j} + w^H_{i,j+1} + 3w^H_{i+1,j} + 3w^H_{i+1,j+1}) \ , \\ w^h_{2i,2j-1} &=& \frac{1}{4}(3w^H_{i,j} + w^H_{i+1,j}) \ , \\ w^h_{2i,2j} &=& \frac{1}{8}(3w^H_{i,j} + 3w^H_{i,j+1} + w^H_{i+1,j} + w^H_{i+1,j+1}) \ . \end{array} \tag{3.62}$$

For p^h the prolongation operator is:

$$\begin{array}{lcl} p^h_{2i,2j} &=& \frac{1}{16}(9p^H_{i,j} + 3p^H_{i+1,j} + 3p^H_{i,j+1} + p^H_{i+1,j+1}) \ , \\ p^h_{2i+1,2j} &=& \frac{1}{16}(3p^H_{i,j} + 9p^H_{i+1,j} + p^H_{i,j+1} + 3p^H_{i+1,j+1}) \ , \\ p^h_{2i,2j+1} &=& \frac{1}{16}(3p^H_{i,j} + p^H_{i+1,j} + 9p^H_{i,j+1} + 3p^H_{i+1,j+1}) \ , \\ p^h_{2i+1,2j+1} &=& \frac{1}{16}(p^H_{i,j} + 3p^H_{i+1,j} + 3p^H_{i,j+1} + 9p^H_{i+1,j+1}) \ . \end{array} \tag{3.63}$$

At boundaries the prolongation operator is adapted to the Dirichlet boundary conditions.

3.3 Results

To conclude this chapter, the performance of the above numerical solution procedure for the Stokes equations will be demonstrated. Firstly in section (*3.3.1*) an example is given which *illustrates* the convergence of the discrete solution to a pre-set continuous solution of the Stokes equations. Next the performance of the multi-grid algorithm is demonstrated in section (*3.3.2*).

3.3.1 Model problem

An artificial model problem is created to illustrate that for this specific model problem the discretization error is of second order in $\delta\xi$. Because of the linearity of the Stokes equations in this particular problem, the truncation error is of the same order in $\delta\xi$ as the discretization error.

On a domain

$$\begin{array}{lcl} x &=& 2\xi^1 - 1 \ , \\ z &=& \xi^2 h(\xi^1) \ , \\ h(x) &=& 1 - \frac{a_3\sqrt{2e}}{a_4} x e^{-\frac{x^2}{a_4^2}} \ , \end{array} \tag{3.64}$$

the following velocity and pressure profiles are taken:

$$\begin{array}{lcl} u &=& 1 - \xi^2 \ , \\ w &=& \xi^1\xi^2(1-\xi^1)(1-\xi^2) \ , \\ p &=& p_w(1-\xi^1) \ , \end{array} \tag{3.65}$$

and with boundary conditions (2.3). Substitution in the Stokes equations (2.31), (2.32) and (2.33) shows that for (3.65) to be the solution the zero righthand side of the Stokes

equations, should be replaced with:

$$\begin{aligned} f^u &= -\epsilon p_w h(\xi^1) - \epsilon^2\xi^2\tfrac{d^2h}{(d\xi^1)^2} + 2\epsilon^2\xi^2(\tfrac{dh}{d\xi^1})^2(h(\xi^1))^{-1} - \epsilon^2(1-2\xi^1)(1-2\xi^2)+ \\ &\quad +\epsilon^2\xi^1(1-\xi^1)(1-4\xi^2)\tfrac{dh}{d\xi^1}(h(\xi^1))^{-1} \ , \\ f^w &= \tfrac{1}{2}\epsilon^3\xi^2(2h(\xi^1)(1-\xi^2) + \tfrac{dh}{d\xi^1}(4\xi^1-2)(2\xi^2-1) + \xi^1\tfrac{dh}{d\xi^1}(1-2\xi^2)(1-\xi^1)+ \\ &\quad -(\tfrac{dh}{d\xi^1})^2\xi^1(1-\xi^1)(2-6\xi^2)/h(\xi^1)) - \epsilon\tfrac{dh}{d\xi^1}/h(\xi^1) + \epsilon 8\xi^1(1-\xi^1)/h(\xi^1) \ , \\ f^p &= \tfrac{dh}{d\xi^1}\xi^2 + 2\xi^1(1-\xi^1)(1-2\xi^2) \ . \end{aligned} \tag{3.66}$$

Consequently, with (3.66) as a righthand side in the numerical solver, the discrete solution u^h, w^h, p^h should converge to u, w, p given by (3.65). This is illustrated below. For the case $\epsilon = 0.1$, $p_w = 100$, $u_0 = 1$, $a_3 = 0.5$ and $a_4 = 0.2$ table (3.2) shows the L_1 norm of the discretization error in u^h, w^h and p^h as a function of the mesh size of the grid. The norm is defined as:

$$\left|p - p^h\right| = \frac{1}{N^2}\sum_{i,j=1}^{N}\left|p - p^h_{ij}\right| \ . \tag{3.67}$$

The solutions were computed on uniform grids. Each row in the table represents a result obtained on a grid with a mesh spacing that is twice as small as the previous row. The table shows that with decreasing mesh spacing the value of the L_1-norm decreases, i.e., u^h, w^h, p^h indeed converge to u, w, p. Moreover, the ratio of the norms taken on two consecutive grids converges to a factor four. This illustrates that the discretization error $\left|u - u^h\right|$ etc. is of second order in this particular example.

N	$\left\|u-u^h\right\|$	$\left\|w-w^h\right\|$	$\left\|p-p^h\right\|$	$\frac{\left\|p-p^H\right\|}{\left\|p-p^h\right\|}$
16	$9.95\cdot10^{-3}$	$6.68\cdot10^{-3}$	$5.31\cdot10^{-1}$	–
32	$2.75\cdot10^{-3}$	$1.41\cdot10^{-3}$	$1.53\cdot10^{-1}$	3.5
64	$7.28\cdot10^{-4}$	$3.33\cdot10^{-4}$	$4.06\cdot10^{-2}$	3.7
128	$1.84\cdot10^{-4}$	$8.22\cdot10^{-5}$	$1.03\cdot10^{-2}$	3.9
256	$4.62\cdot10^{-5}$	$2.04\cdot10^{-5}$	$2.59\cdot10^{-3}$	4.0
512	$1.16\cdot10^{-5}$	$5.10\cdot10^{-6}$	$6.48\cdot10^{-4}$	4.0

Table 3.2: *Order of discretization.*

3.3.2 Multi-grid convergence

To illustrate the performance of the MG solution algorithm, a model problem is taken that is characteristic for the problems to be studied: the flow in a gap with a geometrical "defect" on one of the surfaces. The problem is again given by equation (3.64). In the paragraph (*Local mode analysis*) the smoothing factor μ of the relaxation was estimated as $\mu \approx 0.5$. This implies that a coarse-grid correction cycle with ν_1 pre-relaxations and ν_2 post-relaxations should give an error reduction of a factor $(0.5)^{\nu_1+\nu_2}$ per cycle, independent of the mesh size. Below it is shown to what extend grid-independent convergence of the

solution process is obtained and how the obtained error reduction compares with the theoretical estimate as a function of the problem parameters.

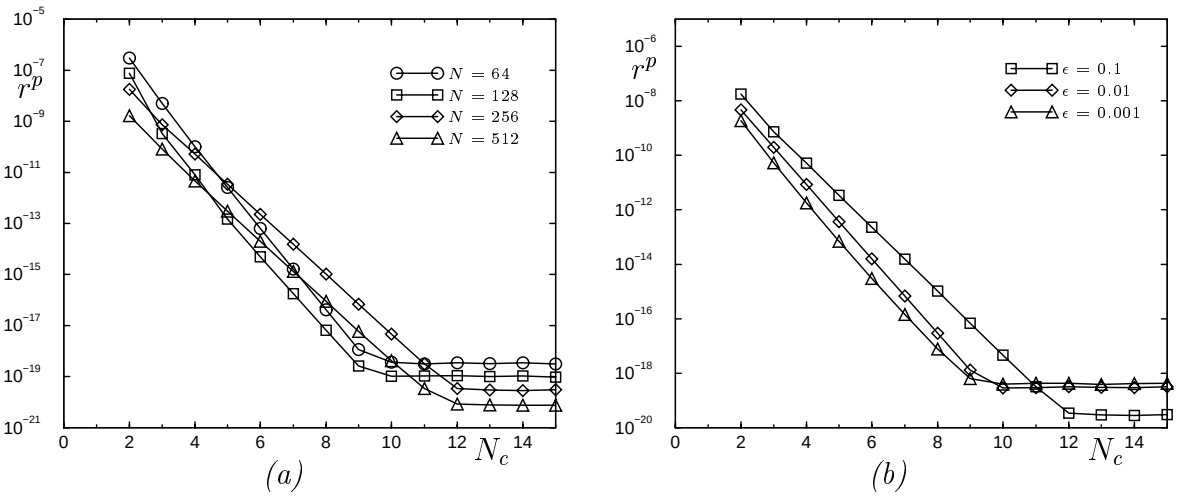

Figure 3.12: *The residual of the continuity equation as function of the number of MG cycles; (a): For different number of grid points. (b): For different ϵ and $N = 256$.*

Firstly, for a given $\epsilon = 0.1$, $a_3 = 0.5$ and $a_4 = 0.2$, figure (3.12a) shows the L_2-norm of the residual of the continuity equation (r^p) as a function of the number (N_c) of coarse-grid correction cycles and the mesh size of the grid. In the calculations W(2,2) cycles were used. The figure shows that the convergence behavior is indeed grid-independent. The error reduction per cycle is roughly a factor 16 until machine precision is reached. For the grid with $N = 256$, figure (3.12b) shows the influence of ϵ on the speed of convergence. Clearly, also for small ϵ the convergence behavior is very good, as was predicted in the paragraph (*Local mode analysis*).

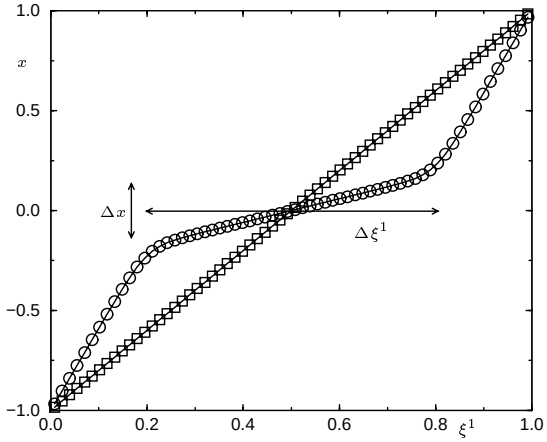

Figure 3.13: *Two kinds of x-coordinate transformation.*

In that paragraph it was explained that the smoothing behavior depends on the type of grid cells. This can be illustrated by monitoring the convergence as a function of the parameters a_3 and a_4. Increasing a_3 and decreasing a_4 is predicted to have a negative effect on the convergence performance because this change in a_3, a_4 coincides with increasing

α_l and decreasing ϵ_l in table (3.1). This can indeed be seen in figures (3.14a) and (3.15a) where $N = 256$ and $\epsilon = 0.01$.

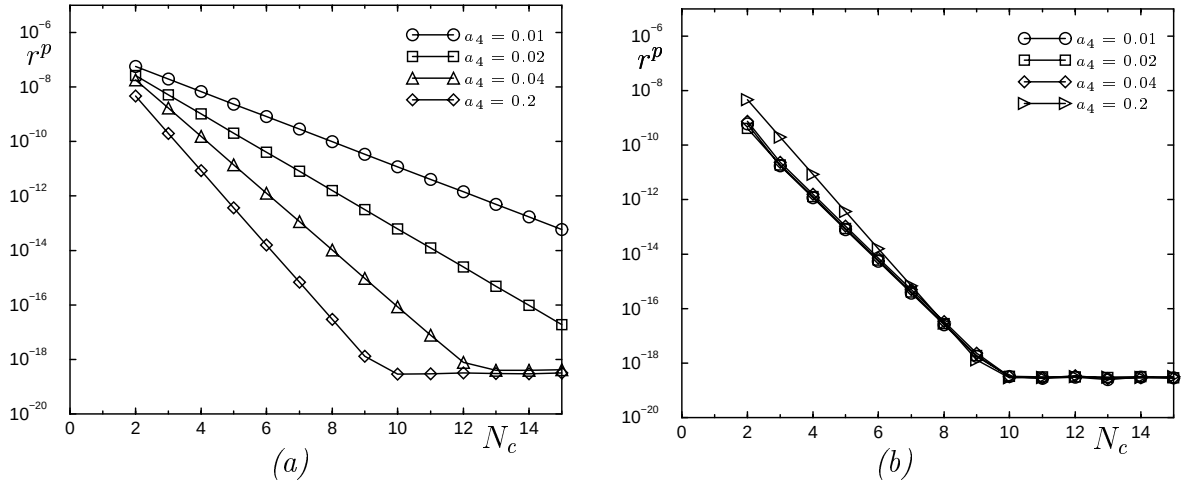

Figure 3.14: *The residual of the continuity equation as function of the number of MG cycles with $a_3 = 0.5$; (a): For different a_4 without x-refinement. (b): For different a_4 with x-refinement.*

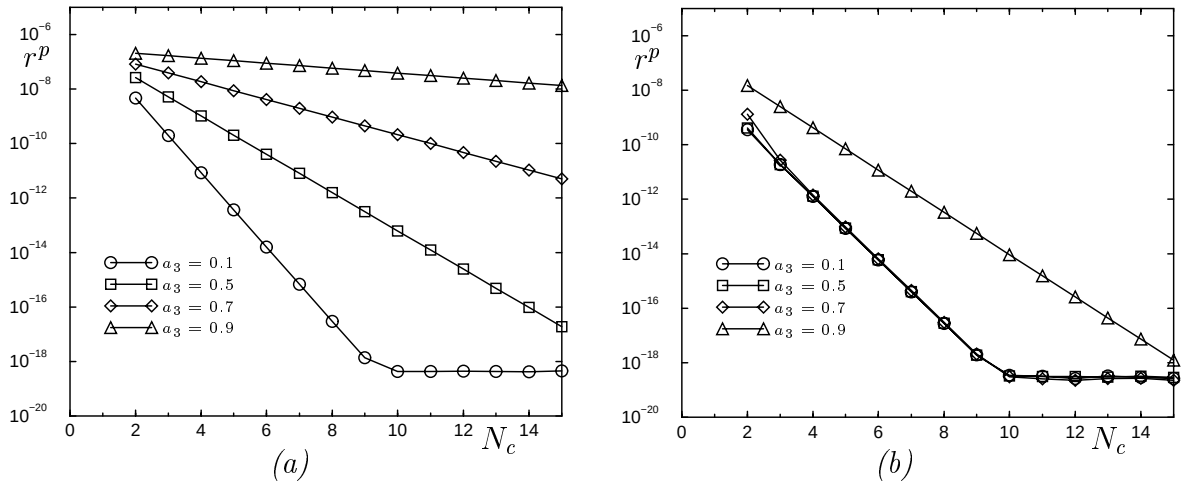

Figure 3.15: *The residual of the continuity equation as function of the number of MG cycles with $a_4 = 0.02$; (a): For different a_3 without refinement. (b): For different a_3 with refinement.*

The obvious remedy is to avoid the occurrence of cells with extreme shape, which can be achieved by refinement of the mesh along the x-axis in the vicinity of the local feature. One can, e.g. take a transformation given by:

$$\begin{aligned} l_1 &= \Delta x - 4\Delta\xi^1 + \Delta x\Delta\xi^1 \ , \\ l_2 &= -1 + \Delta\xi^1 \ , \\ l_3 &= 1 + \Delta\xi^1 \ , \\ x(\xi^1) &= \tfrac{2\Delta\xi^1(-2+\Delta x)\xi^1 - l_1}{2\Delta\xi^1 l_2} + \tfrac{\beta(\Delta x - 2\Delta\xi^1)}{\Delta\xi^1 l_2} \ln\left(\tfrac{1+e^{(l_3-2\xi^1)/(2\beta)}}{e^{l_2/(2\beta)}+e^{-\xi^1/\beta}}\right) \ . \end{aligned} \tag{3.68}$$

Unless stated otherwise, the following values have been used:

$$\begin{aligned} \Delta\xi^1 &= 0.8 \ , \\ \Delta x &= 1.5\ a_3 \ , \\ \beta &= 0.025 \ . \end{aligned} \tag{3.69}$$

In figure (3.13) this x-coordinate transformation has been depicted. The β determines the abruptness of the transition between the region with a small grid spacing and that with a large grid spacing. The Δx confines the region with a small grid spacing and $\Delta\xi^1$ determines the step length in the refined region. Figures (3.14b) and (3.15b) show the positive effect on the MG-convergence. This refinement also gives a smaller truncation error in the kink region than for the case without refinement. The error-reduction factors can be compared with factors found in the literature. A mean value can be calculated from:

$$\rho_{MG} = \left(\frac{r^p(N_c = 8)}{r^p(N_c = 2)} \right)^{\frac{1}{6}} \tag{3.70}$$

For the calculation performed with x-refinement it is found that $\rho_{MG} \approx 0.0625$. When ϵ is very small compared to a_4, meaning that the gradients in the $\xi^2 = constant$ lines in the physical domain are small, a $\rho_{MG} \approx 0.04$ can be found. In [51] also a line version of SCGS is used to numerically solve the incompressible Navier-Stokes equations. The order of sweeping was: even horizontal lines, odd horizontal lines, even vertical lines, odd vertical lines. This is a little bit different from the procedure followed in our case: from left to right vertical lines and from right to left vertical lines. Nevertheless, a comparison is made. In [51] page 83 in table (4.3) for the driven cavity with $Re = 100$ a $\rho_{MG} = 0.055$ was found.

3.4 Pressure-dependent viscosity and/or density

In section (*2.3*) the additions to the flow model necessary, to incorporate a pressure dependent viscosity and/or density have been described. This extended model is necessary for problems with pressure-dependent density (cavitation, gas lubrication) and/or piezo-viscosity. These features require modifications of the numerical solution procedure too. The required changes are briefly discussed in this paragraph. Firstly, it is noted that a pressure-dependent viscosity and/or density can change the character of the problem locally from an elliptic into a hyperbolic problem. In that case the standard second-order discretization used so far can lead to a system of equations that is not a K-matrix. As a result, for the nonlinear problem, convergence problems may occur. To avoid these problems the discretization of the momentum equations and the equation of continuity needs to be changed.

The change of character of the problem and the required modification to the discretization, related to a pressure-dependent density, can already be seen from studying a much simplified model problem. Consider the Reynolds equation with a pressure-dependent viscosity and density in a uniform film, i.e., the Two-Phase model of chapter (*2*) table (2.1), with $\rho = \eta$ and $h(x) = 1$. The equation is linearized by taking the Taylor expansion of ρ around p_0 and omitting the term $\rho(p_0)$, since it only introduces a right-hand side.

A cell-centered FV discretization on a uniform grid with grid spacing δx and a mean value for the pressure on cell faces results in:

$$p_{i-1}\left[-\frac{\epsilon}{\delta x}-3\left.\frac{d\rho}{dp}\right|_{p=p_0}\right]+p_i\left[\frac{2\epsilon}{\delta x}\right]+p_{i+1}\left[-\frac{\epsilon}{\delta x}+3\left.\frac{d\rho}{dp}\right|_{p=p_0}\right]=0\ . \tag{3.71}$$

For $\left.\frac{d\rho}{dp}\right|_{p=p_0}>0$ the third term in equation (3.71) can destroy the K-matrix conditions given in section (*3.2.1*) *Definition 1.* However, an upwind discretization gives:

$$p_{i-1}\left[-\frac{\epsilon}{\delta x}-6\left.\frac{d\rho}{dp}\right|_{p=p_0}\right]+p_i\left[\frac{2\epsilon}{\delta x}+6\left.\frac{d\rho}{dp}\right|_{p=p_0}\right]+p_{i+1}\left[-\frac{\epsilon}{\delta x}\right]=0\ , \tag{3.72}$$

in which case the resulting system of equations does satisfy the K-matrix condition. The lesson taught by this model problem implies that also in the full Stokes problem with pressure-dependent density the discretization of the continuity equation should be taken upwind. The details are given in section (*3.4.1*).

A good upwind discretization for the viscosity appears to be difficult, see equation (A.7), and was omitted. For moderate gradients in the viscosity this is acceptable.

Next the relaxation procedure requires modification. So far, the system of equations to be solved for a given line was a linear system. The pressure dependence of viscosity and density introduces non-linearity. This requires the introduction of a non-linear iterative procedure for the system. The most obvious choice is the use of one or more Newton steps. The advantage of this method is that in the vicinity of the solution it converges fast. However, when the initial guess is far away from the solution it may not converge at all. A convenient way to overcome this problem is to use the Newton process with "backtracking". This approach is also described below in section (*3.4.2.*).

3.4.1 Discretization

The discretization of equations (2.28), (2.29) and (2.30) is carried out in the same manner as in section (*3.1*). Only the discretization of the continuity equation is changed in the case of a pressure-dependent density. In order to obtain a stable discretization, the continuity equation is discretized along the characteristics which are calculated in appendix (*A*): $\frac{dz}{dx}=\frac{w}{u}$, so along the streamlines. To overcome convergence problems in the relaxation method, the use of an upwind scheme in mixed problems (hyperbolic, elliptic) was also used in, for example, the full-potential equation for transonic flow, see [95], page 223 and [94]. The FV discretization of the continuity equation is given by:

$$\begin{aligned}&\delta\xi^2\left\{\rho a^2_{(2)}u\right\}_{i-\frac{1}{2}j}-\delta\xi^2\left\{\rho a^2_{(2)}u\right\}_{i+\frac{1}{2}j}+\\ &\delta\xi^1\left\{\rho(a^1_{(1)}w-a^2_{(1)}u)\right\}_{ij+\frac{1}{2}}-\delta\xi^1\left\{\rho(a^1_{(1)}w-a^2_{(1)}u)\right\}_{ij-\frac{1}{2}}=0\ .\end{aligned} \tag{3.73}$$

The sign of the contravariant velocity components $a^2_{(2)}u$ and $a^1_{(1)}w-a^2_{(1)}u$ determines the direction of the flow perpendicular to the cell face on which it is defined. So, if $a^1_{(1)}w-a^2_{(1)}u>0$ in the point $(i,j-\frac{1}{2})$, the local flow is into the physical cell centered around

(ij). This means that one should take $\rho(p_{ij})$ for $\rho_{ij-\frac{1}{2}}$ to have an upwind discretization. The unknown density values can then be calculated according to:

$$\{\rho u\}_{i-\frac{1}{2}j} = \begin{cases} \rho_{i-1j} u_{i-\frac{1}{2}j} & \text{if } u_{i-\frac{1}{2}j} > 0 \ , \\ \rho_{ij} u_{i-\frac{1}{2}j} & \text{if } u_{i-\frac{1}{2}j} < 0 \end{cases} \tag{3.74}$$

and a similar expression for ρ in the cell face $ij-\frac{1}{2}$:

$$\left\{\rho(a^1_{(1)} w - a^2_{(1)} u)\right\}_{ij-\frac{1}{2}} = \begin{cases} \rho_{ij-1} \left\{(a^1_{(1)} w - a^2_{(1)} u)\right\}_{ij-\frac{1}{2}} & \text{if } \left\{(a^1_{(1)} w - a^2_{(1)} u)\right\}_{ij-\frac{1}{2}} > 0 \ . \\ \rho_{ij} \left\{(a^1_{(1)} w - a^2_{(1)} u)\right\}_{ij-\frac{1}{2}} & \text{if } \left\{(a^1_{(1)} w - a^2_{(1)} u)\right\}_{ij-\frac{1}{2}} < 0 \ . \end{cases} \tag{3.75}$$

The resulting scheme is a conservative discretization because the ρ on the cell faces is calculated in the same way in adjacent cells.

A disadvantage is that the scheme is no longer second-order but only first-order. Consequently it is less accurate. In particular, the results should be interpreted carefully due to the possible effects of artificial "viscosity". However, such effects can be identified when comparing solutions obtained on different grids. Alternatively "defect-correction" can be used to attain second-order accuracy [95]. This approach is not used here.

3.4.2 Line solver

As mentioned above, the equations on a vertical line of cells are now non-linear. They can be solved by a Newton procedure. Let the system of equations for one line be given by:

$$\mathbf{L}^h(\mathbf{u}^h) = 0 \ , \tag{3.76}$$

where $\mathbf{L}^h$ represents the discretized momentum and continuity equations, and $\mathbf{u}^h$ the unknown velocity and pressure components. A Newton step consists of:

$$\mathbf{u}^h_{n+1} = \mathbf{u}^h_n - J_b^{-1} \mathbf{L}^h(\mathbf{u}^h_n) \ , \tag{3.77}$$

where $\mathbf{u}^h_n$ is a first (or current) approximation and J_b, the Jacobian, is defined as:

$$J_b = \left. \frac{\partial \mathbf{L}^h}{\partial \mathbf{u}^h} \right|_{\mathbf{u}^h = \mathbf{u}^h_n} \ . \tag{3.78}$$

When the first approximation is close to the solution, the Newton process converges quadratically, see [20]. However, if the first guess is too far away, divergence may occur. A remedy is to use backtracking in combination with line searching, see [20]. This approach implies that instead of solving equation (3.76), one tries to find the minimum of

$$f_b = \frac{1}{2} \mathbf{L}^h \cdot \mathbf{L}^h \ . \tag{3.79}$$

The minima of equation (3.79) correspond to the zeros of equation (3.76). Only minima with $f_b = 0$ are roots of equation (3.76). To solve equation (3.76) the following iterative process is used:

$$\mathbf{u}^h_{n+1} = \mathbf{u}^h_n + \lambda_b \mathbf{p}_n, \quad 0 < \lambda_b \leq 1 \ . \tag{3.80}$$

For $\mathbf{p}_n$ the Newton step is taken:

$$\mathbf{p}_n = -J_b^{-1}\mathbf{L}^h(\mathbf{u}_n^h) \ . \tag{3.81}$$

The vector $\mathbf{p}_n$ represents a descent direction, meaning that $f_b(\mathbf{u}_{n+1}^h) < f_b(\mathbf{u}_n^h)$. Now there are two possible drawbacks: (a) f_b is decreasing too slowly, relative to the step $\mathbf{p}_n$; (b) the step $\mathbf{p}_n$ is too small, relative to the initial rate of decrease of f_b. The first problem can be overcome by requiring:

$$f_b(\mathbf{u}_{n+1}^h) \leq f_b(\mathbf{u}_n^h) + \alpha_b \nabla f_b(\mathbf{u}_n^h) \cdot (\mathbf{u}_{n+1}^h - \mathbf{u}_n^h) \ . \tag{3.82}$$

The second problem can be overcome by requiring:

$$\nabla f_b(\mathbf{u}_{n+1}^h) \cdot (\mathbf{u}_{n+1}^h - \mathbf{u}_n^h) \geq \beta_b \nabla f_b(\mathbf{u}_n^h) \cdot (\mathbf{u}_{n+1}^h - \mathbf{u}_n^h), \quad \beta_b > \alpha_b \ . \tag{3.83}$$

$\alpha_b = 1 \cdot 10^{-4}$ is often used in literature [64]. Line searching now consists of looking for a λ_b which satisfies both requirements. In the routine used in this work, which is described in [64], too small steps are avoided by a lower bound on the step length. So, to fulfill the requirement in equation (3.82), the minimum of

$$g_b(\lambda_b) = f_b(\mathbf{u}_n^h + \lambda_b \mathbf{p}_n) \tag{3.84}$$

is searched for. This is carried out by approximating $g_b(\lambda_b)$ by a quadratic function with the use of $g_b(0)$ and $g_b'(0)$. If, with this new λ_b, equation (3.82) does not hold, a new λ_b is computed but now g_b is approximated by a cubic. The last step is repeated until equation (3.82) holds. So, backtracking consists of first trying a Newton step ($\lambda_b = 1$). If this does not satisfy equation (3.82), a λ_b that minimizes g_b is searched for in the above described iterative way. A successful application of this method in combination with FMG, can be found in [80]. In the next section the results of some tests with this backtracking method in combination with multi-grid will be demonstrated.

3.4.3 Model problem

To illustrate the convergence of the discretization error for this particular example, a model problem is created in the same way as is done in section (*3.3.1*). The domain is defined as in equation (3.64) with $a_3 = 0.2$, $a_4 = 0.2$ and $\epsilon = 0.1$. The boundary conditions from equation (2.3) are used with $\mathbf{u}_0 = (1, 0)^T$. The righthand sides for the different equations are chosen such that the solution is:

$$\begin{aligned} u &= 1 - \xi^2 \ , \\ w &= 0 \ , \\ p &= \xi^1 \xi^2 (1 - \xi^1)(1 - \xi^2) \ . \end{aligned} \tag{3.85}$$

For the density and the viscosity the following functions have been used:

$$\begin{aligned} \rho &= e^{\beta_\rho p} \ , \\ \eta &= e^{\beta_\eta p} \ . \end{aligned} \tag{3.86}$$

As in section (*3.3.1*) for the iso-viscous incompressible case, the norm of the difference between the exact solution and the discrete solution can be monitored as a function of the mesh size on a uniform grid. First consider the case with a pressure-dependent density but with constant viscosity. Table (3.3) shows the L_1-norm of the error as a function of the mesh size. The table shows that the discretization is convergent. The ratio of the error on two consecutive grids shows that it is of first order. This is as expected because of the first order upwind discretization of the continuity equation.

N	$\left\|u-u^h\right\|$	$\left\|w-w^h\right\|$	$\left\|p-p^h\right\|$	$\frac{\left\|p-p^H\right\|}{\left\|p-p^h\right\|}$
32	$1.58 \cdot 10^{-3}$	$3.56 \cdot 10^{-3}$	$3.29 \cdot 10^{-2}$	–
64	$7.55 \cdot 10^{-4}$	$1.88 \cdot 10^{-3}$	$1.62 \cdot 10^{-2}$	2.0
128	$3.64 \cdot 10^{-4}$	$9.49 \cdot 10^{-4}$	$8.02 \cdot 10^{-3}$	2.0
256	$1.77 \cdot 10^{-4}$	$4.71 \cdot 10^{-4}$	$3.94 \cdot 10^{-3}$	2.1
512	$8.73 \cdot 10^{-5}$	$2.35 \cdot 10^{-4}$	$1.95 \cdot 10^{-3}$	2.0

Table 3.3: *Order of discretization for* $\beta_\rho = 3.0$ *and* $\beta_\eta = 0.0$ *in equation (3.86).*

Next, table (3.4) shows the results obtained, assuming an incompressible fluid ($\beta_\rho = 0$) with pressure-dependent viscosity. For this case the discretization should still be second order as the table indeed shows.

N	$\left\|u-u^h\right\|$	$\left\|w-w^h\right\|$	$\left\|p-p^h\right\|$	$\frac{\left\|p-p^H\right\|}{\left\|p-p^h\right\|}$
32	$1.13 \cdot 10^{-3}$	$1.60 \cdot 10^{-3}$	$1.97 \cdot 10^{-2}$	–
64	$3.11 \cdot 10^{-4}$	$4.57 \cdot 10^{-4}$	$5.43 \cdot 10^{-3}$	3.6
128	$7.97 \cdot 10^{-5}$	$1.13 \cdot 10^{-4}$	$1.40 \cdot 10^{-3}$	3.9
256	$2.02 \cdot 10^{-5}$	$2.87 \cdot 10^{-5}$	$3.53 \cdot 10^{-4}$	4.0
512	$5.04 \cdot 10^{-6}$	$7.54 \cdot 10^{-6}$	$8.86 \cdot 10^{-5}$	4.0

Table 3.4: *Order of discretization for* $\beta_\eta = 4.0$ *and* $\beta_\rho = 0.0$ *in equation (3.86).*

3.4.4 Multi-grid convergence

Finally, the convergence behavior of the complete MG solver for the pressure-dependent viscosity or density is studied. The domain is defined as in equation (3.64) with $a_3 = 0.2$, $a_4 = 0.2$ and $\epsilon = 0.1$. The boundary conditions from equation (2.3) are used with $\mathbf{u}_0 = (1, 0)^T$. The solver was used with W(2,2) cycles. The inter-grid operators used are the same as used for the incompressible iso-viscous flow.

First the case of $\rho = \rho(p)$ is investigated. For this purpose the cavitation model described in section (*2.3.3*) is used. The density pressure equation (2.71) is used, with $\bar{\rho}_0 = 0.01$. In the relaxation process, when relaxing a given line, a few Newton steps

(mostly one or two) are applied to each line for minimizing f_b in equation (3.79). In this step a full Jacobian is used. The lines are visited one by one in downstream direction. However, in some cases where the gradient in the pressure changes rapidly problems occur. Typically, the backtracking algorithm cannot find a solution when at a line the gradient in the pressure changes rapidly. This happens at lines at which the density changes between a constant value and a variable value. This problem can partly be overcome by returning to the line upstream of the line where the relaxation process did not converge. This step may have to be repeated several times. However, for very large values of β_ρ this approach also breaks down. This does not need to concern us for the present study, but is certainly a subject of attention for future research. As the value of β_ρ to be taken is not exactly known anyway and the purpose of our approach is mainly to model flow continuity in a cavitated region, rather than exactly modeling the details of the flow, it can be assumed that β_ρ is not too large.

As long as this is the case, the performance of the solver is as illustrated in figure (3.16). Figure (3.16a) shows the residual of the continuity equation as a function of the number of cycles. Clearly the solver converges. However, the speed of convergence is not grid-independent. This may be attributed to the strong non-linearity in the problem as it is also observed in [80] where also a FMG algorithm is combined with a backtracking algorithm. Nevertheless, from a practical point of view, the rate of convergence on a given grid, even up to quite considerable values of β_ρ, is still very good, see figure (3.16b).

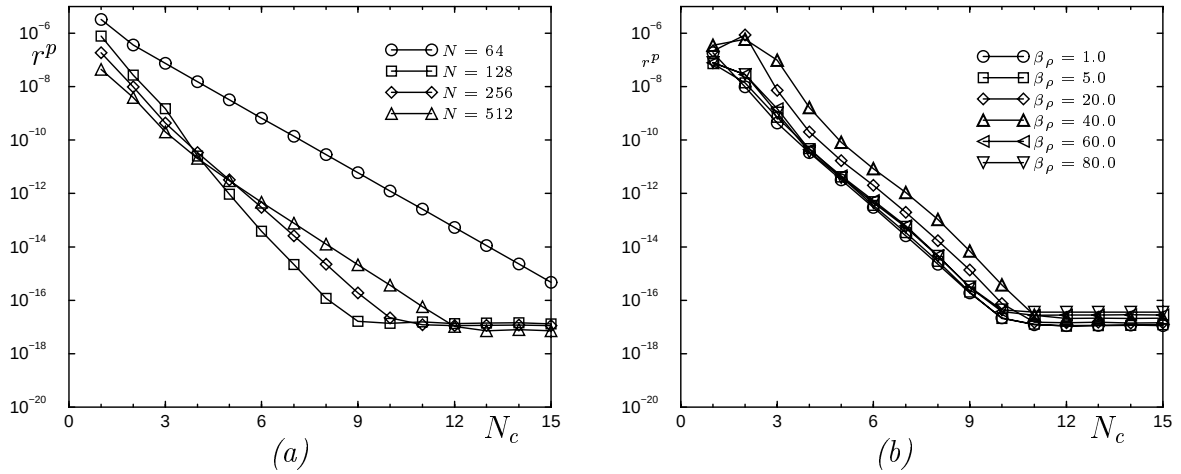

Figure 3.16: *The residual of the continuity equation as function of the number of MG cycles; (a): $\beta_\rho = 1.0$, for different number of grid cells. (b): $N = 256$, for different β_ρ.*

Secondly, consider the case $\rho = constant$ and $\eta = \eta(p)$ defined by equation (2.66). For this case the performance of the MG solver is not that good. As in the previous case the convergence is not grid-independent, see figure (3.17a). Also the convergence rate is less good. Typically a factor three per cycle is obtained. This still means that in two cycles an error reduction of an order of magnitude is obtained which is acceptable for practical use. Another drawback is that the relaxation procedure does not converge for large $\bar{\alpha}_p$ ($\bar{\alpha}_p > 0.03$ in this particular case). Probably the incorporation into the discretization of the direction of the characteristics found in equation (A.7) could result in a convergent relaxation. However, comparing it to the performance for the other cases indicates that

further study is needed.

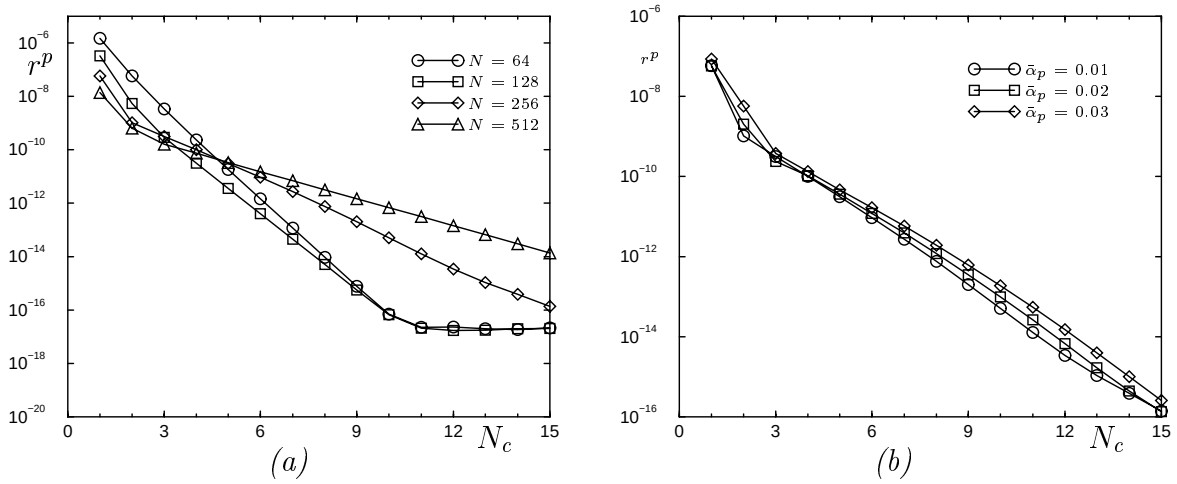

Figure 3.17: *The residual of the continuity equation as function of the number of MG cycles; (a):* $\bar{\alpha}_p = 0.01$*, for different number of grid cells. (b):* $N = 256$*, for different* $\bar{\alpha}_p$*.*

For both cases the standard inter-grid operators seem to be correct. The case of compressible iso-viscous flow gives a good MG performance, only the case of incompressible piezo-viscous flow needs some more attention in the future. This ends the testing part of the two developed solvers. In the following chapters the results obtained with these solvers, are presented.

3.5 Conclusion

In this chapter a numerical solution procedure for the incompressible iso-viscous Stokes equations has been presented. The developed solver can handle domains with small ϵ very well. It was checked whether the discretization converges second-order accurately to a preset solution. It has been shown in figures (3.14), (3.15) that the MG method as used reaches good multi-grid convergence even for high grid line-aspect ratios.

For example, the angle between a grid line $\xi^2 = constant$ and a horizontal line in the physical domain for $a_3 = 0.5$, $a_4 = 0.01$ and $\epsilon = 0.01$ in equation (3.64) gives:

$$\tan(\alpha) = \epsilon \left.\frac{dh}{dx}\right|_{x=0} = -\frac{a_3}{a_4}\sqrt{2\ e\epsilon}\ \epsilon\ , \tag{3.87}$$

thus $\alpha \approx 50^o$ where $\rho_{MG} = 0.064$. As a result the solver is expected to be very well suited to investigate the Stokes effects in the iso-viscous incompressible flow in narrow films induced by surface imperfections.

Finally, the solver was extended to allow for a pressure-dependent density and/or viscosity. For the variable density the multi-grid convergence looks promising, with $\rho_{MG} = 0.089$, but the variable viscosity case needs some more attention in the future: $\rho_{MG} = 0.31$.

Chapter 4

Results for Stokes

In the previous chapter the development and testing of the algorithm for the numerical solution of the Stokes equations was described. In this chapter results are presented for problems representative for the flow in lubricated contacts. For each problem the solution is discussed in detail and compared with the solution of Reynolds' equation. In particular the magnitude of the relative difference between the Stokes solution and the Reynolds solution is measured as a function of characteristic geometry parameters such as an "amplitude" and a "wavelength" of surface imperfections. The objective of the study is to obtain a "rule of thumb" for practical use, indicating when the Reynolds solution is sufficiently accurate and when a better solution is needed. This better solution can either be the Stokes solution but, as is shown in this chapter, to some extent the corrected solution based on a perturbation approach can be used.

4.1 Geometry

The problems discussed in this chapter can all be written in the same form, i.e. as the flow through a channel with dimensionless geometry given by the function

$$h(x) = (1 - a_1)x^{a_2} + a_1 - R'(x) \tag{4.1}$$

where the first two terms represents the "global" shape of the channel and the third term a "local" feature. For this local feature the following function will be assumed:

$$R'(x) = A'_m \frac{\sin(2\pi x/a_4)}{((1 + e^{-a_5(a_3/2-x)})(1 + e^{-a_5(a_3/2+x)}))} \tag{4.2}$$

where

$$A'_m = A_m(1 + e^{-a_5(a_3/2-a_4/4)})(1 + e^{-a_5(a_3/2+a_4/4)}) \tag{4.3}$$

Of the different parameters in the above equations A_m obviously represents the amplitude and a_4 the wavelength. The parameters a_3 and a_5 are a measure of the width of the feature compared to the full length of the channel and an amplitude decay parameter, respectively. As an example, figure (4.1) shows the geometry obtained for $a_1 = 0$, $a_2 = 0$, $a_3 = 0.5$, $a_4 = 0.5$ and $A_m = 0.5$. This geometry clearly represents a single local feature

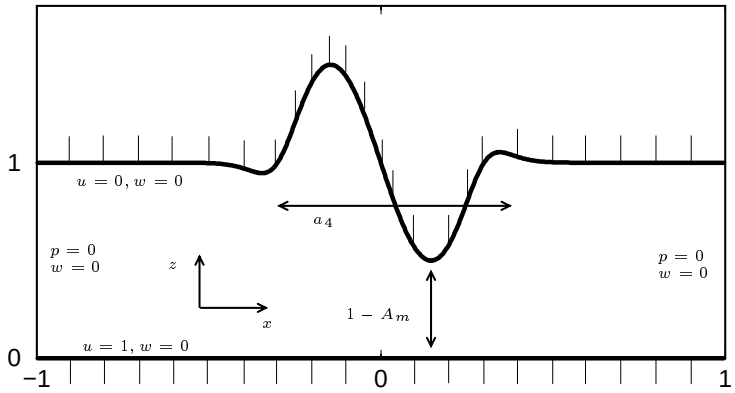

Figure 4.1: *Geometry and boundary conditions for Single local feature.*

in a uniform channel; it is discussed in detail in the following section. Also shown in figure (4.1) are the boundary conditions that will be imposed for all problems throughout this chapter. For the numerical solution procedure on the given domain a grid will be generated using

$$z = \xi^2 h(x(\xi^1)) \ , \ \ (\xi^1, \xi^2) \in [0, 1] \tag{4.4}$$

where $x(\xi^1)$ is defined by equation (3.68). Finally, for each problem a study has been carried out monitoring the difference between the Stokes solution and the Reynolds solution as a function of the governing parameters. For this purpose the quantity $\bar{R}$ as introduced in chapter (*2*) is used:

$$\bar{R} = \frac{\int_{\tilde{\Gamma}_1} p_S(x, z = 0)dx - \int_{\tilde{\Gamma}_1} p_R(x)dx}{\int_{\tilde{\Gamma}_1} p_R(x)dx} \tag{4.5}$$

where the tilde in $\tilde{\Gamma}$ indicates that the pressure is only integrated for positive values.

4.2 Single local feature

For the case of a local feature in a uniform channel as shown in figure (4.1), equation (4.2) has been used, taking the parameters shown in table (4.1).

a_1	a_2	a_3	a_5	$\Delta\xi^1$	Δx	β
1.0	0	a_4	$\frac{16}{a_4}$	0.8	$\frac{3}{2}a_3$	0.025

Table 4.1: *Values of parameters for single local feature.*

As a result the only parameters in the problem are the wavelength a_4, the amplitude A_m, and of course $\epsilon = \frac{H}{L}$, which appears in the Stokes equations. Note that A_m and a_4 represent dimensionless quantities. In physical terms the amplitude of the feature is $A = HA_m$ and its wavelength $\Lambda = La_4$.

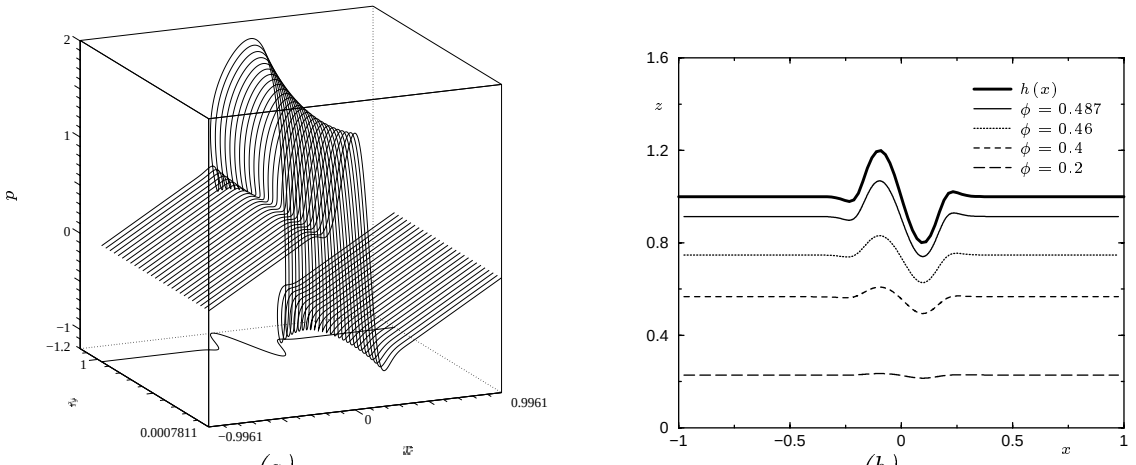

(a) *(b)*

Figure 4.2: *(a): Pressure field. (b): Streamlines. Both as function of x and z for* $\epsilon = 0.1$, $a_4 = 0.4$, $A_m = 0.2$.

Firstly, as an illustration figure (4.2) shows a typical Stokes solution to the problem. Figure (4.2a) shows the pressure field and figure (4.2b) the streamlines. In addition figure (4.3a) shows the pressure at the lower and upper surface as a function of x. Finally, figure (4.3b) shows the horizontal velocity component u and the vertical velocity component w as a function of z for $x = 0$.

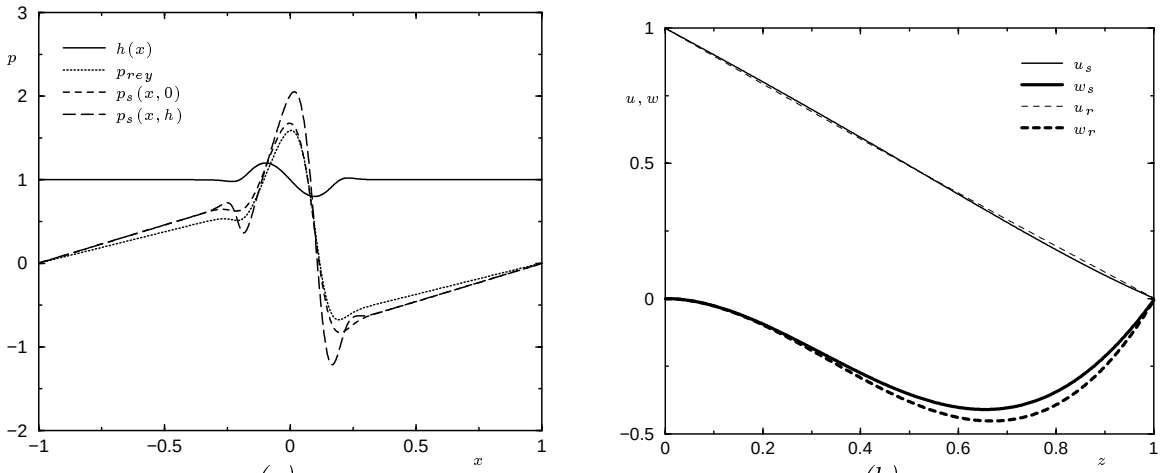

(a) *(b)*

Figure 4.3: *(a): Pressure as function of x for $z = 0$ and $z = h(x)$. (b): u and w velocity components at $x = 0$. Subscript indicates Reynolds (r) and Stokes (s) solution, respectively.*

The solution for the problem without feature would be a zero pressure everywhere, a linear variation of $u(z)$ and $w = 0$. Comparing this with the figures shows that the presence of the feature induces a gradual pressure rise before and after the feature and a sharp local change around the feature.

In figure (4.3a) also the pressure solution obtained from the Reynolds equation is shown. In the region in which the feature is located the Stokes pressure is z-dependent. Note that the Reynolds and Stokes solution do not only differ in the vicinity of the feature.

Also in the "inlet" and "outlet" region preceding and following the feature all the way to the boundary there is a difference, though the difference decreases in magnitude.

The velocity profiles in figure (4.3b) show little difference between the Stokes solution and the Reynolds solution.

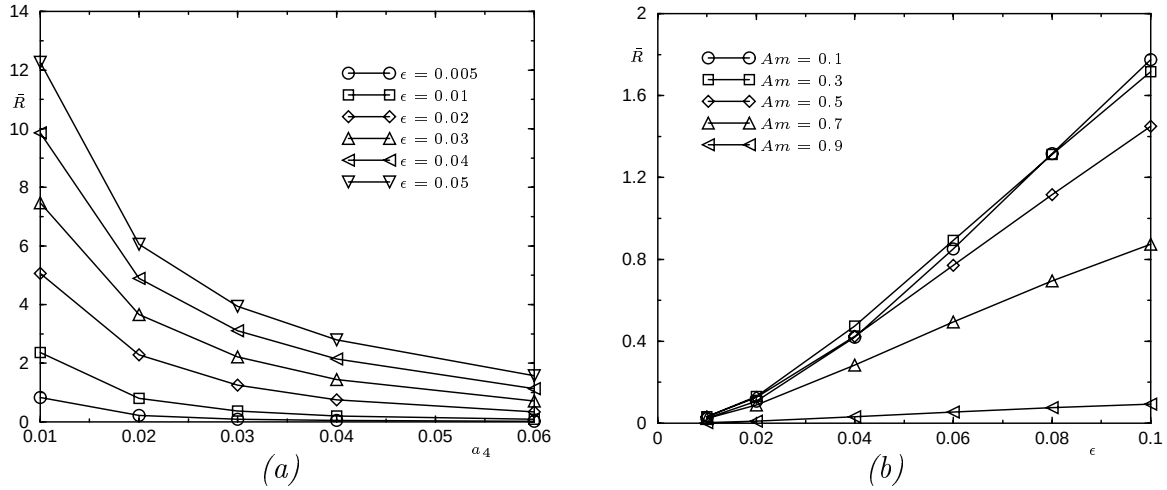

Figure 4.4: *(a):* $\bar{R}$ *for* $A_m = 0.1$. *(b):* $\bar{R}$ *for* $a_4 = 0.1$.

Next, the magnitude of the difference $\bar{R}$ between the Reynolds and the Stokes solution is studied in more detail. First, for a fixed amplitude $A_m = 0.1$ the parameters ϵ and a_4 have been varied, see figure (4.4a). For a given ϵ, with increasing wavelength a_4 the relative difference $\bar{R}$ decreases. Figure (4.4b) shows that with decreasing ϵ the relative difference $\bar{R}$ decreases, regardless of the value of A_m. This is in accordance with common expectations.

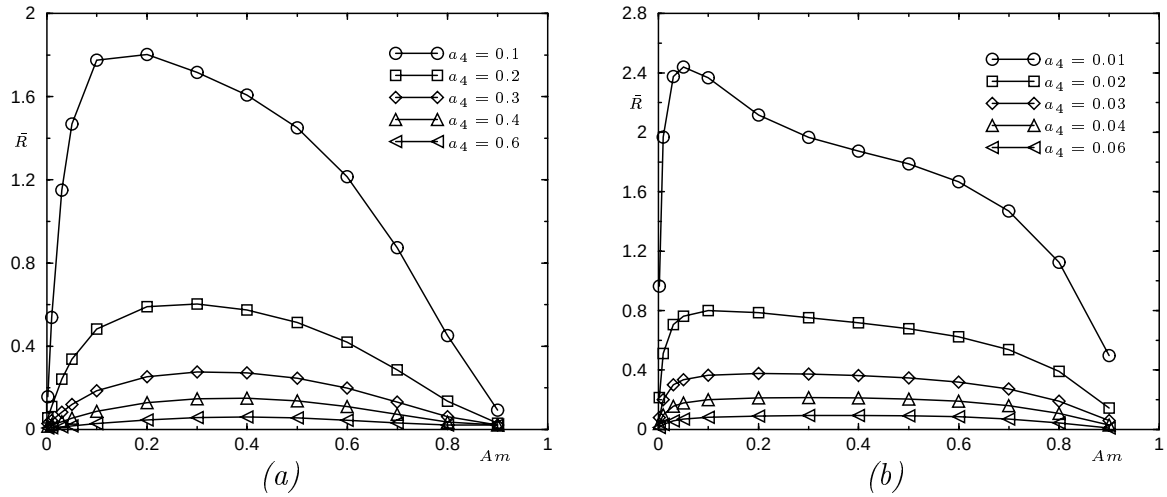

Figure 4.5: $\bar{R}$ *as function of* A_m *for (a):* $\epsilon = 0.1$. *(b):* $\epsilon = 0.01$.

Figure (4.4b) also shows results obtained when keeping a_4 fixed and varying A_m for different ϵ. This figure shows that for a given ϵ the value of $\bar{R}$ increases with decreasing amplitude. This result seems somewhat odd as one would expect the opposite behavior. After all, a larger amplitude gives larger slopes, and one generally couples validity of

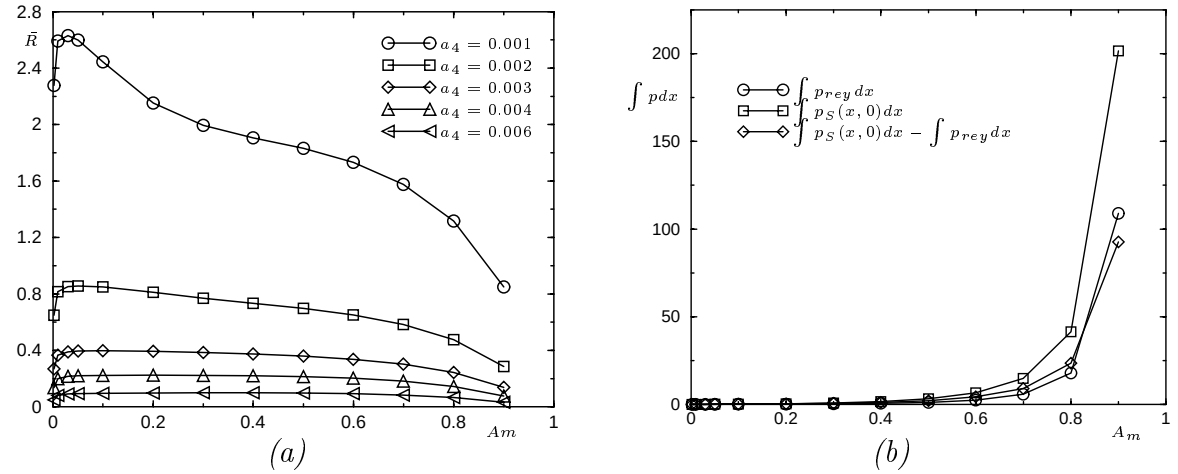

Figure 4.6: *(a): $\bar{R}$ as function of A_m for $\epsilon = 0.001$. (b): Integration of p only for positive p, $\epsilon = 0.001$ and $a_4 = 0.001$.*

Reynolds equation to "small slopes". Apparently this is not always true. This can be seen more clearly from figure (4.5) and (4.6). For different values of ϵ ($\epsilon = 0.1, 0.01, 0.001$) these figures show $\bar{R}$ as a function of A_m and a_4. These figures show that $\bar{R}$ does not monotonously increase or decrease with A_m but that it has a maximum, however, for sufficiently large A_m it decreases with A_m. For a smaller value of ϵ this maximum occurs at a smaller value of A_m.

For small A_m the Stokes solution approaches the Reynolds solution and thus $\bar{R}$ approaches zero. What happens if $A_m \rightarrow 1$? This can be best explained by plotting the integral over the pressure on the lower surface for the different solutions. This has been done to obtain figure (4.6b) where this integration has been performed setting negative pressures equal to zero. It can be seen that in the neighborhood of $A_m = 1$ the integrals over the Stokes pressure, over the Reynolds pressure and the difference between these integrals tend to infinity. But the difference between the integral over the Stokes and Reynolds solution tends less fast to infinity than the integral over the Reynolds solution. This explains the form of $\bar{R}$ as function of A_m. So, relative to the Reynolds solution the Stokes solution does not diverge. It is mentioned here that only points up to $A_m = 0.9$ have been calculated. For amplitudes closer to one the numerical accuracy of the solver will be questionable. The exact behavior of $\bar{R}$ in the limit $A_m \rightarrow 1$ can thus not be predicted.

Secondly, note that in each figure results are shown for values of a_4 that differ, e.g. for $\epsilon = 0.1$ then $0.1 < a_4 < 0.6$, for $\epsilon = 0.01$ then $0.01 < a_4 < 0.06$ and for $\epsilon = 0.001$ then $0.001 < a_4 < 0.006$. This choice has been made on purpose. Now, comparing these figures shows that, approximately, the magnitude of $\bar{R}$ depends only on the ratio ϵ/a_4. So, disregarding the detailed shape of each curve, its level is determined by this ratio. The purpose of this study is to find a general rule indicating when a Reynolds solution is valid. For this problem one thus finds that the difference between the Stokes and the Reynolds solution is a function of ϵ/a_4. As $\epsilon = H/L$ and $a_4 = \Lambda/L$ this means that the validity depends on the value of the ratio H/Λ = film thickness/wavelength feature.

From the results presented here it is estimated that a difference of 10 percent between

the Reynolds and the Stokes solution measured by $\bar{R}$ occurs for $\epsilon/a_4 = H/\Lambda > 0.2$. This is in line with expectations given in literature [25] that a factor of this type, H/Λ, determines the transition between Stokes and Reynolds roughness. In figures (4.5) and (4.6a) it can already be seen that there is a limit for $\bar{R}$ if ϵ/a_4 is kept constant and $\epsilon \to 0$. For different values of ϵ/a_4 this is depicted in figure (4.7). The $\bar{R}$ values have been scaled on the maximum value of $\bar{R}$ for ϵ/a_4 is constant. So it is assumed that $\bar{R}$ reaches a maximum at $\epsilon = 0.005$. Converting to un-scaled variables can shed light on this limit. If H is assumed constant, then Λ is constant, because $\frac{\epsilon}{a_4} = \frac{H}{La_4} = \frac{H}{\Lambda} = constant$, then if $L \to \infty$ the distance between local feature and in/out flow boundary increases. The limit indicates that there is no interaction between the surface feature and the in/out flow boundaries.

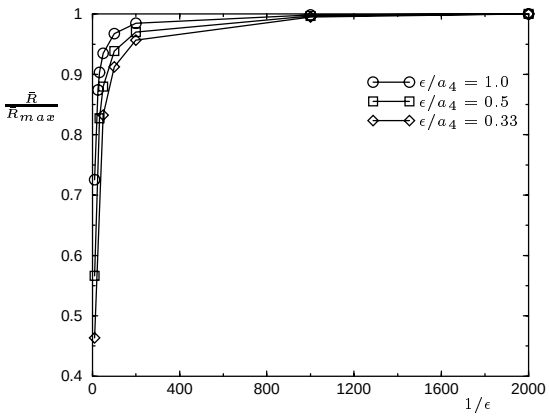

Figure 4.7: *Limit of* $\bar{R}/\bar{R}_{max}$ *if* $\epsilon/a_4 = constant$ *and* $\epsilon \to 0$, *for* $A_m = 0.1$.

A_m	$\bar{R}_{N=128}$	$\bar{R}_{N=256}$	$\bar{R}_{N=512}$	p
0.002	0.9587	0.9636	0.9647	2.5
0.03	2.3608	2.3720	2.3748	2.3
0.1	2.3580	2.3658	2.3678	2.3
0.3	1.9779	1.9689	1.9664	2.2
0.5	1.8218	1.7957	1.7883	2.2
0.7	1.5102	1.4792	1.4700	2.1
0.9	0.4994	0.4983	0.4976	1.4

Table 4.2: *Convergence of* $\bar{R}$ *for* $\epsilon = 0.01$ *and* $a_4 = 0.01$.

Finally some additional calculations have been carried out to illustrate the accuracy of the calculated results. As all equations were discretized with second-order accuracy, also the value of $\bar{R}$ computed for a given case should be $O(\delta\xi^2)$ accurate. This is illustrated in table (4.2). For $\epsilon = 0.01$, $a_4 = 0.01$ and for different values of A_m this table shows $\bar{R}$

on grids with 128×128, 256×256 and 512×512 cells. The order p can be calculated with:

$$p = \frac{\log\left|\frac{\bar{R}-\bar{R}_{N=128}}{\bar{R}-\bar{R}_{N=256}}\right|}{\log\left|\frac{\delta\xi_{N=128}}{\delta\xi_{N=256}}\right|}\ , \tag{4.6}$$

where the "true" value $\bar{R}$ is approximated with the $\bar{R}$ value on the finest grid ($N = 512$). The table shows that indeed a second order convergence is obtained. All the computational results presented in the figures (4.2), (4.3), (4.4), (4.5), (4.6) and (4.7) were obtained on a grid with 512×512 cells. In the next section the perturbation results and the flow field will be presented.

4.2.1 Perturbation SLF

In chapter (*2*) a perturbation approach was presented that can be used to obtain a correction to the Reynolds solution without having to solve the full Stokes equations. For the problem of a Single Local Feature, as discussed in the previous section, such perturbation solutions are compared with the solution of the Reynolds equation and the solution of the Stokes equations. For a characteristic case, the accuracy and convergence of the perturbation in relation with the wavelength of the feature is studied. The perturbation parameter is $\epsilon = H/L$, see section (*2.2*). As the viscosity is constant and the fluid is assumed to be incompressible for the SLF problem, one can obtain the perturbation solutions very cheaply. Up to first-order perturbation this has been explained in section (*2.2*). How to obtain the second-order correction for the pressure is presented in appendix (*C*). So up to second-order the expansion looks like:

$$\begin{aligned} u(x,z) &= u_0(x,z) + \epsilon^2 u_1(x,z) + \epsilon^4 u_2(x,z) \\ w(x,z) &= w_0(x,z) + \epsilon^2 w_1(x,z) + \epsilon^4 w_2(x,z) \\ p(x,z) &= p_0(x) + \epsilon^2 p_1(x,z) + \epsilon^4 p_2(x,z) \end{aligned} \tag{4.7}$$

with expressions for $u_0(x,z)$, $w_0(x,z)$ and $p_0(x)$ from equation (2.53), (2.55) and (2.54), respectively. For $u_1(x,z)$, $w_1(x,z)$ and $p_1(x,z)$ equations (C.4), (C.5) and (2.59) are used. $p_2(x,z)$ follows from equation (C.6). For example, the first-order perturbation only requires the solution of an additional Reynolds type of equation.

Figure (4.8) shows some results obtained for the case $\epsilon = 0.01$, $A_m = 0.4$ and three wavelengths $a_4 = 0.06, 0.04, 0.02$. The figures show the pressure at the surface $z = 0$ and $z = h(x)$ as obtained from the Reynolds equation, the Stokes solution, and the first-and second-order perturbation solution.

As the global features of the SLF solution have been discussed in detail in the previous section, here only the solution in the region around the feature is shown.

Firstly consider the case $a_4 = 0.06$. The first-order perturbation solution to the pressure already differs very little from the Stokes solution, and the second-order perturbation result is an even more accurate approximation to the Stokes solution. Clearly the perturbation in ϵ for this case converges.

With decreasing wavelength the accuracy of the perturbed solutions is expected to decrease. This can be seen from the results shown for the smaller wavelengths a_4. For $a_4 = 0.04$ the perturbation still "converges", i.e. provides an accurate correction to the

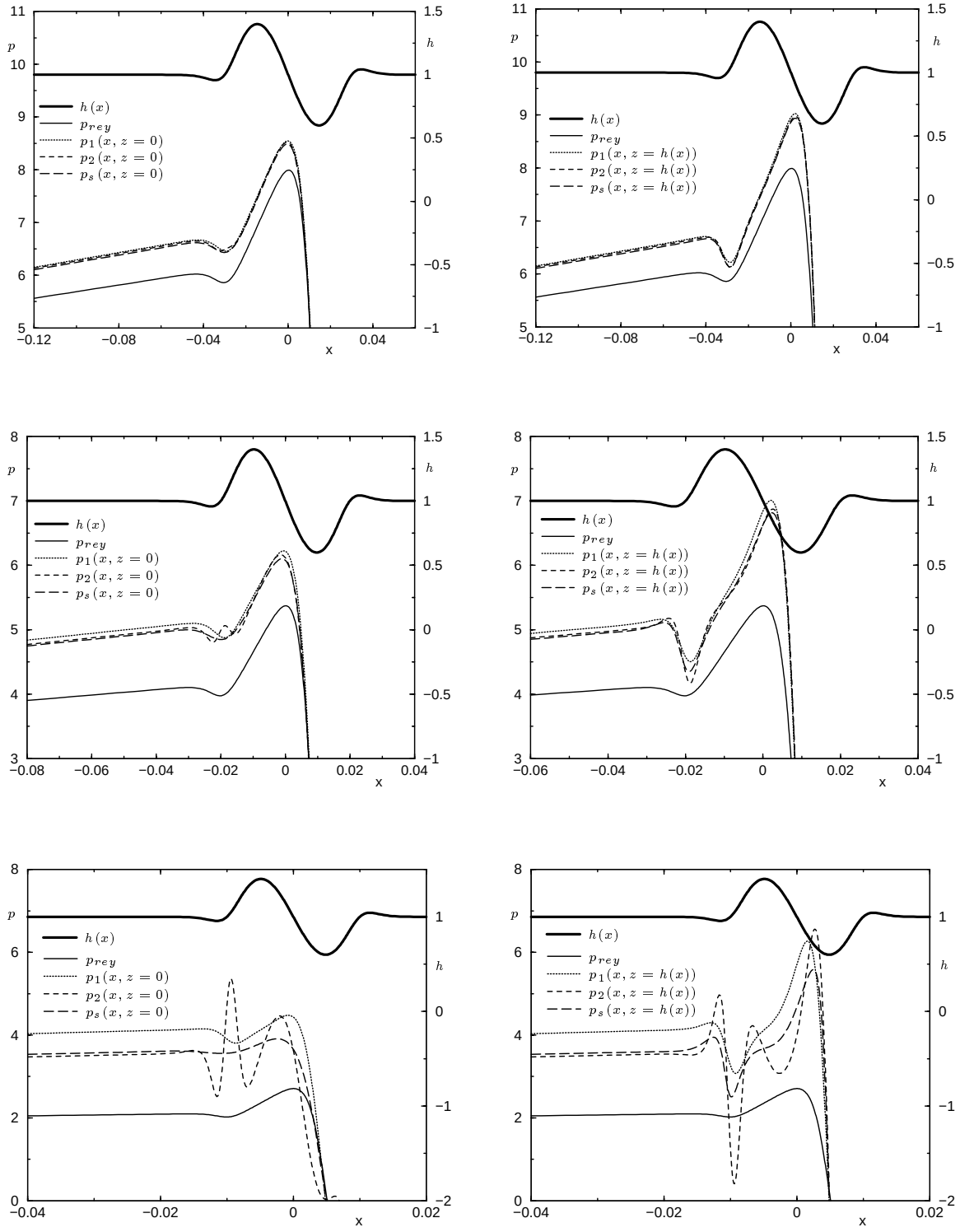

Figure 4.8: *Pressure at the surface $z = 0$ (left) and $z = h(x)$ (right) for the Reynolds solution (p_{rey}), the Stokes solution (p_s) and a first (p_1) and second order (p_2) perturbation solution for the case $\epsilon = 0.01$ and $A_m = 0.4$ while $a_4 = 0.06$ (top), $a_4 = 0.04$ (center) and $a_4 = 0.02$ (bottom).*

Reynolds solution. However, for $a_4 = 0.02$ this is no longer true. The global correction, i.e. the perturbation solution, is accurate in the region away from the feature, but locally at the feature the perturbation results are a very poor approximation to the Stokes results. The perturbation solutions contain a local oscillation with an amplitude that is even larger in the second-order result than in the first-order result. This indicates that locally the perturbation in ϵ does not converge. Apparently the local gradients have become too large for the global parameter ϵ to be an adequate perturbation parameter.

It is observed that in all three cases ($a_4 = 0.06, 0.04, 0.02$) the Stokes pressure is larger than the Reynolds pressure. A closer look at the pressure expansion

$$p(x,z) = p_0(x) + \epsilon\left(\tilde{p}_1(x) + \frac{\partial w_0}{\partial z}\right) + \epsilon^3 \int \left(\frac{\partial^2 w_0}{\partial x^2} + \frac{\partial^2 w_1}{\partial z^2}\right) dz + \epsilon^3 \tilde{p}_2(x) \tag{4.8}$$

shows that this is caused by $\tilde{p}_1(x)$ and $\tilde{p}_2(x)$ because w_0 and w_1 only differ from zero in the region where dh/dx is non zero. The equations for $\tilde{p}_1(x)$ and $\tilde{p}_2(x)$ contain derivatives of h with respect to x, this in contrast with the Reynolds equation. So, the curvature of the feature does not only have a local effect but also a global effect.

For the same cases figure (4.9) shows some velocity results. The left figures show the flow field according to the Stokes solution. The figures on the right show the velocity components u and w as a function of z at the location $x = 0$. These figures show the velocity components from the Reynolds solution, the Stokes solution, and a first-order perturbation result. For the Reynolds solution it can be found from equations (2.53) and (2.55) that at $x = 0$:

$$u = 1 - z \tag{4.9}$$

and

$$w = z^2(1-z)\frac{dh}{dx} \tag{4.10}$$

because $h = 1$ and $\frac{dp}{dx} = 0$. This means that the u profile is the same for $a_4 = 0.06, 0.04, 0.02$ and for the w profile only the minimum value of w changes.

The figure shows that for $a_4 = 0.06$ and $a_4 = 0.04$ the perturbation solution of the velocity field is a good approximation of the Stokes solution.

For $a_4 = 0.02$ the first-order perturbation results are not an improvement on the Reynolds solution. They predict a back-flow in the top of the domain. The predicted re-circulation flow field does not seem realistic. The Stokes solution predicts a much smaller recirculation zone. It is situated on top of the line $\phi = 0.494$ in the wave in figure (4.9). The Reynolds equation does not predict this type of recirculation. So, perturbation theory is not capable of predicting these recirculation zones correctly.

In general there are two types of recirculation for the SLF. The first type, which is also predicted by the Reynolds equation, contains a back-flow generated for an amplitude $A_m > 0.5$. In figure (4.10a) a Stokes velocity solution is shown for $\epsilon = 0.01$, $A_m = 0.9$ and $a_4 = 0.06$. It shows such a recirculation zone which extends to the inflow boundary. The second, very local type is not predicted by the Reynolds equation. It occurs when $\epsilon/a_4 = O(1)$ and also the series expansion in terms of ϵ can not adequately predict this recirculation. An example of this type of recirculation is given in figure (4.10b). Note that in this case the bulk of the fluid is passing the feature below. This recirculation is of the

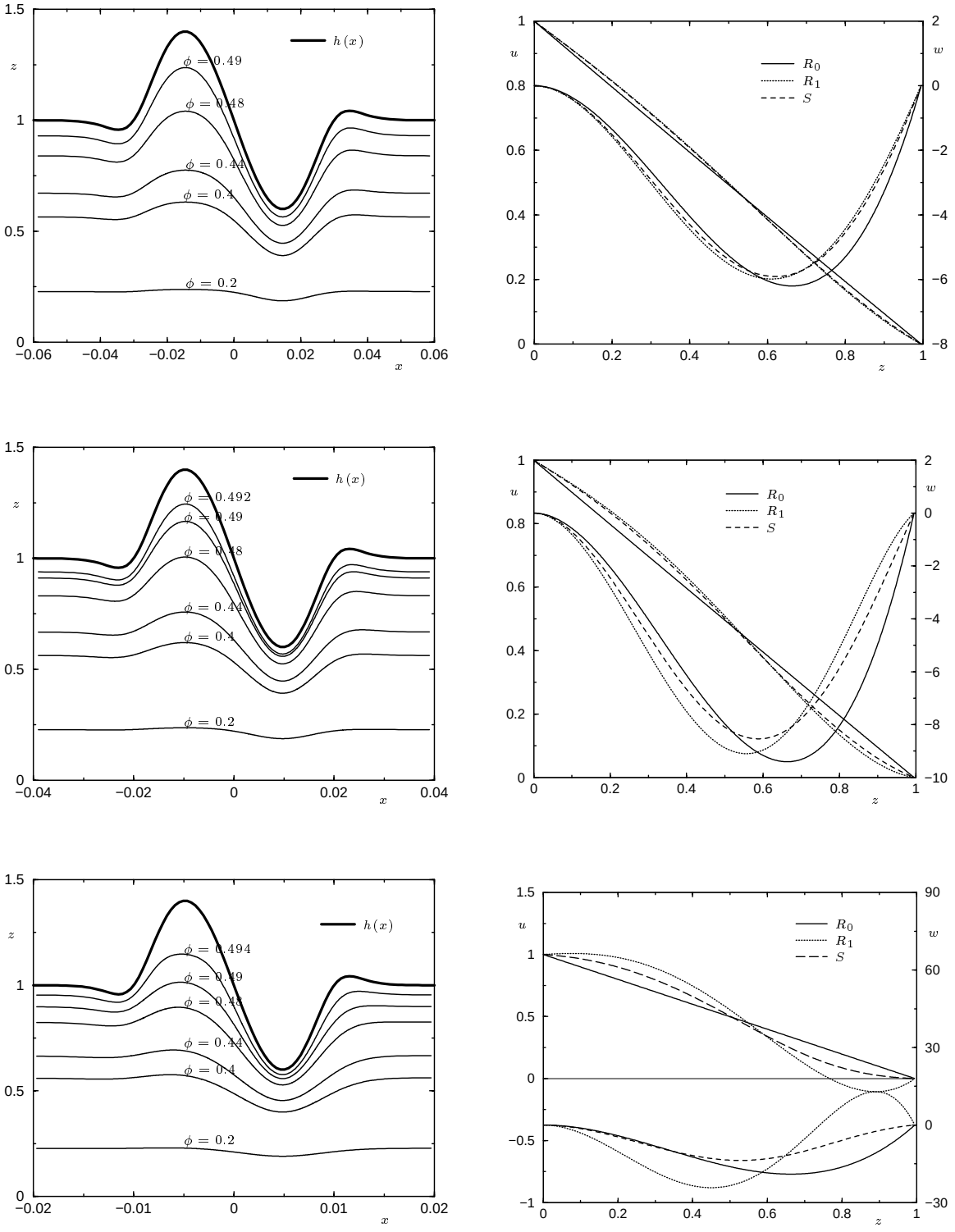

Figure 4.9: *Streamlines of Stokes velocity field (left) and velocity components* $u(z)$ *and* $w(z)$ *at* $x = 0$ *(right) for the Stokes (S) solution, the Reynolds* (R_0) *solution and the first-order perturbation* (R_1) *solution for the case* $\epsilon = 0.01$ *and* $A_m = 0.4$*, while* $a_4 = 0.06$ *(top),* $a_4 = 0.04$ *(center) and* $a_4 = 0.02$ *(bottom).*

same type as found in the case of a driven cavity problem, see [47]. From figure (4.10) it is clear that the amplitude induced recirculation has a much stronger effect on the flow than the short wavelength induced recirculation. A combination of both recirculation patterns can occur when $\epsilon/a_4 = O(1)$ and $A_m > 0.5$.

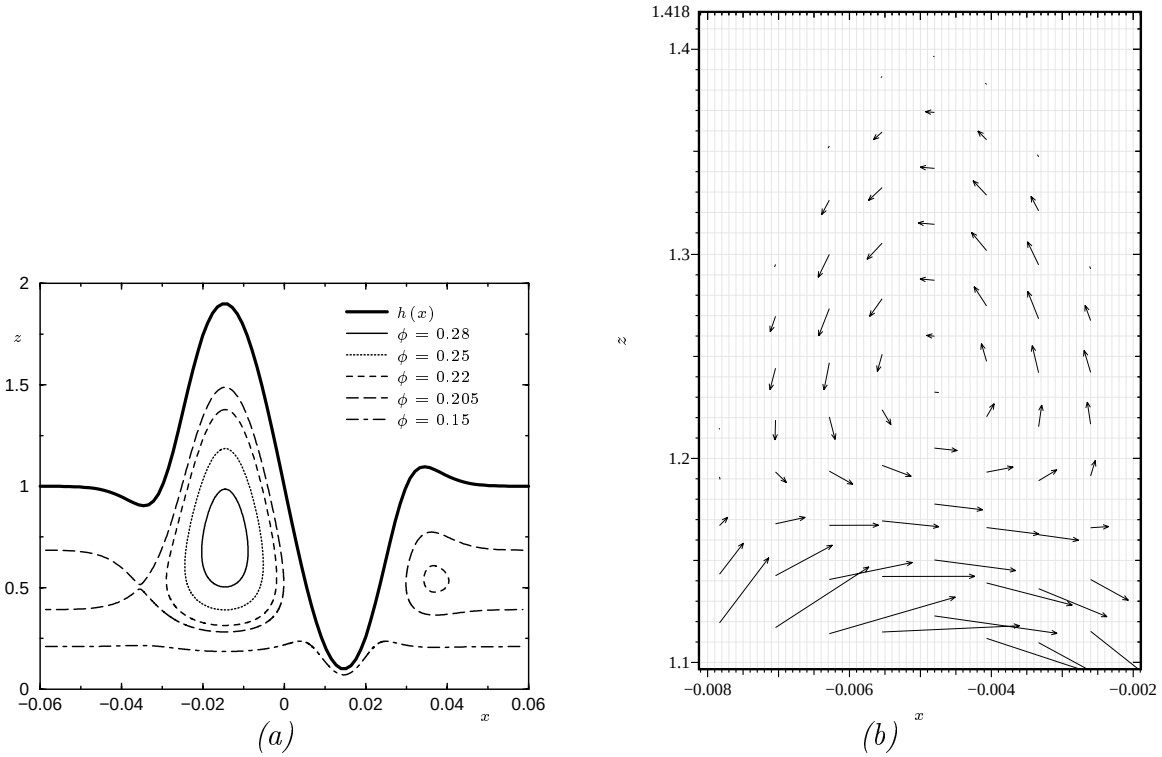

(a) *(b)*

Figure 4.10: *Two types of recirculation for* $\epsilon = 0.01$. *(a): Large amplitude induced recirculation* $A_m = 0.9$ *and* $a_4 = 0.06$. *(b): Short wavelength induced recirculation* $A_m = 0.4$ *and* $a_4 = 0.02$

Similar calculations have been performed for larger values of the amplitude. The global tendency is the same. For large wavelengths the perturbation theory provides accurate corrections on a global as well as on a local scale. For small wavelengths the perturbation theory breaks down locally. In contrast with the small-amplitude case now there is no convergence of the global pressure distribution to the Stokes solution for smaller wavelength. Finally, for a given ϵ the breakdown of the perturbation theory is not only governed by ϵ/a_4 but also by A_m. This is due to the fact that terms in the Stokes equations multiplied by some power of ϵ are no longer $O(1)$ if for example A_m/a_4 or A_m/a_4^2 are large, as was explained in section (*2.2*).

Naturally the behavior illustrated above is also reflected in global parameters of the solution such as the $\bar{R}$ value used to measure the difference between the Stokes solution and the Reynolds solution. This is illustrated in table (4.3) and in figure (4.11), where the $\bar{R}$ value is obtained comparing the Stokes solution, the first-and second-order perturbation pressure for the case $\epsilon = 0.01$, $A_m = 0.4$ and different values of a_4. The table shows that for a large wavelength the $\bar{R}$ value based on the perturbation solution is quite accurate. However, the error increases with decreasing wavelength, yielding poor results when the perturbation theory breaks down. Note that for $a_4 = 0.02$ the result is still quite good.

a_4	R_{p_1}	R_{p_2}	R_S
0.06	0.1028	0.0993	0.0944
0.04	0.2356	0.2180	0.2123
0.03	0.4227	0.3677	0.3626
0.02	0.9600	0.6848	0.7168
0.01	3.8751	–	1.8746

Table 4.3: *$\bar{R}$ values for the SLF with $\epsilon = 0.01$ and $A_m = 0.4$: for first-order perturbation ($\bar{R}_{p_1}$), for second-order perturbation ($\bar{R}_{p_2}$) and for Stokes solution ($\bar{R}_S$).*

As was shown in figure (4.8) for this case the accuracy of the perturbation pressure is quite acceptable globally but is very poor locally. Because $\bar{R}$ is dominated by the global difference, this is only moderately reflected in the value of $\bar{R}$.

Next, for a given wavelength $a_4 = 0.04$ and $\epsilon = 0.01$ figure (4.11) shows the value of $\bar{R}$ based on the first-and second-order perturbation solution and the Stokes solution as a function of the amplitude A_m. The results are obtained for $\epsilon = 0.01$. For this case, even for large amplitudes, the value of $\bar{R}$ is predicted quite accurately by the perturbation solution.

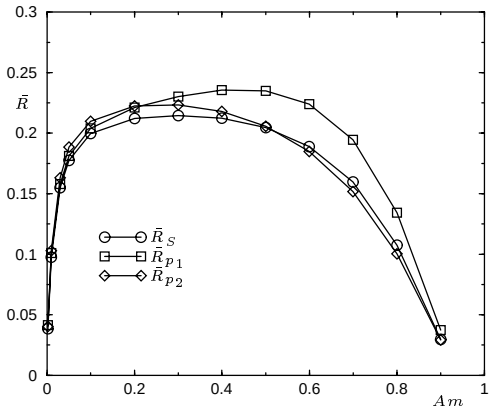

Figure 4.11: *The $\bar{R}$ values for the Stokes ($\bar{R}_S$) solution, the first-order perturbation ($\bar{R}_{p_1}$) solution and the second-order perturbation ($\bar{R}_{p_2}$) solution for the SLF with $\epsilon = 0.01$ and $a_4 = 0.04$.*

In conclusion, in this section it has been shown that for the SLF, a perturbation theory yields accurate corrections to the Reynolds solution as long as the ratio ϵ to wavelength is not too large. For large values of (ϵ/a_4), see section *(2.2)*, the global correction of the level of the pressure solution will still be reasonable, however, the predicted local pressure field and the velocity field are inaccurate. In such cases better results may be obtained with a more sophisticated perturbation approach, using different expansion parameters in different regions, i.e. ϵ on a global scale and some $\epsilon A_m/a_4$ on a local scale.

Finally, for the present case of iso-viscous, incompressible flow, the perturbation solutions could be obtained easily. It should be noted that for the more general case of a

pressure-dependent density and viscosity the entire series expansion is much more complicated.

4.3 Multiple local feature

A single local feature as discussed in the previous section is of course an exceptional case. In general the surface geometry will be more complex. Therefore as a next step consider the case of a more complex feature, a waviness of a certain width. Such a "multiple local feature" can also be created with equation (4.2) by taking a_3 larger than the wavelength. Firstly a typical example will be presented. In figure (4.12) the pressure field and the streamlines are shown for the case $\epsilon = 0.01$, $A_m = 0.2$, $a_3 = 0.05$ and $a_4 = 0.01$. The x-axis has been enlarged to show the feature.

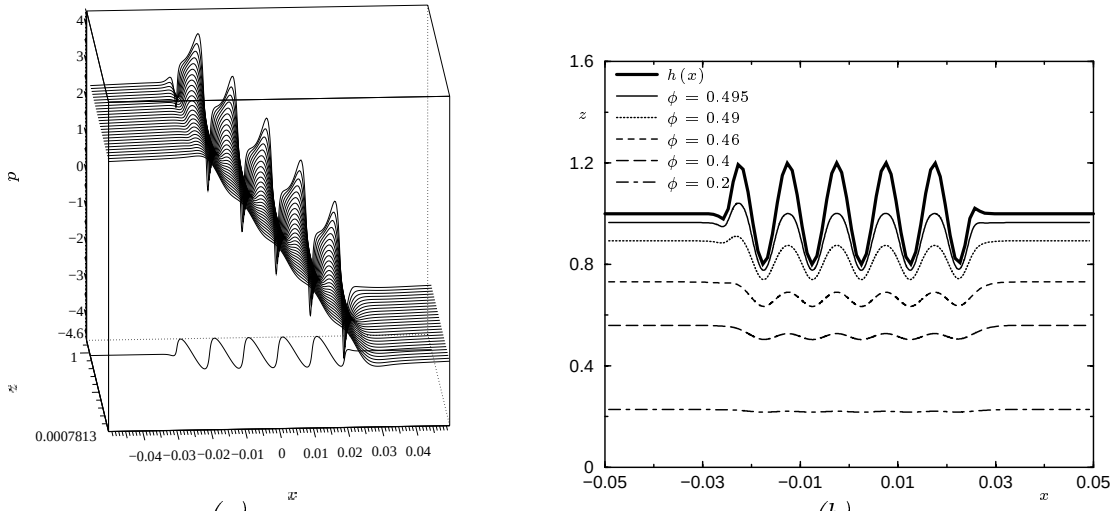

(a) *(b)*

Figure 4.12: *Results of Stokes flow for the MLF. (a): Pressure field. (b): Streamlines. Both as function of x and z for $\epsilon = 0.01$, $a_3 = 0.05$, $a_4 = 0.01$ and $A_m = 0.2$.*

The pressure on the lower and upper surface for the Stokes and Reynolds solution are shown in figure (4.13a). The pressure tends to zero at $x = -1$ and $x = 1$. The Reynolds pressure solution is much lower than the Stokes solution as was already found for the SLF. In figure (4.13b) the u and w velocity components at $x = 0$ are shown for the Stokes and Reynolds solution as function of z. The Reynolds solution for u and w is given by equations (4.9) and (4.10), respectively. The correspondence for the pressure and velocity field with the SLF is clear. For this configuration there are recirculations in the tops of all five waves. This local type of recirculation was already encountered in the SLF and is not predicted by the Reynolds equation.

In figure (4.14a) the pressure as function of x is plotted for different numbers of waves. It can be seen that the solutions overlap in parts of the domain. This is also reflected in figure (4.14b) where the $\bar{R}$ is shown as a function of A_m for different numbers of waves. Because of the correspondence between the different multiple wave solutions it is not needed to study more extensive the multiple local feature. The results for the SLF

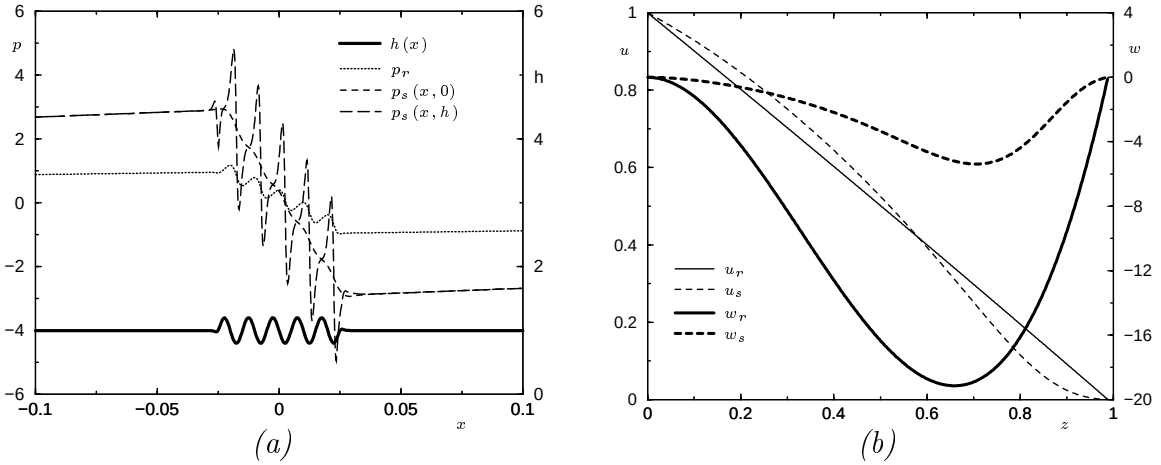

(a) (b)

Figure 4.13: *Results for the MLF for* $\epsilon = 0.01$, $a_3 = 0.05$, $a_4 = 0.01$ *and* $A_m = 0.2$. *(a): Pressure and film thickness as function of* x. *(b):* u *and* w *velocity components at* $x = 0$ *as function of* z.

contains all relevant information for the Stokes flow between two parallel plates of which one contains a sinusoidal feature.

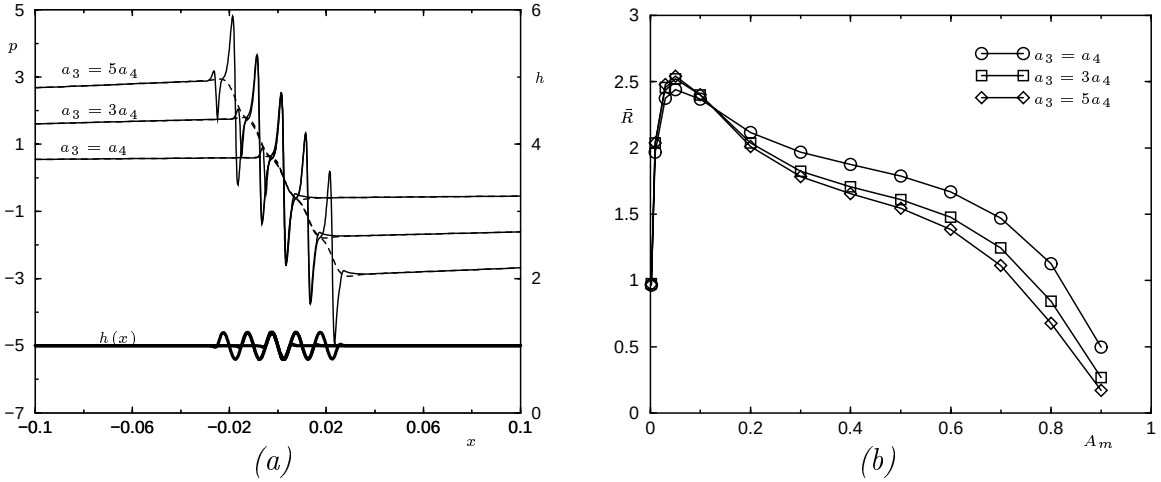

(a) (b)

Figure 4.14: *Results for the MLF. (a): Stokes pressure solution at* $z = h$ *(solid line) and* $z = 0$ *(dotted line) for* $\epsilon = 0.01$, $A_m = 0.2$ *and* $a_4 = 0.01$ *and different* a_3. *(b): The* $\bar{R}$ *values for different* a_3, $\epsilon = 0.01$ *and* $a_4 = 0.01$.

4.4 EHL relevant geometry

The surfaces encountered in hydrodynamic lubrication are normally not flat on a global scale. In tribology the contacting surfaces are approximated by parabola. In this section the contact is modeled by a flat lower surface and a 4^{th}-order parabolic upper surface. The almost horizontal part of the upper surface in the middle of the contact can be seen as the result of the deformation of the upper surface which occurs in EHL contacts.

Again, in order to describe the upper boundary, equations (4.1) and (4.2) have been used, together with the parameters in table (4.1). But now a_1 is variable and $a_2 = 4$. The variables to be varied are: ϵ, a_1, A_m and a_4. The boundary conditions are the same as for the SLF and are shown in figure (4.1).

Firstly, as an illustration, figure (4.15) shows a typical Stokes solution to the problem. Figure (4.15a) shows a pressure field and figure (4.15b) shows the streamlines.

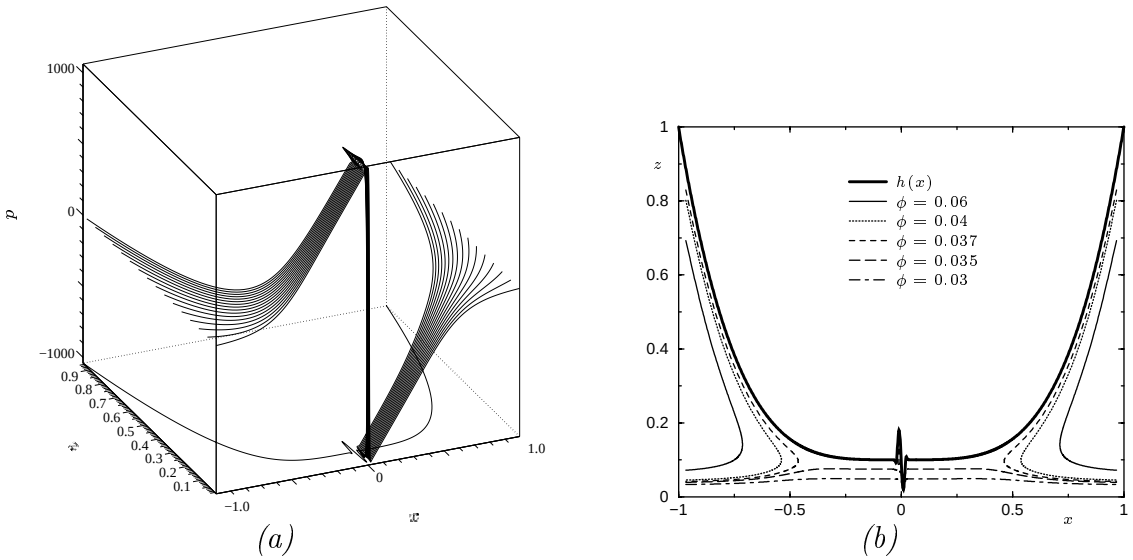

Figure 4.15: *(a): Pressure field and upper boundary $h(x)$. (b): Streamlines. Both as function of x and z for $\epsilon = 0.1$, $a_1 = 0.1$, $a_4 = 0.04$, $A_m = 0.08$.*

The pressure field has the same global form as for the SLF, except that the pressure gradient in the z direction near $x = 0$ is small compared to the global pressure rise in x direction. The stream lines show that at the entrance and at the exit of the contact a recirculation occurs. Also there is a local recirculation in the top of the feature, although this is not visible in figure (4.15b). Figure (4.16a) shows the pressure at the lower and at the upper surface as a function of x. Finally, figure (4.16b) shows the horizontal velocity component u and the vertical velocity component w as a function of z at the x coordinate where $h(x)$ has a local maximum ($x = -0.01$). Figure (4.16a) shows that the Stokes pressure is larger than the Reynolds pressure. This was also found for the SLF. The Stokes pressures at the lower surface and that at the upper surface are the same. Only in the region near the waviness there is a difference. The u velocity field in figure (4.16b) shows that there is a recirculation in the top of the waviness for the Stokes as well as for the Reynolds solution. The w velocity field is nearly zero for both solutions. For the Reynolds solution this is logical, because dh/dx is zero at $x = -0.01$. As has been done for the SLF, the value of $\bar{R}$ has been calculated to quantify the difference between the Stokes and the Reynolds solution. For three situations the $\bar{R}$ value has been calculated. Firstly, for $\epsilon = 0.1$ and $a_1 = 0.1$. Secondly, for $\epsilon = 0.01$ and $a_1 = 0.1$. Finally, for $\epsilon = 0.1$ and $a_1 = 0.01$. The results are shown in figure (4.17). In figures (4.17a), (4.17b) and (4.17c) the $\bar{R}$ is plotted as function of amplitude A_m for different values of the wavelength a_4. It is shown that with decreasing wavelength (a_4) the accuracy of the Reynolds solution decreases, as was already found for the SLF. However, in contrast to the SLF results, the

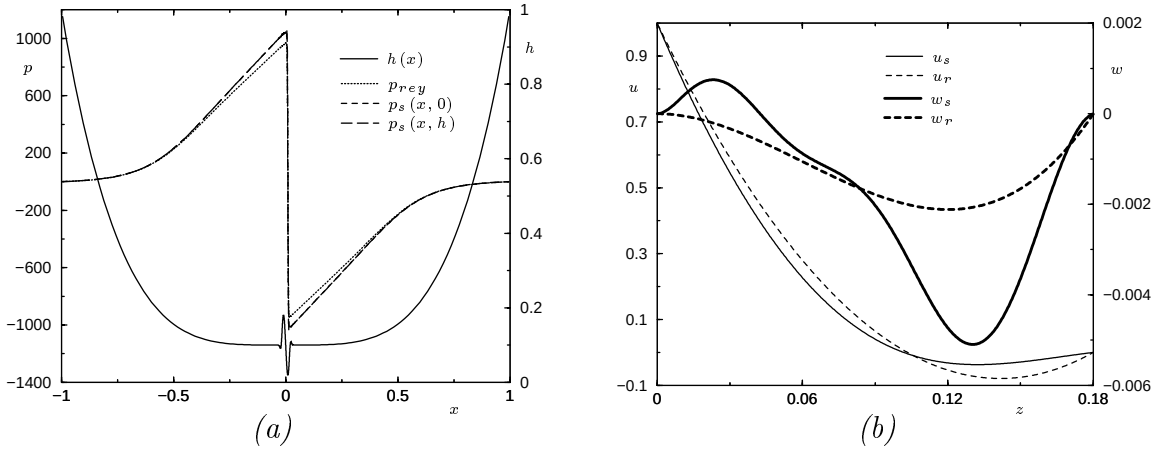

(a) (b)

Figure 4.16: *(a): Pressure as function of x for $z = 0$ and $z = h(x)$. (b): u and w velocity components at $x = 0$. Subscript indicates the Reynolds (r) or the Stokes (s) solution.*

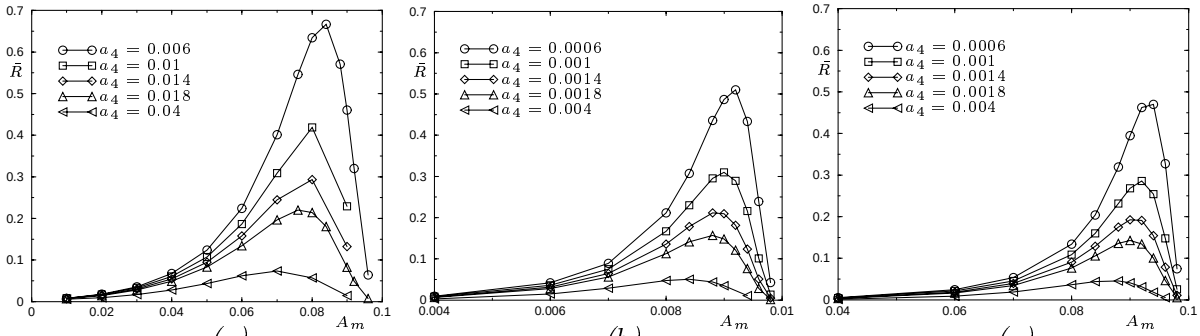

(a) (b) (c)

Figure 4.17: *The $\bar{R}$ value as function of A_m for different a_4. (a): $\epsilon = 0.1$ and $a_1 = 0.1$. (b): $\epsilon = 0.1$ and $a_1 = 0.01$. (c): $\epsilon = 0.01$ and $a_1 = 0.1$.*

amplitude of the feature has a stronger effect. Only for large amplitudes there will be a big difference between the Stokes and Reynolds solution.

Note that for the cases shown in figure (4.17) the wavelengths are chosen such that the factor $\epsilon a_1/a_4$ is the same. It is clear that the figures give more or less the same result. Only the first case, $\epsilon = 0.1$ and $a_1 = 0.01$, is a little bit different because here ϵ is still big and there might be some interaction between the inflow/outflow boundaries and the waviness.

Where does the ratio ϵ/a_4 originate from? It was found in chapter (*2*) that $\frac{dh}{dx}$ and higher derivatives are important and can destroy the effect of a small ϵ in a series expansion. However, the value $\epsilon \left.\frac{dh}{dx}\right|_{x=0} \approx -\frac{2\pi A_m \epsilon}{a_4} \sim \frac{A_m \epsilon}{a_4}$ can not predict if the solutions of the Reynolds equation are valid. Firstly, the parabolic shape in figure (4.17) excludes this parameter because the same $\bar{R}$ value coincides with different $\frac{A_m \epsilon}{a_4}$. Secondly, if only points before the maximum value are considered in figure (4.17), e.g. the points $A_m = 0.008$, $a_4 = 0.0006$, $\bar{R} = 0.2114$ and $A_m = 0.0088$, $a_4 = 0.0014$, $\bar{R} = 0.2115$ with $\frac{A_m}{a_4} = 13.33$ and $\frac{A_m}{a_4} = 6.29$, respectively, it is clear that the same $\bar{R}$ value coincides with different $\frac{A_m}{a_4}$. A better parameter seems to be the maximum value of $\epsilon \left.\frac{dh}{dx}\right|_{max} \approx -\frac{2\pi\epsilon a_1}{a_4} \sim \frac{\epsilon a_1}{a_4}$ by

taking $A_m \to a_1$. In physical parameters it follows that $\frac{\epsilon a_1}{a_4} = \frac{H a_1}{L a_4} = \frac{H_{loc}}{\Lambda}$. So, to have more than ten percent deviation between the Stokes and the Reynolds solution according to $\bar{R}$, $\frac{H_{loc}}{\Lambda} > 0.25$ must hold. The amplitude of the feature is still unbounded. For a single local feature the maximum in $\bar{R}$ is reached for small amplitudes. For EHL relevant geometries an amplitude close to the local film thickness is needed to reach a maximum. The parameter $\frac{H_{loc}}{\Lambda}$ confirms the expectations of [25].

4.4.1 Perturbation EHL relevant geometry

The same perturbation analysis, that was used in section (*4.2.1*) for the SLF, will be used here. In figure (4.18) some results are shown, for the case $\epsilon = 0.1$, $a_1 = 0.1$, $A_m = 0.08$ and two wavelengths $a_4 = 0.04, 0.018$.

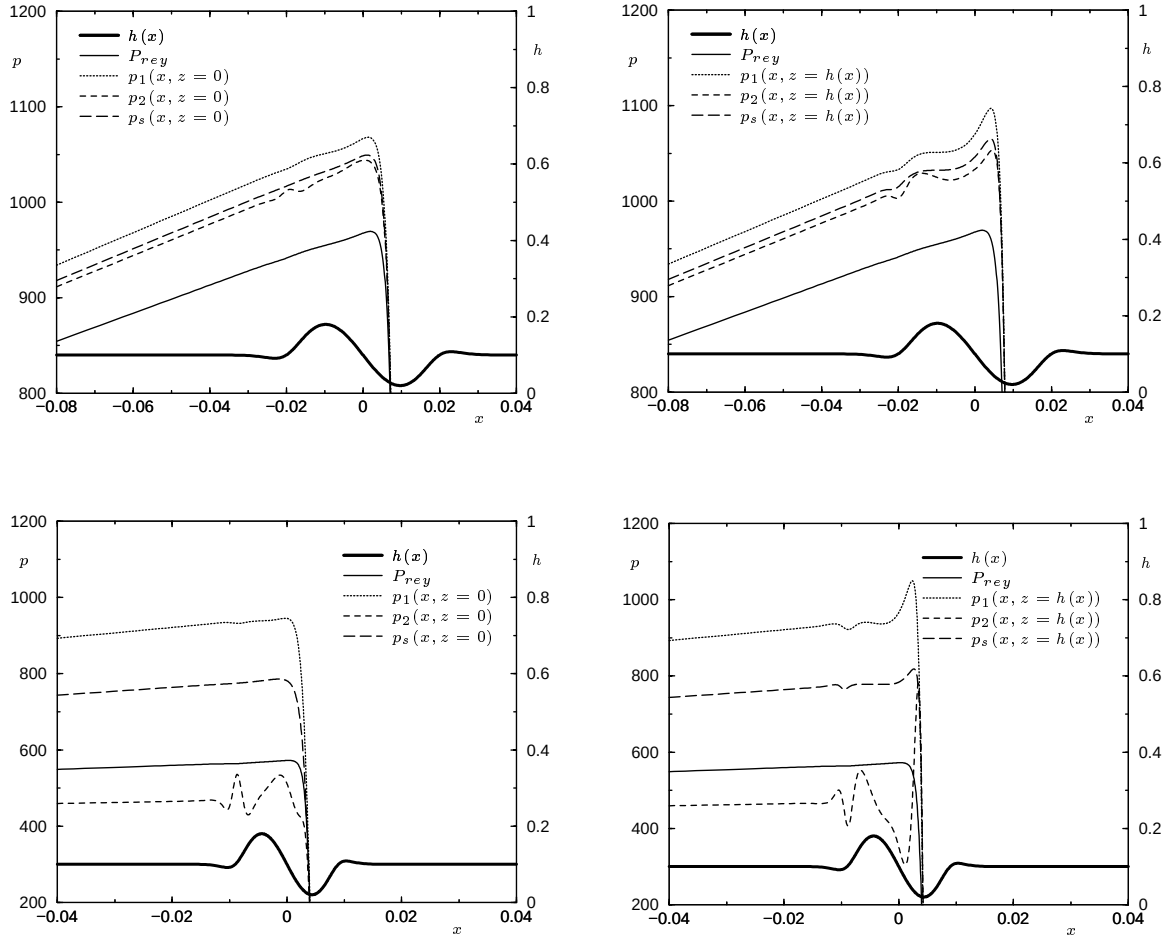

Figure 4.18: *Pressure at the surface $z = 0$ (left) and $z = h(x)$ (right) for the Reynolds solution (p_{rey}), the Stokes solution (p_s) and a first-(p_1) and second-order (p_2) perturbation solution for the case $a_4 = 0.04$ (top) and $a_4 = 0.018$ (bottom) while for both cases $\epsilon = 0.1$, $a_1 = 0.1$ and $A_m = 0.08$.*

The figures show the pressure at the surface $z = 0$ and $z = h(x)$ as obtained from the Reynolds equation, the Stokes solution, and the first-and second-order perturbation

solution. As the global features of the solution have been discussed in detail in the previous section, here only the solution in the region around the feature is shown. First consider the case $a_4 = 0.04$. The first-order perturbation solution is already a great improvement on the Reynolds solution. The second-order perturbation result is an even more accurate approximation to the Stokes solution. Clearly the perturbation in ϵ for this case converges. With decreasing wavelength the accuracy of the perturbed solutions is expected to decrease. This can be seen from the results shown for a smaller wavelength. For $a_4 = 0.018$ the perturbation solution does not converge on a local scale, in the region of the feature, but also not on a global scale. With increasing perturbation order, the series expansion diverges more and more from the Stokes solution and the parameter ϵ is not an adequate perturbation parameter anymore. It is observed that in both cases $(a_4 = 0.04, 0.018)$ the Stokes pressure is higher than the Reynolds pressure as was found for the SLF.

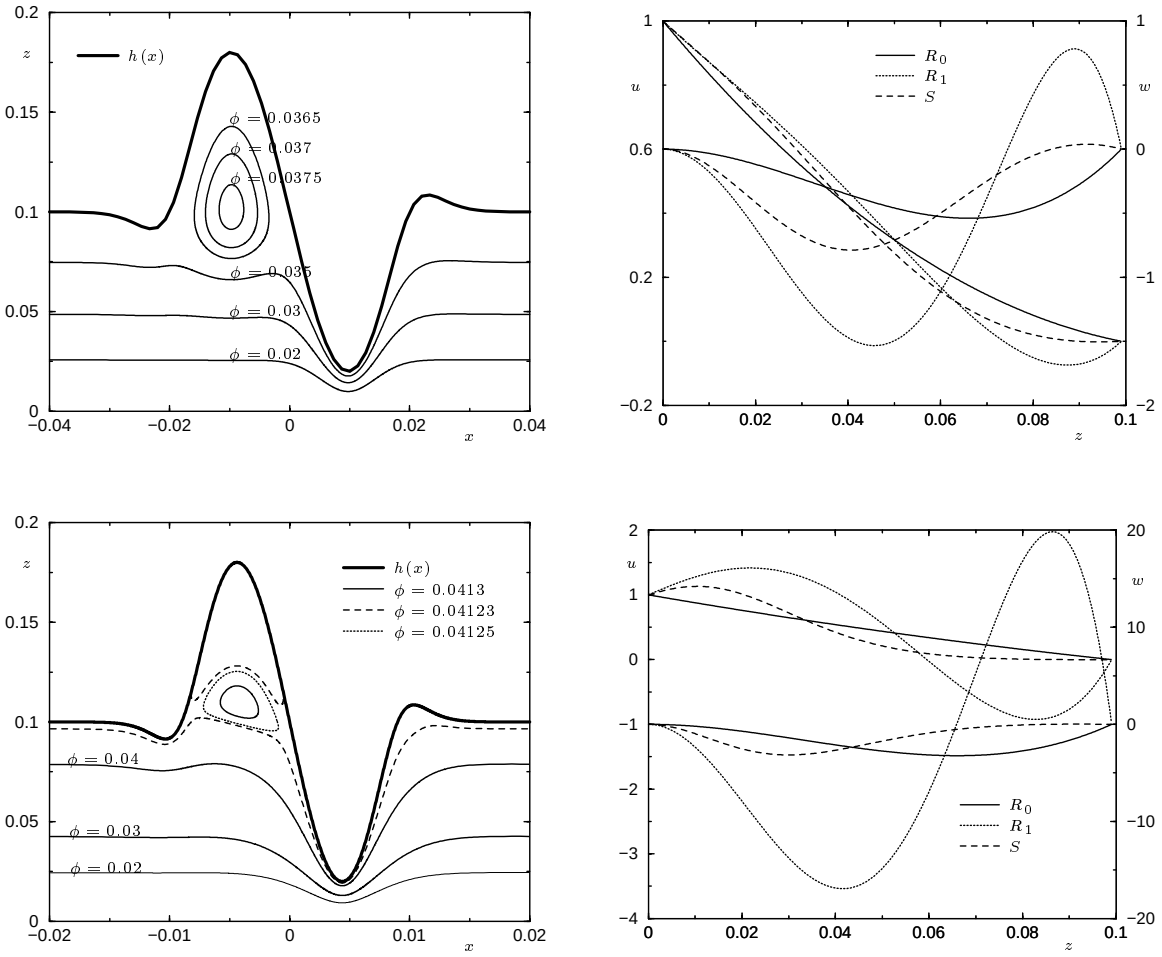

Figure 4.19: *Streamlines of velocity field (left) and velocity $u(z)$ and $w(z)$ at $x = 0$ (right) for the Stokes (S) solution, the Reynolds (R_0) solution and the first order perturbation (R_1) solution for the case $a_4 = 0.04$ (top) and $a_4 = 0.018$ (bottom) and for both cases $\epsilon = 0.1$, $a_1 = 0.1$ and $A_m = 0.08$.*

For the same cases figure (4.19) shows some velocity results. The left figures show the

flow-field according to the Stokes solutions. The figures on the right show the velocities u and w as a function of z at the location $x = 0$. These figures show the velocity components according to the Reynolds solution, the Stokes solution, and a first-order perturbation result. The first-order perturbation results for $a_4 = 0.04$ for the u and w velocity components at $x = 0$ are improvements on the Reynolds solution but too large, as can be seen in figure (4.19). Both solutions predict a recirculation in the top of the wave. The Reynolds solution predicts a smaller recirculation and the first-order perturbation a larger recirculation, compared to the Stokes solution. For $a_4 = 0.018$ the first-order perturbation correction is much too large, compared to the Stokes solution. A visual inspection of the flow field of the first-order perturbation shows that it is not realistic anymore. Besides a large recirculation in the top of the wave, for large ratios $\epsilon a_1/a_4$, in this case for $a_4 \leq 0.018$, another recirculation appears on top of the first one. This secondary recirculation, already reported in the section (*4.1.1*), can neither be predicted by the Reynolds equation nor by a perturbation analysis in ϵ. They are rather small compared to the large recirculation.

That the global pressure correction to the Reynolds solution, given by the perturbation analysis, is correct is also illustrated by the calculation of the $\bar{R}$ values. For $\epsilon = 0.1$, $a_1 = 0.1$ and $a_4 = 0.04$ the $\bar{R}$ values as function of the amplitude have been plotted in figure (4.20). For three solutions $\bar{R}$ is shown in this figure. For: the first-order and second-order perturbation solutions and for the Stokes solution. It can be seen that a higher-order series expansion results in a better prediction of the $\bar{R}$. These kinds of calculations were not repeated for smaller wavelengths because of the lack of convergence. So, in contrast to the SLF where up to 20 percent deviation between the Stokes solution and the Reynolds equation could be predicted by the perturbation analysis, a maximum of roughly 10 percent applies.

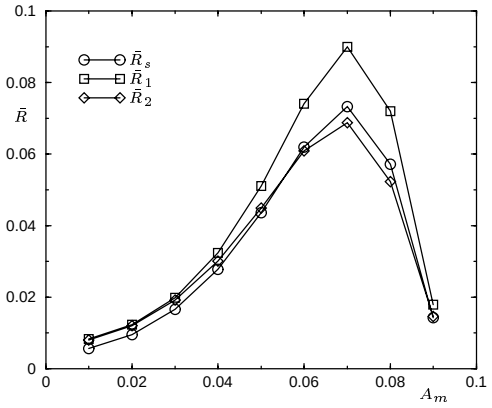

Figure 4.20: *The $\bar{R}$ value when $\epsilon = 0.1$, $a_1 = 0.1$ and $a_4 = 0.04$ in the case of the Stokes($\bar{R}_s$) solution and in the case of first($\bar{R}_1$) and second($\bar{R}_2$) order perturbation analyze.*

4.5 Conclusion

With respect to the Stokes model, used to describe the flow in a narrow contact geometry the following conclusions can be drawn.

- For a single sinusoidal feature in a nominally uniform film the ratio H/Λ determines the difference between the Stokes and the Reynolds solution. If this ratio is $O(1)$, differences greater than ten percent, e.g. in the predicted effect on the lift force, can be expected.
- The results from the single wave also hold for the multiple wave situation.
- For moderate wavelengths of the local feature the developed perturbation theory can predict the Stokes solution very well.
- In the case of a more realistic contact surface, a paraboloid with a single local feature superimposed on it, the ratio H_{loc}/Λ determines the difference between the Stokes and the Reynolds solution, where, H_{loc} is the film-thickness at the location of the feature. If this ratio is $O(1)$ and the amplitude of the feature is close to the film-thickness (H_{loc}), differences greater than ten percent occur. Also here, for moderate wavelength and amplitude of the local feature the developed perturbation theory can predict the Stokes solution very well.

Chapter 5

Compressibility and piezo-viscous effects

In the previous chapter the differences between the solution of the Stokes equations and that of the Reynolds equation were studied as a function of the ratio $\epsilon = H/L$ and characteristics of the surface geometry such as wavelength and amplitude.

The limitation to the validity of the Reynolds equation related to the contact geometry is well known and quantifying it was the main objective of the work, presented in Chapter (*4*). To really isolate the effects of geometry, the lubricant was assumed to be incompressible and iso-viscous. Also "cavitation" was ignored and the load carrying capacity was computed using a Sommerfeld assumption. In this chapter the effects of compressibility, cavitation and piezo-viscosity are studied.

Compressibility and cavitation are related, see chapter (*2*). It was shown that the limitation of the pressure to the vapor pressure could be implemented via a specific density pressure relation. Some results obtained with this algorithm are presented here.

However, compressibility is also important for another reason. Much less known than the geometric limitation to the validity of the Reynolds equation is its limited validity in relation to pressure-dependent density and viscosity. These effects are of particular importance for the fields of gas lubrication and EHL.

5.1 Compressibility: Gas lubrication

Shortly after the discovery of the mechanism of hydrodynamic lubrication by Reynolds the possibility to use gas, or, more precisely, air, as a lubricant was explored [52]. One obvious advantage of air lubrication is that it is nearly always available. Alternatively, in the case of compressors or equipment working with gases one might well use the processed gas itself for lubrication. Some other potential advantages of lubrication with gas are the extremely low friction that can be achieved due to the low viscosity and the corresponding very low frictional heating. However, these advantages did not outweigh the disadvantages:

- Most gases have no boundary lubrication properties. Thus, when the surfaces touch during start up, running out or, incidentally, e.g. due to vibrations, damage of the

surface may occur very easily leading to complete failure. Protection against these situations requires a "back-up" lubrication mechanism.

- The load capacity that can be generated by aerodynamic lubrication alone is often not sufficient for practical situations. Aero-static "help" with externally supplied pressure can partly solve this problem.

As a result, gas lubrication remained a small field for a long time. Only after the second World War the first real practical applications were developed. Relevant references are [21], [29] and [17].

The past decade has seen a renewed interest in gas lubrication. In particular, applications in the computer industry have stimulated this interest, e.g. hard disk sliders and the head-tape interface. Many publications have appeared in which the lubrication of these problems in relation with geometry (of the slider) have been studied numerically. In all these cases the Reynolds equation is used to describe the flow. In some cases it is corrected for special effects occurring in very thin films (Knudsen effect) but the validity of the equation itself has rarely been questioned. This forms the topic of the present section.

As a model problem the flow below a step geometry is taken. The problem is illustrated in figure (5.1). This problem can be seen as a section taken from a "grooved" bearing. The lower surface moves with a certain velocity and of particular interest is the generated load bearing capacity in relation to this speed and the step geometry. The gas is assumed to obey the ideal gas law, see equation (2.67). The fluid motion can be described by the Reynolds equation (2.68) or by the Stokes equations in the form (2.8), (2.9) and (2.10). In both cases the factor of proportionality between the density and the pressure can be divided out of the fluid motion equations. The dimensionless viscosity is held fixed to unity. The geometry of the "step" is defined by:

$$h(x) = 1 - \frac{a_1}{(1 + e^{-a_2(a_3 - x)})(1 + e^{-a_2(a_3 + x)})} \ . \tag{5.1}$$

For the Stokes solution the grid is generated by:

$$z = \xi^2 h(x(\xi^1)) \ , \ \ (\xi^1, \xi^2) \in ([0,1],[0,1]) \ , \tag{5.2}$$

where $x(\xi^1)$ is defined by equation (3.68). The boundary conditions are also given in figure (5.1). The parameter of interest is the lift force. For the Stokes case this force has two components, see section (*2.4*). Substitution of $\eta = 1$ (iso-viscous) and $\left.\frac{\partial u}{\partial x}\right|_{z=0} = 0$ in equation (2.79) gives

$$F_p = \int_{-1}^{1} p(x, z=0)\, dx \ \text{ and } F_w = -\frac{4}{3}\epsilon \int_{-1}^{1} \left.\frac{\partial w}{\partial z}\right|_{z=0} dx \ . \tag{5.3}$$

In this study $\epsilon (= 0.005)$, $a_1 (= 0.5)$ and $a_3 (= 0.05)$ will be fixed as we have already studied the geometrical limitations of the validity of the Reynolds equation. Here we wish to focus on the compressibility aspects only. The relevant input parameters are ϵ, the surface velocity u_1 and a_2. The parameter a_2 is proportional to the slope of the step

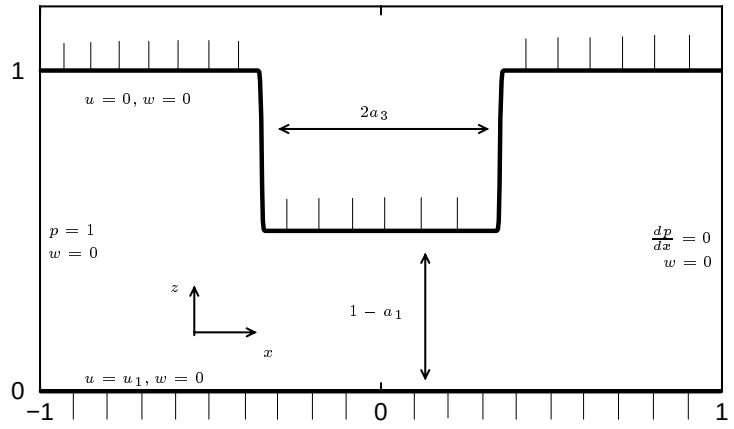

Figure 5.1: *Geometry and boundary conditions for Single Local Feature in the case of gas lubrication.*

because $\left.\frac{dh}{dx}\right|_{x=a_3} \approx \frac{a_1 a_2}{4}$ if $a_2 a_3 \gg 1$. The solutions will be compared with the solutions of the Reynolds equation. For this case the Reynolds equation is given by:

$$\frac{d}{dx}\left[-ph^3\frac{dp}{dx} + \frac{6u_1}{\epsilon}ph\right] = 0 \tag{5.4}$$

and the predicted lift force by:

$$F_{rey} = \int_{-1}^{1} p(x)dx \tag{5.5}$$

From equation (5.4) it can be seen that the Reynolds solution is determined by the parameter u_1/ϵ. This is the equivalent of the usual bearing number $\Lambda_n = \frac{6u_1}{\epsilon}$ in terms of the non-dimensional variables used here.

In the introduction it was mentioned that gas bearings generally have a limited maximum load capacity. For the present problem the Reynolds solution has a high-speed limit that can be calculated from equation (5.4). Integrating with respect to x and taking the limit $\frac{\epsilon}{u_1} \to 0$ gives:

$$6ph = c_1 \ , \tag{5.6}$$

where the integration constant c_1 follows from the pressure boundary condition $6p(x = -1)h(x = -1) = 6 = c_1$. In the high-speed limit the lift force can be calculated according to:

$$F^{\infty}_{rey} = \int_{-1}^{1} \frac{1}{h}dx \ . \tag{5.7}$$

So, for a given geometry this limit can be computed easily. If $a_3 \to \infty$, representing exactly a step, the integral can be evaluated: $F^{\infty}_{rey} = 2.1$. The shape of the pressure profile is given by $p = 1/h$.

Figures (5.2) and (5.3) show a typical solution to the problem for $a_2 = 1343$ and $u_1 = 0.05$. Figure (5.2) also shows the pressure profile and the streamlines of the Stokes solution. The streamline picture shows a small recirculation zone in front of the step. This recirculation is also present in the Reynolds solution. In figure (5.3a) the velocity as function of z is shown for $x = -0.1$. The Reynolds and the Stokes solution are more or less

the same. Also shown in figure (5.3) is the pressure as a function of x at the surface $z = 0$ and $z = h$ and also the Reynolds solution. For this case the two solutions obviously differ very little. The solution shows everything that were to be expected: a "block-shaped" pressure distribution along the restriction with a "boundary layer" in front and after the restriction in which it builds up and drops down to unity, respectively. Based on the Reynolds solution one would now expect the width of this boundary layer to decrease with increasing speed.

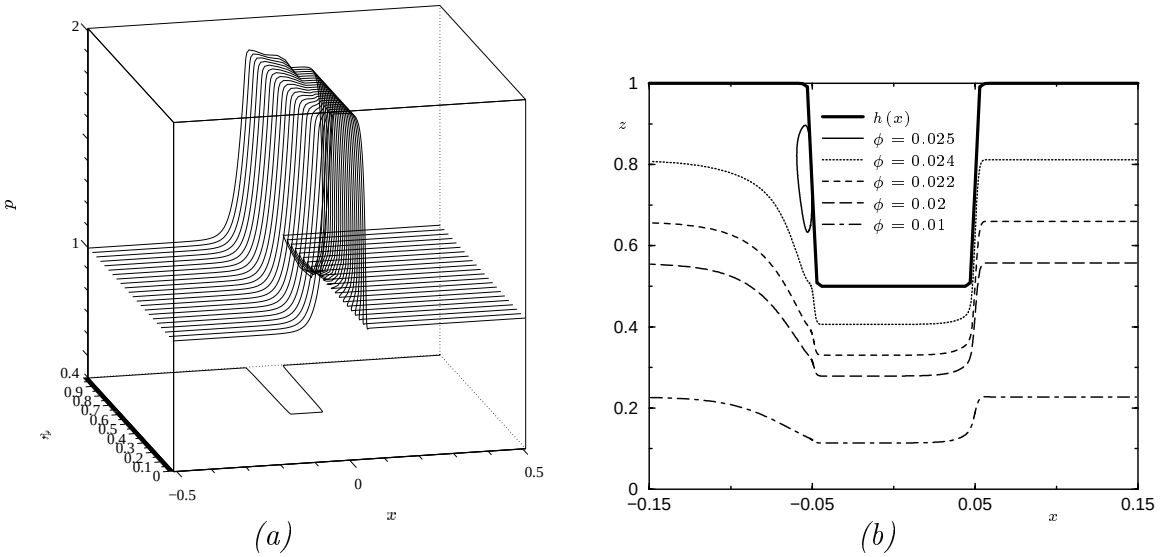

(a) *(b)*

Figure 5.2: *Stokes solution. (a): Pressure field. (b): Streamlines. Both as function of x and z for $\epsilon = 0.005$, $u_1 = 0.05$ and $a_2 = 1343$.*

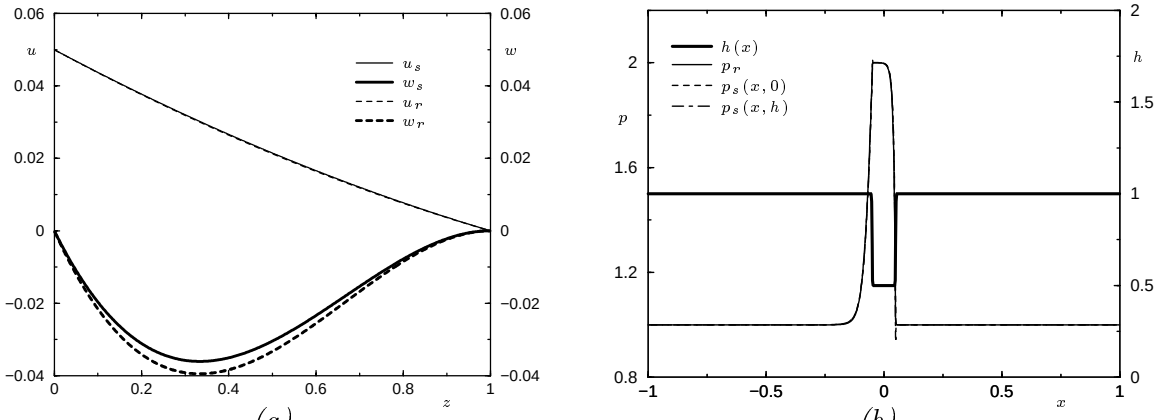

(a) *(b)*

Figure 5.3: *(a): u and w velocity components at $x = -0.1$. (b): Pressure as function of x for $z = 0$ and $z = h(x)$. Subscript indicates if it is a Reynolds (r) or a Stokes (s) solution. $\epsilon = 0.005$, $u_1 = 0.05$ and $a_2 = 1343$.*

Figure (5.4) shows the computed pressure profiles at $z = 0$ and $z = h$ as a function of u_1 for the Reynolds and the Stokes solution to the problem. Clearly the Reynolds solution exhibits the aforementioned behavior, however, the Stokes solution does not. At

first, with increasing u_1 the block shape indeed appears, and the pressure profiles at $z = 0$ and $z = h$ differ little. However, with increasing u_1 the pressure profile moves away from the block shape and at the same time the profile at $z = 0$ and that at $z = h$ starts to differ. For $z = 0$ the high pressure at the restriction, followed by a low pressure in its wake, is replaced by a gradual increase along the restriction and a gradual decrease in its wake. At the surface $z = h$ the pressure profile tends to exhibit a narrow peak at the leading edge of the restriction and also here along the restriction it is not constant but shows a gradual decrease. In the wake of the restriction ($x > 0.05$) a zone of very low pressure is formed (nearly vacuum). The length of this zone increases with increasing u_1.

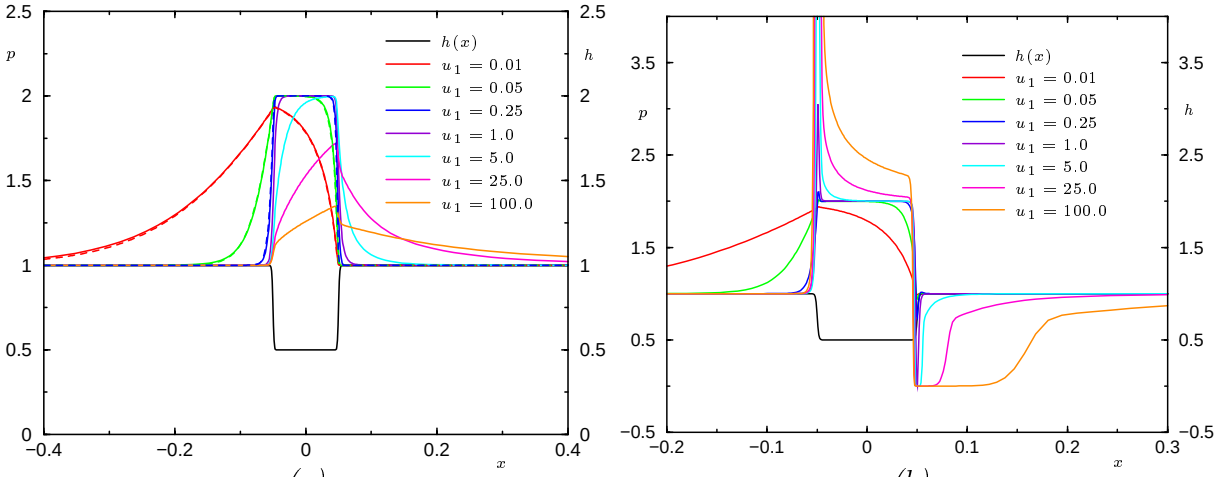

Figure 5.4: *Pressure as function of x for $\epsilon = 0.005$, $a_2 = 1343$ and different u_1 for the Stokes (drawn lines) and Reynolds (dashed lines) solutions to the gas bearing problem. (a): Pressure at $z = 0$. (b): Pressure at $z = h$.*

Table (5.1) shows the computed load capacity of the configuration as a function of u_1 for the Stokes and Reynolds solution. The computed lift forces for the two solutions differ little and, quite remarkably, in spite of the fact that the Stokes solution to the pressure does not seem to have a high-speed limit, the lift force does. Moreover, its limiting value is the same as the one predicted by the Reynolds model.

The effect of the slope of the side wall of the step is the next topic of investigation. This slope is determined by a_2. The angle between the side of the step and a horizontal line in the physical world is determined by:

$$\tan(\alpha) = \epsilon \left.\frac{dh}{dx}\right|_{x=a_3} \approx \frac{\epsilon a_1 a_2}{4} \ , \tag{5.8}$$

for $a_2 a_3 \gg 1$. Three situations have been calculated: $a_2 = 582$ ($\alpha = 20^o$), $a_2 = 1343$ ($\alpha = 40^o$) and $a_2 = 2771$ ($\alpha = 60^o$). The results for the pressure profiles for $u_1 = 25.0$ are shown in figure (5.5). The pressure on the lower surface is not much affected by a change in a_2. The width of the pressure peak on the upper surface in front of the step decreases with increasing a_2 and the length of the almost vacuum region behind the step also decreases

		Stokes			*Reynolds*
u_1	Λ_n	F_p	F_w	$F_p + F_w$	F_{rey}
0.01	12.0	2.1947	0	2.1947	2.1802
0.05	60.0	2.1245	0	2.1245	2.1157
0.25	300.0	2.1101	0	2.1101	2.1015
1.0	1200.0	2.1084	0	2.1084	2.0994
5.0	6000.0	2.1081	0.0003	2.1084	2.0991
25.0	30000.0	2.1072	0.0010	2.1082	2.0990
100.0	120000.0	2.0892	0.0102	2.0994	2.0990

Table 5.1: *Computed lift force (load capacity) for gas lubrication problem for Reynolds solution (F_{rey}) Stokes solution (F_p, F_w) as a function of the bearing number Λ_n. The Reynolds limit for infinite Λ_n is $F_{rey}^{\infty} = 2.1$.*

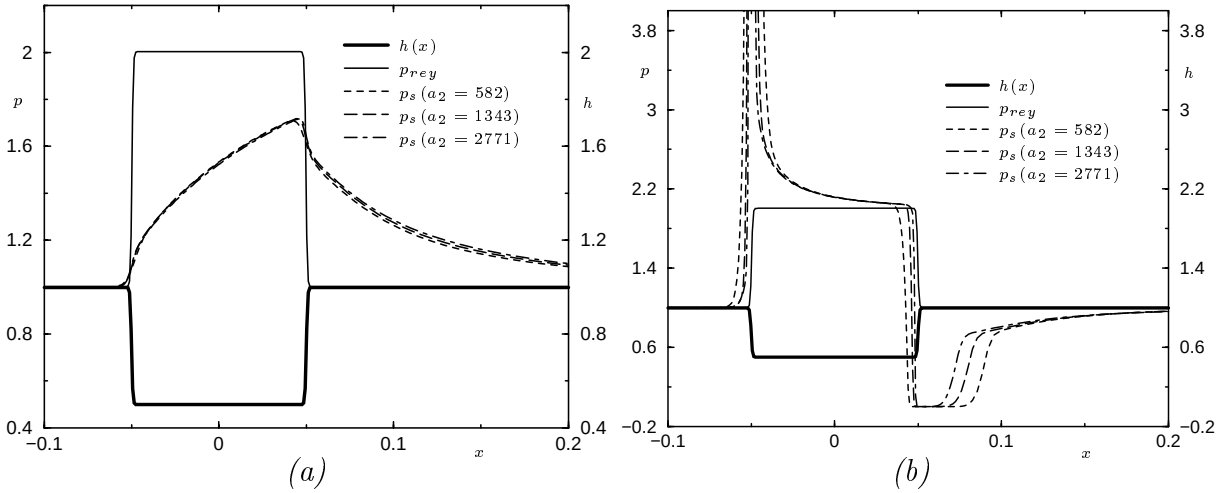

Figure 5.5: *Pressure as function of x for $\epsilon = 0.005$, $u_1 = 25.0$ and different a_2 for the Stokes (p_s) and Reynolds (p_{rey}) solutions to the gas bearing problem. (a): Pressure at $z = 0$. (b): Pressure at $z = h$.*

with increasing a_2. The height of the pressure peak on the upper surface in front of the step increases with increasing a_2.

So, if one fixes the lower surface speed and steepens the side walls, the pressure along the upper surface will resemble the high speed limit $p = \frac{1}{h}$ with a pressure peak before the step and a pressure dip behind the step. The lower surface pressure will be hardly affected by a change in a_2 but it is totally different from the high-speed limit for the Reynolds pressure.

Finally, table (5.2) gives the computed lift force according to the Stokes and Reynolds solution for different a_2 and $u_1 = 0.01$ and $u_1 = 25.0$, respectively. The table shows that, again, the lift capacity computed, with the Stokes solver, differs little from the value predicted by application of the Reynolds equation.

		Stokes			*Reynolds*
Λ_n	a_2	F_p	F_w	$F_p + F_w$	F_{rey}
12.0	582	2.1894	0	2.1894	2.1755
12.0	1343	2.1947	0	2.1947	2.1802
12.0	2771	2.1970	0	2.1970	2.1825
30000.0	582	2.1046	0.0005	2.1051	2.0976
30000.0	1343	2.1072	0.0010	2.1082	2.0990
30000.0	2771	2.1090	0.0013	2.1103	2.0996

Table 5.2: *Computed lift force (load capacity) for gas lubrication problem for Reynolds solution (F_{rey}) Stokes solution (F_p, F_w) as a function of the step parameter a_2. The Reynolds limit for infinite Λ_n is $F_{rey}^{\infty} = 2.1$.*

In summary, comparison of the Reynolds and Stokes solutions for the gas lubricated step geometry has shown that:

- On the lower surface the pressure as a function of x differs from the Reynolds solution for large u_1, nevertheless the same lift force is created.
- The steepness of the step influences the extend of the region where a pressure peak/dip occurs. This peak/dip is not predicted by the Reynolds equation.

So it is concluded that in order to predict the lift force one can generally use the Reynolds equation, but the predicted pressure profiles should be handled with care.

Λ_n	$1/\rho_{MG}$
12	19.5
60	28.0
300	52.6
1200	63.5
6000	84.6
30000	120.0
120000	256.0

Table 5.3: *Average error reduction factor per V(2,2) cycle of the Stokes solver as a function of Λ_n for $\epsilon = 0.005$ and $a_2 = 1343$.*

To conclude this section, some details are given regarding the numerical performance of the algorithm for the solution of the Stokes equations. The above solutions were all obtained using a FMG algorithm with 5 V(2,2) cycles per level. The finest grid contained 256×256 cells. The discretization of the continuity equation was done with the first order upstream scheme presented in section (*3.4.1*). In the line relaxation process the line search algorithm was not needed. The numerical solver exhibited excellent performance. In fact, with increasing u_1 the performance even improved. This is illustrated in table (5.1). This table gives the average error reduction per cycle defined as: $\rho_{MG} = \left[\frac{r^p(N_c=5)}{r^p(N_c=1)}\right]^{\frac{1}{4}}$.

For large u_1 the MG cycle tends to be an exact solver. This is due to the strong downstream dependence in the problem and the use of an upstream discretization.

As a first-order discretization was used, it is important to check whether observed tendencies in the solution are perhaps a result of artificial "viscosity". This applies in particular to the solutions for high u_1. Therefore convergence of the solution with decreasing mesh size was checked. Some results are shown in figure (5.6). This figure shows the pressure as a function of x at $z = 0$ of the Stokes solution for grids with $64, 128, 256, 512$ cells. Also shown is a plot of the contour lines of the pressure. The figure shows that with decreasing mesh size the solution converges, although this process for the pressure contours is quite slow, as could be expected from the use of a first order scheme. However, clearly the computed pressure profile is accurate and as a result the differences between the Stokes solution and the Reynolds solution, observed for high u_1, are not due to artefacts resulting from the discretization.

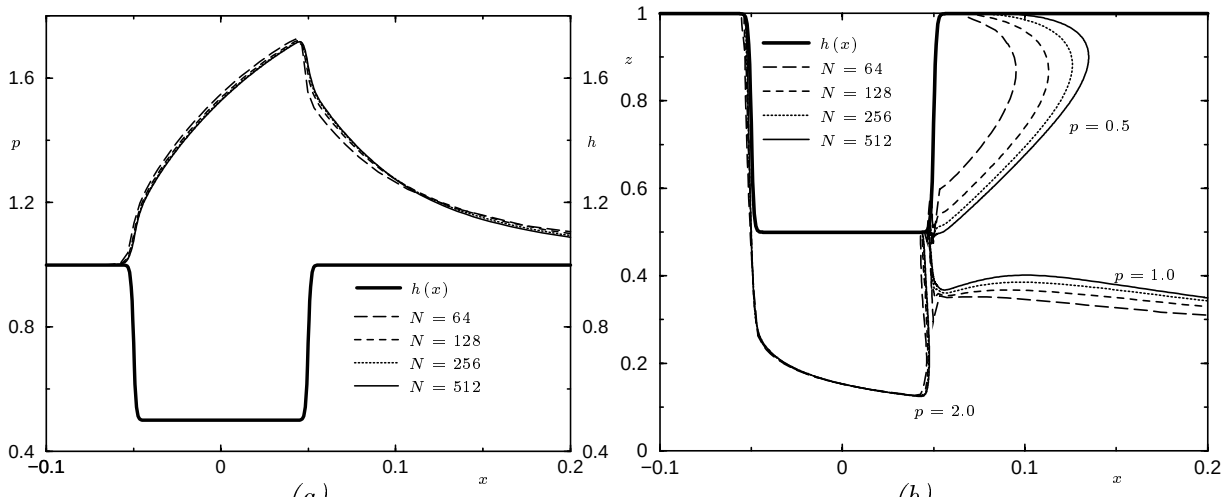

Figure 5.6: *(a): Pressure as a function of x at $z = 0$ for the Stokes solution on different grids. (b): Also shown the contour plot of the pressure for the Stokes solution on different grids.* $\epsilon = 0.005$, $u_1 = 25.0$ *and* $a_2 = 1343$.

5.2 Compressibility: Cavitation

If the lubricant is a liquid and the pressure drops below the vapor pressure it will cavitate. For most lubricated contacts this phenomenon will occur in regions where the gap widens, most notably in the exit region of the contact.

To account for this behavior in simulations, an extension of the Stokes model or the Reynolds model is needed. In their standard form both models allow an unlimited pressure drop, and if $p = 0$ at the boundaries they will predict significant negative pressures in widening regions. In these cases the computed lift force will be wrong. For example, the computed pressure profile below a parabolic surface with $p = 0$ at the boundaries will be anti-symmetric and thus have zero predicted net lift force. However, in reality the negative pressures will be limited to the vapor pressure. As the difference between the

vapor pressure and the atmospheric pressure is small compared to the pressure generated in the gap, it is justified to take both to be zero and compute the lift force using only the positive part of the pressure field. This "Sommerfeld" approach was used to obtain the results presented in chapter (*4*) as can be seen from the definition of the lift force difference $\bar{R}$.

However, the most accurate way is to extend the model such that pressures lower than the vapor pressure will not occur. For models based on the Reynolds equation this is commonly done by imposing the separate condition $p > p_v$ (in practice $p > 0$) and then solve a complementarity problem. For the Stokes equations this approach is not suited because, if in the region where $p \leq p_v$ the Stokes equations are replaced by for example $p = p_v$ and $u = 0$, $w = 0$, the continuity equation does not hold on the cavitation boundary. In section (*2.3.3*) a two-phase model was proposed, to overcome this problem.

It was shown that this two-phase model could be used in both the Reynolds and the Stokes model. In chapter (*2*) it has already been validated that when implemented in a Reynolds model this approach gives similar results to those obtained with the usual complementarity approach. In this section results obtained with the Stokes model will be presented.

Firstly, to show some typical behavior of the cavitation model, the problem of the flow below a parabolic surface is studied (rigid, iso-viscous limit of EHL). Secondly, the flow in a uniform film with a single local feature is revisited. For this problem the differences between the Reynolds and Stokes solution were investigated in detail using the quantity $\bar{R}$. The objective here is to verify that $\bar{R}$, computed using Stokes solutions obtained with the cavitation model, behaves in the same way as Stokes solutions obtained without the cavitation model.

5.2.1 Parabolic gap

Equations (2.8), (2.9) and (2.10) or in the transformed form (2.28), (2.29) and (2.30) are used to describe the flow underneath a parabola. The geometry of the parabola is defined by equation (4.1) where $a_1 = 0.2$, $a_2 = 2$ and $A_m = 0$. The viscosity is assumed to be constant. The density is assumed to depend on the pressure according to (2.71). The coordinate transformation from the physical domain to the computational domain is given by equation (5.2) where $x(\xi^1) = 2\xi^1 - 1$. So, to generate the grid, there is no refinement in the x-direction. The boundary conditions are $p = 0, w = 0$ at the inlet and at the outlet. The problem was solved using an FMG algorithm with 5 W(2,2) cycles per grid level. The solutions presented were obtained using 6 levels with a coarsest grid consisting of 8×8 cells. Some details regarding performance and convergence of the solver for this problem will be given at the end of this section.

With respect to the solution itself the effect of the parameter β_ρ of the cavitation model will be investigated. As a reminder: β_ρ represents the slope in the density-pressure relation around the vapor pressure point. A larger β_ρ implies a steeper slope and will affect the solution in and near the cavitation region. Results will be presented for $0.1 \leq \beta_\rho \leq 400$. In figures (5.7), (5.8) and (5.9) a typical solution is shown for $\epsilon = 0.01$, $p_v = -300.0$ and $\beta_\rho = 0.1$. Figure (5.7) shows the pressure and density profile as a function of x and z. It is observed that the density suddenly increases to unity at $x \approx 0.6$. Such a rapid change

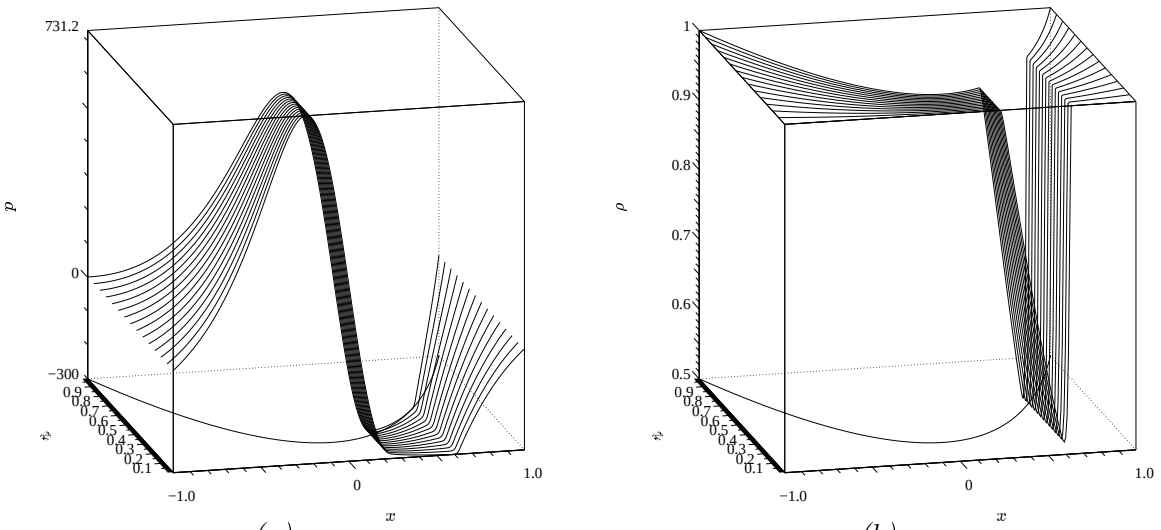

(a) *(b)*

Figure 5.7: *(a): Pressure profile. (b): Density profile. Both as function of x and z for $\epsilon = 0.01$, $\beta_\rho = 0.1$, $p_v = -300.0$.*

is also observed in the streamline picture (5.8a). The u- and w-velocity profiles for the Stokes and the Reynolds solution as function of z at $x = 0.5$ are almost exactly the same.

Figure (5.9a) shows for the same case the pressure at $z = 0$ computed using the Reynolds model and the Stokes model, respectively. If cavitation had not been accounted for, the solution would have been anti-symmetric. Clearly now the pressure minimum is limited to the vapor pressure. Note that the width of the cavitated region will depend on the value of the vapor pressure. For this case where p_v is taken significantly lower than the boundary pressure one observes a pressure drop reaching the vapor pressure at about $x = 0.2$ and a return to the liquid pressure at about $x = 0.6$. For the value $\epsilon = 0.01$ taken here, the Reynolds and Stokes solutions differ very little. Therefore only the pressure at the lower surface is shown. Figure (5.9b) also shows an enlargement of the pressure profile in the cavitated region together with the density. This figure once again shows very little difference between the Reynolds and Stokes results, which implies that the pressure and, thus, the density will vary little as a function of z.

Figure (5.10) and (5.11) show the contour plots of the density using $\beta_\rho = 0.1, 50, 100$ and 400, respectively. Comparing the results for $\beta_\rho = 50, 100$ and 400 with the result for $\beta_\rho = 0.1$ shows that the width of the cavitated region is not changed. However, the iso-contour of the density in this region are no longer straight lines. This implies that p varies as a function of z and that in this region the Reynolds and the Stokes solutions differ. In particular, with increasing β_ρ a region of very low density develops close to the upper surface. As in this region the density equals the vapor density, this can be interpreted as a "bubble". The development of such a fully vaporized region or "bubble" for increasing β_ρ is also illustrated in figure (5.12) where ρ is plotted as a function of z at $x = 0.5$ for different β_ρ. Note that as a function of z the transition from the fully-vaporized region to the region with $\rho > 0.01$ at $x = 0.5$ is gradual. Furthermore, it can be seen in figure (5.12) that for increasing β_ρ the density near $z = 0$ approaches unity. It is mentioned that, physically, one would also expect this to happen near the lower surface as for the

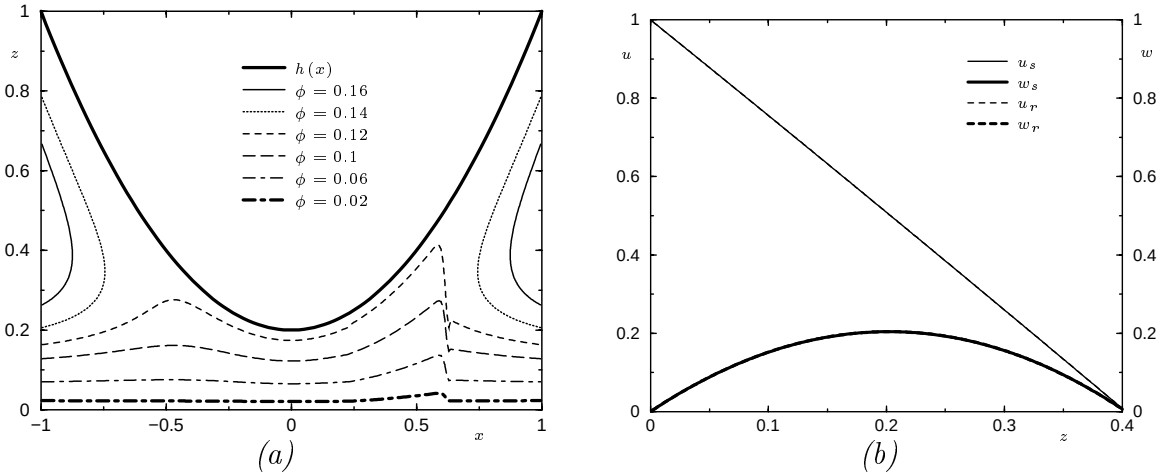

(a) (b)

Figure 5.8: *(a): Streamlines as function of x and z. (b): u and w velocity components at $x = 0.5$. Subscript indicates if it is a Reynolds (r) or a Stokes (s) solution.* $\epsilon = 0.01$, $\beta_\rho = 0.1$, $p_v = -300.0$

present case the lower surface supplies the lubricant.

An interesting question is if this formation of a fully-vaporized region is related to the pressure solution by some parameter. One can calculate the difference $\Delta\tilde{p} = p(x, z = h(x)) - p(x, z = 0)$, at the point where p reaches a minimum in the non-cavitating case. It was found that if $\Delta\tilde{p} > \frac{\pi}{2\beta_\rho}$ and the minimum pressure in the non-cavitating case is lower than p_v, a fully-vaporized region occurs.

For the solutions shown in figures (5.10) and (5.11), even though the solution inside the cavitated region changes, the boundaries of this region remain straight. This can be ascribed to the small value of ϵ. For a larger value of ϵ these lines will no longer be straight. This is illustrated in figure (5.13a) which shows a result obtained for $\epsilon = 0.5$, $p_v = -8.0$ and $\beta_\rho = 10.0$. In figure (5.13b) it is shown that the density approaches unity on the lower surface but now for $\beta_\rho = 10.0$.

How do the values for β_ρ used here relate to physically relevant values? For a mineral oil at standard conditions flowing through a hydrodynamically lubricated contact the following values can be estimated:

$$\begin{aligned} \eta_o &= 100.0 \cdot 10^{-3} \text{ [kg/ms]} \\ \rho_l &= 1000.0 \text{ [kg/m}^3\text{]} \\ \rho_v &= 1.0 \text{ [kg/}m^3\text{]} \\ a_v &= 500.0 \text{ [m/s]} \\ H &= 0.1 \cdot 10^{-6} \text{ [m]} \\ u_0 &= 1.0 \text{ [m/s]} \end{aligned} \tag{5.9}$$

With these values the value of β_ρ in equation (2.72) can be calculated: β_ρ=2.0. So, the z-dependency in the density for the problem discussed here, occurs in reality, if H is much smaller and/or u_0 is much larger.

Summarizing it is concluded that the cavitation model yields the desired "physical" behavior from the viewpoint of lift force computations, i.e. it provides a lower limit to the pressure. The width of the cavitation region will be determined by the magnitude of

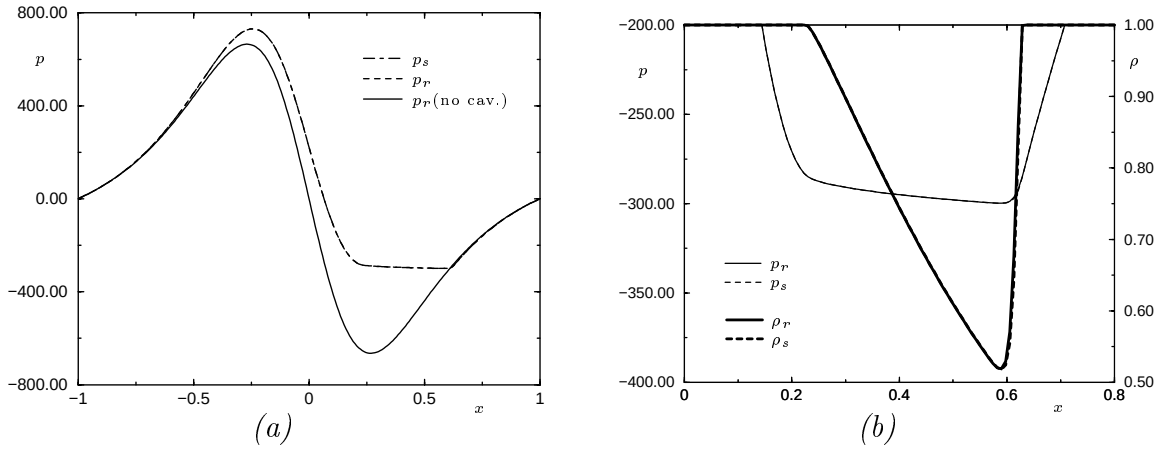

Figure 5.9: *(a): The pressure at $z = 0$ as function of x for the Reynolds solution without cavitation, the Reynolds solution with cavitation and the Stokes solution with cavitation. (b): Zoom in of the pressure and density at $z = 0$ as function of x for the Reynolds and the Stokes solution with cavitation in the cavitation region, $\epsilon = 0.01$, $p_v = -300.0$ and $\beta_\rho = 0.1$.*

the vapor pressure itself. The solution inside this region will depend on the parameter β_ρ. For large β_ρ in this region a z-dependent pressure and density is found showing once again that the density-pressure relation induces differences between Stokes and Reynolds solutions in thin films.

To conclude this section some details about the performance of the numerical algorithm will be given. For the gas-lubricated contact convergence was excellent. However, for the cavitation problem it strongly depends on the value of β_ρ. For a large β_ρ sharp changes in the pressure occur in a small region. In such cases the modified Newton step, as described in section (*3.4.2*), does not find a root for the system of equations at one line. In that case the set of equations at the previous line is solved again, followed by the set of equations at the "bad" line. This procedure is repeated until the "bad" line is solved. The lines where this difficulty occurs are the ones near the point where the fluid starts to cavitate and the point where the mixture returns to a liquid. At the first point dp/dx changes very rapidly. At the second point there is a jump in dp/dx, see figure (2.6). These phenomena also have a strong effect on the MG performance. This is illustrated in table (5.4) where the average error reduction over 5 cycles is shown as a function of β_ρ.

β_ρ	0.1	1.0	10.0	50.0	100.0	200.0	400.0
ρ_{MG}	10.3	8.8	3.5	3.2	3.2	9.4	2.1

Table 5.4: *Average error reduction factor per W(2,2) cycle of the Stokes solver as a function of β_ρ for $N = 256$, $\epsilon = 0.01$ and $p_v = -300.0$*

To improve convergence for large β_ρ, special measures need to be taken in the MG algorithm concerning interpolation of correction and computation of the coarse grid operator. Such modifications should be the subject of further research.

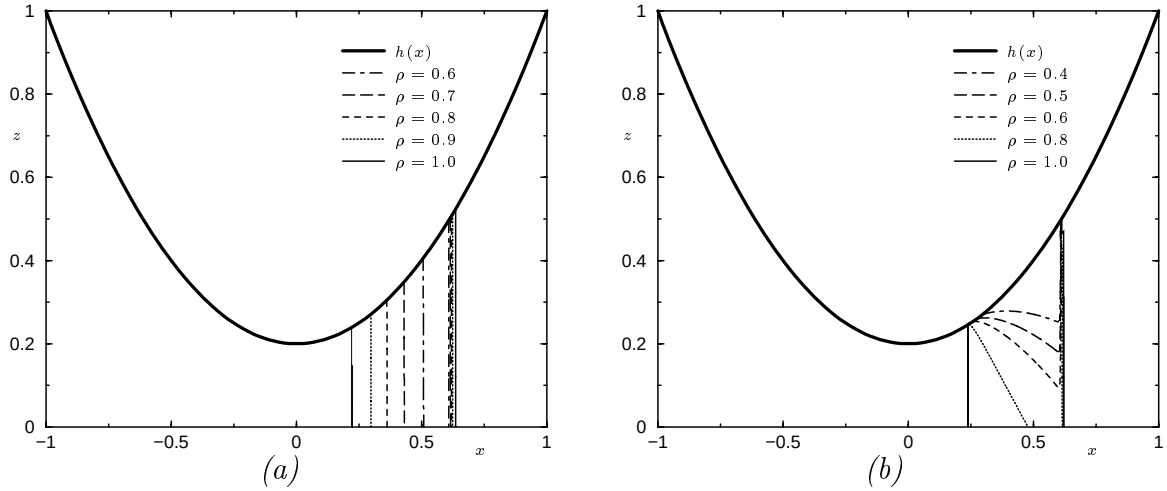

Figure 5.10: *Contour plot of the density for* $\epsilon = 0.01$ *and* $p_v = -300.0$. *(a):* $\beta_\rho = 0.1$. *(b):* $\beta_\rho = 50.0$.

Finally an illustration is given of the convergence of the solution with decreasing mesh size ($N = 128, 256, 512$) for $\epsilon = 0.01$, $p_v = -300.0$ and $\beta_\rho = 100.0$. In figure (5.14a) the contour line $\rho = 0.5$ is shown for the solution on different grids. In figure (5.14b) the density as function of z at $x = 0.5$ is shown. These figures show that with decreasing mesh size the solution converges.

5.2.2 Cavitation: SLF

In this section the case of a single local feature in a uniform gap is revisited but now taking into account cavitation. For the case studied here the geometry is given by:

$$h(x) = 1 - \frac{a_3\sqrt{2e}}{a_4} x e^{-\left(\frac{x}{a_4}\right)^2} \quad . \tag{5.10}$$

This is slightly different from the geometry considered in chapter (*4*) to avoid numerical difficulties near the point where the harmonic part in equation (4.2) is dimmed by the exponential part. From Fourier analysis of (5.10) it follows that the wavelength of the feature is $\lambda = \frac{2\pi}{\sqrt{2}} a_4 \approx 4.4 a_4$.

The boundary conditions are $p = 1.0$, $w = 0$ on the inlet boundary and $dp/dx = 0$, $w = 0$ on the outlet boundary. A constant viscosity is assumed. Results will be presented for $\epsilon = 0.01$ and different values of a_3 and a_4. The vapor pressure is assumed to be $p_v = 0$ and the vapor density $\rho_0 = 0.01$. The parameter β_ρ will be varied. The problem is solved with the same numerical algorithm as used in the previous section. The grid has been generated using

$$z = \xi^2 h(x(\xi^1)) \ , \ \ (\xi^1, \xi^2) \in [0,1] \ , \tag{5.11}$$

where $x(\xi^1)$ is defined by equation (3.68). An FMG algorithm was used with 6 levels, using 12×12 cells on the coarsest grid.

Figures (5.15) and (5.16) show a characteristic solution for the problem with cavitation ($\beta_\rho = 10.0$). In figure (5.15) the pressure and density profile are shown for $a_3 = 0.01$ and

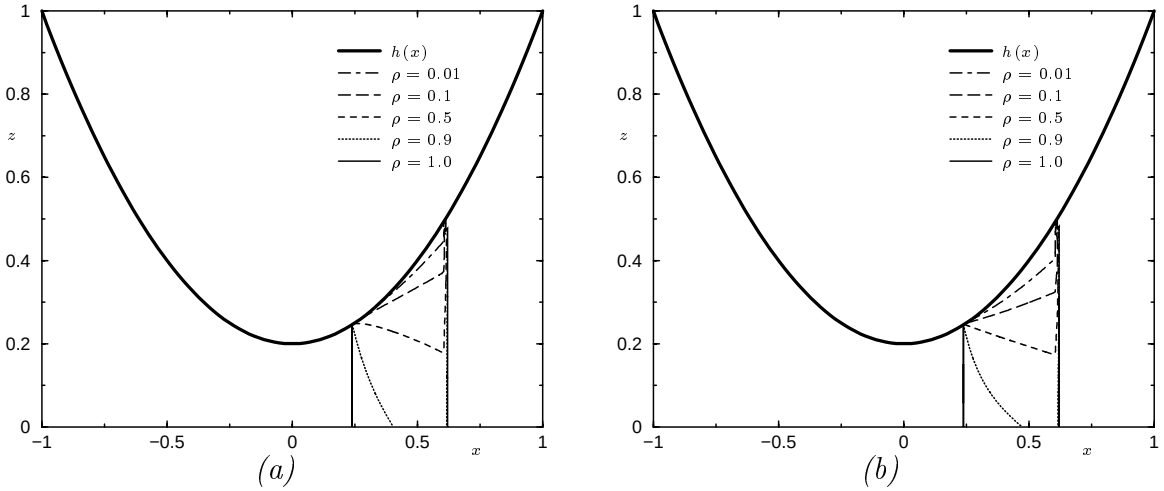

Figure 5.11: *Contour plot of the density for* $\epsilon = 0.01$ *and* $p_v = -300.0$. *(a):* $\beta_\rho = 100.0$. *(b):* $\beta_\rho = 400.0$.

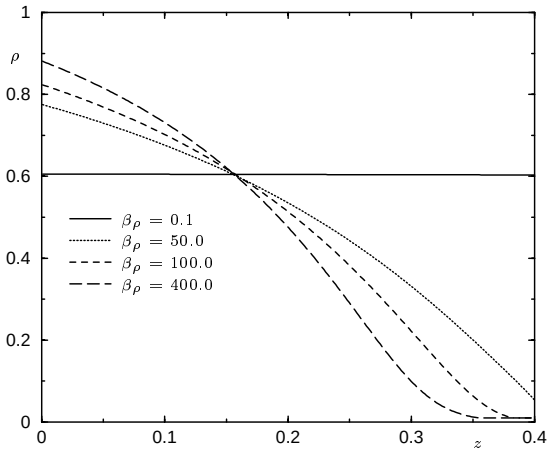

Figure 5.12: *Density as function of* z *at* $x = 0.5$ *for* $\epsilon = 0.01$ *and* $p_v = -300.0$.

$a_4 = 0.6$. From this figure it can be seen that after a pressure rise, induced by the feature, the pressure drops to zero and remains zero. The density upstream of the feature is 1.0 and downstream of the feature it approximates 0.9. Only near the feature the density drops to the vapor density. Figure (5.16a) shows a streamline plot of the flow. Figure (5.16b) shows the $u-$ and $w-$velocity profile at $x = 0.015$.

Next the influence of the wavelength and the amplitude on the solution is studied. In figure (5.17) the density and the film thickness are shown as function of x for different amplitudes (a_3) and wavelengths (a_4). Figure (5.17a) shows that an increase of the amplitude causes a fully vaporized region. Also a change in wavelength can cause this phenomenon, see figure (5.17b). So, in addition to β_ρ, also the geometry determines the structure of the solution of the cavitated region.

This influence of the geometry on the density can best be evaluated by looking at the contour plots of the density. In figure (5.18) the density has been plotted for different

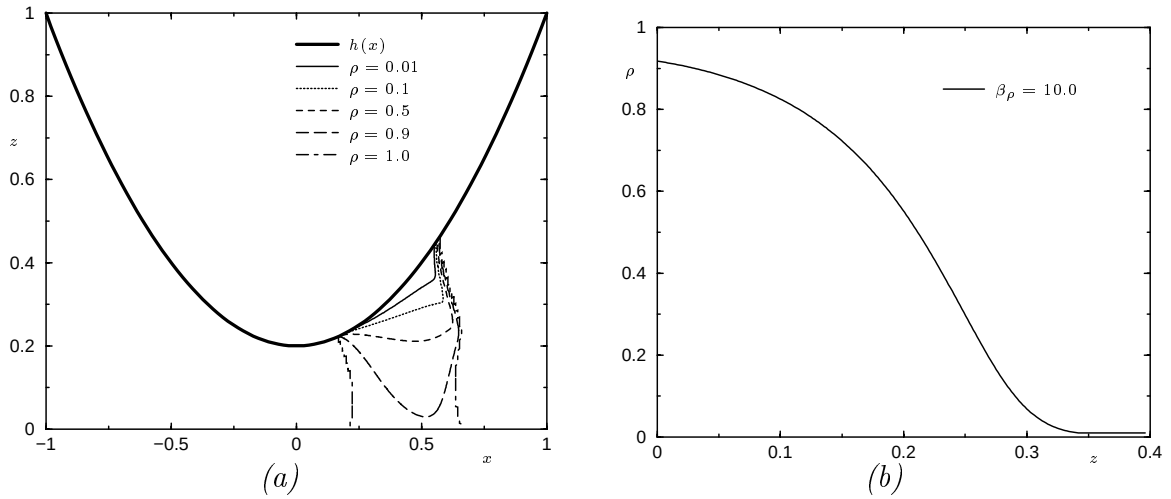

Figure 5.13: *(a): Contour plot of the density. (b): Density as function of z at $x = 0.5$. For $\epsilon = 0.5$, $p_v = -8.0$ and $\beta_\rho = 10.0$.*

amplitudes. It can be observed that the region with $\rho < 0.9$ increases with increasing amplitude and that a fully vaporized region arises. In the same way figure (5.19) shows the effect of the wavelength. It can be concluded that an increase in wavelength causes a decrease of the region with $\rho < 0.9$ and the fully vaporized region may disappear. Furthermore, the solution approximates the Reynolds solution where the density is only a function of x. Finally, the effect of β_ρ on the solution is illustrated in figure (5.20). Based on the results presented in the previous section for the flow under a parabola it may be expected that an increase of β_ρ increases the z-dependence of the density and the formation and size of the vaporized region. This is exactly what figure (5.20) shows. In chapter (*4*) it was found that a decrease in wavelength increases the difference between the Stokes and the Reynolds solutions. The amplitude was found to be less important. In the case of cavitation it turns out that not only the wavelength is an important parameter but also the amplitude of the feature. A large ratio of wavelength to film-thickness will not be likely in, for example, EHL contacts, but a large amplitude may occur. Also in the case of a geometry, which itself does not result in a strongly z-dependent density, this may still be caused by increasing β_ρ. For example, a change in the lower surface speed or a decrease in H can result in a large β_ρ.

In chapter (*4*) solutions of the Reynolds equation and the Stokes equations were compared using $\bar{R}$. In this section the values of $\bar{R}$ obtained for the present SLF problem without cavitation will be compared with values of $\bar{R}$ computed using solutions satisfying the cavitation condition. The effects of wavelength, amplitude and β_ρ on the computed values of $\bar{R}$ for the problem without cavitation and on the computed values of $\bar{R}$ for the problem with cavitation are illustrated in table (5.5) and in figure (5.21). Table (5.5) shows that in both cases, with and without cavitation, an increase of the wavelength (a_4) results in a decrease of the $\bar{R}$ value and that the $\bar{R}$ values found for $\beta_\rho = 10.0$ do not differ much from the $\bar{R}$ values found in the non-cavitating case. Furthermore, this table shows an increase of the $\bar{R}$ value for increasing β_ρ. It tends to have a limit. Figure (5.21) shows the $\bar{R}$ value as function of the amplitude (a_3) in the cavitated and in the non-cavitated

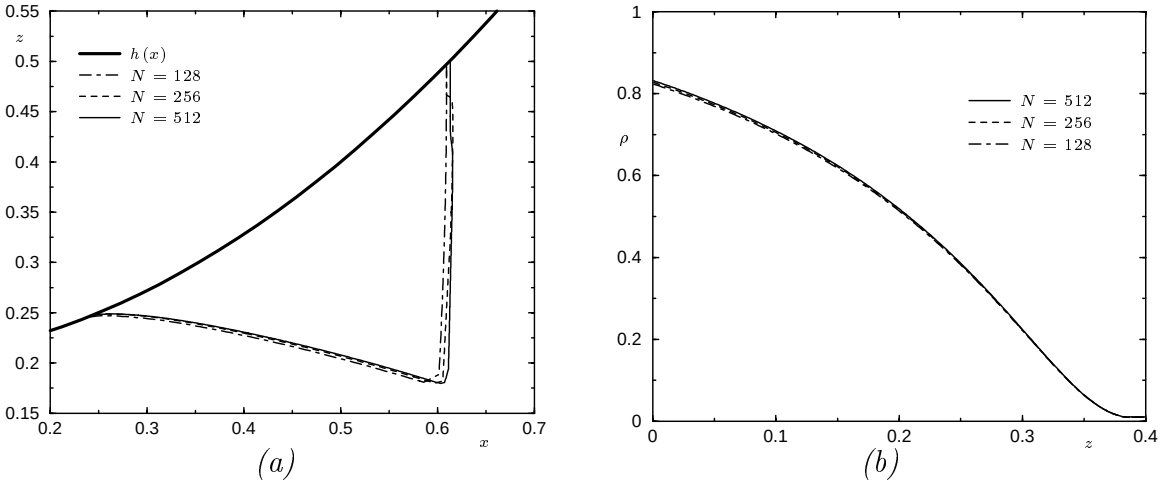

(a) (b)

Figure 5.14: *(a): Contour plot of the iso-density contour $\rho = 0.5$ for the Stokes solution on different grids. (b): Density as function of z at $x = 0.5$ for the Stokes solution on different grids. $\epsilon = 0.01$, $p_v = -300.0$ and $\beta_\rho = 100.0$.*

	β_ρ			
a_4	10.0	50.0	100.0	No cavitation
0.005	0.8554	-	-	0.8154
0.01	0.2399	0.2567	0.2589	0.2493
0.02	0.0664	-	-	0.0624

Table 5.5: *The relative lift force parameter $\bar{R}$ value for different a_4, β_ρ and in the case of no cavitation. For $\epsilon = 0.01$ and $a_3 = 0.4$. A bar indicates a not computed point.*

case. It is noted that both models give more or less the same $\bar{R}$ values, only for small amplitudes there is difference between both models. This figure can be compared with the line $a_4 = 0.04$ in figure (4.5b). It is then observed that they resemble each other as is expected, because in both cases the ratios ϵ to wavelength are approximately the same and for the SLF this ratio determines the value of $\bar{R}$.

Finally, in section (*5.2.1*) a relation between $\frac{\pi}{2\beta_\rho}$ and $\Delta\tilde{p} = p(x,h) - p(x,0)$, at the point where p reaches a minimum in the non-cavitating case, was found to indicate the existence of a fully-vaporized region. For the SLF this relation no longer holds.
In summary, the following conclusions can be drawn with respect to the SLF with cavitation.

- The cavitation model can effectively prevent the pressure from dropping below a preset value, the vapor pressure.

- The $\bar{R}$ values computed with or without a two-phase cavitation model are comparable.

- In certain cases a fully-vaporized region occurs. From experiments it is known that a bubble is present. The model does open the possibility to investigate micro-

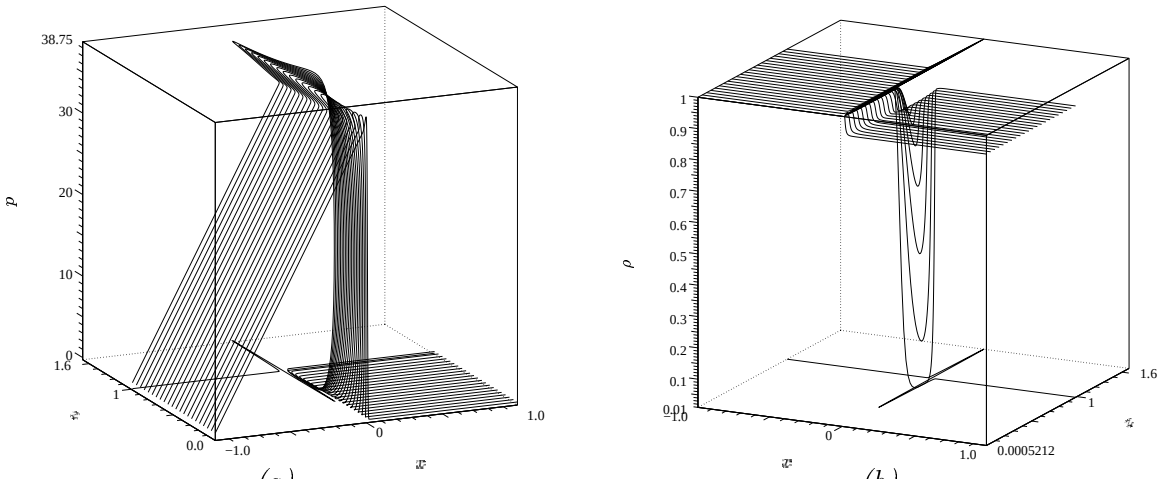

Figure 5.15: *Stokes solution for SLF. (a): Pressure profile. (b): Density profile. Both as function of x and z. $\epsilon = 0.01$, $\beta_\rho = 10.0$, $a_3 = 0.6$ and $a_4 = 0.01$.*

cavitation inside a lubricated contact which is not possible with the Reynolds equation. The latter does not predict fully-vaporized regions.

To conclude this section, again a few results regarding convergence and accuracy are presented. The error reduction per MG cycle, ρ_{MG}, strongly depends on the values of β_ρ, a_3 and a_4. This is illustrated in table (5.6). This shows a decrease in the cycle performance for increasing steepness of the grid-lines in the physical domain and for increasing β_ρ. The method is obviously not optimal in handling the sharp change in pressure.

		a_4		
a_3	β_ρ	0.005	0.01	0.02
0.2	10.0	-	6.7	-
0.4	10.0	4.2	4.9	5.7
0.4	50.0	-	9.7	-
0.4	100.0	-	7.4	-
0.6	10.0	-	2.0	-

Table 5.6: *Average error reduction factor per W(2,2) cycle of the Stokes solver for $\epsilon = 0.01$. A bar indicates a not computed point.*

Convergence of the solution with decreasing mesh size can be shown in many ways. One simple way is to look at the contour line of a specific density value of a solution obtained on grids with different cell size. This is illustrated in figure (5.22). On the coarse-grid the iso-contour looks ragged due to inaccuracy. The wiggle gradually disappears with decreasing mesh size.

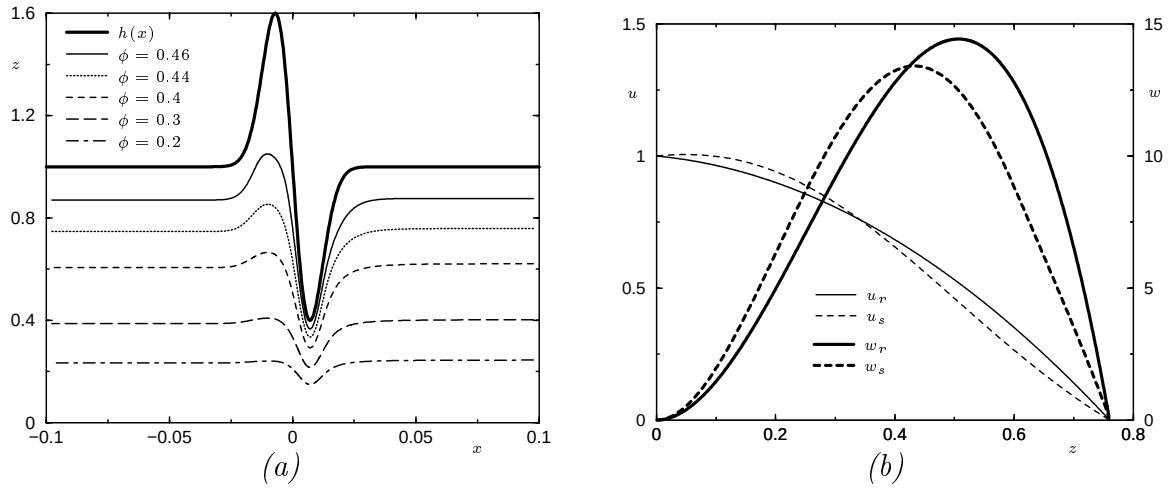

(a) (b)

Figure 5.16: *Stokes solution for SLF. (a): Streamlines. (b): u and w velocity components at $x = 0.015$. Subscript indicates if it is a Reynolds (r) or a Stokes (s) solution. $\epsilon = 0.01$, $\beta_\rho = 10.0$, $a_3 = 0.6$ and $a_4 = 0.01$.*

5.3 Piezo-viscous effects

The most important conclusion of the previous sections is that even if $\epsilon = H/L$ is small this does not automatically imply that the pressure does not vary over the film (as a function of z) which is the key assumption when deriving the Reynolds equation. The occurrence of large gradients in the density was shown to lead to a z-dependence in the pressure. In [1] it was pointed out that the same should happen for rapid changes of the viscosity induced by changes of the pressure.

In this section some results are presented that confirm this prediction. Simulations were performed solving the Stokes equations (2.8), (2.9) and (2.10) for the single local feature problem assuming an exponential viscosity-pressure relation. The gap geometry is again given by equation (5.10). The grid is generated by equation (5.11) where $x(\xi^1)$ is defined by equation (3.68) with the parameters $a_1 = 1$, $\beta = 0.025$, $\Delta x = 4.5a_4$ and $\Delta\xi^1 = 0.6$. The boundary conditions are $p = 0$ and $w = 0$ on the inlet and outlet. The density is assumed to be constant and the viscosity pressure equation (2.66) is used. The parameter ϵ is fixed at $\epsilon = 0.1$. FMG with five levels and a coarsest grid of 12×12 is used. Results are presented for different values of a_3 (amplitude), a_4 (wavelength) and $\bar{\alpha}_p$ (pressure-viscosity coefficient). The important ratio between local film thickness and wavelength can be approximated by $H_{loc}/\Lambda \approx \epsilon/(4.4a_4)$. As was shown in chapter (*4*) this parameter gives an indication of the "geometrically" induced difference between the Reynolds and the Stokes solution for constant viscosity. In figure (5.23a) the pressure as a function of x is shown for $a_3 = 0.2, a_4 = 0.2$. In this case $H_{loc}/\Lambda \approx 0.1$ and there is already a moderate difference between the Stokes and the Reynolds solution for $\eta = 1$. Figure (5.23b) shows the result for $\bar{\alpha}_p = 0.19$. This figure shows that the viscosity-pressure dependence significantly increases the difference between the Reynolds and the Stokes pressure. One can observe that the pressure according to the Stokes solution also globally differs from the Reynolds pressure. Furthermore, one observes that the maxima in p at $z = 0$ and $z = h$ do not occur at the same point as was the case for $\eta = 1$.

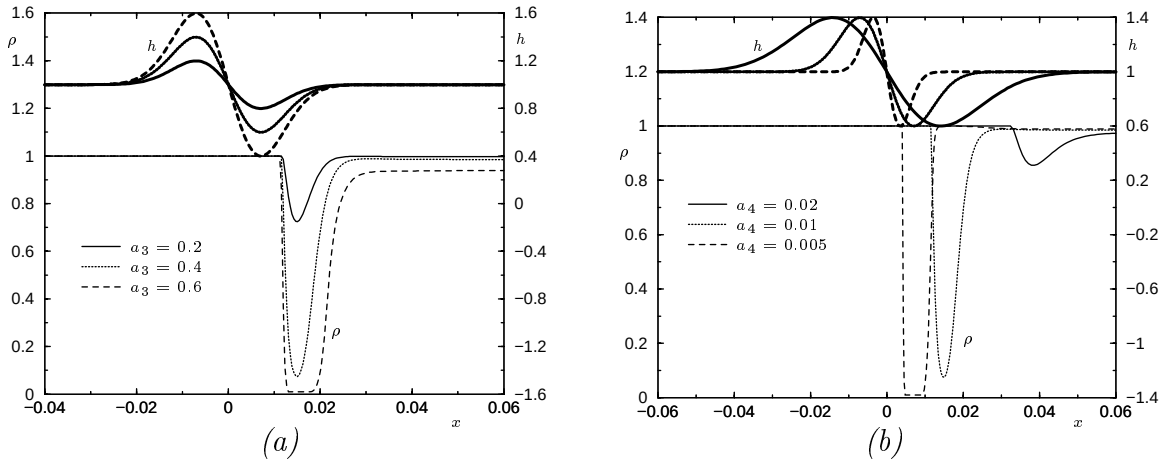

Figure 5.17: *The density and film-thickness at $z = h$ as function of x for $\epsilon = 0.01$ and $\beta_\rho = 10.0$. (a): Different amplitudes a_3 and $a_4 = 0.01$. (b): Different wavelengths a_4 and $a_3 = 0.4$.*

In figure (5.24) the u and w velocity components as function of x have been plotted at $x = 0$. For the iso-viscous as well as for the piezo-viscous case the Reynolds equation predicts that at $x = 0$, where $\frac{dp}{dx} \approx 0$ and $h = 1$, the velocity profiles have the following form:

$$u(0, z) = 1 - z \ , \tag{5.12}$$

$$w(0, z) = z^2(1 - z)\frac{dh}{dx} \ , \tag{5.13}$$

see equation (2.40) and (2.45). In figure (5.24a) it can be seen that also the Stokes solution for the u velocity profile is a straight line and that the location of the minimum of the w velocity profile is the same as is found with the Reynolds solution. However, in the piezo-viscous solution for $\bar{\alpha}_p = 0.19$, see figure (5.24b), the Stokes solution for the u-velocity profile is no longer a straight line and the location of the minimum of the w-velocity profile has shifted to the left.

To quantify the difference between the Stokes and the Reynolds solutions, the relative lift force difference $\bar{R}$ is used again. Figure (5.25)(a) shows $\bar{R}$ as a function of $\bar{\alpha}_p$ for three different wavelengths a_4 and an amplitude $a_3 = 0.2$. The figure shows that with increasing $\bar{\alpha}_p$ the difference in the lift force predicted by the Reynolds equation and the Stokes equations increases. This effect appears to be stronger with increasing wavelength. Next, figure (5.25b) shows the value of $\bar{R}$ as a function of $\bar{\alpha}_p$ for different amplitudes keeping the wavelength fixed. Again $\bar{R}$ increases with increasing $\bar{\alpha}_p$ with a stronger effect for larger a_3. Both figures clearly show that a geometrically induced difference between the solutions of the Reynolds and the Stokes equations is significantly amplified by the viscosity pressure dependence. To what extend are the values for $\bar{\alpha}_p$ assumed above realistic? This can be seen as follows. Taking

$$\begin{array}{lcl} \eta_o & = & 100.0 \cdot 10^{-3} \ [\mathrm{kg/ms}] \\ \alpha_p & = & 2.0 \cdot 10^{-8} \ [\mathrm{s^2\ m/kg}] \\ H & = & 0.1 \cdot 10^{-6} \ [\mathrm{m}] \\ u_0 & = & 1.0 \ [\mathrm{m/s}] \end{array} \tag{5.14}$$

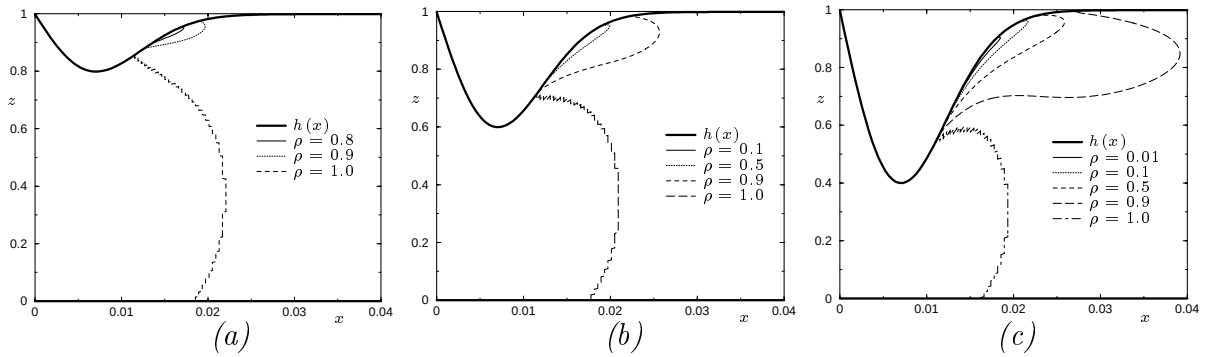

(a) *(b)* *(c)*

Figure 5.18: *Effect of amplitude on solution of SLF problem with cavitation: contour plot of the density,* $\beta_\rho = 10.0$, $a_4 = 0.01$. *(a):* $a_3 = 0.2$. *(b):* $a_3 = 0.4$. *(c):* $a_3 = 0.6$.

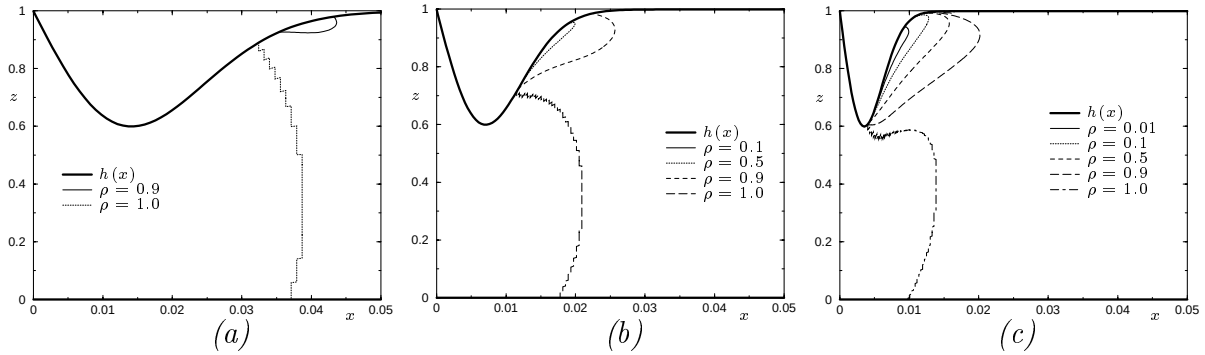

(a) *(b)* *(c)*

Figure 5.19: *Effect of wavelength on solution of SLF problem with cavitation: contour plot of the density,* $\beta_\rho = 10.0$, $a_3 = 0.4$. *(a):* $a_4 = 0.02$. *(b):* $a_4 = 0.01$. *(c):* $a_4 = 0.005$.

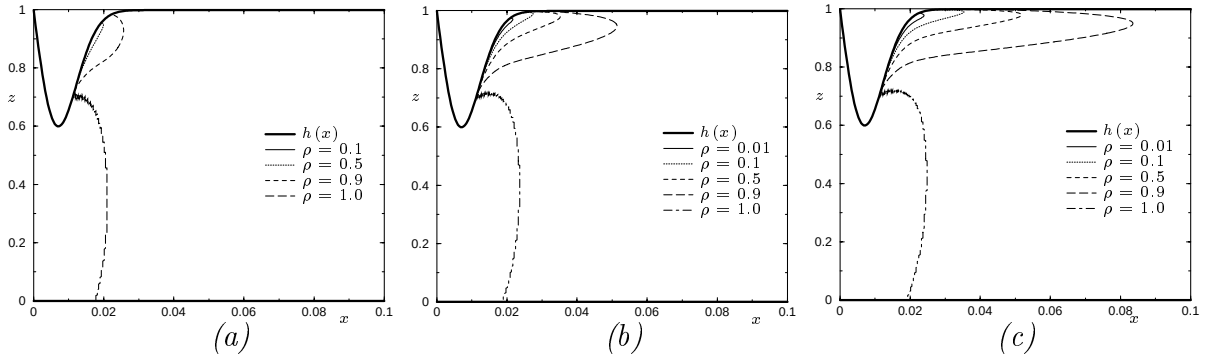

(a) *(b)* *(c)*

Figure 5.20: *Effect of* β_ρ *on solution of SLF problem with cavitation: contour plot of the density,* $a_3 = 0.4$, $a_4 = 0.01$. *(a):* $\beta_\rho = 10.0$. *(b):* $\beta_\rho = 50.0$. *(c):* $\beta_\rho = 100.0$.

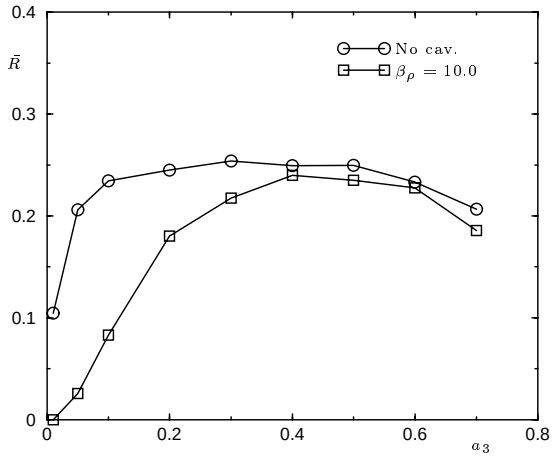

Figure 5.21: *The $\bar{R}$ value as function of the amplitude a_3 for $\epsilon = 0.01$ and $a_4 = 0.01$.*

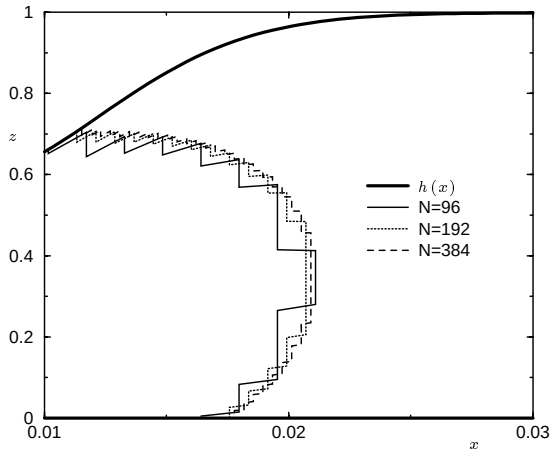

Figure 5.22: *Contour plot of constant density line $\rho = 0.5$ on different grids. Stokes solution for the SLF problem $\epsilon = 0.01$, $a_3 = 0.4$ and $a_4 = 0.01$.*

which are realistic values for a tribological problem it follows that $\bar{\alpha}_p = \frac{\alpha_p \eta_0 u_0}{H} = 0.02$ and if u_0 is increased with a factor of 10 than $\bar{\alpha}_p = 0.2$.

Finally a few words about the performance of the solver. The algorithm shows a rather poor MG convergence and for large $\bar{\alpha}_p$, ϵ/a_4, a_3 it does not converge at all. This is a subject for future research. However, the results, presented here, are sufficient to illustrate the basic phenomenon that viscosity-pressure dependence has a significant effect on the difference between the Reynolds and Stokes solution for the SLF. This indicates that there are some interesting questions to be answered in future EHL research where viscosity-pressure dependence is one of the key phenomena explaining film formation.

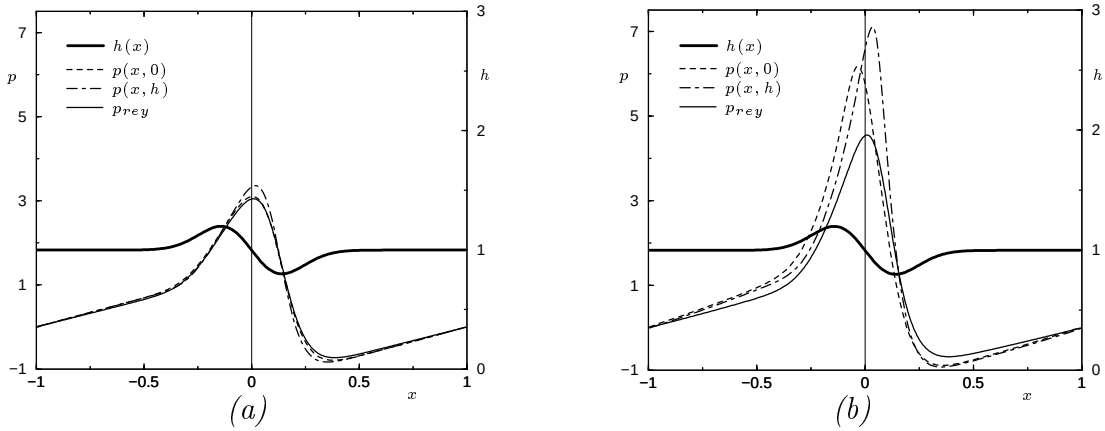

Figure 5.23: *The Stokes pressure at the lower surface ($p(x,0)$), at the upper surface ($p(x,h)$), the Reynolds pressure (p_{rey}) and the film thickness ($h(x)$) for $\epsilon = 0.1$ and $a_3 = 0.2, a_4 = 0.2$. (a): $\bar{\alpha}_p = 0.0$. (b): $\bar{\alpha}_p = 0.19$.*

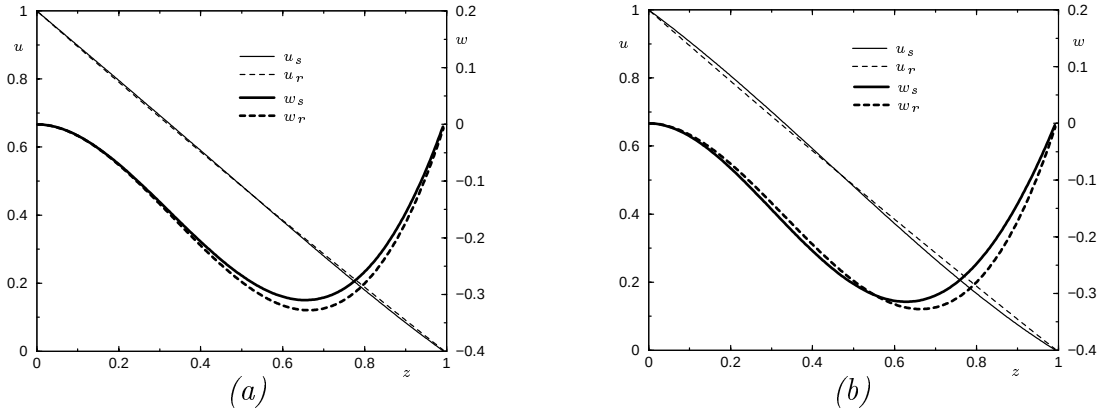

Figure 5.24: *The u and w velocity components at $x = 0.0$. (a): $\bar{\alpha}_p = 0.0$. (b): $\bar{\alpha}_p = 0.19$. Subscript indicates if it is a Reynolds (r) or a Stokes (s) solution. $\epsilon = 0.1$ and $a_3 = 0.2, a_4 = 0.2$.*

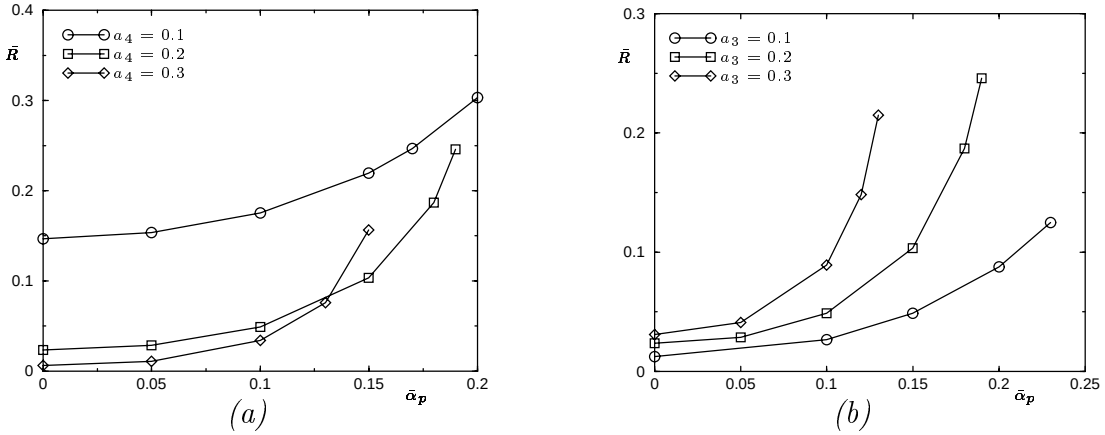

Figure 5.25: *$\bar{R}$ as function of $\bar{\alpha}_p$ for $\epsilon = 0.1$. (a): $a_3 = 0.2$. (b): $a_4 = 0.2$.*

Conclusions

The aim of the research presented in this thesis was to establish criteria concerning the validity of the Reynolds equation for the prediction of the flow in lubricated contacts. This equation is derived from the Navier-Stokes equations under the assumption that the ratio $\epsilon = H/L$ of gap height and gap length is small and that it is a slow-viscous flow. An intermediate description can be derived by omitting the inertia terms in the N-S equations. This results in the Stokes equations. Most lubricated contacts have a small ϵ on a global scale. However, as technical surfaces are never perfectly smooth on a local scale, this may no longer be true. The question then is how large the error will be that is made when using the Reynolds equation compared to using the Stokes equations.

In order to investigate the difference between the Stokes and the Reynolds solutions, the flow in a uniform channel with a surface feature on one of the surfaces, and the flow below a parabolically shaped surface was investigated. It was found that multi-grid techniques can effectively solve the discretized Stokes equations for thin films.

To quantify the difference between the Reynolds and the Stokes solution the relative load difference parameter $\bar{R}$ was introduced. The $\bar{R}$ was monitored as a function of the characteristic parameters of the geometry. From this study it was concluded that the important parameter seems to be the ratio of film thickness and wavelength, thereby confirming the hypothesis of [25].

It was found that, for channel flows, deviations of more than ten percent between the Reynolds and the Stokes solutions occur if $H/\Lambda > 0.2$ holds. For more general domains one should take for H the local film thickness (at the location of the feature) and the amplitude close to the film thickness. Comparing this with the values of H/Λ in practice it is concluded that in most cases Reynolds roughness is found and the Reynolds equation is valid. It was also shown that perturbation analysis is a cheap way of approximating the Stokes solution for moderate values of the ratio H/Λ and of the amplitude.

Apart from the geometry of the contact also compressibility and piezo-viscous effects can influence the validity of the Reynolds equation. This was shown for a model problem taken from gas-bearing application. It was found that, besides the geometry of the domain, the lower surface speed can cause a cross-film dependent pressure. For the two-phase cavitation model it was shown that a steeply varying density as a function of the pressure can cause a cross-film dependent pressure. In the case of piezo-viscosity already existing differences between the Stokes and the Reynolds solutions can be amplified if the pressure-viscosity coefficient is increased.

Recommendations for further research

It appears that geometrically induced differences between the Reynolds and the Stokes solution will be rare in EHL contacts. But if one wants to have a closer look at what the precise effect is on the load carrying capacity of the contact one could use an expression for the pressure from perturbation analysis in an existing EHL solver. The validity of the assumption that the convective terms can be neglected in the neighborhood of a local feature could be a topic for further study.

The gas-bearing model results call up some questions concerning the calculated high speed pressure profile. To what extent are the pressure profiles that were found realistic, and what is the effect of inertia in this regime?

For small β_ρ the MG performance for the two-phase model is quite good. An increase of β_ρ decreases the MG performance. So, if one wants to do more research on cavitation with the two-phase model, one should investigate the MG scheme more precisely. Is there a better relaxation procedure? What about the coarse-grid operator? What kind of inter-grid operators should be used? A good starting point could be the study of the full potential equation, see [74], [94]. This is also a partially elliptic/hyperbolic equation.

Piezo viscosity appears to result in a distinct difference between the Reynolds and the Stokes solutions in an EHL contact. Also here some numerical problems (no MG convergence) were encountered for too large viscosity-pressure coefficients. A remedy is probably to use some kind of an upwind discretization in the direction of the characteristics such as given by A.7.

Appendix A

Determination type of equation

Partial differential equations can be divided into three main categories: elliptic, parabolic and hyperbolic. Simple examples are: the Laplace equation, the diffusion equation and the wave equation. They differ in the way a disturbance in the solution is transported through the domain. The lines along which the disturbance is transported are called characteristics. It is also possible that the partial differential equation is a combination of the above mentioned types. Also systems of partial differential equations can be classified in the above categories. For a mathematical introduction to this topic see [100].

For a system of quasi-linear first-order partial differential equations of the form:

$$A\frac{\partial \mathbf{u}}{\partial x} + B\frac{\partial \mathbf{u}}{\partial z} = C\mathbf{u} + \mathbf{c} \ , \tag{A.1}$$

where $\mathbf{u}$ and $\mathbf{c}(\mathbf{x}, \mathbf{z})$ are n-component column vectors and A, B and C are $n \times n$ matrix functions of x, z and $\mathbf{u}$. The slope of the characteristics in the (x, z) plane are determined by the eigenvalues λ_i of $A^{-1}B$, i.e.

$$\frac{dz}{dx} = \lambda_i, \quad i = 1...n \ . \tag{A.2}$$

With the eigenvalues and eigenvectors of $A^{-1}B$ the following division can be made.

1. If the λ_i's are complex-valued then the system is elliptic.
2. If the λ_i's are real and the n eigenvectors are linearly independent then the system is hyperbolic.
3. if the λ_i's are real and not all n eigenvectors are linearly independent then the system is parabolic.

A.1 Incompressible, piezo-viscous flow

In this case η is a function of p and ρ is constant. Equations (2.11), (2.12) and (2.13) with $\epsilon = 1$ can be written as:

$$(1 - 2\eta_p[u_x])\frac{\partial p}{\partial x} - \eta_p[w_x + u_z]\frac{\partial p}{\partial z} - \eta(\frac{\partial^2 u}{\partial x^2} + \frac{\partial^2 u}{\partial z^2}) = 0 \ , \tag{A.3}$$

$$(1-2\eta_p[w_z])\frac{\partial p}{\partial z}-\eta_p[w_x+u_z]\frac{\partial p}{\partial x}-\eta(\frac{\partial^2 w}{\partial x^2}+\frac{\partial^2 w}{\partial z^2})=0\ , \tag{A.4}$$

$$\frac{\partial u}{\partial x}+\frac{\partial w}{\partial z}=0\ , \tag{A.5}$$

where $\eta_p=\frac{d\eta}{dp}$, $u_x=\frac{\partial u}{\partial x}$, $u_z=\frac{\partial u}{\partial z}$, $w_x=\frac{\partial w}{\partial x}$ and $w_z=\frac{\partial w}{\partial z}$.

The terms in brackets will be kept constant in this analysis. After introduction of the new variables $s_1=\frac{\partial u}{\partial z}$, $s_2=-\frac{\partial w}{\partial z}=\frac{\partial u}{\partial x}$ and $s_3=\frac{\partial w}{\partial x}$ the above equations can be written in the form (A.1) with

$$A=\begin{bmatrix} 0 & 1 & 0 & 0 & 0 & 0\\ 1 & 0 & 0 & 0 & 0 & 0\\ 0 & 0 & 0 & -1 & 0 & 0\\ 0 & 0 & 0 & 0 & 1 & 0\\ 0 & 0 & 1-2\eta_p[u_x] & 0 & -\eta & 0\\ 0 & 0 & -\eta_p[w_x+u_z] & 0 & 0 & -\eta \end{bmatrix},B=\begin{bmatrix} 0 & 0 & 0 & 0 & 0 & 0\\ 0 & 1 & 0 & 0 & 0 & 0\\ 0 & 0 & 0 & 0 & 1 & 0\\ 0 & 0 & 0 & 0 & 0 & 1\\ 0 & 0 & -\eta_p[w_x+u_z] & -\eta & 0 & 0\\ 0 & 0 & 1-2\eta_p[w_z] & 0 & \eta & 0 \end{bmatrix} \tag{A.6}$$

and $\mathbf{u}=\{u,w,p,s_1,s_2,s_3\}^T$, $C\mathbf{u}=\{s_3,0,0,0,0,0\}^T$, $\mathbf{c}=\mathbf{0}$. Because $Det[A]=-\eta+2\eta\eta_p u_x$ the eigenvalues of $A^{-1}B$ can be found: $\lambda_{1,2}=0$, $\lambda_{3,4}=\mp I$ and

$$\lambda_{5,6}=\frac{-\eta_p[u_z+w_x]\mp\sqrt{D}}{1+2\eta_p[w_z]}\ , \tag{A.7}$$

where

$$D=\eta_p^2([u_z+w_x]^2-4[u_xw_z])-1\ .$$

The $\lambda_{1,2}$ can be omitted because they result from the transformation of the second-order system to the first-order system. This means that the system is fully elliptic if $D<0$. This is always the case in the constant-viscosity case. If $D=0$ then the system is partially parabolic. If $D>0$ then the system is partially hyperbolic.

A.2 Compressible, piezo-viscous flow

The density and the viscosity are both functions of the pressure. Equations (2.8), (2.9) and (2.10) with $\epsilon=1$ can be written as:

$$(1+\frac{1}{3}\eta_p(2[w_z]-4[u_x]))\frac{\partial p}{\partial x}-\eta_p[w_x+u_z]\frac{\partial p}{\partial z}-\frac{4}{3}\eta\frac{\partial^2 u}{\partial x^2}-\frac{1}{3}\eta\frac{\partial^2 w}{\partial x\partial z}-\eta\frac{\partial^2 u}{\partial z^2}=0\ , \tag{A.8}$$

$$(1+\frac{1}{3}\eta_p(2[u_x]-4[w_z]))\frac{\partial p}{\partial z}-\eta_p[w_x+u_z]\frac{\partial p}{\partial x}-\frac{4}{3}\eta\frac{\partial^2 w}{\partial z^2}-\frac{1}{3}\eta\frac{\partial^2 u}{\partial x\partial z}-\eta\frac{\partial^2 w}{\partial x^2}=0\ , \tag{A.9}$$

$$u\rho_p\frac{\partial p}{\partial x}+\rho\frac{\partial u}{\partial x}+w\rho_p\frac{\partial p}{\partial z}+\rho\frac{\partial w}{\partial z}=0\ , \tag{A.10}$$

where $\rho_p=\frac{\partial\rho}{\partial p}$, $\eta_p=\frac{d\eta}{dp}$, $u_x=\frac{\partial u}{\partial x}$, $u_z=\frac{\partial u}{\partial z}$, $w_x=\frac{\partial w}{\partial x}$ and $w_z=\frac{\partial w}{\partial z}$. The terms in brackets will be kept constant in this analysis. After introduction of the new variables $s_1=\frac{\partial u}{\partial x}$, $s_2=\frac{\partial w}{\partial x}$,

$s_3 = \frac{\partial u}{\partial z}$ and $s_4 = \frac{\partial w}{\partial z}$ the above equations can be written in the form (A.1) with

$$A = \begin{bmatrix} 1 & 0 & 0 & 0 & 0 & 0 & 0 \\ 0 & 1 & 0 & 0 & 0 & 0 & 0 \\ 0 & 0 & 0 & 0 & 0 & -1 & 0 \\ 0 & 0 & 0 & 0 & 0 & 0 & -1 \\ 0 & 0 & 1 + \frac{1}{3}\eta_p(2[w_z] - 4[u_x]) & -\frac{4}{3}\eta & 0 & 0 & -\frac{1}{3}\eta \\ 0 & 0 & -\eta_p[w_x + u_z] & 0 & -\eta & 0 & 0 \\ \rho & 0 & u\rho_p & 0 & 0 & 0 & 0 \end{bmatrix},$$

$$B = \begin{bmatrix} 0 & 0 & 0 & 0 & 0 & 0 & 0 \\ 0 & 0 & 0 & 0 & 0 & 0 & 0 \\ 0 & 0 & 0 & 1 & 0 & 0 & 0 \\ 0 & 0 & 0 & 0 & 1 & 0 & 0 \\ 0 & 0 & -\eta_p[w_x + u_z] & 0 & 0 & -\eta & 0 \\ 0 & 0 & 1 + \frac{1}{3}\eta_p(2[u_x] - 4[w_z]) & -\frac{1}{3}\eta & 0 & 0 & -\frac{4}{3}\eta \\ 0 & \rho & w\rho_p & 0 & 0 & 0 & 0 \end{bmatrix} \tag{A.11}$$

and $\mathbf{u} = \{u, w, p, s_1, s_2, s_3, s_4\}^T$, $C\mathbf{u} = \{s_1, s_2, 0, 0, 0, 0, 0\}^T$, $\mathbf{c} = \mathbf{0}$. Because $Det[A] = \frac{4}{3}\eta^2\rho_p u$ the eigenvalues of $A^{-1}B$ can be found: $\lambda_{1,2} = 0$, $\lambda_{3,4} = -I$, $\lambda_{5,6} = I$ and $\lambda_7 = \frac{w}{u}$. The $\lambda_{1,2}$ can be omitted because they result from the transformation of the second-order system to the first-order system. In compressible flow the system is partially hyperbolic with characteristics along w/u independent of the viscosity.

Appendix B

Determination speed of sound

In the two phase model the minimum speed of sound in a mixture of liquid and bubbles is required. In the following an estimate for the minimum speed of sound is deduced. For a detailed discussion see [3], pp. 93. This parameter is then used in equation (2.71). The speed of sound in a fluid is defined as:

$$a^2 = \left(\frac{\partial p}{\partial \rho}\right)_s \ , \tag{B.1}$$

where $()_s$ indicates a constant entropy. Only in the transition region between the liquid and the vapor state the density is not constant and the speed of sound is not infinite (see figure (2.4)). This is typical for the used model. Obviously, in reality the speeds of sound in the vapor and in the liquid have finite values.

To determine the speed of sound in the mixture the volume fraction (α^a) of the vapor bubbles in the mixture is introduced. The actual density is then a linear combination of the liquid density and the vapor density:

$$\rho = \alpha^a \rho_v + (1 - \alpha^a)\rho_l \ . \tag{B.2}$$

It is assumed that the bubbles in the mixture are small enough to follow the fluid when an acoustical wave passes. In that case, the ratio $\beta^a = \frac{\alpha^a \rho_v}{\rho}$ is a conservative quantity (i.e. the mass does not change when an acoustical wave passes). It can be substituted in equation (B.2) and results in:

$$\frac{1}{\rho} = \frac{\beta^a}{\rho_v} + \frac{1 - \beta^a}{\rho_l} \ . \tag{B.3}$$

This can be differentiated with respect to p and after some manipulations the following equation can be found

$$\frac{1}{a^2 \rho} = \frac{\alpha^a}{a_v^2 \rho_v} + \frac{1 - \alpha^a}{a_l^2 \rho_l} \ . \tag{B.4}$$

With the use of equation (B.2) it can be rewritten in a more useful form:

$$a = \frac{\sqrt{\rho_l \rho_v} a_v a_l}{\sqrt{(\rho_l(1 - \alpha^a) + \rho_v \alpha^a)(\rho_v a_v^2 (1 - \alpha^a) + \alpha^a \rho_l a_l^2)}} \ . \tag{B.5}$$

The minimum speed of sound in the mixture can now be deduced by solving $\frac{da}{d\alpha^a}\Big|_{\alpha^a=\alpha^a_{min}} = 0$ and substituting α^a_{min} back into equation (B.5). The α^a_{min} is given by:

$$\alpha^a_{min} = \frac{\rho_v^2 a_v^2 - 2\rho_v\rho_l a_v^2 + \rho_l^2 a_l^2}{2(\rho_l - \rho_v)(\rho_l a_l^2 - \rho_v a_v^2)} \ . \tag{B.6}$$

If $\rho_l \gg \rho_v$ than $\alpha^a_{min} \to \frac{1}{2}$ and the following expression for the minimal speed of sound is found

$$a_{min} = 2a_v\sqrt{\frac{\rho_v}{\rho_l}} \ . \tag{B.7}$$

Appendix C

Second-order perturbation

In this appendix the expansion of the Stokes equation in $\gamma(=\epsilon^2)$ will be carried out up to second order. The development of the first-order approximation has been explained in Section *2.2*. The second-order expansion of the Stokes equations can now be deduced by substituting equation (2.49) in equations (2.46), (2.47) and (2.48) and equating equal orders in γ^2.

$$\epsilon\frac{\partial p_2}{\partial x} - \frac{\partial^2 u_2}{\partial z^2} = \frac{\partial^2 u_1}{\partial x^2} \ , \tag{C.1}$$

$$\epsilon\frac{\partial p_2}{\partial z} = \frac{\partial^2 w_1}{\partial z^2} + \frac{\partial^2 w_0}{\partial x^2} \ , \tag{C.2}$$

$$\frac{\partial u_2}{\partial x} + \frac{\partial w_2}{\partial z} = 0 \ . \tag{C.3}$$

On the four boundaries of the domain the perturbation variables take the following values: $u_2 = 0, w_2 = 0, p_2 = 0$. The right-hand sides in the above equations contain known functions, resulting from lower-order perturbation results. The w_0 is given in equations (2.55). The first-order perturbation u_1 follows from twice integrating equation (2.56) with respect to z and is given by:

$$u_1 = \frac{c_2 z(z-h)}{2h^3} + \frac{z(z-h)(-30c_1\epsilon z^2 - 90z^2h + 9c_1\epsilon h^2 - 10zh^2 + 32h^3)(h')^2}{30h^5} + \frac{z(c_1\epsilon + 4h)(15z^3 - 20z^2h + 3zh^2 + 2h^3)h''}{60h^4} \ , \tag{C.4}$$

where c_1 and c_2 are integration constants following from integrating equation (2.54) and equation (2.60) respectively, with respect to x from -1 to 1. For convenience the short-hand notations $h' = dh/dx$, $h'' = d^2h/dx^2$ etc. have been introduced. An expression for w_1 can be found through equation (2.58) with the use of the explicit form of u_1.

$$w_1 = \frac{z^2(z-h)(-30c_1\epsilon z^2 - 72z^2h + 9c_1\epsilon h^2 - 12zh^2 + 16h^3)(h')^3}{30h^6} + \frac{c_2 z^2(z-h)h'}{2h^4} + \frac{z^2(z-h)(36c_1\epsilon z^2 - 9c_1\epsilon zh + 108z^2h - 19c_1\epsilon h^2 - 12zh^2 - 64h^3)h'h''}{60h^5} - \frac{z^2(z-h)^2(3z+h)(c_1\epsilon + 4h)h'''}{60h^4} \ . \tag{C.5}$$

The integration of equation (C.2) with respect to z gives an expression for the pressure correction p_2:

$$\epsilon p_2 = \int \left[\frac{\partial^2 w_0}{\partial x^2} + \frac{\partial^2 w_1}{\partial z^2} \right] dz + \tilde{p}_2(x) \ , \tag{C.6}$$

where $\tilde{p}_2$ is unknown. An explicit expression for ϵp_2 can now be found by substituting w_0 and w_1 in equation (C.6).

$$\begin{aligned}
\epsilon p_2 = \tilde{p}_2(x) + \frac{z c_2 h'(3z-2h)}{2h^4} + \\
\frac{z(h')^3(-75c_1\epsilon z^3 + 60c_1\epsilon z^2 h - 180 z^3 h + 27 c_1 \epsilon z h^2 + 120 z^2 h^2 - 18 c_1 \epsilon h^3 + 84 z h^3 - 32 h^4)}{30 h^6} + \\
\frac{z h' h''(45 c_1 \epsilon z^3 - 45 c_1 \epsilon z^2 h + 135 z^3 h - 15 c_1 \epsilon z h^2 - 120 z^2 h^2 + 19 c_1 \epsilon h^3 - 78 z h^3 + 64 h^4}{30 h^5} + \\
\frac{z h'''(c_1\epsilon + 4h)(-15 z^3 + 20 z^2 h - 6 z h^2 - 4 h^3)}{120 h^4} \ .
\end{aligned} \tag{C.7}$$

Upon substitution of equation (C.7) in equation (C.1) and double integration with respect to z an expression for u_2 can be found. This u_2 can be substituted in equation (C.3). This equation can be integrated with respect to z between 0 and $h(x)$. Using the boundary conditions and the Leibnitz rule the following equation can be deduced:

$$\begin{aligned}
\frac{d}{dx}\Bigg[-h^3 \frac{d\tilde{p}_2}{dx} + \frac{-4(h')^4(9c_1\epsilon + 46h)}{525} + \frac{c_2 h h''}{10} - \frac{h^2 (h'')^2 (80 c_1 \epsilon + 107 h)}{1050} + \\
\frac{3 c_2 (h')^2}{5} - \frac{118 h (h')^2 h''(c_1\epsilon + 8h)}{525} - \frac{2 h^2 h' h'''(22 c_1 \epsilon + 17 h)}{525} + \\
\frac{71 h^3 h''''(c_1\epsilon + 4h)}{4200} \Bigg] = 0 \ .
\end{aligned} \tag{C.8}$$

This is again a Reynolds type of equation for the unknown function $\tilde{p}_2$. It can be solved by numerical integration. From equation (C.7) it can be seen that the solution consists of two parts: in the global part, represented by $\tilde{p}_2(x)$, an overall correction is introduced, so the pressure profile not only changes at the location of a local feature; in the local part, where h' changes rapidly, the pressure is also a function of z.

Appendix D

Truncation error of the discrete continuity equation

In this appendix it is shown that for the discretization of the constant density continuity equation, proposed in chapter (*3*), the truncation error is of second order in $(\delta\xi^1, \delta\xi^2)$. In the discretized continuity equation (3.4) the contravariant base vectors are replaced by the covariant base vectors. The continuity equation is then given by:

$$\begin{aligned}&\left[a^2_{(2)}u\right]_{i+\frac{1}{2}j}\,\delta\xi^2 - \left[a^2_{(2)}u\right]_{i-\frac{1}{2}j}\,\delta\xi^2 + \\ &\left[-a^2_{(1)}u + a^1_{(1)}w\right]_{ij+\frac{1}{2}}\,\delta\xi^1 - \left[-a^2_{(1)}u + a^1_{(1)}w\right]_{ij-\frac{1}{2}}\,\delta\xi^1 = 0\ .\end{aligned} \tag{D.1}$$

After division of equation (D.1) by $\delta\xi^1\delta\xi^2$ and using the transformation (3.16) it follows that:

$$\begin{aligned}&\frac{(h_{i+\frac{1}{2}}u_{i+\frac{1}{2}j} - h_{i-\frac{1}{2}}u_{i-\frac{1}{2}j})}{\delta\xi^1} + \frac{(h_{i+\frac{1}{2}} - h_{i-\frac{1}{2}})(\xi^2_{j-\frac{1}{2}}u_{ij-\frac{1}{2}} - \xi^2_{j+\frac{1}{2}}u_{ij+\frac{1}{2}})}{\delta\xi^1\delta\xi^2} + \\ &\frac{(x_{i+\frac{1}{2}} - x_{i-\frac{1}{2}})(w_{ij+\frac{1}{2}} - w_{ij-\frac{1}{2}})}{\delta\xi^1\delta\xi^2} = 0\ ,\end{aligned} \tag{D.2}$$

where $h = h(\xi^1)$ and $x = x(\xi^1)$. In this equation the following bilinear interpolations are used:

$$u_{ij-\frac{1}{2}} = \frac{1}{4}(u_{i-\frac{1}{2}j} + u_{i+\frac{1}{2}j} + u_{i-\frac{1}{2}j-1} + u_{i+\frac{1}{2}j-1})\ , \tag{D.3}$$

and

$$u_{ij+\frac{1}{2}} = \frac{1}{4}(u_{i-\frac{1}{2}j} + u_{i+\frac{1}{2}j} + u_{i-\frac{1}{2}j+1} + u_{i+\frac{1}{2}j+1})\ . \tag{D.4}$$

For each quantity in equation (D.2) the Taylor approximation around the grid point (i, j) is substituted. If the function u is sufficiently smooth the following Taylor expansion can be written:

$$\begin{aligned}u_{i+\frac{1}{2}j+1} = u_{ij} &+ \frac{\delta\xi^1}{2}\left(\frac{\partial u}{\partial\xi^1}\right)_{ij} + \delta\xi^2\left(\frac{\partial u}{\partial\xi^2}\right)_{ij} + \frac{(\delta\xi^1)^2}{8}\left(\frac{\partial^2 u}{\partial(\xi^1)^2}\right)_{ij} + \\ &\frac{\delta\xi^1\delta\xi^2}{2}\left(\frac{\partial^2 u}{\partial\xi^1\partial\xi^2}\right)_{ij} + \frac{(\delta\xi^2)^2}{2}\left(\frac{\partial^2 u}{\partial(\xi^2)^2}\right)_{ij} + \frac{(\delta\xi^1)^3}{48}\left(\frac{\partial^3 u}{\partial(\xi^1)^3}\right)_{ij} +\end{aligned}$$

$$\frac{(3\delta\xi^1)^2\delta\xi^2}{24}\left(\frac{\partial^3 u}{\partial^2\xi^1\partial\xi^2}\right)_{ij}+\frac{3\delta\xi^1(\delta\xi^2)^2}{12}\left(\frac{\partial^3 u}{\partial\xi^1\partial^2\xi^2}\right)_{ij}+$$
$$\frac{(\delta\xi^2)^3}{6}\left(\frac{\partial^3 u}{\partial(\xi^2)^3}\right)_{ij}+O((\delta\xi^1)^4,(\delta\xi^2)^4) \tag{D.5}$$

where $()_{ij}$ indicates that the function between the brackets is evaluated at the grid point (i,j). Also for h and x Taylor approximations around the point (i,j) can be developed. After substitution of the Taylor approximations in equation (D.2) it follows that:

$$\frac{(h_{i+\frac{1}{2}}u_{i+\frac{1}{2}j}-h_{i-\frac{1}{2}}u_{i-\frac{1}{2}j})}{\delta\xi^1}+\frac{(h_{i+\frac{1}{2}}-h_{i-\frac{1}{2}})(\xi^2_{j-\frac{1}{2}}u_{ij-\frac{1}{2}}-\xi^2_{j+\frac{1}{2}}u_{ij+\frac{1}{2}})}{\delta\xi^1\delta\xi^2}+$$
$$\frac{(x_{i+\frac{1}{2}}-x_{i-\frac{1}{2}})(w_{ij+\frac{1}{2}}-w_{ij-\frac{1}{2}})}{\delta\xi^1\delta\xi^2}=$$
$$\left(\frac{\partial}{\partial\xi^1}\left[a^2_{(2)}u\right]\right)_{ij}+\left(\frac{\partial}{\partial\xi^2}\left[-a^2_{(1)}h'u+a^1_{(1)}w\right]\right)_{ij}+$$
$$(\delta\xi^1)^2\left(\frac{h}{24}\frac{\partial^3 u}{\partial(\xi^1)^3}+\frac{h''}{8}\frac{\partial u}{\partial\xi^1}-\frac{h'''}{24}\xi_j^2\frac{\partial u}{\partial\xi^2}-\frac{h'}{8}\xi_j^2\frac{\partial^3 u}{\partial(\xi^1)^2\partial\xi^2}+\frac{x'''}{24}\frac{\partial w}{\partial\xi^2}\right)_{ij}+$$
$$(\delta\xi^2)^2\left(-\frac{h'}{4}\frac{\partial^2 u}{\partial(\xi^2)^2}-\frac{h'}{6}\xi_j^2\frac{\partial^3 u}{\partial(\xi^2)^3}+\frac{x'}{24}\frac{\partial^3 w}{\partial(\xi^2)^3}\right)_{ij}+O((\delta\xi^1)^3,(\delta\xi^2)^3) \tag{D.6}$$

Equation (D.6) shows that the truncation error of the in this work used discretization for the continuity equation is of second-order in $(\delta\xi^1,\delta\xi^2)$. From equation (D.6) it is also clear that steep gradients in h can increase the truncation error. A remedy is to refine the grid. It is also mentioned that a local refinement of the grid in the x-direction can decrease certain terms in the truncation error.

Bibliography

[1] **Bair, S., Khonsari, M. and Winer, W.O.**, 1998, "High-pressure rheology of lubricants and limitations of the Reynolds equation", *Tribology International*, **31**, No. 10, pp. 573-586.

[2] **Barus, C.**, 1893, "Isothermals, isopiestics and isometrics relative to viscosity", *Am. J. of Science*, **45**, pp. 87-96.

[3] **Biesheuvel, A.**, 1995, "Golven in twee fasenstroming", J.M. Burgerscentrum; research school for fluid mechanics, Netherlands.

[4] **Brandt, A. and Dinar, N.**, 1979, "Multigrid solutions to flow problems.", *Numerical Methods for Partial Differential Equations*, Ed. S. Parter, Academic, New York, pp. 53-147.

[5] **Brandt, A.**, 1982. "Guide to multigrid development", *Multigrid methods: Lecture notes in Mathematics* **960**, Ed. W. Hackbusch and U. Trottenberg, Springer Verlag, Berlin, pp. 220-312.

[6] **Briggs, W.L.**, 1987, "A multigrid tutorial", SIAM.

[7] **Cameron, A.**, 1966, "The principles of lubrication", Longmans Green and co ltd, London, UK.

[8] **Cann, P.M., Spikes, H.A., and Hutchinson, J.**, 1996, "The development of a spacer layer imaging method for mapping elastohydrodynamic contacts", *STLE Transactions*, V 36, 4, pp. 915-921.

[9] **Chen, Y. and Heister, S.D.**, 1994, "A numerical treatment for attached cavitation", *Jour. Fluids Eng.*, **116**, pp. 613-618.

[10] **Cheng, H.S., and Dyson, A.**, 1977, "Elastohydrodynamic lubrication of circumferentially-ground rough disks", *ASLE Transactions*, **21**, pp. 25-40.

[11] **Chow, L.S.H., and Cheng, H.S.**, 1976, "The effect of surface roughness on the average film thickness between lubricated rollers", *ASME J. of Tribology*, pp. 177-124.

[12] **Chow P.L., and Saibel E.A.**, 1978, "On the roughness effect in hydrodynamic lubrication", *ASME J. of Tribology*, **100**, pp. 176-180.

[13] **Christensen, H.**, 1970, "Stochastic models for hydrodynamic lubrication of rough surfaces", *Proc. Inst. Mech. Eng.*, **184**, 1, pp. 1013-1026.

[14] **Christensen ,H.**, 1971, "Some aspects of the functional influence of surface roughness in lubrication", *Wear*, **17**, pp. 149-163.

[15] **Christensen, H., and Tonder, K.**, 1971, "The hydrodynamic lubrication of rough bearing surfaces of finite width", *ASME J. of Tribology*, pp. 324-330.

[16] **Christensen, H., and Tonder, K.**, 1973, "The hydrodynamic lubrication of rough journal bearings", *ASME J. of Tribology*, pp. 166-172.

[17] **Constantinescu, V.N.**, 1969, "Gas lubrication", A.S.M.E, New York.

[18] **Dai, R.X., Dong, Q. and Szeri, A.Z.**, 1992, "Approximations in hydrodynamic lubrication.", *Jour. Trib.*, Vol. 114, pp. 14-25.

[19] **Delannoy, Y. and Kueny, J.L.**, 1990, "Two-phase flow approach in unsteady cavitation modeling.", *Cavitation and multiphase flow* **98**, ASME FED, pp. 153-158.

[20] **Dennis, J.E. and Schnabel, R.B.**, 1983, "Numerical methods for unconstrained optimization and nonlinear equations", Prentice-Hall.

[21] **Dowson, D.**, 1979, "History of tribology", Longman Group Limited, London.

[22] **Dowson, D. and Taylor, C.M.**,1979,"Cavitation in bearings", *Ann. Rev. Fluid Mech.*, **11**, pp. 35-66.

[23] **Dowson, D., and Higginson, G.R.**, 1959, "A numerical solution to the elasto-hydrodynamic problem", *J. of Mech. Eng. Science*, **1**, pp. 6.

[24] **Dowson, D., and Higginson, G.R.**, 1966, "Elastohydrodynamic lubrication", The Fundamentals of Roller and Gear Lubrication, Pergamon Press, Oxford, Great Britain.

[25] **Elrod, H.G.**, 1973, "Thin-film lubrication theory for Newtonian fluids with surfaces possessing striated roughness or grooving", *Jour. Lub. Tech.*, pp. 484-489.

[26] **Elrod, H.G.**, 1977, "A review of theories for fluid dynamic effects of roughness on laminar lubricating films", *Proceedings of the Leeds Lyon conference on tribology.*

[27] **Elrod, H.G.**, 1979, "A general theory for laminar lubrication with Reynolds roughness", *Jour. Lub. Tech.*, **101**, pp. 8-14.

[28] **Ertel, A.M.**, 1939, "Hydrodynamic lubrication based on new principles", *Akad. Nauk SSSR Prikadnaya Mathematica I Mekhanika*, V 3, 2, pp. 41-52.

[29] **Fuller, D.**, 1992, "Friction and wear of Gas-lubricated bearings", *in P.J. Blau (ed.), A.S.M. Handbook, Friction, Lubrication and Wear Technology*, **18**, A.S.M., pp. 522-534.

[30] **Goglia, P.R., Cusano, C., and Conry, T.F.**, 1984, "The effects of irregularities on the elastohydrodynamic lubrication of sliding line contacts, part I: Single irregularities", *ASME J. of Tribology*, **106**, pp. 104-112.

[31] **Goglia, P.R., Cusano, C., and Conry, T.F.**, 1984, "The effects of irregularities on the elastohydrodynamic lubrication of sliding line contacts, part II: Wavy surfaces", *ASME J. of Tribology*, **107**, pp. 113-119.

[32] **Grubin, A.N., and Vinogradova, I.E.**, 1949, "Investigation of the contact of machine components", F. Ketova (ed.) Central Scientific Research Institute for Technology and Mechanical Engineering (Moscow), Book No. 30, (DSIR translation No. 337).

[33] **Gümbel, L.**, 1916, "Uber geschmierte Arbeitsräder", *Z. ges. Turbinenwesen*, **13**, pp. 357.

[34] **Hackbusch, W.**, 1985. "Multi-grid methods and applications.", Springer Verlag, Berlin.

[35] **Hackbusch, W.**, 1992. "Elliptic differential equations, theory and numerical treatment.", Springer series in computational mathematics **18**, Springer Verlag Berlin.

[36] **Hamrock B.J., and Dowson, D.**, 1977, "Isothermal elastohydrodynamic lubrication of point contacts", part I, Theoretical Formulation, *ASME J. of Lub. Tech.*, **98**, pp. 223-229.

[37] **Hamrock B.J., and Dowson, D.**, 1977, "Isothermal elastohydrodynamic lubrication of point contacts", part III, Fully Flooded Results, *ASME J. of Lub. Tech.*, **99**, pp. 264-276.

[38] **Harlow, F. and Welch, J.**, 1965, "Numerical calculation of time-dependent viscous incompressible flow", *Phys. Fluids*, **8**, pp. 2182-2189.

[39] **Hoeijmakers, H.W.M. , Janssens, M.E. and Kwan, W.**, 1998, "Numerical simulation of sheet cavitation", *Proceedings of the third international symposium on cavitation*, Grenoble, France.

[40] **Joppich, W**, 1996, "Grundlagen der Mehrgittermethode", GMD, Sankt Augustin.

[41] **Kaneta, M**, 1992, "Effects of surface roughness in elastohydrodynamic lubrication", *JSME*, III, **35**, No 4, pp. 535-546.

[42] **Kingsbury, A.**, 1910, "Thrust bearings", US Patent No. 947242.

[43] **Kubota, A., Kato, H., and Yamaguchi, H.**, 1992, "A new modeling of cavitating flows: A numerical study of unsteady cavitation on a hydrofoil section", *Jour. Fluid Mech.*, **240**, pp. 59-96.

[44] **Martin, H.M.**, 1916, "Lubrication of gear teeth", *Engineering*, **102**, pp. 119-121.

[45] **Michell, A.G.M.**, 1905, "Improvements in thrust and like bearings", British Patent No 875.

[46] **Michell, A.G.M.**, 1905, "The lubrication of plane surfaces", *Z. Math. Phys.*, V 52, 2, pp. 123-137.

[47] **Moffat, H.K.**, 1964, "Viscous and resistive eddies near a sharp corner", *J. Fluid Mech.*, **18**, pp. 1-18.

[48] **Myllerup, C.M. and Hamrock, B.J.**, 1992, "Local effects in thin film lubrication", *Proceedings of the* 19^{th} *Leeds Lyon conference on tribology.*

[49] **Myllerup, C.M. and Hamrock, B.J.**, 1994, "Perturbation approach to hydrodynamic lubrication theory", *Journal of Tribology*, **116**, pp. 110-118.

[50] **Noordmans, J.**, 1996, "Solutions of highly anisotropic Stokes equations for lubrication problems", ECCOMAS 96.

[51] **Oosterlee, K.**, 1993. "Robust multigrid methods for the steady and unsteady incompressible Navier-Stokes equations in general coordinates.", Ph.D. Thesis, Delft University, The Netherlands.

[52] **Pan, C.H.T.**, 1990, "Gas lubrication (1915-1990)", *Achievements in Tribology: on the* 75^{th} *Anniversary of the A.S.M.E. Research Committee on Tribology*, A.S.M.E., New York.

[53] **Patankar, S. V. and Spalding D. B.**,1972, "A calculation procedure for heat and mass transfer in three-dimensional parabolic flows", *Int. J. Heat Mass Transfer*, **15**, pp. 1787-1806.

[54] **Patir, N., and Cheng, H.S.**, 1978, "An average flow model for determining effects of three-dimensional roughness on partial hydrodynamic lubrication", *ASME J. of Tribology*, **100**, pp. 12-17.

[55] **Patir, N., and Cheng, H.S.**, 1978, "Effect of surface roughness orientation on the central film thickness in EHD contacts", *Proc. 1977 Leeds Lyon Symposium on Tribology*, Elsevier, pp. 15-21.

[56] **Patir, N., and Cheng, H.S.**, 1979, "Application of average flow model to lubrication between rough sliding surfaces", *ASME J. of Tribology*, **101**, pp. 220-230.

[57] **Pertusevich, A.I.**, 1951, "Fundamental conclusions from the contact hydrodynamic theory of lubrication", *Izv. Akad. Nauk SSR (OTN)*, **3**, pp. 209-223.

[58] **Phan-Thien, N.**, 1981, "On the effects of parallel and transverse stationary random surface roughness in hydrodynamics lubrication", *Proc. Roy. Soc. Lond*, A, **374**, pp. 569-591.

[59] **Phan-Thien, N.**, 1981, "On the effects of the Reynolds and Stokes surface roughnesses in a two-dimensional slider bearing", *Proc. Roy. Soc. Lond. A*, **377**, pp. 349-362.

[60] **Phan-Thien, N.**, 1982, "Hydrodynamic lubrication of rough surfaces", *Proc. Roy. Soc. Lond.*, A, **383**, pp. 439-446.

[61] **Phan-Thien, N.**, 1982, "On the mean Reynolds equation in the presence of homogeneous random surface roughness", *ASME J. of Tribology*, **49**, pp. 476-480.

[62] **Phan-Thien, N., and Atkinson, J.D.**, 1982, "On the effects of homogeneous Reynolds roughness in a two-dimensional slider bearing with exponential film thickness", *ASME J. of Tribology*, **104**, pp. 220-226.

[63] **Prakash, J.**, 1984, "On the lubrication of rough rollers", *ASME J. of Tribology*, **106**, pp. 211-217.

[64] **Press, W.H., Flannery, S.A., Teukolsky, S.A. and Vetterling, W.T.**, 1992, "Numerical recipes in C: The art of scientific programming", Cambridge university press.

[65] **Reynolds, O.**, 1886, "On the theory of Lubrication and its Application to Mr. Beauchamps Tower's Experiments, including an Experimental Determination of the Viscosity of Olive Oil", *Phil. Trans.*, **177**, pp. 157-234.

[66] **Rhie, C.M. and Chow, W.L.**, 1983, "Numerical study of the turbulent flow past an airfoil with trailing edge seperation", *AIAA journal*, **21**, pp. 1525-1532.

[67] **Richtmyer, R.D. and Morton, K.W.**, 1967, "Difference methods for initial value problems", 2nd edn, London: Wiley-Interscience.

[68] **Roelands, C.J.A.**, 1966, "Correlational aspects of the viscosity-temperature - pressure relationship of lubricating oils", Ph.D. Thesis, Technische Hogeschool Delft, The Netherlands, (V.R.B., Groningen, The Netherlands).

[69] **Saad, Y.**, 1996, "Iterative methods for sparse linear systems", Boston [etc.] : PWS.

[70] **Sadeghi, F., and Sui, P.C.**, 1989, "Compressible elastohydrodynamic lubrication of rough surfaces", *ASME J. of Tribology*, **99**, pp. 2-6.

[71] **Sassenfeld H, and Walther, A.**, 1954, "Gleitlagerberechnungen", *VDI Forschungsheft 441*, Deutscher Ingenieur Verlag GMBH, Düsseldorf Germany.

[72] **Schäfer, C.T., Giese, P. and Woolley, N.H.**, 1999, "Elastohydrodynamically lubricated line contact based on the Navier-Stokes equations", *Proceedings of the* 26^{th} *Leeds Lyon conference on tribology.*

[73] **Sommerfeld, A.**, 1904, "Zur hydrodynamischen Theorie der Schmiermittelreibung", *Z. für Mathematik und physik*, **50**, pp. 97-155.

[74] **South, J.C. and Brandt, A.**, 1976, "Application of a multi-level grid method to transonic flow calculations", NASA Langley Research Center, ICASE report 76-8, Hampton, Virginia.

[75] **Stüben, K., Trottenberg, U.**, 1982, "Multigrid Methods: Fundamental Algorithms, Model Problem Analysis and Applications", *Multigrid methods: Lecture notes in Mathematics* **960**, Ed. W. Hackbusch and U. Trottenberg, pp. 1-176, Springer Verlag, Berlin.

[76] **Sun, D.C.**, 1978, "On the effects of two-dimensional Reynolds roughness in hydrodynamic lubrication", *Proc. R. Soc. Lond. A.*, **364**, pp. 89-106.

[77] **Sun, D.C. and Chen, K.K.**, 1977, "First effects of Stokes roughness on hydrodynamic lubrication", *Jour. Lub. Tech.*, pp. 2-9.

[78] **Teale, J.L., and Lebeck, A.O.**, 1980, "An evaluation of the average flow model for surface roughness effects in lubrication", *ASME J. of Tribology*, **106**, pp. 440-447.

[79] **Thompson, M.C. and Ferziger, J.H.**, 1989, "An adaptive multigrid technique for the incompressible Navier-Stokes equations.", *J. Comput. Phys.*, **82**, pp. 94-121.

[80] **Thompson, C.P. and Lezeau, P.**, 1998, "Application of the full approximation storage method to the numerical simulation of two-dimensional steady incompressible viscous multiphase flows", *Int. J. Numer. Meth. Fluids*, **28**: pp. 1217-1239.

[81] **Tower, B.**, 1883, "First report on friction experiments (friction of lubricated bearings)", *Proc. Instn mech. Engrs*, Nov. 1883, 632-659.

[82] **Tripp, J.H.**, 1983, "Surface roughness effects in hydrodynamic lubrication: The flow factor method", *ASME J. of Tribology*, **105**, pp. 458-465.

[83] **Tripp, J.H., and Hamrock, B.J.**, 1985, "Surface roughness effects in elastohydrodynamic contacts", *Proc. 1984 Leeds Lyon Symposium on Tribology*, Elsevier, pp. 30-39.

[84] **Tzeng, S.T., and Saibel, E.**, 1967, "Surface roughness effects on slider bearing lubrication", *ASLE trans.*, **10**, pp. 334-338.

[85] **Tzeng S.T., and Saibel E.**, 1967, "On the effects of surface roughness in the hydrodynamic lubrication theory of a short journal bearing", *Wear*, **10**, pp. 179-184.

[86] **Vanka, S. P.**, 1985, "Block-implicit calculation of steady turbulent recirculating flows", *Int. J. Heat Mass Transfer*, **28**, pp. 2093-2103.

[87] **Vanka, S. P.**, 1986, "Block-implicit multigrid solution of Navier-Stokes equations in primitive variables", *J. Comput. Phys.*, **65**, pp. 138-158.

[88] **Venner, C.H.**, 1991, "Multilevel solution of the EHL line and point contact problems", Ph.D. Thesis, University of Twente, Enschede, The Netherlands.

[89] **Venner C.H. and Lubrecht, A.A.**, 1994, "Numerical simulation of a transverse ridge in a circular EHL contact under rolling/sliding", *Journal of tribology*, **116**, pp. 751-761.

[90] **Venner, C.H., and Lubrecht, A.A.**, 2000, "Multilevel methods in lubrication", Elsevier, Tribology Series 37, Ed. D. Dowson.

[91] **Venner, C.H., Kaneta, M., and Lubrecht, A.A.**, 2000, "Surface Roughness in Elastohydrodynamically Lubricated Contacts", *Proceedings of the 26th Leeds-Lyon Conference, Leeds, Sept 1999*, Elsevier Tribology Series, **38**, Ed. Dowson et al. pp. 25-36.

[92] **Venner, C.H., Kaneta, M., Nishikawa, H., and Jacod, B.**, 2001, "Effects of Waviness on the film thickness in a circular EHL contact under rolling/sliding", *Proceedings Int. Tribology Conference, Nagasaki 2000., in press*

[93] **Warsi, Z.U.A.**, 1993. "Fluid dynamics, theoretical and computational approaches", CRC Press, cop.

[94] **Wees van der, A.J.**, 1988, "A nonlinear multigrid method for three-dimensional transonic potential flow", Ph.D. Thesis, Delft University of Technology, The Netherlands.

[95] **Wesseling, P.**, 1992. "An introduction to multigrid methods", John Wiley & Sons.

[96] **Whitehouse, D.J.**, 1994, "Handbook of surface metrology", Institute of physics publishing, Bristol.

[97] **Wijnant, Y.H., Venner, C.H., and Larsson, R.**, 1999, "Effects of Structural Vibrations on the Film Thickness in an EHL circular contact", *ASME J. of Tribology*, **121**, 259-264.

[98] **Wittum, G.**, 1989, "Multi-grid methods for Stokes and Navier-Stokes equations with transforming smoothers: algorithms and numerical results", *Numer. Math.*, **54**, pp. 543-563.

[99] **Wittum, G.**, 1990, "The use of fast solvers in computational fluid dynamics", *(Notes on Numerical Fluid Mechanics* **29***), Proc. 8th GAMM Conference on Numerical Methods in Fluid Mechanics*, Ed. P. Wesseling, Vieweg, Braunschweig, pp. 574-581.

[100] **Zauderer, E.**, 1989, "Partial Differential Equations of Applied Mathematics", 2nd edn., John Wiley & Sons, New York.